Volume 17, Number 1, 2023

Technical University of Cluj-Napoca
North University Centre of Baia Mare
Faculty of Engineering
Electrical, Electronic and Computer Engineering Department

Volume 17, Number 1, 2023

Carpathian Journal of Electrical Engineering

Carpathian Journal of Electrical Engineering

ISSN 1843 - 7583

UTPRESS PUBLISHER

TECHNICAL UNIVERSITY
OF CLUJ-NAPOCA

NORTH UNIVERSITY CENTRE OF BAIA MARE
FACULTY of ENGINEERING

ELECTRICAL, ELECTRONIC AND
COMPUTER ENGINEERING DEPARTMENT

Carpathian Journal of Electrical Engineering

Volume 17, Number 1, 2023

ISSN 1843 – 7583
http://cee.cunbm.utcluj.ro/cjee/

EDITOR-IN-CHIEF

Liviu NEAMȚ — Technical University of Cluj-Napoca, Romania

ASSOCIATE EDITOR

Mircea HORGOȘ — Technical University of Cluj-Napoca, Romania
Ovidiu COSMA — Technical University of Cluj-Napoca, Romania

EDITORIAL SECRETARY

Olivian CHIVER — Technical University of Cluj-Napoca, Romania

SCIENTIFIC BOARD

Gene APPERSON	Digilent Inc. SUA
Cristian BARZ	Technical University of Cluj-Napoca, Romania
Iulian BIROU	Technical University of Cluj-Napoca, Romania
Florin BREABĂN	Artois University, France
Vasilis CHATZIATHANASIOU	*Aristotle* University of Thessaloniki, Greece
Clint COLE	Washington State University, SUA
Iuliu DELESEGA	Polytechnic University of Timişoara, Romania
Luis Adriano DOMINGUES	Brazilian Electrical Energy Research Center, Brazil
Francis Boafo EFFAH	Kwame Nkrumah University of Science & Technology, Ghana
Zoltan ERDEI	Technical University of Cluj-Napoca, Romania
Patrick FAVIER	Artois University, France
Emmanuel Asuming FRIMPONG	Kwame Nkrumah University of Science & Technology, Ghana
Ştefan MARINCA	Analog Devices, Ireland
Andrei MARINESCU	Research and Testing Institute ICMET, Romania
Oliviu MATEI	Technical University of Cluj-Napoca, Romania
Tom O'DWYER	Analog Devices, Ireland
Ioan ORHA	Technical University of Cluj-Napoca, Romania
Sorin PAVEL	Technical University of Cluj-Napoca, Romania
Desire RASOLOMAMPIONONA	Warsaw University of Technology, Poland
Toufik SEBBAGH	University of 20 Août 1955 – Skikda, Algeria
Alexandru SIMION	*Gheorghe Asachi* Technical University of Iasi, Romania
Adam TIHMER	University of Miskolc, Hungary
Radu TÎRNOVAN	Technical University of Cluj-Napoca, Romania
Theodoros D. TSIBOUKIS	*Aristotle* University of Thessaloniki, Greece
Jan TURAN	Technical University of Kosice, Slovakia
Jozsef VASARHELYI	University of Miskolc, Hungary
Andrei VLADIMIRESCU	University of California, Berkeley, USA

CONTENTS

REGULAR PAPERS:

OPTIMAL PID CONTROLLER BASED ON AN IMPROVED SPARROW SEARCH ALGORITHM FOR MULTI-AREA FREQUENCY CONTROL

Amobi Edward **OKOLO**, Elvis **TWUMASI,** Emmanuel Asuming **FRIMPONG**
Department of Electrical and Electronic Engineering, Kwame Nkrumah University of Science and Technology Kumasi, Ghana
Okoloedward19@gmail.com, etwumasi.coe@knust.edu.gh, eafrimpong.soe@knust.edu.gh

Keywords: Area control error, automatic generation control, load frequency control, sparrow search algorithm, PID controller.

Abstract*: To boost power system reliability there must be a good scheme for the automatic generation control to maintain the generation-load balance. The development of this scheme started with the enhancement of the sparrow search algorithm, where the initial population and producer selection was targeted to improve the search quality. The enhancement made was used to optimize the gain parameters of the PID controller increasing the overall system performance. The proposed scheme was tested on the two-area power system in the MATLAB/Simulink environment and comparisons were made with recent publications. Integral time absolute error (ITAE) was used as the performance index. The proposed method shows improved performance with minimum settling time. This work presents the enhancement of the sparrow search algorithm for the automatic generation control of a two-area non-reheat thermal power system.*

1. INTRODUCTION

The goal of a proper electric power system is to supply power to consumers and retain its stability in the process as they have a generation-load balance, therefore sudden changes in generating system capacity or demand could cause a major imbalance[1]. With advancements made over the years, modern power systems now exist as an interconnection between areas and utilities with Tie-lines acting as the medium of power exchange[2] with one of the major identified areas of concern being frequency control [3].

It is imperative for the sustained supply of electricity to consumers to have a good frequency regulation scheme as the lack of any control method after an abrupt load change would cause a deviation in the frequency used in regulating the system. The major factors influencing the proper functioning of the regulating strategy in an AGC system are the controller placement and the level of controller optimization.

Conventionally, load frequency control is designed with an integral controller because it provides very low or zero steady-state deviation as the error signal in the feedback loop is evaluated, however, gives a poor dynamic response[4]. To attend to this setback the use of variable structure control[5], optimal control[6], and linear feedback[4] were proposed. However, the requirement of an in-depth system state became a problem as it was difficult to estimate completely. Consequently, intelligent controllers[3], classical controllers[7], and fuzzy logic controllers[8] have been used to improve on this setback. These techniques are, however, non-adaptive and, in some cases, would require training data offline or randomizing the values of certain parameters, inherently making them sub-optimal. With the various methods proposed, classical controllers such as PID are commonly used by industries. This controller is prone to a lot of errors as the gain parameters are either randomized or un-optimally selected. With the employment of metaheuristic algorithms due to their optimization problem-solving ability in recent times such as particle swarm optimization (PSO) algorithm [9] and teaching learning-based optimization (TLBO) algorithm[2] to optimize this controller, the results still fall short of optimal performance as the algorithms are not properly optimized for these function. The necessity therefore arises to use a better optimized and accurate method for the AGC regulating strategy. The contents of this paper address this challenge. This paper proposes the use of an enhanced sparrow search algorithm (SSA) to search the gain parameters of the PID controller.

2. THEORETICAL BACKGROUND

2.1. Sparrow Search Algorithm Optimization

The SSA as described by [10] is enhanced by targeting the initial population and producer selection to improve the search quality and speed. The key components of the algorithm are described below.

The sparrow search algorithm works on the basic foraging principle, with producers being the group in the population that searches for food and the scroungers being the group that follows the producers around to get food, while some members of the population perform anti-predation action, warning the others of dangerous predators causing the whole population to relocate.

The initial sparrow positions in the population are described as

$$x = \begin{bmatrix} x_{1,1} & x_{1,2} & \cdots & \cdots & x_{1,d} \\ x_{2,1} & x_{2,2} & \cdots & \cdots & x_{2,d} \\ \vdots & \vdots & \vdots & \vdots & \vdots \\ x_{n,1} & x_{n,2} & \cdots & \cdots & x_{n,d} \end{bmatrix} \tag{1}$$

where number and dimension of sparrow are given as '*n*' and '*d*' respectively.

The fitness of the established sparrows is given as

$$Fx = \begin{bmatrix} F[(x_{1,1} & x_{1,2} & \cdots & \cdots & x_{1,d}]) \\ F[(x_{2,1} & x_{2,2} & \cdots & \cdots & x_{2,d}]) \\ \vdots & \vdots & \vdots & \vdots & \vdots \\ F[(x_{n,1} & x_{n,2} & \cdots & \cdots & x_{n,d}]) \end{bmatrix} \tag{2}$$

The Producer location update is given as

$$x_{i,j}^{t+1} = \begin{cases} x_{i,j}^{t}.\, exp\left(\frac{-i}{\alpha.iter_{max}}\right) & if \;\; R_2 < ST \\ x_{i,j}^{t} + Q.L \;\; if & R_2 \geq ST \end{cases} \tag{3}$$

where current iteration is indicated by *t*, *j* represents the dimension, *i* represents the current sparrow, the highest iteration is represented by $iter_{max}$, α is chosen as a random number between 0 and 1, ST ∈[0.5,1] is the safety threshold, the alarm value is represented by R2 ∈ [0,1], Q is a random number that follows a normal distribution, and *L* is a 1 × d matrix with all ones. A safe sparrow population is represented as $R_2 < ST$ while $R_2 \geq ST$ means the sparrows face danger.

The Scroungers location update is given as

$$x_{i,j}^{t+1} = \begin{cases} Q.\, exp\left(\frac{x_{worst}^{t} - x_{i,j}^{t}}{i^2}\right) & if \; i > \frac{n}{2} \\ x_{i,j}^{t+1} + \left|x_{i,j}^{t} - x_{p}^{t+1}\right|.\, A^{+}.L \quad otherwise \end{cases} \tag{4}$$

In the above equation the optimal position inhabited by the producer is given as Xp, the current global worst position is indicated as X_{worst} and A+ = $A^T(AA^T)^{-1}$ where *A* represents a matrix of 1 × d whose elements is randomly assigned 1 or −1.

The anti-predation action location update is given as

$$x_{i,j}^{t+1} = \begin{cases} x_{best}^{t} + \beta\,.\,|x_{i,j}^{t} - x_{best}^{t}| & if\; f_i > f_g \\ x_{i,j}^{t} + K.\left(\frac{\left|x_{i,j}^{t} - x_{worst}^{t}\right|}{(f_i - f_w) + \varepsilon}\right) & if\; f_i = f_g \end{cases} \tag{5}$$

The current global optimal location is denoted as x_{best}^{t}, the step size control parameter is given as β, with variance of 1 and mean of 0, K ∈ [−1, 1] is the sparrow flying movement indicator. The current sparrow fitness, the global best and worst sparrow values are given as, f_i, f_g and f_w respectively and ε is put in place to avoid prevent zero divison error. Sparrows at the edge and middle of the population are given as $f_i > f_g$ and $f_i = f_g$.

2.2. Automatic Generation Control

The interconnected power system is made up of several controlling areas with the generators acting as one unit. Contained in each area is the load drawn, the generator, the prime mover or turbine, and the governor. As the system load increases the turbine speed drops to allow the governor to adjust the input to the level of the new load. If the deviation to the turbine speed caused by the load increase, reduces, the system error signal reduces while the governor control mechanism gets closer to the constant speed maintenance threshold[11]. This, however, does not guarantee it gets to the exact point in the threshold required to maintain that constant speed as the turbine-governor control alone forces all generating units to respond irrespective of the location of load change. The addition of secondary control, however, guarantees the turbine speed returns to its initial set point. This entire scheme where a change in load would require an equivalent change in a generation to maintain the system frequency is known as Automatic Generation Control (AGC) also referred to as load frequency control[12]. The objectives of the LFC are fairly simple. The first is to maintain frequency uniformly, the second is to ensure the load is split among the generators, and lastly is to regulate tie-line flow. The use of the turbine-governor control is referred to as the primary control while the use of a supplementary control is known as the secondary control.

2.3. SSA-Based Pid Design

A load change by any area should be absorbed by that area. To achieve this the tie-line power and frequency deviation are added to the loop integrating the secondary controller into the system. This is also known as the tie-line bias control which is the basis for the conventional load frequency control. Therefore, by a linear combination, the net change observed by the system in the frequency and tie-line flows is weighted to an error unit known as the area control error ACE.

$$ACE_i = \Delta P_{tie_i} + B_i \Delta f_i \tag{6}$$

Where i in ACE_i denotes the area for the area control error unit. ΔP_{tie_i} denotes a change in tie line flow, B_i is the bias factor at each area i, and Δf_i is the frequency change.

The controller function is based on a feedback control principle. The three major parameters for this controller are the proportional gain value, the integral gain value, and the derivative gain value[13]. These three parameters have varying reactions when actively operating. The response to recent or current errors is decided by the proportional function, the response to the sum of recent errors is controlled by the integral function and the response to the rate of error change is determined by the derivative function[8]. When in operation in a feedback control system the cumulative sum of these three parameters is used to make adequate adjustments to the system. To tune the PID controller optimally it needs to be integrated into the system. The integration of the ACE to the PID controller is given as

$$U_i(t) = K_p ACE_i + K_i \int ACE_i dt + K_d \frac{d(ACE_i)}{dt} \tag{7}$$

where K_p, K_i, and K_d represent the proportional, integral and derivative gain parameters of the PID controller. $U_i(t)$ is the controlled input to the PID controller.

2.4. Objective Function

The best PID controller gains for a system depend on the desired performance, as measured by a performance index. The most common performance index is the integral criterion, which measures the total accumulated error over time. Examples of integral criterion-based performance indices include integral absolute error (IAE), integral square error (ISE), integral time absolute error (ITAE), and integral time multiples of square error (ITSE)[14]. With IAE there is a degree of difficulty in computing the error's absolute value analytically and as such systems with this criterion give a slow response. Though impractical for real-time analytical works, it is often employed in a system digital simulation. ISE produces less overshot but has a large settling time as it focuses on larger errors. The ITSE though having an extra time error function and prioritizing errors with longer duration tends to give large outputs when the reference has a sudden change in its value. The ITAE also has an extra time error function and giving priority to long-duration errors reduces the system overshoot and increases the system settling time, with works from [14],[15], and [16] showing significant system improvement while using the ITAE. The ITAE for a two-area power system is represented as objective function *J*

$$J = \int_{t=0}^{t_{final}} t(|\Delta f_1| + |\Delta f_2| + |\Delta P_{tie}|)dt \tag{8}$$

From the equation above Δf_1 and Δf_2 indicate the deviation in system frequency for area 1 and 2 while ΔP_{tie} is change in tie line power and t_{final} is the duration of simulation.

$$\Delta f_i = \frac{U_i(t)}{B(K_i \int dt + K_p + K_d \frac{d}{dt})} - \frac{\Delta P_{tie}}{B} \tag{9}$$

Equation 9 represents the gain parameters of the PID controller as object to frequency change in any area:

$$\Delta P_{tie} = \frac{U_i(t)}{K_i \int dt + K_p + K_d \frac{d}{dt}} - B\Delta f_i \tag{10}$$

Equation 10 represents the gain parameters of the PID controller as object to change thr line power.

The LFC is solved as an optimization problem with constraints and the controller parameter being the boundaries of the constraints. In this case the PID controller. The objective function J is minimized using the equation below.

$$\begin{Bmatrix} K_{p,min} \le k_p \le k_{p,max} \\ K_{i,min} \le k_i \le k_{i,max} \\ K_{d,min} \le k_d \le k_{d,max} \end{Bmatrix} \tag{11}$$

The gain parameters are chosen randomly from 0 to 1, making 0 the lower bound and 1 the upper bound.

3. THE ENHANCED SPARROW SEARCH ALGORITHM

3.1. Opposition Based-Initialization

The initialization of the sparrow population greatly affects its search ability. Therefore, the opposition-based initialization is applied. The idea is that the random initialization of a search agent could make it far from the ideal position. Taking the opposite of the search agent in a defined search space makes brings it closer to the ideal position[17]. If a search space has boundaries “a” and “b” and the agent generated is x, the opposite of this agent would be given as:

$$X_{opp} = (a + b) - x \tag{12}$$

3.2. Improved Producer Selection

The sparrow population selects individuals with good fitness values as the producers. This may reduce the efficiency as the population almost entirely depends on this group for

survival. The fitness of every sparrow generated is assessed and the average fitness is calculated. Individuals with fitness values above average are selected as producers. Thus, giving the function of the producers to highly fit members. The average fitness is given as:

$$F_{average} = \frac{f1+f2+\cdots fn}{N} \quad (13)$$

This improvement is called the Adaptive opposition SSA (AOSSA).

4. IMPLEMENTATION OF ADAPTIVE-OPPOSITION BASED SSA (AOSSA) IN PID CONTROLLER

1 step Parameter initialization. Population size, Max number of iterations, objective or fitness function, boundary limits, and dimension
2 step The PID controller parameters are randomly generated as the search agents. These are the P, I, and D gain constant of the controller
3 step Evaluate the opposite of the generated search agents
4 step The fitness function of the generated search agents is evaluated using J
5 step The average of the fitness function is taken
6 step Generate alarm value randomly
7 step Position update for the producer
8 step Position Update for the scroungers
9 step Anti-Predation position update for the population
10 step Calculate fitness value from the updated locations
11 step If the new location is better than the old update it
12 step Analogously the controller gain parameters are modified
13 step If the stopping criterion is reached the best parameter variable are given as outputs else the process is repeated from step 7

4. TESTING

A two-area interconnected system with non-reheat thermal power plants is used as the test system. A case study involving a step load change is applied to both areas as shown.

The controller to be used for this work replaces the original secondary controller with a slight change. The controller placement is imperative to the overall effectiveness of the scheme. Therefore, to improve the tie-line control the secondary controller replaces the

original control strategy placed on the tie-line. The parameters of the system are given in *figure 1* [11].

.

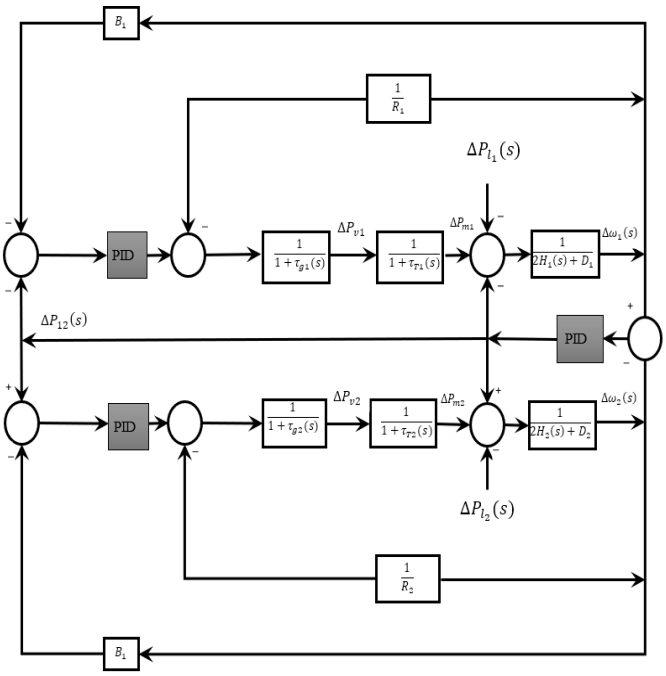

Fig.1 Two-area AGC diagram with PID controller

Table 1. Transposing principle

AREA	1	2
Speed Regulation (R)	0.05	0.0625
Frequency-Sensitive Load Coefficient (D)	0.6	0.9
Inertia Constant (H)	5	4
Base Power	1000MVA	
Governor Time Constant (Tg)	0.2	0.3
Turbine Time Constant (Tt)	0.5	0.6
Step Load	0.1875	0.140

The proposed model was simulated in MATLAB 2021 in a computer designed with, Intel(R) Core (TM) i7-8750H CPU @ 2.20GHz 2.21 GHz, 8.00 GB (7.89 GB usable) RAM, 64-bit operating system, x64-based processor, and Windows 11 Pro.

To test the effectiveness of the proposed scheme it is tested on 3 different AGC two-area systems.

The first test (test 1) is carried out on a modified non-reheat thermal power system [11] comparing PID tuned with the classical method, PID tuned with original SSA and PID tuned with AOSSA.

The second test (Test 2) is carried out on a standard non-reheat thermal power system [18] with a step load of 0.014 and 0.028 in areas 1 and 2 respectively, comparing an adaptive PI-GA control technique to the PID tuned with AOSSA

The third test (Test 3) is carried out on a standard thermal power system [9] with a step load of 0.2 and 0.1 in areas 1 and 2 respectively, comparing a PID tuned with Particle swarm optimization to the PID tuned with AOSSA

All system loading conditions are modified at t=0. The system results are then analyzed for the Area control error for areas 1 and 2, the frequency response for areas 1 and 2, and the Tie-line response and are compared on basis of Peak overshoot, Peak undershoots, and Settling time.

NB: Tests 2 and 3 use a table for comparing values as the complete data points are unavailable.

6. RESULTS AND ANALYSIS

6.1. *Opposition Based-Initialization Results for the optimized load frequency control scheme*

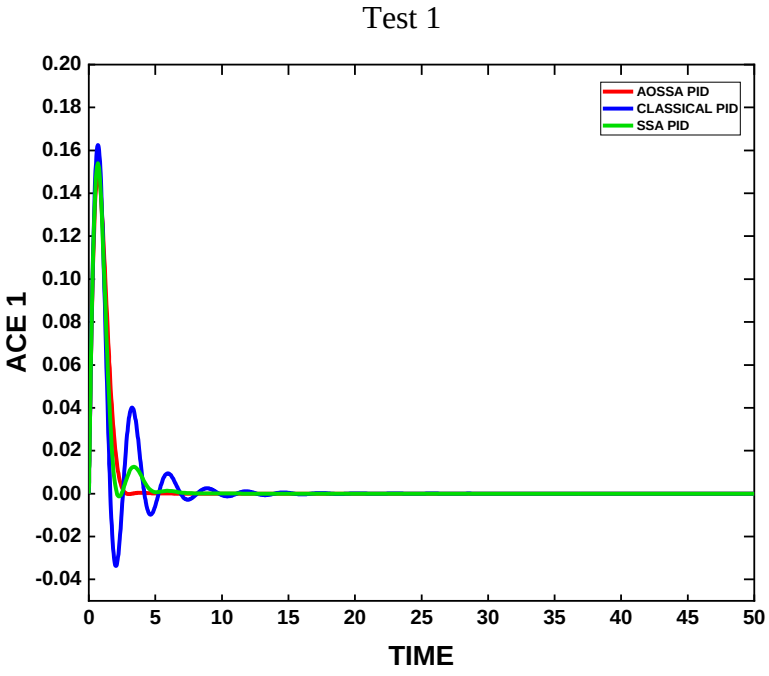

Fig. 1. ACE 1(test 1)

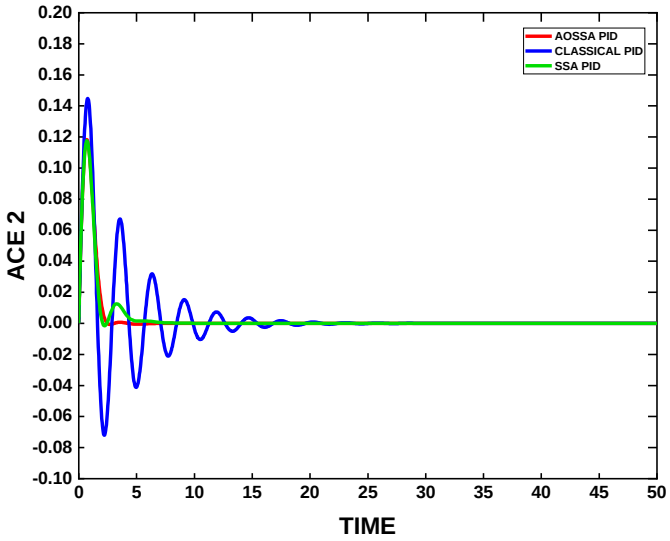

Fig. 2. ACE 2(test 1)

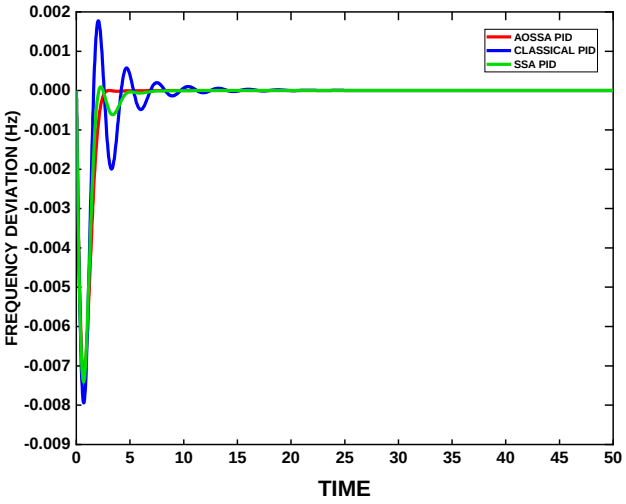

Fig. 3. Frequecy response Area 1(test 1)

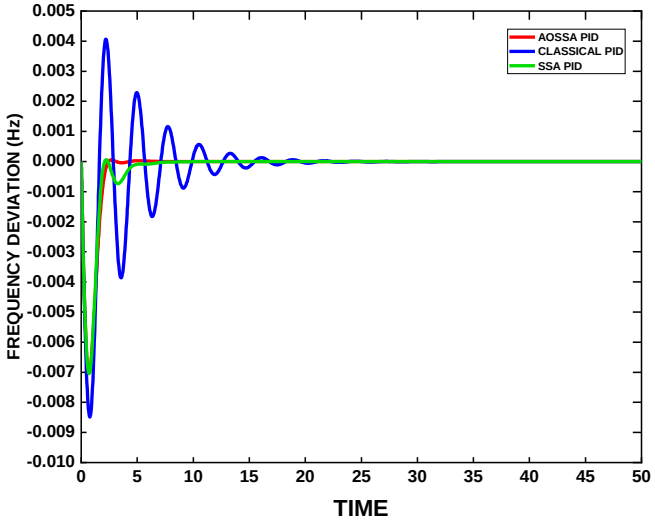

Fig. 4. ACE 1 Frequency Response Area 2(test 1)

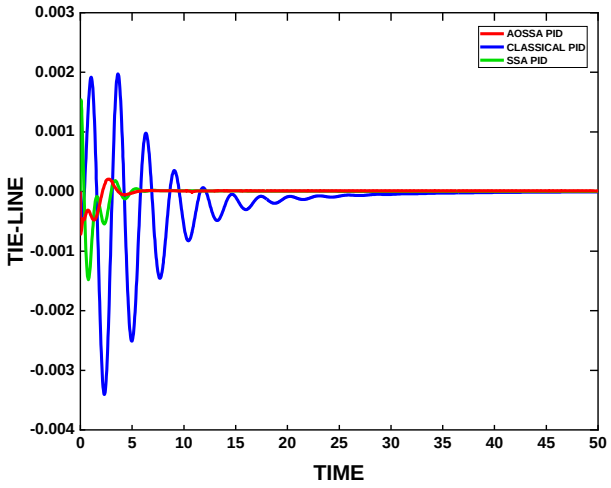

Fig. 5. Tie-line response (test 1)

Table 1. test 2 and 3 results

Evaluations	*PI-GA*	*AOSSA*		*PSO*	*AOSSA*
	Test 2			*Test 3*	
ACE 1					
OVERSHOOT	*0.0022*	***0***		*0.15*	***0.1473***
UNDERSHOOT	***0.001***	*0.016*		*0.00008*	***0***
SETTLING TIME	*7*	***5.5***		*7.5*	***2.9***
ACE 2					
OVERSHOOT	*0.0009*	***0***		*0.1035*	***0.1177***
UNDERSHOOT	***0.0032***	*0.0115*		*0.0002*	***0***
SETTLING TIME	*7.2*	***6.5***		*11*	***2.618***
TIE-LINE					
OVERSHOOT	*0.0018*	***0.001***		*0.0015*	***0.000224***
UNDERSHOOT	***0.0002***	*0.0058*		*0.003*	***0.0007***
SETTLING TIME	*8*	***6.4***		*20*	***5.8***
Δf_1					
OVERSHOOT	*0.0025*	***0.0015***		*0.0001*	***0***
UNDERSHOOT	***0.0028***	*0.037*		*0.0072*	***0.007***
SETTLING TIME	*10*	***4.1***		*16*	***2.597***
Δf_2					
OVERSHOOT	*0.0041*	***0***		*0.000003*	***0***
UNDERSHOOT	***0.0048***	*0.027*		*0.00615*	***0.007***
SETTLING TIME	*10*	***7***		*20*	***2.85***

6.2. Test analysis

The results presented *figure 2* which represents area control error measurement for area 1, shows that the PID controller tuned with the AOSSA has a 9% improvement in peak overshoot, 100% improvement in peak undershoot, 83.4% improvement in settling time in comparison to the PID controller tuned with the classical method and 4.3% improvement in peak overshoot, 100% improvement in peak undershoot and 45.3% improvement in settling time in comparison with the PID controller tuned with the original sparrow search algorithm. *Figure 3* which represents the area control error measurement for area 2 shows the PID controller tuned with AOSSA having a 17%, 100% and 97% improvement in peak overshoot, peak undershoot and settling time respectively in comparison to the PID controller tuned with the classical method and a 0%, 0% and 6.5% improvement in peak overshoot, peak undershoot and settling time respectively in comparison to the PID controller tuned with the original SSA.

Figure 4 representing the frequency response in area 1 shows a 100%, 9% and 97% improvement the proposed method has over the PID controller tuned with the classical method in peak overshoot, peak undershoot and settling time respectively and a 100%, 2.3% and 64% improvement the proposed method has over the PID controller tuned with the original SSA in peak overshoot, peak undershoot and settling time respectively. Figure 5 representing the frequency response in area 2 shows a 100%, 16.7% and 87.7% improvement the proposed method has over the PID controller tuned with the classical method in peak overshoot, peak undershoot and settling time respectively and a 0%, 0.7% and 33.7% improvement the proposed method has over the PID controller tuned with the original SSA in peak overshoot, peak undershoot and settling time respectively.

The tie-line power flow represented by *figure 6* shows a 98.5%, 95% and 3% improvement the proposed method has over the PID controller tuned with the classical method in peak overshoot, peak undershoot and settling time respectively and a 0%, 0.7% and 33.7% improvement the proposed method has over the PID controller tuned with the original SSA in peak overshoot, peak undershoot and settling time respectively. Table 2 depicts the performance of the of the proposed method in comparison with methods in literature. Table 2 shows in bold the method with the better performance in each measured category. Test 2 shows the PID tuned with AOSSA having a better performance in peak overshoot and settling time in comparison PI-GA in all evaluations provided. Test 3 shows the PID controller tuned with AOSSA having a better performance in peak overshoot, peak undershoot and settling time in comparison to the PID controller tuned with PSO.

The results show the proposed control scheme having the best performance in peak overshoots, peak undershoots, and settling time when compared to the PID tuned with the classical method and PID tuned with the original sparrow search algorithm.

7. CONCLUSION

Firstly, a modification was made to the sparrow search algorithm to improve the adaptability and search quality. This improvement is called the Adaptive opposition-based sparrow search algorithm. (AOSSA). The improvement targeted the initial sparrow population and the producer selection. The enhancement made was used to search the gain parameters of the PID controller, then 3 tests were performed. The control scheme proposed performed better than the other control schemes, having a better settling time and a good dynamic performance. Overall, the enhancement made in this paper achieved the load frequency control objective with sufficient improvements.

REFERENCES

[1] P. M. Anderson, *Protection against Abnormal System Frequency,* in Power System Protection, IEEE, 2010.

[2] M. K. Debnath, *Automatic Generation Control of a two area multi-unit interconnected power system with Proportional-Integral-Derivative controller with Filter (PIDF) optimized by TLBO algorithm,* 2016 Int. Conf. Circuit, Power Comput. Technol., pp. 1–6, 2016.

[3] S. Bhongade, H. O. Gupta, and B. Tyagi, *Artificial neural network based automatic generation control scheme for deregulated electricity market,* 2010 9th Int. Power Energy Conf. IPEC 2010, pp. 1158–1163, 2010, doi: 10.1109/IPECON.2010.5696997.

[4] M. Nagendra and M. Krishnarayalu, *PID Controller Tuning using Simulink for Multi Area Power Systems,* Int. J. …, vol. 1, no. 7, pp. 1–9, 2012, [Online]. Available: http://www.researchgate.net/publication/231582561_PID_Controller_Tuning_using_Simulink_for_Multi_Area_Power_Systems/file/d912f506fcf4449ddd.pdf.

[5] Z. M. Al-Hamouz and Y. L. Abdel-Magid, *Variable structure load frequency controllers for multiarea power systems,* Int. J. Electr. Power Energy Syst., vol. 15, no. 5, pp. 293–300, 1993, doi: 10.1016/0142-0615(93)90050-W.

[6] Y. L. Karnavas, *On the optimal control of interconnected electric power systems in a re-structured environment using genetic algorithms,* WSEAS Trans. Syst., vol. 4, no. 8, pp. 1248–1258, 2005.

[7] M. K. Debnath, T. Jena, and R. K. Mallick, *Novel PD-PID cascaded controller for automatic generation control of a multi-area interconnected power system optimized by grey wolf optimization (GWO),* 1st IEEE Int. Conf. Power Electron. Intell. Control Energy Syst. ICPEICES 2016, pp. 1–6, 2017, doi: 10.1109/ICPEICES.2016.7853271.

[8] R. Verma, S. Pal, and S. Sathan, *Intelligent automatic generation control of two-area hydrothermal power system using ANN and fuzzy logic,* Proc. - 2013 Int. Conf. Commun. Syst. Netw. Technol. CSNT 2013, pp. 552–556, 2013, doi: 10.1109/CSNT.2013.119.

[9] H. A. Illias, N. Nurjannah, and H. Mokhlis, *Optimal Performance of Automatic Generation Control for Two-Area Power System using Particle Swarm Optimization*, 3rd IEEE Int. Virtual Conf. Innov. Power Adv. Comput. Technol. i-PACT 2021, pp. 1–5, 2021, doi: 10.1109/i-PACT52855.2021.9696446.

[10] J. Xue and B. Shen, *A novel swarm intelligence optimization approach: sparrow search algorithm*, Syst. Sci. Control Eng., vol. 8, no. 1, pp. 22–34, 2020, doi: 10.1080/21642583.2019.1708830.

[11] *[Hadi_Saadat]_Power_System_Analysis(BookZa.org).pdf.*

[12] Prabha Kundur - *Power System Stability and Control (part 2)*-McGraw-Hill Professional (1994).

[13] K. J. Åström and T. Hägglund, *PID controllers: theory, design and tuning*, vol. 2. 1995.

[14] D. Guha, P. Kumar, and S. Banerjee, *Load frequency control of interconnected power system using grey wolf optimization*, Swarm Evol. Comput., pp. 1–19, 2015, doi: 10.1016/j.swevo.2015.10.004.

[15] R. K. Sahu, S. Panda, and S. Padhan, *A hybrid firefly algorithm and pattern search technique for automatic generation control of multi area power systems, I*nt. J. Electr. Power Energy Syst., vol. 64, pp. 9–23, 2015, doi: 10.1016/j.ijepes.2014.07.013.

[16] R. K. Sahu, S. Panda, and G. T. Chandra Sekhar, *A novel hybrid PSO-PS optimized fuzzy PI controller for AGC in multi area interconnected power systems*, Int. J. Electr. Power Energy Syst., vol. 64, pp. 880–893, 2015, doi: 10.1016/j.ijepes.2014.08.021.

[17] H. R. Tizhoosh, *Opposition-based learning: A new scheme for machine intelligence*, Proc. - Int. Conf. Comput. Intell. Model. Control Autom. CIMCA 2005 Int. Conf. Intell. Agents, Web Technol. Internet, vol. 1, pp. 695–701, 2005, doi: 10.1109/cimca.2005.1631345.

[18] I. K. Otchere, K. A. Kyeremeh, and E. A. Frimpong, *Adaptive PI-GA Based Technique for Automatic Generation Control with Renewable Energy Integration*, 2020 IEEE PES/IAS PowerAfrica, PowerAfrica 2020, pp. 2020–2023, 2020, doi: 10.1109/PowerAfrica49420.2020.9219960.

[19] N. Kurakula, M. Nithya, and C. N. S. Kalyan, *Enhancement in AGC Performance of Multi Area Interconnected Power System with Practical Constraints using WCA based PIDD Controller*, 2022 2nd Int. Conf. Power Electron. IoT Appl. Renew. Energy its Control. PARC 2022, pp. 1–6, 2022, doi: 10.1109/PARC52418.2022.9726598.

EXTENDED APPLIED DATA CLEANING METHODS IN OUTLIER DETECTION FOR RESIDENTIAL CONSUMER

Dacian I. **JURJ**, Dan D. **MICU**, Alexandru G. **BERCIU**, Mircea **LANCRAJAN**, Levente **CZUMBIL**, Andrei **BENDE**, Bogdan A. **MITRACHE**, Alexandru **MUREȘAN**

Technical University of Cluj-Napoca

dacian.jurj@ethm.utcluj.ro, Dan.Micu@ethm.utcluj.ro, Alexandru.Berciu@campus.utcluj.ro, lancranjanmircea98@gmail.com, Levente.CZUMBIL@ethm.utcluj.ro, andrei.bende28@gmail.com, bogdan.mitrache99@gmail.com, Alexandru.Muresan@ethm.utcluj.ro

Keywords: Energy measurement; Artificial intelligence; Statistics; Probabilistic computing; Data science; Data aggregation; Algorithms; Energy efficiency

Abstract*: This paper delves into the subject of outlier detection techniques tailored for unique datasets related to residential energy consumption. Building upon the current state of research [1] we introduce the Grubbs and Z-score methods and investigate a range of outlier detection strategies encompassing statistical, probabilistic, and machine learning algorithms. The findings underscore the importance of outlier detection in the Romanian residential energy sector.*

1. INTRODUCTION

Outlier detection in energy data plays a pivotal role in ensuring the accuracy and reliability of energy management systems [2]. By identifying and addressing anomalies, utilities and energy managers can gain a clearer understanding of consumption patterns, optimize energy distribution, and prevent potential system failures [3]. Moreover, detecting outliers, aids in eliminating data errors, facilitating more precise forecasting [4], and enhancing the overall efficiency of energy systems. In essence, it serves as a foundational step in refining energy data analysis and driving informed decision-making in the energy sector [5]. In the current study, serving as an extension to the article "Applied data cleaning methods in outlier detection for residential consumer" [1], the outlier detection methodologies tailored for specialized datasets related to residential energy consumption are examined. This

exhaustive research covers a broad range of outlier detection techniques in data cleaning, from statistical and probabilistic methods to advanced machine learning algorithms. Notably, the Z-score [6] and Grubbs [7] methods are introduced and integrated into this expanded investigation, enhancing the analytical depth.

2. CONTEXT

Understanding the nature of a dataset is essential when applying algorithms or mathematical methods [8], especially when distinguishing energy consumption patterns across residential, industrial, and public buildings. Energy consumption characteristics differ significantly among residential homes, public infrastructures, and industrial facilities due to diverse usage patterns, energy needs, and operational demands [9]. Residential energy use is shaped by factors like home size, design, occupancy, construction materials, lifestyle, and appliance usage. Typically, residential energy patterns show spikes during morning and evening, reflecting daily routines, and dip during the night. Seasonal changes, such as increased heating or cooling needs during harsh weather, also play a role. Moreover, individual behaviors, household income, and occupants' education levels further influence these patterns [10]. Public structures, like schools, hospitals, and government offices, have energy patterns distinct from residential settings. Given their high occupancy and continuous operations, their energy use remains relatively consistent throughout the day, with higher consumption on weekdays than weekends. Unlike residences, seasonal fluctuations in energy use in public buildings are less pronounced, mainly due to their climate control systems [11].

Industrial sectors, including factories and warehouses, have unique energy consumption patterns driven by their production activities, machinery operations, and specific requirements. The energy demand in these settings is often high and consistent, influenced by machinery and equipment operations. However, energy use can vary based on production timelines, work shifts, and the nature of the industry. For instance, chemical industries might have different energy needs compared to textile ones. Industries linked to agriculture might see seasonal shifts in energy use, reflecting harvest times or changing product demands [12].

The importance of outlier detection in residential energy consumption arises from the diverse and ever-changing monthly energy use patterns. In contrast to public or industrial settings, monthly household energy consumption is influenced by numerous, primarily static, technical factors. These include home features, resident lifestyles, and energy use behaviors, which are often affected by seasonal changes [9].

In Romania, the energy sector is regulated by European directives mandating the installation of smart meters in residences by Distribution System Operators (DSO) [13]**Error! Reference source not found.**. However, the rollout of this initiative has been delayed, with DSOs typically manually reading meters every 3-6 months. While new

regulations advocate for monthly readings, a disconnect exists between governmental intentions and the present capabilities of DSOs.

A significant shift occurred in the Romanian energy market in 2021 when it embraced free-market principles [14]. This change has spurred discussions on introducing various services and concepts, like demand response, differential tariffs, and local energy communities. Technically, these services necessitate precise monthly energy consumption data across all sectors, including households. Yet, due to current metering constraints, such data remains elusive.

For instance, the idea behind energy communities revolves around consolidating numerous households within similar geographic regions into a single organizational structure. This encourages them to actively engage in the energy market, promoting bi-directional energy exchanges (prosumers). In this context, precise monthly energy consumption predictions are crucial for securing smart energy contracts and negotiating favorable future [15].

A significant hurdle in Romania is obtaining accurate residential energy consumption data, primarily sourced from physical or digital energy bills. Given that current Romanian regulations require DSOs to check meters every 3-6 months, utility companies often resort to estimations. This approach frequently leads to substantial variations and anomalies in monthly billing, complicating the task of algorithms aiming to identify and rectify such patterns [16]. Consequently, due to these metering challenges, billed energy often doesn't mirror actual consumption, highlighting the need for a precise data adjustment method.

Such inconsistencies often manifest as outliers or anomalous data points, which significantly deviate from typical energy consumption trends. Identifying and addressing these outliers in the residential sector is pivotal for ensuring data accuracy in energy analysis, billing, and forecasting. This sets the stage for a robust data processing approach tailored [17] for the evolving needs of the Romanian energy market.

3. PREVIOUS RESULTS

The findings from previous research [1] indicated that the IQR method was the most effective, accurately identifying 69.45% of outliers. Both the MAD and MOVMAD methods displayed commendable results, detecting outliers at rates of 62.89% and 48.10%, respectively. In contrast, the LOF method's performance was less satisfactory, pinpointing just 23.83% of outliers.

Generally, the outlier detection techniques discussed in this study necessitate a substantial volume of data for precise outcomes. Despite the inherent challenges with residential energy consumption datasets, which typically comprise 12 data points annually, the researchers successfully adapted most of the algorithms. However, the parameters used

for testing DBSCAN didn't match the outlier profiles, suggesting a need for further refinement of this method.

These insights underscore the effective implementation of the discussed methodology on datasets pertaining to the residential energy domain. Proper outlier identification is pivotal for data quality enhancement, deeper insights into energy consumption trends, and facilitating informed decisions in the residential arena. The findings advocate for the IQR method, succeeded by MAD and MOVMAD, as potential techniques for outlier detection in domestic energy data. Still, there's a call for more research to further hone these detection methods for superior precision.

4. METHOD USED

Given that statistical models have demonstrated greater efficiency with smaller data volumes in detecting outliers from the tested energy data consumption, the Z-score [18] and Grubbs [19] methods were selected for this study analysis. Both techniques are renowned for their efficacy in statistical analysis and outlier detection. By integrating these methods, the research aims to address the existing gaps and elevate the accuracy of data cleaning, ensuring more reliable and robust results in the realm of energy consumption analysis.

The Z-score [8], often referred to as the standard score, measures how many standard deviations a data point is from the mean of a set of data. It's a useful metric in statistics to identify outliers, as it quantifies the extent to which a particular observation deviates from the norm.

Mathematically, the Z-score for an individual data point x is calculated as:

$$\mathrm{Z} = \frac{x-\mu}{\sigma} \tag{1}$$

where:

- x is the individual data point.
- μ is the mean of the dataset.
- σ is the standard deviation of the dataset.

A Z-score [8] of 0 indicates that the data point's score is identical to the mean score. A Z-score of 1.0 indicates a value that is one standard deviation from the mean. Z-scores may be positive or negative, with a positive value indicating the score is above the mean and a negative score indicating it is below the mean. In many contexts, a Z-score above 2.0 or below -2.0 is considered an outlier, but this threshold can vary based on the specific application or field of study.

Grubbs' Test [19] is a statistical test used to detect outliers in a univariate data set that follows an approximately normal distribution. The test works by comparing the absolute deviation of a suspected outlier from the sample mean to the sample standard deviation. If this ratio is sufficiently large, the data point can be considered an outlier.
Mathematically, the Grubbs' statistic *G* for a given observation *xi* is calculated as:

$$G = \frac{\max(x_i - \bar{x})}{s} \quad (2)$$

where:

- x_i is the individual data point being tested.
- $\bar{x}$ is the sample mean.
- s is the sample standard deviation.

4. RESULTS

In this study, data was collected from 100 volunteering households. This data was then anonymized, cataloged, and subsequently analyzed. Energy consumption information was sourced from energy bills. However, it became evident that the recorded data didn't truly mirror the genuine energy usage patterns of the households. This discrepancy arose from the data processing system that relied on "estimations" and "energy meter readings". In Table 1 each data point represented the monthly energy consumption over the course of a year.

Table 1. Tested consumption energy data collected under a single database

User	1	2	3	4	5	6	7	8	9	10	11	12
1	74,00	79,00	74,00	74,00	61,00	66,00	65,00	54,00	54,00	17,00	127,00	58,00
2	NA	105,00	67,00	70,00	9,00	9,00	31,00	82,00	8,82	133,00	126,00	NA
3	68,00	76,00	68,00	72,00	648,00	95,00	252,00	116,00	54,00	351,00	100,00	128,00
4	131,00	60,00	99,00	88,00	52,00	58,00	73,00	52,00	62,00	51,00	53,00	66,00
5	76,00	74,00	67,00	53,00	128,00	NA	62,00	66,00	209,00	55,00	69,00	187,00
.	.	.	.	.	.	.	.	.	.	.	.	.
35	270,00	250,00	285,00	260,00	265,00	290,00	300,00	325,00	300,00	285,00	275,00	270,00
36	98,00	123,00	10,00	71,00	98,00	223,00	90,00	70,00	223,00	74,00	15,00	69,00
37	87,00	80,00	96,00	86,00	30,00	20,00	25,00	28,00	45,00	67,00	47,00	35,00
38	118,00	45,00	41,00	23,00	7,00	21,00	32,00	43,00	33,00	27,00	27,00	42,00
.	.	.	.	.	.	.	.	.	.	.	.	.
98	280,00	289,00	272,00	250,00	200,00	240,00	255,00	310,00	280,00	280,00	250,00	300,00
99	89,00	115,70	112,10	153,50	153,50	33,90	53,67	NA	137,10	118,00	NA	132,00
100	306,00	272,00	293,00	286,00	258,00	294,00	289,00	320,00	245,00	286,00	293,00	348,00

The proposed methods for detecting outliers, IQR (Interquartile Range), LOF (Local Outlier Factor), MAD (Median Absolute Deviation), and MOVMAD (Moving Median Absolute Deviation), underwent a rigorous validation process. This validation encompassed the analysis of energy consumption data derived from both public buildings [5] and residential buildings [1], reflecting their versatility and applicability across different contexts.

To gain a comprehensive understanding of these outlier detection methods, energy consumption data were collected and integrated into a unified database, as meticulously detailed in Table 2 and 3. Subsequently, a comparative analysis was conducted, pitting these techniques against the Z-score and Grubbs methods.

Prior to conducting the algorithm tests, any instances of missing data and irregularities were visually identified, allowing for an initial evaluation of the algorithms' accuracy. The abnormal data within the consumption profile was highlighted under the "HUMAN I" category and was specifically emphasized in Table 2 and 3 for User 5 and User 36. Likewise, the absence of a data point for User 5 and the visually identified outliers for User 36 were brought to attention in *figure 1* and *figure 2*.

Table 2. Algorithms precision over consumption energy of User 5

	1	**2**	**3**	**4**	**5**	**6**	**7**	**8**	**9**	**10**	**11**	**12**
User 5	76,00	74,00	67,00	53,00	128,00	NA	62,00	66,00	209,00	55,00	69,00	187,00
HUMAN I												
IQR	F	F	F	F	F	F	F	F	T	F	F	T
MAD	F	F	F	F	T	T	F	F	T	F	F	T
MOVMAD	F	F	F	F	F	F	F	F	T	F	F	F
LOF	F	F	F	F	T	T	F	F	T	F	F	T
Z-SCORE	F	F	F	F	F	F	F	F	T	F	F	F
GRUBBS	F	F	F	F	T	T	T	F	T	F	F	T

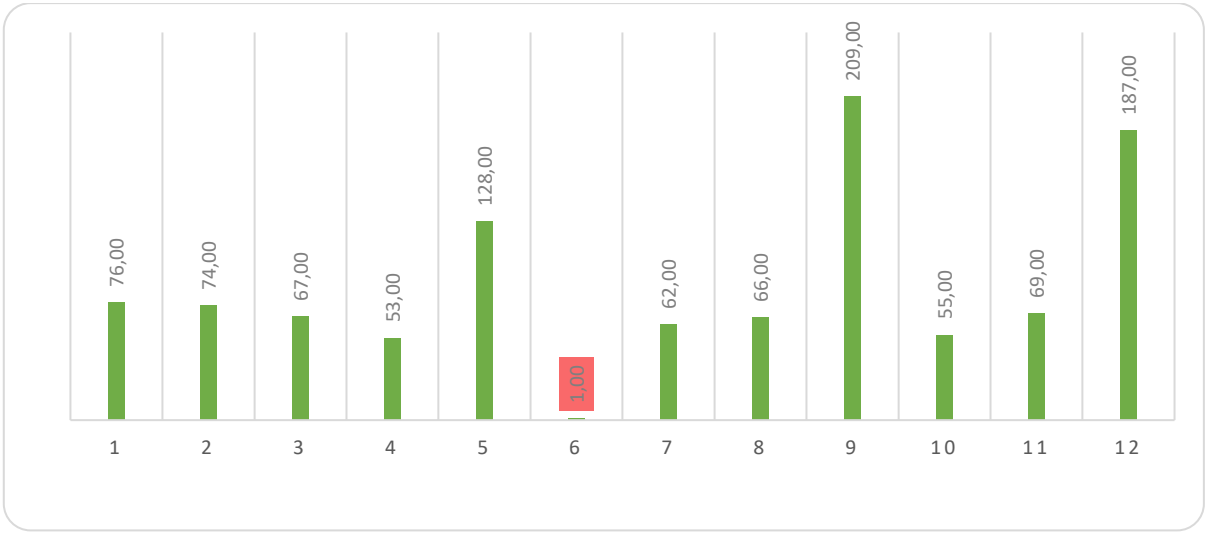

Fig. 1. User 5 missing data point for month 6

In order to evaluate the accuracy of the outlier detection methods, a scoring system was introduced. The scoring method was designed to avoid binary outcomes where points are awarded solely for 100% accuracy. The algorithms were classified as "T" (True) if they correctly identified the visually identified outlier and as "F" (False) if they either misclassified the outlier or highlighted a different one. This approach enables a more precise assessment by considering the granularity of points assigned, thereby reducing the presence of black and white scenarios.

If a method successfully identified all outliers, it was assigned a score of 1, as shown in previous study [1]. However, if the method erroneously classified non-outliers as outliers or failed to detect genuine outliers, the final score was calculated using the following formula:

$$\boldsymbol{Score} = \frac{\boldsymbol{Number\ of\ correct\ detections}}{\boldsymbol{Number\ of\ total\ detections}} \tag{3}$$

Table 3. Algorithms precision over consumption energy of User 36

	1	2	3	4	5	6	7	8	9	10	11	12
User 36	98,00	123,00	10,00	71,00	98,00	223,00	90,00	70,00	223,00	74,00	15,00	69,00
HUMAN I												
IQR	F	F	F	F	F	T	F	F	T	F	F	F
MAD	F	F	T	F	F	T	F	F	T	F	F	F
MOVMAD	F	F	F	F	F	T	F	F	T	F	T	F
LOF	F	F	T	F	F	T	F	F	T	F	T	F
Z-SCORE	F	F	F	F	F	T	F	F	T	F	F	F
GRUBBS	F	F	F	F	F	F	F	F	F	F	F	F

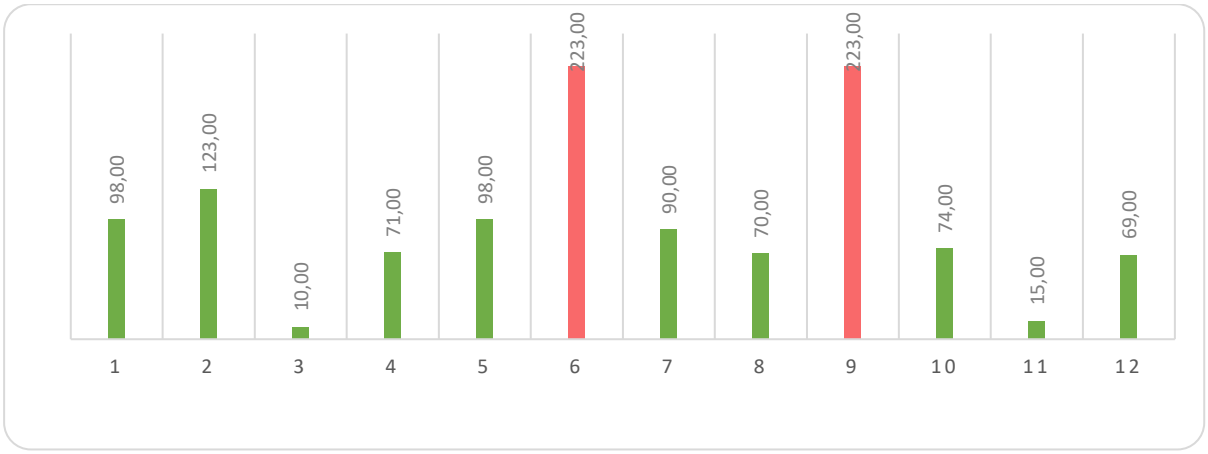

Fig. 2. User 36 extreme outlier data for month 6 and 9

Considering the results obtained from both Table 2 and Table 3, we can observe the following scores for the tested algorithms:

- **IQR** consistently performs exceptionally well in both evaluations, earning a perfect score of 1 in both instances.

- **MAD** demonstrates strong and consistent performance, achieving a score of 0.75 in Table 2 and a perfect score of 1 in Table 3.
- **MOVMAD** maintains a moderate level of accuracy, with scores of 0.33 in Table 2 and 0.66 in Table 3.
- **LOF** and **Z-score** exhibit similar performance, scoring 0.75 in Table 2 and 0.5 and 1, respectively, in Table 3.
- **Grubbs** shows variability in performance, with a score of 0.6 in Table 2 and a score of 0 in Table 3, suggesting room for improvement.

Table 4. The scoring applied to algorithm accuracy of detecting outliers

	IQR	MAD	MOVMAD	LOF	Z-SCORE	GRUBBS
User 1	1	1	0	0,5	1	0,5
User 2	0	0	0	0,22	0	1
User 3	0,5	1	0,5	0,5	0,5	0,66
User 4	1	1	0	0,33	1	1
User 5	1	0,75	0,33	0,75	0,33	0,6
.	.	.	.	.	.	.
User 35	1	1	0	0	0	0
User 36	1	1	0,66	0,5	1	0
User 37	1	1	1	0	1	1
User 38	1	1	0	0,25	1	0,5
.	.	.	.	.	.	.
User 98	1	1	0	0	0	1
User 99	0	0,75	0,5	0,75	0,33	0
User 100	1	1	1	0	0	0

Table 5. Final scoring and outlier detection accuracy over the tested algorithms:

	Scor	%
IQR	49,31	69,45
MAD	44,65	62,89
MOVMAD	34,15	48,10
LOF	16,92	23,83
Z-SCORE	43,14	60,76
GRUBBS	19,15	26,97

Applying the scoring method to the analyzed data from 100 users, as presented in Table 5, IQR emerges as the leading performer, securing a score of 49.31, which translates to an impressive accuracy rate of 69.45%. MAD also demonstrates robust performance, garnering a score of 44.65 and achieving an accuracy rate of 62.89%. MOVMAD maintains a reasonable accuracy rate of 48.10% while scoring 34.15. Z-score, while displaying promise with a score of 43.14, attains a slightly lower accuracy rate of 60.76%. Conversely, LOF and Grubbs exhibit lower scores and accuracy rates, with LOF registering 16.92 (23.83%) and Grubbs scoring 19.15 (26.97%). In summary, the IQR and MAD methods excel in accurately

identifying outliers for this dataset, closely followed by MOVMAD and Z-score. Although LOF and Grubbs have their merits, they demonstrate relatively lower accuracy rates. Thus, for this particular dataset and evaluation, the IQR and MAD methods appear to offer the most reliable options for outlier detection.

5. CONCLUSION

When we compare the Z-score and Grubbs methods to the other outlier detection techniques, some interesting observations come to light: Firstly, both the Z-score and Grubbs methods hold their own in terms of their performance, falling somewhere in the middle of the pack. While they may not achieve the highest accuracy rates seen in some of the other methods, they display competitive scores and show potential for effectively identifying outliers in the context of residential energy consumption data. The IQR and MAD methods achieve the highest accuracy rates still Z-score perform significantly better than LOF and Grubbs. In scenarios where a balanced approach is essential, Z-score and Grubbs may be preferred choices. There is room for improvement in the Z-score and Grubbs methods. Further optimization could enhance their accuracy and reliability. In conclusion, the evaluation of the Z-score and Grubbs methods in this study suggests their potential as valuable tools for outlier detection. However, to further validate their effectiveness and robustness, future research endeavors should aim to test these methods with larger volumes of data. The scalability and adaptability of Z-score and Grubbs to more extensive datasets are crucial aspects that warrant exploration to ensure their reliability in various real-world applications and scenarios.

ACKNOWLEDGEMENT

This paper was financially supported by the Project "Network of excellence in applied research and innovation for doctoral and postdoctoral programs" / InoHubDoc, project co-funded by the European Social Fund financing agreement no. POCU/993/6/13/153437.

REFERENCES

[1] Jurj, Dacian I., Alexandru G. Berciu, Alexandru Muresan, Mircea Lancranjan, Levente Czumbil, Dan D. Micu, Andrei Bende, and Bogdan A. Mitrache. "Applied data cleaning methods in outlier detection for residential consumer." In *2023 10th International Conference on Modern Power Systems (MPS)*, pp. 01-04. IEEE, 2023.

[2] D. I. Jurj, D. D. Micu, L. Czumbil, A. G. Berciu, M. Lancrajan and D. M. Bărar, "Analysis of Data Cleaning Techniques for Electrical Energy Consumption of a Public Building," *2020 55th International Universities Power Engineering Conference (UPEC)*, Turin, Italy, 2020, pp. 1-6, doi: 10.1109/UPEC49904.2020.9209781.

[3] D. Jurj, A. Polycarpou, L. Czumbil, A. Berciu, M. Lancranjan, D. Barar and D. Micu, "Extended

Analysis of Data Cleaning for Electrical Energy Consumption Data of Public Buildings," in 12th Mediterranean Conference on Power Generation, Transmission, Distribution and Energy Conversion (MEDPOWER), Online, 2020.

[4] D. Jurj, L. Czumbil, B. Bârgăuan, A. Ceclan, A. Polycarpou and D. Micu, "Custom Outlier Detection for Electrical Energy Consumption Data Applied in Case of Demand Response in Block of Buildings," Sensors, no. 21, p. 2946, 2021.

[5] Zhang, J., Zhang, H., Ding, S., & Zhang, X. (2021). Power Consumption Predicting and Anomaly Detection Based on Transformer and K-Means. *Frontiers in Energy Research*, *9*, 779587.

[6] V. Aggarwal, V. Gupta, P. Singh, K. Sharma and N. Sharma, "Detection of Spatial Outlier by Using Improved Z-Score Test," 2019 3rd International Conference on Trends in Electronics and Informatics (ICOEI), Tirunelveli, India, 2019, pp. 788-790, doi: 10.1109/ICOEI.2019.8862582.

[7] X. Guangcheng, C. Wenli, L. Xingzhi, Z. Ke, Z. Bo and S. Hongliang, "Research and Application of Verification Error Data Processing of Electricity Meter Based on Grubbs Criterion," 2019 International Conference on Smart Grid and Electrical Automation (ICSGEA), Xiangtan, China, 2019, pp. 13-17, doi: 10.1109/ICSGEA.2019.00012.

[8] S. K. Aggarwal, L. M. Saini and A. Kumar, "Electricity price forecasting in deregulated markets: A review and evaluation," Electrical Power and Energy Systems, no. 31, pp. 13-22, 2009.

[9] L. Perez-Lombard, J. Ortiz and C. Pout, "A review on buildings energy consumption information," Energy and Buildings, no. 40, pp. 394-398, 2008.

[10] Nikolaos Zografakis, Angeliki N. Menegaki, Konstantinos P. Tsagarakis, Effective education for energy efficiency, Energy Policy, Volume 36, Issue 8, 2008,

[11] Yang Wang, Jens Kuckelkorn, Fu-Yun Zhao, Di Liu, Alexander Kirschbaum, Jun-Liang Zhang, Evaluation on classroom thermal comfort and energy performance of passive school building by optimizing HVAC control systems, Building and Environment, Volume 89, 2015

[12] "Manufacturing Energy Consumption Survey 2018," Administration, U.S. Energy Information, Feb. 2021.

[13] "Smart Metering deployment in the European Union," [Online]. Available: https://ses.jrc.ec.europa.eu/smart-metering-deploymenteuropean- union.

[14] "Art 20 Energia electrică | Lege 123/2012," [Online]. Available: https://lege5.ro/Gratuit/gmzdenjwga/art-20-energia-electrica-lege-123-2012?dp=gyytmmbzge3dm.

[15] S. K. Aggarwal, L. M. Saini and A. Kumar, "Electricity price forecasting in deregulated markets: A review and evaluation," Electrical Power and Energy Systems, no. 31, pp. 13-22, 2009.

[16] Chanda, S.S., Banerjee, D.N. Omission and commission errors underlying AI failures. *AI & Soc* (2022).

[17] A. G. Berciu, D. Jurj, L. Czumbil, D. D. Micu and E. H. Dulf, "Energy Pulse – the Efficient Solution for Monitoring Electricity Consumption from Decentralized Data Sets," *2021 9th International Conference on Modern Power Systems (MPS)*, Cluj-Napoca, Romania, 2021, pp.

1-6, doi: 10.1109/MPS52805.2021.9492626.

[18] Vikas Khare, Cheshta Khare, Savita Nema, Prashant Baredar, Chapter 2 - Data visualization and descriptive statistics of solar energy system, Editor(s): Vikas Khare, Cheshta Khare, Savita Nema, Prashant Baredar, Decision Science and Operations Management of Solar Energy Systems, Academic Press, 2023,

[19] K. K. L. B. Adikaram, M. A. Hussein, M. Effenberger, T. Becker, "Data Transformation Technique to Improve the Outlier Detection Power of Grubbs' Test for Data Expected to Follow Linear Relation", *Journal of Applied Mathematics*, vol. 2015, Article ID 708948, 9 pages, 2015. https://doi.org/10.1155/2015/708948

ANALYSIS OF DIFFERENT DEEP LEARNING APPROACHES BASED ON DEEP NEURAL NETWORKS FOR PERSON RE-IDENTIFICATION

Adnan **RAMAKIĆ**[1], Zlatko **BUNDALO**[2], Dušanka **BUNDALO**[3]

[1] *Technical Faculty, University of Bihać, Bihać, Bosnia and Herzegovina*, [2] *Faculty of Electrical Engineering, University of Banja Luka, Banja Luka, Bosnia and Herzegovina*, [3] *Faculty of Philosophy, University of Banja Luka, Banja Luka, Bosnia and Herzegovina*

adnan.ramakic@unbi.ba, zlatbun2007@gmail.com, dusbun@gmail.com

Keywords: ***Deep Neural Network (DNN), Person Identification, Person Re-Identification, Convolutional Neural Network (CNN)***

Abstract*: In this work, different deep learning approaches based on deep neural networks for person re-identification were analyzed. Both identification and re-identification of people are frequently required in various fields of human life. Some of the most common applications are in various security systems where it is necessary to identify and track a particular person. In the case of person identification, the identity of a particular person needs to be established. In the case of re-identification, the main task is to match the identity of a particular person across different, non-overlapping cameras or even with the same camera at different times. In this work, three different deep neural networks were used for the purpose of person re-identification. Two of them were user-defined, while one of them is a pre-trained neural network adapted to work with a specific dataset. Two neural networks used were Convolutional Neural Networks (CNN). For the defined experiment, it was used own dataset with 13 subjects in gait.*

1. INTRODUCTION

Person identification and re-identification are important tasks in many aspects of human life. It is often necessary to determine the identity of a particular person, that is, to identify a particular person. This is a challenging task for which many methods have been developed in the last decades. Most of these methods are based on certain physiological or behavioral characteristics of the human body. The methods based on the mentioned characteristics are called biometric methods. Biometric methods are usually divided into two

groups: physiological and behavioral biometric methods. Accordingly, there are methods based on a person's fingerprint or palm print, iris or retina (eye elements), face, gait, voice, or signature that are used in various applications.

The methods listed above are implemented in different ways and use different features based on the above characteristics. In general, an identification system can be divided into two parts. The first part is used to create a database (or in this paper denoted as *dataset*) in which images are usually captured for each person, e.g., using an RGB camera (Red, Green, Blue) or an RGB-D device (Red, Green, Blue - Depth). The images captured are stored in the database and depend on the method used. For example, if the implemented method is based on a person's face (face recognition), images containing people's faces are captured. On the other hand, if the method is based on gait (gait recognition), images with a person walking upright are usually captured and used. In the further course of the process, the aforementioned images can be subjected to different types of processing, depending on the method implemented. Features can also be extracted from the images and used, but this also depends on the method used. Accordingly, the extracted features may be also contained in the database. The second part of the identification system is the identification part, where the new image (or extracted features) of a particular person is matched with the images or features stored in the database. The above described can be roughly represented as in *figure* 1.

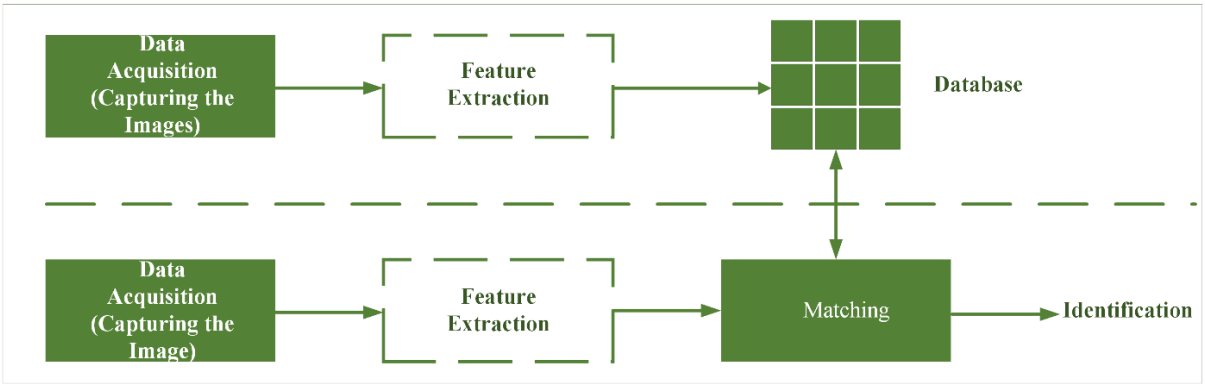

Fig. 1. An Example of Identification System with Defined Steps

While person identification involves establishing the identity of a particular person, re-identification involves matching the identity of a particular person across different, non-overlapping cameras or even with the same camera at different time frames.

Nowadays, various methods for identification and re-identification are implemented using machine learning in such a way that a model is created, trained with the data, and the created model is then used for identification or re-identification tasks. Machine learning approaches typically use classifiers such as k-Nearest Neighbors (kNN) [1], Support Vector Machines (SVM) [2], or Linear Discriminant (LD) [3]. In addition to machine learning, deep learning approaches are also used, usually using a deep neural networks (DNN).

In this work, different approaches based on deep learning have been investigated. In this context, different deep neural networks were created and analyzed. An experiment was conducted with deep neural networks using a custom dataset. Accordingly, the experiment, the experimental setup and the obtained results have been described in the following chapters.

2. THE DATASET AND EXPERIMENTAL SETUP

In this work, a custom dataset was used for the defined experiment. The dataset used contains 13 people, during a walk (in gait), recorded with different camera positions. A stereo camera was used to create the dataset and multiple video footages were available for each person. The dataset was recorded in nice weather. The video footages have high resolution. Accordingly, the extracted images also have a high resolution. A drawback of the dataset can be during extraction of silhouettes, because some people wear clothes with similar colors as background. The size of the dataset (video footages in *.avi*) is about 1,5 GB. For each of the 13 people, different images were extracted from the recorded video footages and used in the experiment.

This was implemented so that in each video containing a particular person, the person was detected and tracked in each frame. To detect upright people, *vision.PeopleDetector* in Matlab [4] [5] may be used. In this context, a bounding box was formed around the person and this part of the scene was extracted and saved as an image in RGB format. This is shown in *figure* 2. The resolution of the extracted images containing only a person (green rectangular part in *figure* 2) was 185 x 375.

Fig. 2. Detected Person in One Video Frame

This procedure was performed for each of the 13 people. In other words, in the dataset there are 13 folders (*Person1, Person2 ... Person13*) containing the images for each person. The mentioned procedure is illustrated in *figure* 3. The aforementioned extracted images are suitable for re-identification applications because the images are in RGB format and the people in all the captured images are wearing the same clothes. More specifically, said images can be used for short-term re-identification applications. For identification applications and long-term re-identification applications [6] [7] [8] [9] [10] [11], some longer-term features should be defined and used.

Various representations of silhouettes of people are often used as longer-term features, and many of the methods presented are based on them. An example of such a method is the well-known gait recognition method called Gait Energy Image (GEI) [12]. GEI is defined as an image containing silhouettes of a person over a gait cycle that are normalized, aligned, and temporally averaged. Some examples of silhouette images and GEI images from the Casia Dataset B [13] [14] [15] are shown in *figure 4* and *figure 5*.

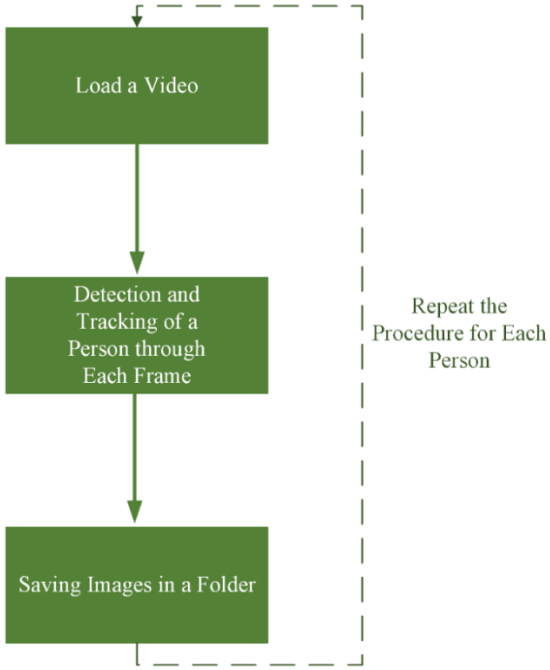

Fig. 3. The Procedure for Dataset Creation

Once the dataset was created, three different deep neural networks were created and used for the experiment. The main idea was to create two different neural networks, with the first neural network having a feature input layer as the first layer. The features from the images would first be extracted and stored in a table and then used with the neural network created. In the case of the second neural network, the first layer is intended to be an image input layer. In this case, only images should be loaded to be used with the created neural network without prior feature extraction. In the third case, a pre-trained neural network was defined for use.

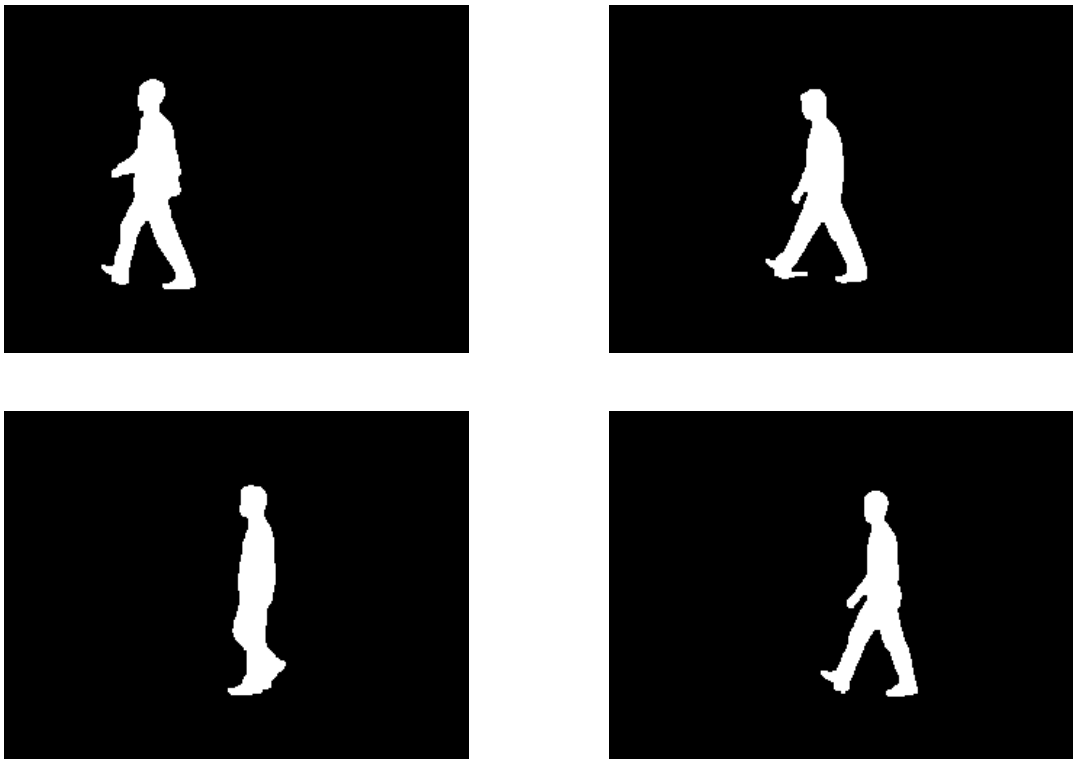

Fig. 4. Examples of Silhouette Images from Casia Dataset B [13] [14] [15]

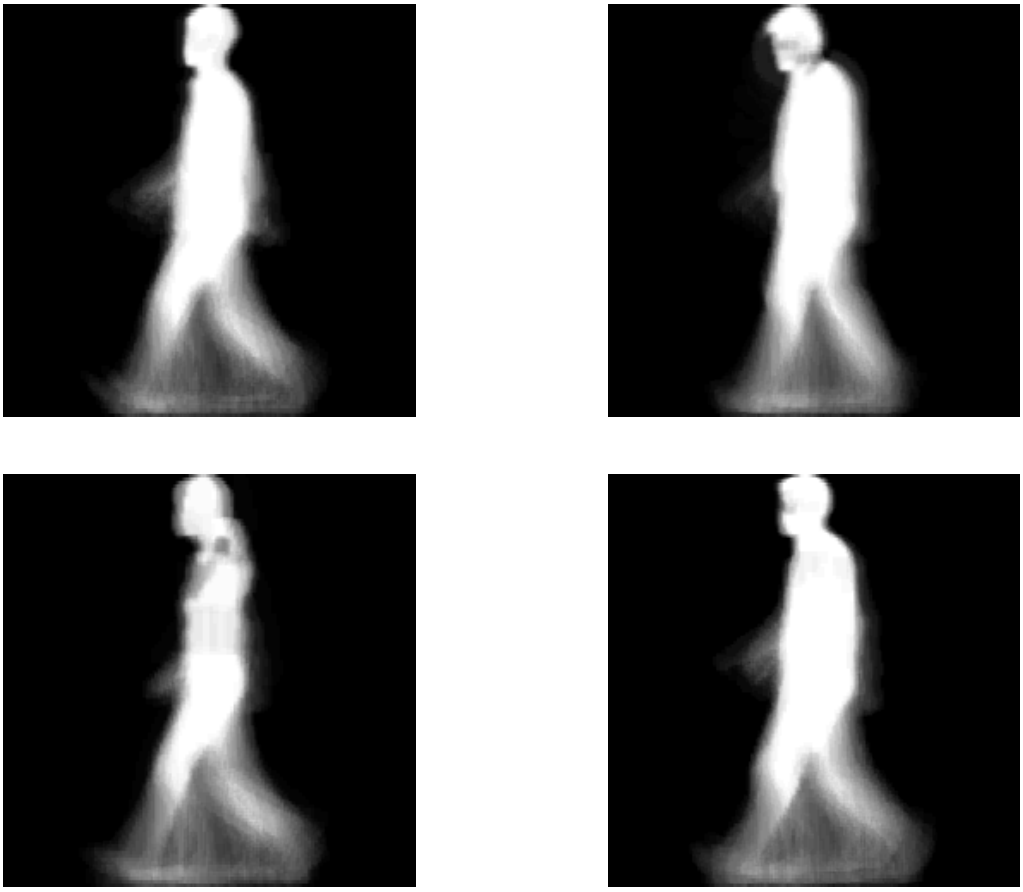

Fig. 5. Examples of GEI Images from Casia Dataset B [13] [14] [15]

Matlab was used for the mentioned experiment and for the creation of the dataset. For the creation of the dataset, a separate program was created for this purpose. It should be noted that Python, TensorFlow and Keras have also been analyzed, tested and used for the same purpose.

The first neural network (hereinafter marked with DNNf) uses extracted features from the images of the dataset. This was done using a *bag of visual words* (*bagOfFeatures* in Matlab, with defined parameters *VocabularySize - 500* and *PointSelection* as *Detector*) [16] [17], where the visual vocabulary was created by default from Speeded-Up Robust Features (SURF) [18]. The mentioned features were stored in a table. DNNf consists of seven layers, the first layer being the feature input layer (*featureInputLayer*). Different numbers and types of layers were tested, but with the mentioned seven layers and defined parameters, satisfactory results were obtained.

The seven defined layers are:

1. *featureInputLayer*
2. *fullyConnectedLayer*
3. *batchNormalizationLayer*
4. *reluLayer*
5. *fullyConnectedLayer*
6. *softmaxLayer*
7. *classificationLayer.*

The extracted features stored in the table were divided into a training and a testing part, with 70 percent used for training and 30 percent for testing. Other training options for the DNNf include 30 epochs, a learning rate of 0,001 and the Adaptive Moment Estimation Optimizer (Adam) [19] was used. The best results were obtained with the above settings.

The second neural network (hereinafter marked with DNNi) is a Convolutional Neural Network (CNN). The DNNi uses the images without prior feature extraction. The images were only loaded as the first layer is the image input layer (*imageInputLayer*). Also, in this case, different numbers and types of layers were analyzed and tested. With defined eight layers and defined parameters, satisfactory results were obtained.

DNNi consists of following eight layers:

1. *imageInputLayer*
2. *convolution2dLayer*
3. *batchNormalizationLayer*
4. *reluLayer*
5. *maxPooling2dLayer*
6. *fullyConnectedLayer*
7. *softmaxLayer*
8. *classificationLayer.*

The images used were also split in the ratio of 70 percent for training and 30 percent

for testing. Other options defined for DNNi are 30 epochs, a learning rate of 0,001 and Stochastic Gradient Descent with Momentum (SGDM) [20] was used. Also, the best results were obtained with the above defined settings.

In addition to the deep neural networks created and described above (DNNf and DNNi), a pre-trained neural network was also used. The pre-trained neural network used is *GoogLeNet* [21] [22], a convolutional neural network. *GoogLeNet* [21] [22] was used and adopted to work with the dataset described above. This was done in such a way that two layers were replaced and adapted to the dataset. The layers mentioned are *fullyConnectedLayer* and *classificationLayer*. In the *fullyConnectedLayer*, the *OutputSize* parameter was set to *13*, which corresponds to the number of subjects in the dataset. The images used were split in the ratio of 70 percent for training and 30 percent for testing. Other training options for the *GoogLeNet* include 30 epochs, a learning rate of 0,001 and the SGDM was used, as in case DNNi.

3. RESULTS AND DISCUSSION

With the settings defined above and the neural networks described, the following results were obtained using the dataset described. In the case of DNNf, the accuracy was 90,8%. When DNNi was used, the accuracy was 91,7% which is higher compared to DNNf. In the case of *GoogLeNet*, pre-trained neural network, the accuracy was 99,4%. The results presented above are shown in table 1 and *figure 6*.

Table 1. The Obtained Results with Defined Settings and Used Dataset

Deep Neural Network Used	**Accuracy**
DNNf	90,8%
DNNi	91,7%
GoogLeNet	99,4%

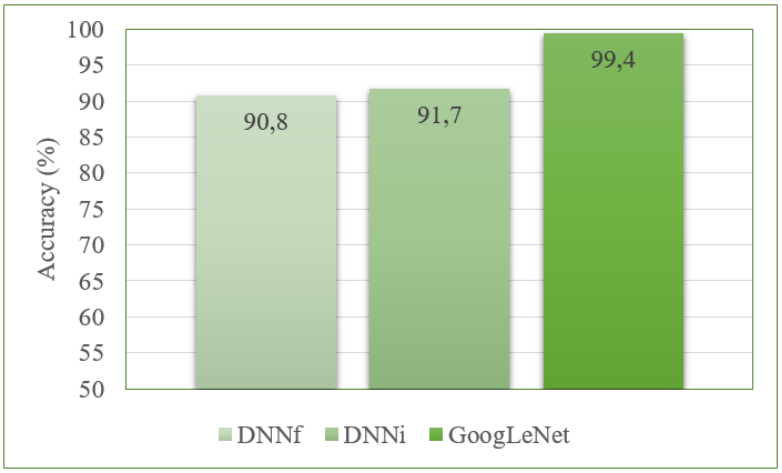

Fig. 6. The Obtained Results for the Deep Neural Networks Used

As can be seen from table 1 and *figure* 6, the pre-trained deep neural network *GoogLeNet* achieved the best overall result. This was to be expected, since *GoogLeNet* is a more complex neural network that has been pre-trained and validated on a large number of different images. With a relatively simple adaptation to use a custom dataset, the aforementioned deep neural network can easily be used for this type of application.

The created deep neural network, called DNNi, had the second best results and slightly better results compared to another created deep neural network (DNNf) that uses extracted features. On the other hand, DNNf has a much shorter training time. Moreover, the results of DNNf and DNNi can be improved by additional optimizations and adding some extra layers.

It should be noted that it is easier to work with deep neural networks such as DNNi and *GoogLeNet* compared to DNNf. The two deep neural networks mentioned, DNNi and *GoogLeNet*, have an image input layer as the first layer. This means that no explicit feature extraction is required in this case. For use with DNNi and *GoogLeNet*, only images containing people in gait should be loaded. In the case of DNNf, explicit feature extraction is required because the first layer is a feature input layer.

4. CONCLUSION

In this work, different deep learning approaches were analyzed. Person identification and re-identification applications are important in many areas of human life. In person identification, the identity of a particular person needs to be established. In person re-identification the main task is to match the identity of a particular person across different, non-overlapping cameras or with the same camera at different times. For example, in different security systems, some kind of identification or re-identification is often required.

Various methods have been developed for the aforementioned identification and re-identification applications. The mentioned methods are usually based on various physiological or behavioral characteristics of a person. Nowadays, identification and re-identification methods are usually implemented using various machine learning and deep learning approaches.

In this work, three different approaches based on deep neural networks were analyzed. For this purpose, two deep neural networks were created, while the third deep neural network used is pre-trained and adapted for use with a specific dataset. The first deep neural network created (DNNf) has a feature input layer as its first layer and uses extracted features from the images of the dataset. The second deep neural network (DNNi) is a convolutional neural network (CNN) and has as its first layer an image input layer into which only images to be used with said deep neural network are loaded. The third deep neural network used is the pre-trained neural network *GoogLeNet*.

The experiment with the defined deep neural networks was performed and the results

were presented. For this purpose, a custom dataset containing 13 people in gait was used. The best overall result had the pre-trained deep neural network *GoogLeNet*.

In future research, it is planned to analyze and use a larger dataset containing a larger number of people in gait. In addition, it is also interesting to study different points of view and conditions where people wearing similar clothing. Accordingly, other deep neural network architectures will also be analyzed and studied.

REFERENCES

[1] L. E. Peterson, *K-Nearest Neighbor*, Scholarpedia, 4(2), 1883, 2009.

[2] S. R. Gunn, *Support Vector Machines for Classification and Regression*, ISIS Technical Report, 14(1), 5-16, 1998.

[3] R. A. Fisher, *The Use of Multiple Measurements in Taxonomic Problems*, Annals of Eugenics 7(2), 179-188, 1936.

[4] N. Dalal and B. Triggs, *Histograms of Oriented Gradients for Human Detection*, IEEE Computer Society Conference on Computer Vision and Pattern Recognition, 886-893, IEEE, 2005.

[5] Official Web Page of Mathworks, *vision.PeopleDetector (Documentation)*, Link:*https://www.mathworks.com/help/vision/ref/vision.peopledetector-system-object.html* [Accessed 15/5/2023]

[6] K. Lenac, D. Sušanj, A. Ramakić and D. Pinčić, *Extending Appearance Based Gait Recognition with Depth Data*, Applied Sciences, 9(24), 5529, MDPI, 2019.

[7] A. Ramakić and Z. Bundalo, *Gait Recognition as an Approach for People Identification*, In: International Symposium on Innovative and Interdisciplinary Applications of Advanced Technologies, 717-726, Springer, 2023.

[8] A. Ramakić, Z. Bundalo and D. Bundalo, *An Example of Solution for Data Preparation Required for Some Purposes of People Identification or Re-Identification*, Journal of Circuits, Systems and Computers, *https://doi.org/10.1142/S0218126623501645*, World Scientific, 2022.

[9] A. Ramakić, Z. Bundalo and D. Bundalo, *A Method for Human Gait Recognition from Video Streams Using Silhouette, Height and Step Length*, Journal of Circuits, Systems and Computers, 29(7), 2050101, World Scientific, 2020.

[10] A. Ramakić, Z. Bundalo and Ž. Vidović, *Feature Extraction for Person Gait Recognition Applications*, Facta Universitatis, Series: Electronics and Energetics, 34(4), 557-567, 2021.

[11] A. Ramakić, D. Sušanj, K. Lenac and Z. Budalo, *Depth-based Real-time Gait Recognition*, Journal of Circuits, Systems and Computers, 29(16), 2050266, World Scientific, 2020.

[12] J. Han and B. Bhanu, *Individual Recognition Using Gait Energy Image*, IEEE Transactions on Pattern Analysis and Machine Intelligence, 28(2), 316-322, IEEE, 2005.

[13] S. Yu, D. Tan, and T. Tan, *A Framework for Evaluating the Effect of View Angle, Clothing and Carrying Condition on Gait Recognition*, In: 18th International Conference on Pattern Recognition (ICPR), 441-444, IEEE, 2006.

[14] S. Zheng, J. Zhang, K. Huang, R. He, and T. Tan, *Robust View Transformation Model for Gait Recognition*, In: 18th International Conference on Image Processing, 2073-2076, IEEE, 2011.

[15] Official Web Page of the Institute of Automation, Chinese Academy of Sciences, Link: *http://www.cbsr.ia.ac.cn/english/Gait\%20Databases.asp* [Accessed 15/5/2023]

[16] G. Csurka, C. Dance, L. Fan, J. Willamowski and C. Bray, *Visual Categorization with Bags of Keypoints*, In: Workshop on Statistical Learning in Computer Vision (ECCV), 1-2, 2004.

[17] D. Nister and H. Stewenius, *Scalable Recognition with a Vocabulary Tree*, In: Computer Society Conference on Computer Vision and Pattern Recognition (CVPR), 2161-2168, IEEE, 2006.

[18] H. Bay, A. Ess, T. Tuytelaars and L. Van Gool, *Speeded-Up Robust Features (SURF)*, Computer Vision and Image Understanding, 110(3), 346-359, Elsevier, 2008.

[19] D.P Kingma and J. Ba, *Adam: A Method for Stochastic Optimization*, arXiv preprint arXiv: 1412.6980, 2014.

[20] K.P. Murphy, *Machine Learning: A Probabilistic Perspective*, MIT PRESS, 2012.

[21] C. Szegedy, W. Liu, Y. Jia, P. Sermanet, S. Reed, D. Anguelov, and A. Rabinovich, *Going Deeper With Convolutions*, IEEE Conference on Computer Vision and Pattern Recognition, 1-9, IEEE, 2015.

[22] Official Web Page of Mathworks, GoogLeNet, Link:*https://www.mathworks.com/help/deeplearning/ref/googlenet.html* [Accessed 15/5/2023]

THE ELECTRICAL RESISTANCE OF THE LUBRICANT FILM IN THE CASE OF THE HYDRODYNAMIC SLIDING BEARING SUBJECTED TO SHOCKS

Ioan Marius **ALEXANDRESCU**, Radu **COTETIU**, Adriana **COTETIU**,
Dinu **DARABA**, Ioana Laura **ALEXANDRESCU**
Technical University of Cluj-Napoca
Ioan.Alexandrescu@imtech.utcluj.ro

Keywords: minimal lubricating film, electrical resistance, radial sliding bearing.

Abstract: *This paper presents experimental research on electrical resistance of the lubricant film, shock absorption in the lubricating film, under different static and dynamic load conditions. We focus on determination of the minimal lubricating film which estimates the minimum lubricating thickness between spindle and bushing in the case of the hydrodynamic sliding bearing subjected to shocks*.

1. INTRODUCTION

The main objective of the experimental tests was to determine the minimum electrical resistance of the lubricant film, under different static and dynamic load conditions. The geometry of the lubricant film will be approximated with a surface of constant thickness, equal to the minimum thickness of the lubricant film under static loading conditions [3]. The minimum electrical resistance of the lubricant film estimates the minimum thickness of the oil film between the spindle and the bearing [1].

In the framework of the experimental research, an additive mineral oil for bearings was used, type LA 32, STR 5152-89, viscosity class ISO VG 32[2].

The electrical resistance of the lubricant film was determined by executing a resistive circuit between the spindle and the bearing, which includes a standard resistor R_{12} = 49 KΩ [4], [5]. The measuring chain used to determine the minimum electrical resistance of the lubricant film between the spindle and the bearing is shown in *figure 1*.

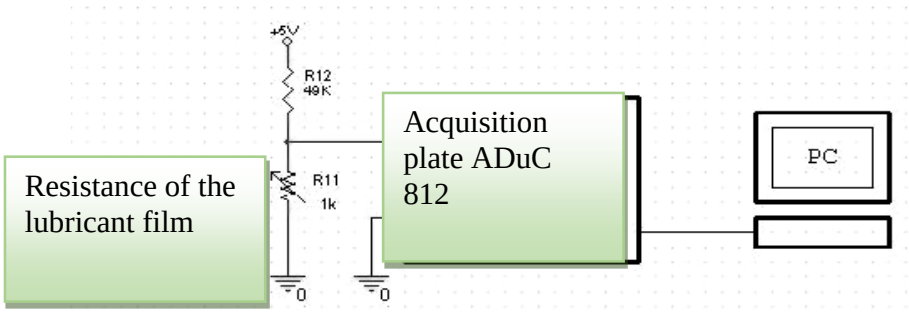

Fig. 1. Measuring chain

2. EXPERIMENTAL MEASUREMENT OF THE ELECTRICAL RESISTANCE OF THE LUBRICANT FILM

The experimental stand with the electrical circuit for measuring the minimum electrical resistance of the lubricant film is shown in *figure 2*, and a detail regarding the measuring chain in *figure 3*.

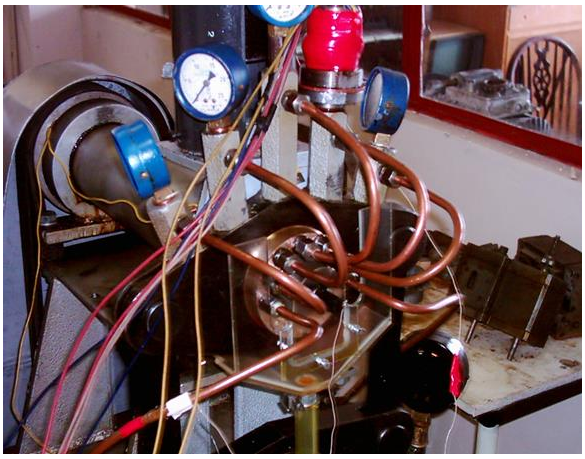

Fig. 2. The experimental stand

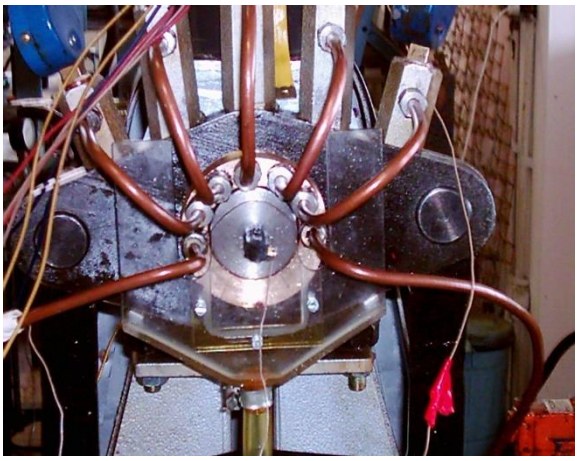

Fig. 3. Resistive circuit detail

The minimum resistance of the lubricant film, determined experimentally, as a function of supply pressure, dynamic load and static load for different spindle speeds is presented in *figure 4* for the case n =370 rpm, p_{in} =1.5 bar; *figure 5* for the case n = 600 rpm, p_{in} =3 bar, *figure 6* for the case n = 960 rpm, p_{in} = 8 bar.

The static regime is represented for the impact height H = 0 cm, respectively the dynamic regime is represented for the three heights, H =5 cm, H = 20 cm and H = 40 cm, corresponding to the forces F_1 = 1665 N, F_2 = 2356 N, F_3 = 3332.5 N.

The influence of speed and supply pressure respectively the influence of the static load at different speeds depending on the supply pressure on the minimum electrical resistance of the

lubricant film depending on the dynamic load for the two cases of static load G_1 = 2250 N, respectively G_2 = 4500 N, is presented in *figure 4*, *figure 5* and *figure 6*.

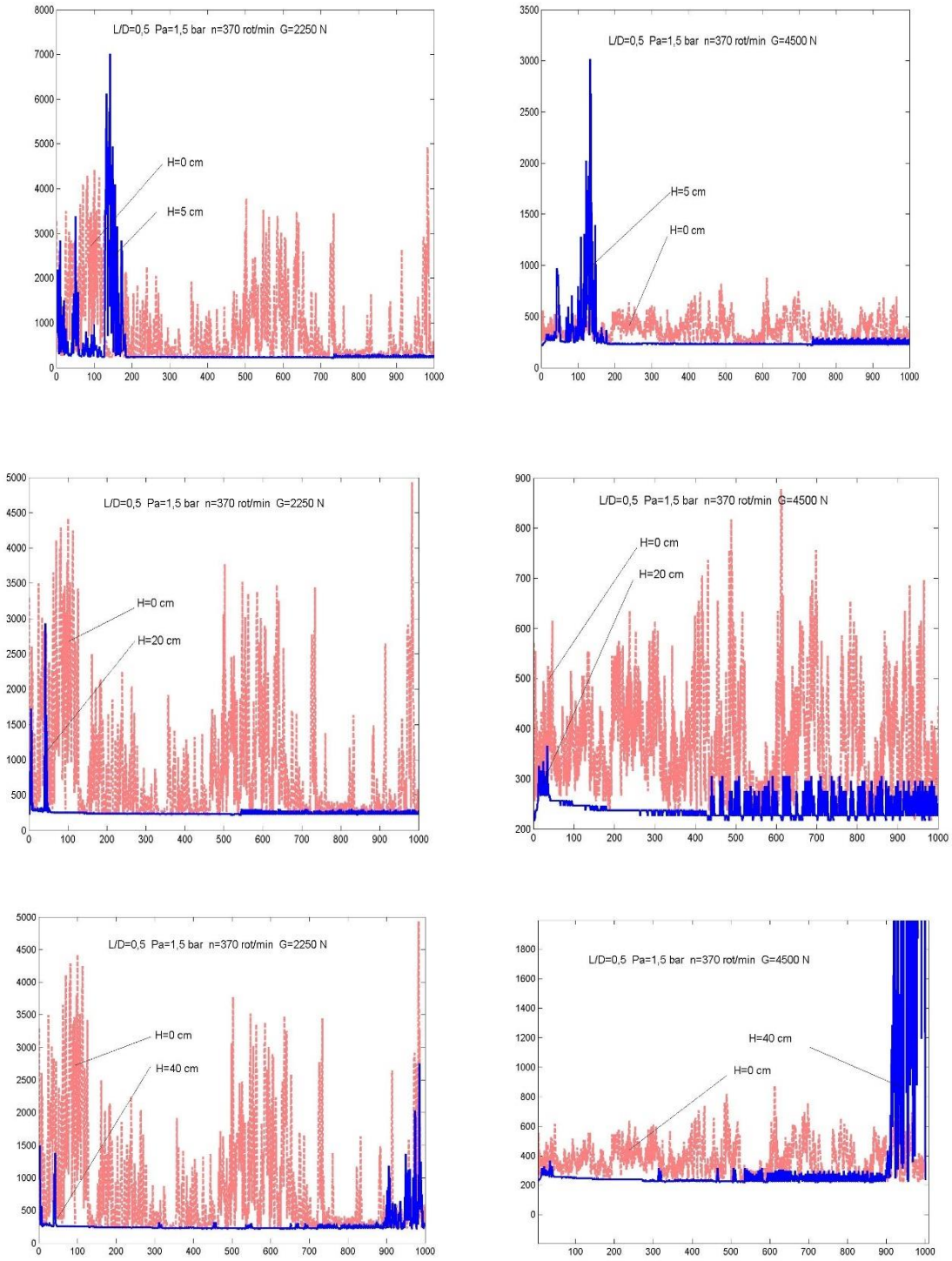

Fig. 4. Minimum electrical resistance of the lubricant film for the speed n = 370 rpm, p_{in} = 1.5 bar, depending on the static and dynamic loads

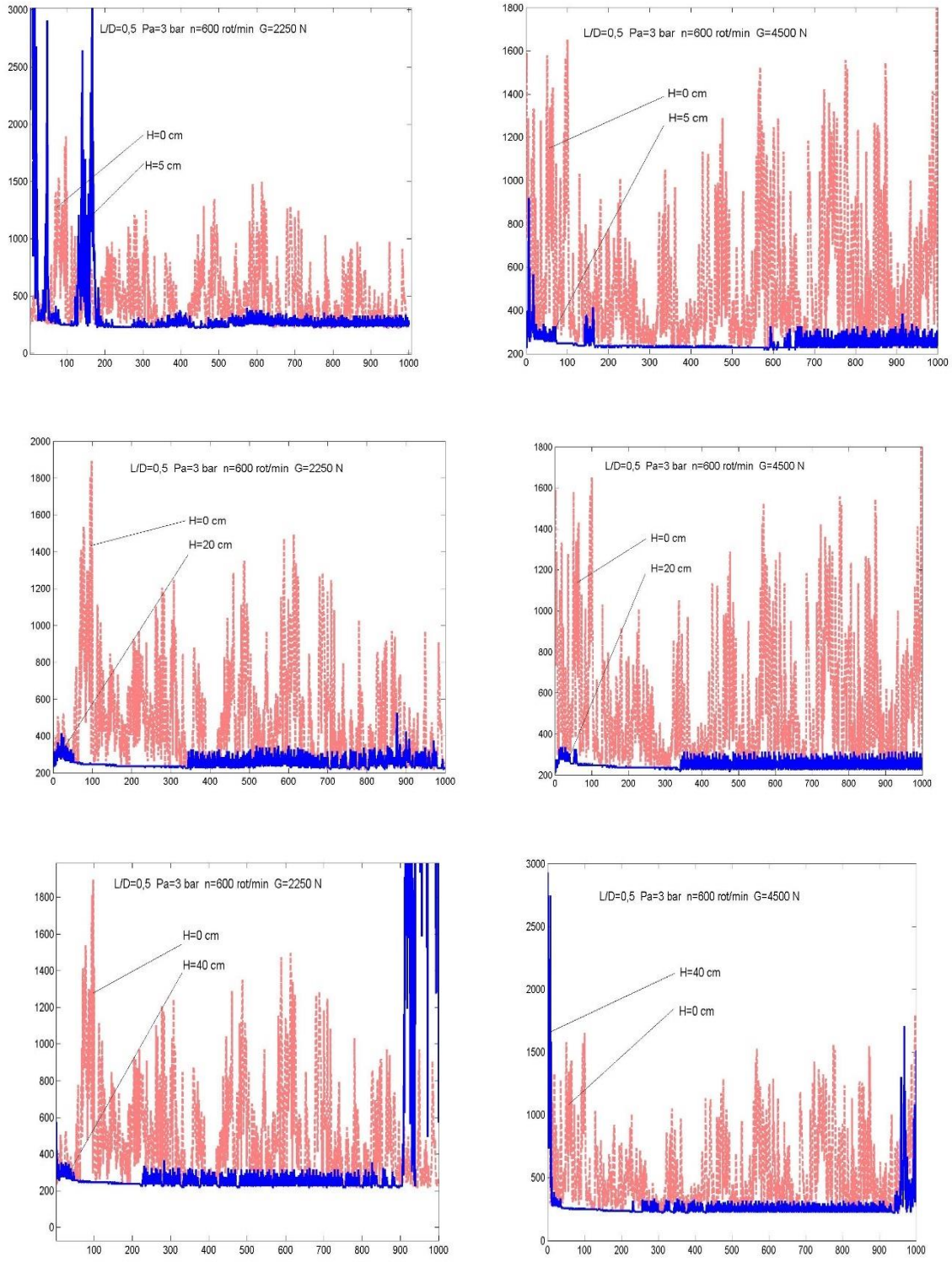

Fig. 5. Minimum electrical resistance of the lubricant film for speed n = 600 rpm, p_{in} = 3 bar, depending on static and dynamic loads

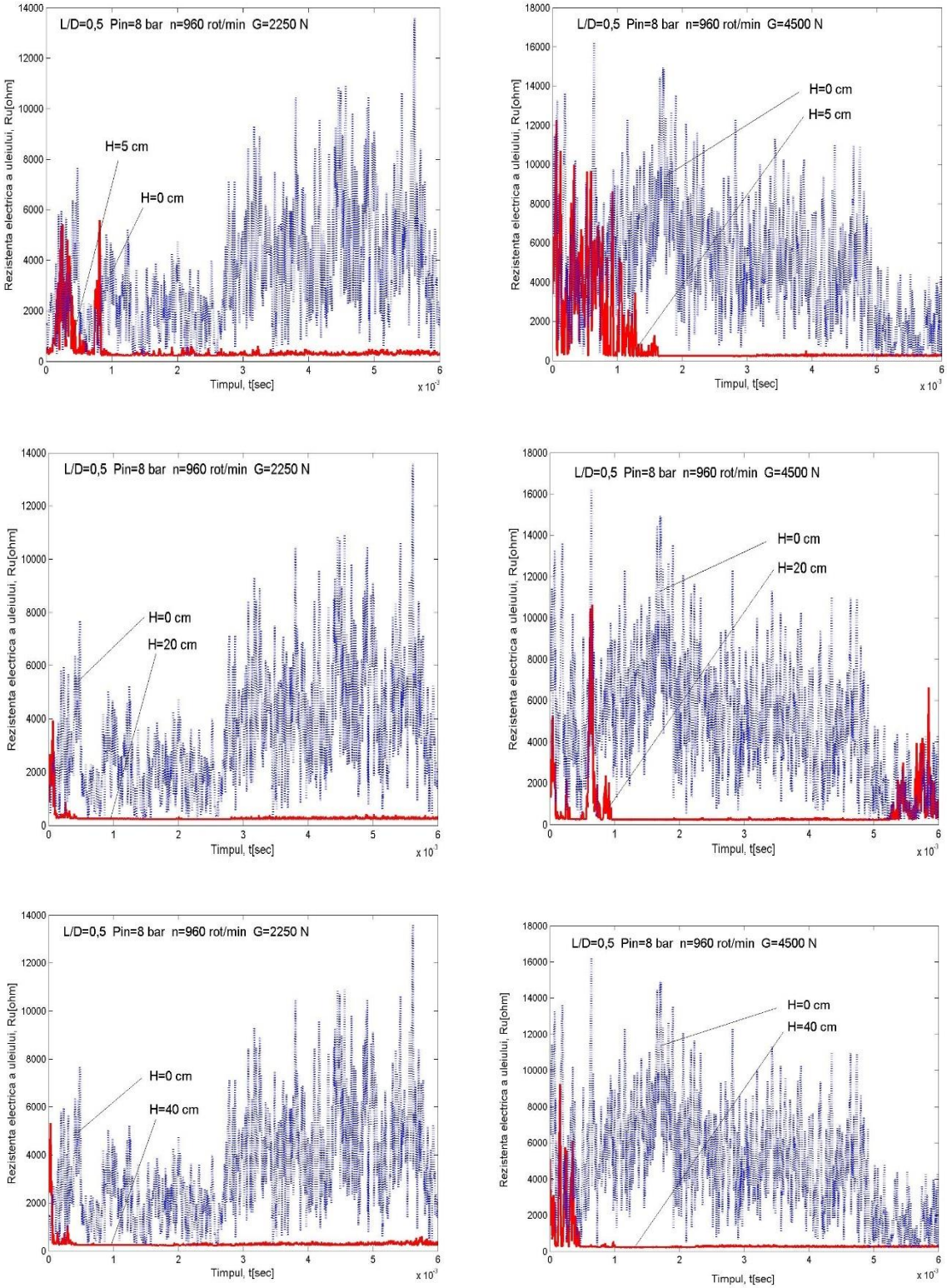

Fig. 6. Minimum electrical resistance of the lubricant film for the speed n = 960 rpm, p_{in} = 8 bar, depending on the static and dynamic loads

3. CONCLUSIONS

The following can be noted:

- the higher the dynamic shock load, the lower the electrical resistance of the film, the decrease occurring progressively with increasing load (retention time of the lubricant in the contact area decreasing with increasing load);
- the higher the static load, the lower the electrical resistance of the lubricant film;
- the higher the spindle speed, the higher the electrical resistance of the lubricant film under static operating conditions;
- for the studied radial bearing, with the application of the dynamic load for n = 370 rpm, a decrease in the average value of the lubricant film resistance is observed in relation to the value in the static regime between 2.13 – 2.97 times, for the static load G_1 = 2250 N, respectively between 1.13 – 2.39 times, for the static load G_2 = 4500 N; the drastic decrease in the thickness of the lubricant film in the area corresponding to the moment of the shock is noted, with the observation that retention of the lubricant film is observed in the contact area;
- by increasing the spindle speed to 600 rpm, the increase in the electrical resistance of the lubricant film is noticeable; the lower the static load, the higher the resistance of the lubricant film (1.19 times higher in the case of G_1 = 2250 N than in the case of G_2 = 4500 N);
- with the application of the dynamic load for n = 600 rpm, a decrease in the average value of the lubricant film resistance is observed in relation to the value in the static regime between 10.7 – 12.11 times, for the static load G_1 = 2250 N, respectively between 9.93 – 10.42 times, for the static load G_2 = 4500 N;
- at the spindle speed of 960 rpm, when the dynamic load is applied, there is a decrease in the average value of the lubricant film resistance in relation to the value in the static regime between 18.7 and 22.67 times, for the static load G_1 = 2250 N, respectively between 12.87 – 19.81 times, for the static load G_2 = 4500 N.

REFERENCES

[1] I. M. Alexandrescu, *Studiul comportării lagărelor radiale cu ungere hidrodinamică în condiţiile funcţionării cu şocuri şi vibraţii*. Teza de doctorat, Universitatea Tehnică Cluj-Napoca, 2005.

[2] I. M. Alexandrescu, R. I. Coteţiu, S. Haragâş, *Research on the load bearing force in narrow sliding radial bearings (L < 0,7 D) operating in shock conditions*. Acta Technica Napocensis,

Technical University of Cluj-Napoca, Series Applied Mathematics, Mechanics, and Engineering Vol. 62, Issue II, pp. 299-308, 2019.

[3] O. Chiver, N. Burnete, I. R. Şugar, L. Neamţ, E. Pop, *Study on Gear Ratio of Battery Electric Vehicles*, Ingineria Automobilului, Issue: 59, Bucureşti, pp. 11-16, 2021.

[4] National Instruments, *Data Acquisition Product Guide*, 2001.

[5] Analog Devices Inc, *ADuC 812 MicroConverter*, 2003.

ALTERNATIVE LOW-COMPLEXITY APPROACHES FOR PAPR REDUCTION IN FBMC-OQAM SYSTEMS

Salima **SENHADJI**, Fethi Tarik **BENDIMERAD**

LTT Laboratory, Department of telecommunications, Abou Bakr Belkaid University, Tlemcen, Algeria
salima.senhadji@univ-tlemcen.dz

Keywords: FBMC-OQAM, PAPR, TR, TD, TC

Abstract*: Recently, the Filter Bank Multi-Carrier with Offset-QAM modulation (FBMC-OQAM) system proved to be a strong candidate wave that can replace the conventional OFDM (Orthogonal Frequency Division Multiplexing) through several properties in future mobile generations (5G and 5G+). However, it faces a significant issue, which is high Peak-to-Average-Power-Ratio (PAPR) as all advanced waveforms. Many researchers have proposed either hybrid or non-hybrid techniques adapted to the FBMC-OQAM structure to minimize the PAPR parameter. Nevertheless, all of these techniques suffer from high complexity, which is a significant challenge in practical implementations. Therefore, in this paper, we propose two alternative low-complexity approaches, TD and TC, to effectively mitigate the PAPR problem in FBMC-OQAM systems. Both proposed hybrid schemes achieve superior PAPR performance compared to the conventional TR and very competitive results in comparison to the existing literature algorithms while requiring less computational complexity.*

1. INTRODUCTION

In recent times, the regular growth of collective needs has forced numerous technical challenges that need to be addressed to effectively realize the user requirements for wireless communication services, as well as high spectral, energy efficiency, and connectivity. For this reason, the physical layer of modern wireless communication systems has evolved a lot, which has allowed the development of this sector in a dizzying way. For example, in the 4G standard OFDM waveform is implemented [1]. It has been a popular choice among communication systems. Nevertheless, the OFDM waveform is not appropriate for highly developed radio systems due to a few limitations, such as high latency and low spectral

efficiency. Consequently, it has become important to look for another alternative to the conventional OFDM for 5G and 5G+. Up to date, numerous new filtered waveforms, such as F-OFDM [2], FBMC [3], [4], GFDM [5], and UFMC [6], have been suggested for 5G and 5G+ [7]. Among these waveforms, Filter Bank Multicarrier modulation (FBMC-OQAM) is a strong candidate waveform for 5G and 5G+ applications, based on filter bank treatment to ensure better spectral efficiency than OFDM. However, as with all multicarrier systems, high PAPR is considered a serious problem in FBMC-OQAM [8]. This problem reduces the power efficiency of the high-power amplifier. To avoid this crucial issue, we need some PAPR reduction algorithms. In the literature, we can find several algorithms that are adopted for each waveform, whether for OFDM or FBMC. At present, a lot of interest is being given to the FBMC-OQAM PAPR mitigation issue since a large number of published papers are interested in PAPR reduction in FBMC-OQAM. In [9], the authors proposed a new TR scheme for the FBMC/OQAM structure. In [10], the authors recommended a joint solution founded on ACE and the Tone Reservation techniques for high peak power mitigation. H. Wang and al., in reference [11], offered a combined PAPR mitigation technique for FBMC/OQAM built on MDB-PTS and Tone Reservation scheme to ensure better PAPR reduction. In [12], the authors proposed a new approach for high peak power mitigation in FBMC/OQAM founded on SLM and MDB-PTS methods to achieve better PAPR reduction while maintaining good BER performance. Z. He in [13] has proposed a low complexity Partial Transmit Sequence (PTS) method for PAPR mitigation in FBMC-OQMA signals. S. Ren and al., in [14], suggested a low complexity algorithm that combines SPTS and TR to enhance the PAPR mitigation. D. Kong in [15] has introduced a novel Discrete Fourier Transform (DFT)-based PTS technique that effectively reduces the PAPR of the system while maintaining good BER performance. The authors in [16] and [17] recommended two hybrid schemes, TR&DC and TR&Compd for low PAPR in FBMC-OQAM systems. In [18], the authors suggested an optimized PTS technique using Discrete Swarm Optimization (DSO) to achieve better PAPR reduction performance. M. Ango and al., in [19] recommended an enhanced-PTS with a low complexity search algorithm to minimize the PAPR. In [20], the authors proposed a new SLM approach founded on a modified forest optimization algorithm for PAPR reduction in the FBMC system. M. Hussein and al., in reference [21], offered an improved harmony search optimization for hybrid Clipping-PTS PAPR reduction in the FBMC system. The authors in [22] recommended a new hybrid approach based on companding and PTS methods for PAPR reduction of 5G waveforms.

In this study, we shed light on the hybrid PAPR minimization class by presenting new alternative algorithms with the aim of decreasing the PAPR in FBMC-OQAM systems without added computational complexity. The paper is structured as: In Section 2, the FBMC-OQAM and PAPR are presented. In Section 3, the principle of Tone Reservation is addressed, and the suggested algorithms are outlined. In Section 4, the simulation results are discussed. The last part marks some conclusions.

2. FBMC SYSTEM

The FBMC-OQAM system has been the subject of extensive research. It is observed to be a potential wave in future wireless communication systems. Contrary to the CP-OFDM waveform, FBMC modulation is an efficient PHY-layer with inherent ability under spectral coexistence scenarios. This has led to the exploration of FBMC-OQAMA in various applications, including MIMO systems [23], 6G networks [24], and even indoor optical wireless communications using LIFI technology [25]. The FBMC-OQAM signal is formed by using a group of sub-carriers, which are filtered by a group of filters. The transmitted FBMC-OQAM [26], symbol and M transmitted symbols are written, respectively as:

$$u^{FBMC}(t) = \sum_{n=0}^{N-1} [R_m^{\dot{n}}\beta(t - mT) + jI_m^{\dot{n}}\beta(t - mT - \frac{T}{2})]e^{jn(\frac{2\pi}{T}t + \frac{\pi}{2})} \quad (1)$$

$$U(t) = \sum_{m=0}^{M-1} u^{FBMC}(t), \qquad 0 \le t \le \left(M + \varepsilon - \frac{1}{2}\right)T \quad (2)$$

Where: The imaginary and real parts of the m^{th} symbol on the n^{th} sub-carrier are represented by $R_m^{\dot{n}}$, $I_m^{\dot{n}}$. The PHYDYAS filter [4] is denoted by $\beta(t)$.

Figure 1 shows a schematic of FBMC/OQAM symbols repartition. Every symbol has a time delay that is distributed alternatively between the real and imaginary parts. Each data block spans over $4.5\,T$ because of the employment of OQAM modulation and filter bank technique. To estimate the peak to average power ratio (PAPR) of the filter bank signal, the stable part of the signal is considered, which is defined from $(\varepsilon + 1/2)N/2$ to $MN + (\varepsilon + 1/2)N/2$ (see *Fig. 1*). This part contains MN samples, which is then separated into M intervals of duration T. Consequently, the PAPR of every interval is estimated using equation (3). To analyze the dynamic of filter bank signals, we exploit the CCDF given by equation (4).

$$PAPR\ (dB) = 10log_{10}\frac{max_{it \le t \le (i+1)T}(|U(t)|^2)}{E(|U(t)|^2)} \quad (3)$$

$$CCDF\ (PAPR) = Pr(PAPR > P_T) \quad (4)$$

3. ALTERNATIVE SCHEMES

3.1. Tone reservation

TR is a PAPR mitigation strategy [27], for any multicarrier design, such as FBMC and CP-OFDM waveforms. TR is based on canceling out high peaks through the use of some

reserved tones that are orthogonal to the data tones and do not convey any useful data. The TR scheme subsists of adding a time-domain signal $Cr(t)$ to the initial signal $U(t)$to reduce the PAPR. Though the resulting PAPR of $\big(U(t) + Cr(t)\big)$ must be lower than the initial PAPR of $U(t)$. The foremost advantage of the tone reservation strategy is its effectiveness and simplicity in reducing the envelope fluctuation in filter bank symbols. On the other hand, various trade-offs must be considered, for example, the number of iterations, PRTs, and numerical complexity. The following describes the step-by-step process of the Tone Reservation mechanism for FBMC-OQAM data blocks:

Algorithm 1: TR algorithm

1 Indicate the amount of **PRT** $\boldsymbol{Z}$ **,** and iteration $\boldsymbol{I}$ and the clipping level $\boldsymbol{\gamma}$, for **TR;**
2 Generate $\boldsymbol{U(t)}$ **FBMC-OQAM** signal by using Eq (1) and Eq (2)**;**
3 Clip $\boldsymbol{U(t)}$ signal at $\boldsymbol{\gamma}$ as :

$$\overline{\boldsymbol{U(t)}} = \begin{cases} \boldsymbol{U(t)} & |\boldsymbol{U(t)}| \le \boldsymbol{\gamma} \\ \boldsymbol{\gamma e^{j\varphi_u}} & |\boldsymbol{U(t)}| > \boldsymbol{\gamma} \end{cases}$$

4 Compute the clipping noise as: $\boldsymbol{e(t)} = \overline{\boldsymbol{U(t)}} - \boldsymbol{U(t)}$**;**
5 Switch it to the frequency domain $\boldsymbol{E(f)}$;
6 Re-modulate $\boldsymbol{C(f)}$ to form $\boldsymbol{Cr(t)}$**;**
7 Add $\boldsymbol{Cr(t)}$ to $\boldsymbol{U(t)}$ to get the **TR-FBMC-OQAM;**
8 Compute the **PAPR** of $\boldsymbol{U_{TR}(t)}$ signal by using Eq (2)**;**

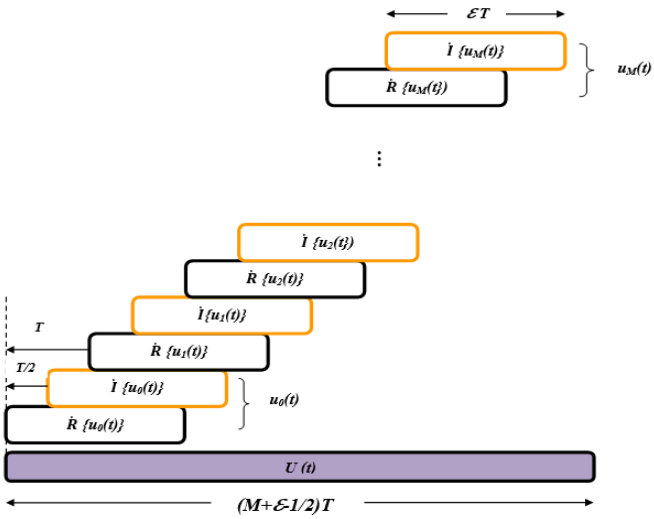

Fig. 1. FBMC-OQAM symbols repartitions.

3.2. TD and TC Schemes

The high peak to average power ratio (PAPR) in filter bank multicarrier symbols can present a major challenge in wireless systems. This issue has been tackled with various techniques of PAPR mitigation, but many of them entail increased complexity and cost. In

general, higher numerical complexity requires higher energy consumption for signal processing. Therefore, optimizing this parameter is important for reducing power consumption and prolonging the battery life of mobile devices. The main spotlight of this study is to reduce the PAPR in FBMC-OQAM symbols in a simple and effective way without additional complexity and without BER degradation. For this, we present our proposed algorithms, TR&DC (TD) [16] and TR&Compd (TC) [17]. Both suggested schemes are based on TR method [11], [14] with two other boosters' techniques deep clipping (DC) [28], and Mu-Law [29] (see *Fig. 2*), to improve the PAPR reduction in filter bank systems. These two methods are very effective in reducing the dynamic range of multicarrier signals. Both methods TD and TC, (see *Fig. 3*), share the same first step, which is the tone reservation (TR) process, they differ in the second step. In the TD algorithm, TR-FBMC-OQAM symbols are clipped by deep clipping (DC) [28]. In a detailed way, we can say that TR can minimize the dynamic range of FBMC symbols but cannot cancel all peak power. For this, we recommend the use of the deep clipping function (DC) which is a simple and enhanced version of clipping to deeply clip high amplitudes, and to get better PAPR reduction. To control the depth of clipping, a parameter known as the clipping depth factor has been provided (see *Fig. 2*).This suggested TD technique for PAPR reduction combines the efficiency of the first stage (TR) with the reduced computational complexity of the second step (DC), providing improved PAPR reduction without added complexity. To not impact our signal, we used the optimal values of depth clipping and the clipping level for DC fonction to maintain the best BER performance (see Table 2). The main contributions of TD are: Firstly, compared to the TR algorithm, we use a small number of iterations and tones to have a relatively low PAPR FBMC signal. Then, adopt the deep clipping (DC) method to provide efficient PAPR minimization without added computational complexity and easy implementation. Secondly, compared to existing hybrid PAPR minimization algorithms in the literature, we find that the majority of works use very complex algorithms such as ACE-TR hybridization, PTS-TR, SLM-PTS and SLM-TR, which require a large number of operations (IFFT/FFT), as well as Side Informations 'SI' transmission for SLM and PTS. So in TD, we don't need to send SI, and we only need two operations (IFFT/FFT) to generate a correction signal (1 iteration), which could be advantageous for reducing algorithm complexity. Thirdly, we can adjust the depth factor, clipping threshold and TR parameters (Z, I) to achieve a compromise between computational complexity, PAPR reduction and BER perfomance.

On the other hand, in TC, as a second step after TR, we apply the Mu-Law [29] mechanism, which is a simple and effective companding technique to correct more all TR data blocks to ensure better PAPR reduction. Mu-law compandig is an amplitude limiting scheme that is easy to implement in any digital system.various forms of nonlinear companding, such as A-law and Mu-law are studied in the literature. Through the use of various functions, the companding technique reduces the PAPR by compressing high amplitudes and expanding lower ones. The contributions of TC are: Firstly, we run the TR

with low iteration times and tones to obtain FBMC signals with low PAPR, then we apply the Mu-Law companding function to give a better reduction. Secondly, if we compare the scientific work based on the Mu-Law in the literature, we find that all the articles use very large ∂ values (Mu-law ratio), for example: ∂ = 255, which degrades the BER of the system due to the compression processes, so in our algorithm, we have proved that with a small value of ∂, we can have an excellent reduction, as in our case ∂ = 1. This benefits distortion reduction. Thirdly, the TC algorithm is remarkably flexible in terms of parameter adaptation (∂ parameters of the Mu-Law and other TR parameters such as (Z, I)) to achieve a compromise between PAPR reduction, reduced complexity, and BER quality. Finaly, we can say that to achieve the best results for both TD and TC schemes, we have to select the optimal combination of parameters because if we increase I, the complexity will increase, and if we use a large number of Z we will lose the bit rate, and if we use large values of clipping level and compandig parameter, we will degrade the BER performance.

The proposed schemes TD and TC for FBMC-OQAM symbols PAPR mitigation follow algorithm 2. In the following section, we estimate the performance of the three algorithms (TR, TD, and TC) and compare them.

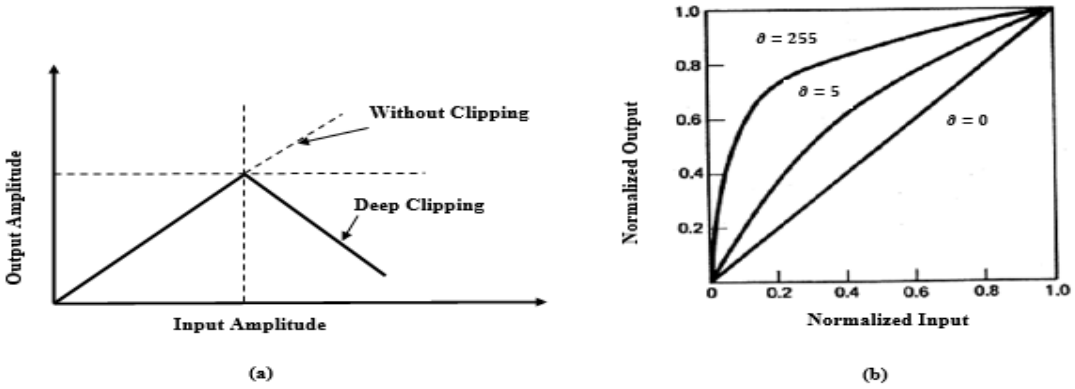

Fig. 2. (a) Deep clipping and (b) Mu-law companding.

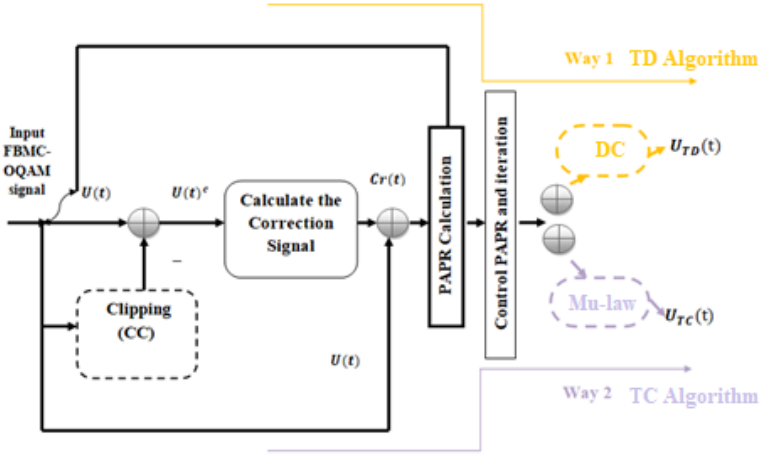

Fig. 3. TD and TC PAPR mitigation treatments.

Algorithm 2: Alternative Algorithms

1. **STEP I:TR**
2. Indicate the clipping level $\boldsymbol{\gamma}$, the number of reserved tones **Z** and iteration **I** for TR;
3. Generate $\boldsymbol{U(t)}$ FBMC-OQAM signal by using Eq(1) and Eq(2);
4. Clip $\boldsymbol{U(t)}$ signal at $\boldsymbol{\gamma}$:

$$\widehat{U(t)} = \begin{cases} U(t) & |U(t)| \le \gamma \\ \gamma e^{j\varphi_u} & |U(t)| > \gamma \end{cases}$$

5. Generate $\boldsymbol{Cr(t)}$ signal by :
   - Compute the clipping noise $\boldsymbol{e(t) = \widehat{U(t)} - U(t)}$;
   - Switch it to the frequency domain $\boldsymbol{E(f)}$;
   - Re-modulate $\boldsymbol{C(f)}$ to get $\boldsymbol{Cr(t)}$;
6. Add $\boldsymbol{Cr(t)}$ to $\boldsymbol{U(t)}$ to get $\boldsymbol{U_{TR}(t)}$;
7. **STEP II:**
   - **For TD**
8. Clip $\boldsymbol{U_{TR}(t)}$ by **DC** mechanism at a clipping level $\boldsymbol{D}$ and the clipping-depth factor$\boldsymbol{\mu}$.

$$\widetilde{U(t)}_{TD} = \begin{cases} U_{TR}(t) & |U_{TR}(t)| \le D \\ D - \mu(U_{TR}(t) - D) & D < |U_{TR}(t)| \le \dfrac{1+\mu}{\mu} D \\ 0 & |U_{TR}(t)| > \dfrac{1+\mu}{\mu} D \end{cases}, 0 \le \left(M + \varepsilon - \frac{1}{2}\right) T$$

   - **For TC**
9. Apply **Mu-Law** to the$\boldsymbol{U_{TR}(t)}$ signal as:

$$U_{TC}(t) = \frac{J \log\left(1 + \dfrac{\partial |U_{TR}(t)|}{J}\right)}{\log(1+\partial)} sgn\left(U_{TR}(t)\right)$$

10. **STEP III:PAPR CALCULATION**
11. Determine the PAPR of **TD&TC-FBMC-OQAM** using equation (4).

3.3. Complexity analysis

The numerical complexity was the main priority for both proposed TD and TC techniques due to the importance of this parameter in the energy consumption of FBMC systems. In this work, the complexity is evaluated in terms of the complex multiplications required for all M data blocks in an FBMC-OQAM frame. The compared systems use the same structure for Modulation and Demodulation. We consider that the complexity of an IFFT/FFT of N-point is $Nlog2N$, and the complexity of PPN is εN (ε is the overlap factor for PHYDYAS filter). Both algorithms are essentially based on TR treatment, so we can say that the complexity of TD and TC depends on the calculation of the attenuation signal in the time (c) and frequency (C) domains. More clearly, in each iteration of TR, the estimation of C and c requires two IFFT/FFT operations and two PPNs in order to compute the correction signal. The complexity of the TR for one iteration and M data blocks is reported in Table 1.

Moreover, in TD and TC, the deep clipping and Mu-law function (no iterations) do not add complexity to the TR algorithm. However, the complexity of TD and TC presents the same complexity as TR, which unfortunately increases with the number of iterations of this technique.

Table 1. Complexity of the proposed algorithms.

Algorithms	Majors operations in 1 iteration TR	Temporal complexity
TR	2 x (IFFT/FFT) et 2 x (PPN)	MI[2 x O (N $\log_2$ N)+2εN]
TD	2 x (IFFT/FFT) et 2 x (PPN)	MI[2 x O (N $\log_2$ N)+2εN]
TC	2 x (IFFT/FFT) et 2 x (PPN)	MI[2 x O (N $\log_2$ N)+2εN]

4. SIMULATION RESULTS

In this section, we present some numerical results for the three methods (TD, TC, and TR) using the most merit criteria for PAPR reduction methods in literature, which are CCDF, PSD, BER, complexity, SI and debit loss. Simulations are guided for an FBMC-OQAM system based on 4-OQAM modulation, 64 subcarriers, 16 data blocks, and a prototype filter named PHYDYAS with ($\varepsilon = 4$) is used. The simulation environment is shown in Table 2.

Table 2. Simulation parameters for TR, DC and Mu-law.

Parameters	*Values*
Reserved tones	*Z=8*
Iteration times	*I=8*
Clipping level for TR	*γ=2.1*
Clipping level for DC	*D=3*
Depth factor for DC	*μ=0.6*
Mu-law ratio	*∂ =1*

4.1. CCDF

The CCDFs comparison of TD, TC, and TR is shown in *Figure 4*, with a fixed threshold for the three algorithms equal to 2.1 dB and a fixed number of iterations, PRTs ($I = 8, Z = 8$). From the CCDFs curves, we can observe that when the CCDF is 10^{-3}, among three mechanisms TD, TC and TR, TC algorithm decreases by a gain equal to $4dB$, TD decreases by 3.5dB, while TR decreases the PAPR by $3dB$. It can be noted that the TC performs better than the TD and TR in terms of PAPR reduction. *Figure 5* presents the CCDFs of the TD with $I = 12$ iterations, TC with $I = 6$ iterations, TR with $I = 12$ iterations and the original FBMC-OQAM signal. We can notice that TC reduces the PAPR by 3.8 dB with only six iterations. Closer gain is reached with TD method however, with $I = 12$. We can notice that TC with a small number of iterations (6) has a superior gain compared to TD. This means that using the

TC algorithm with only 6 iterations resulted in a larger improvement in terms of numerical complexity compared to using the TD algorithm. Therefore, it is always recommended to thoroughly evaluate the performance of different algorithms with different parameter settings on a given task before making a final decision on which algorithm to use in practice.

4.2. BER

Figure 6 illustrates the BER performance of the proposed techniques TD and TC in an AWGN channel in the case of absence of HPA and by using the same simulation parameters as in Table 2. From the figure, we find that the proposed algorithms present good results in terms of BER, which are close to each other and to the BER of the original FBMC signal. In other words, we can say that our algorithms do not degrade the BER performance before the non-linear amplification.

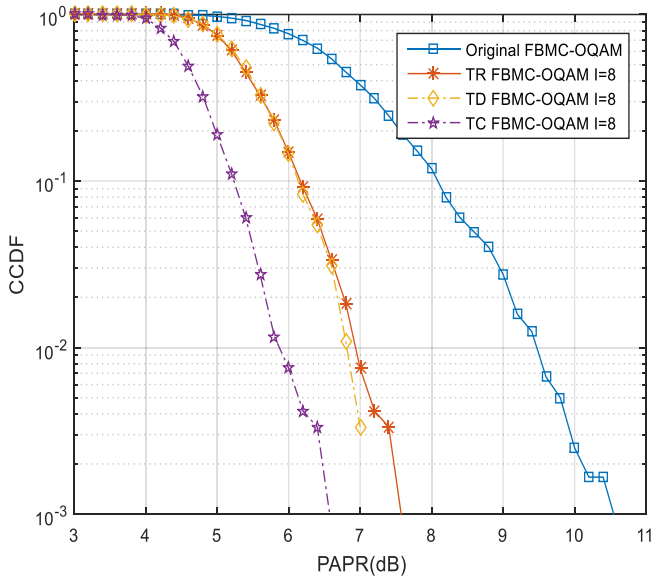

Fig. 4. CCDF measurements of the TD, TC and TR methods with eight iterations.

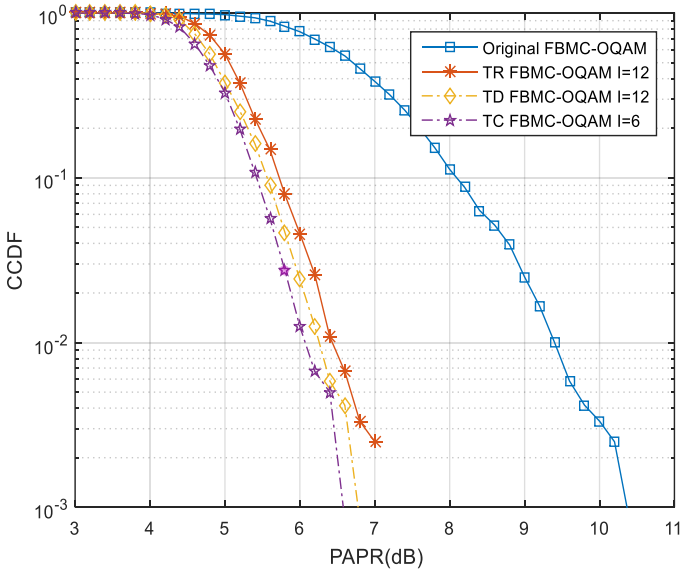

Fig. 5. CCDF measurements of the TD, TC and TR methods with different iteration time.

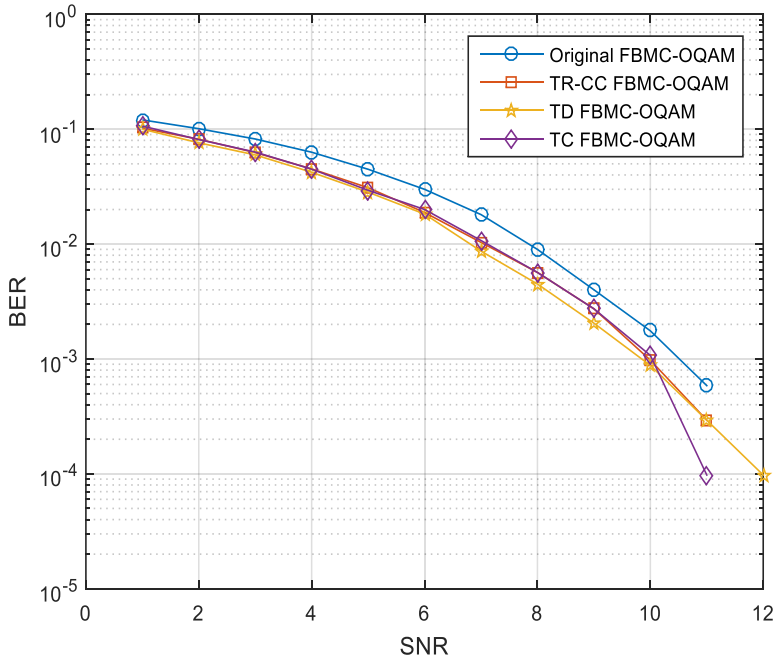

Fig. 6. BER performance of the TD, TC and TR methods in AWGN channel.

4.3. PSD

In our investigation, we also carried out simulations in terms of PSD for TD, TC, TR, and FBMC-OQAM original without the presence of an HPA. From *figure 7*, we can clearly see that the PSD of TC and TD coincide with the FBMC-OQAM signal without PAPR reduction. We can note that our suggested methods for PAPR reduction do not increase the PSD for the FBMC-OQAM symbols in the case of absence of non-linear HPA.

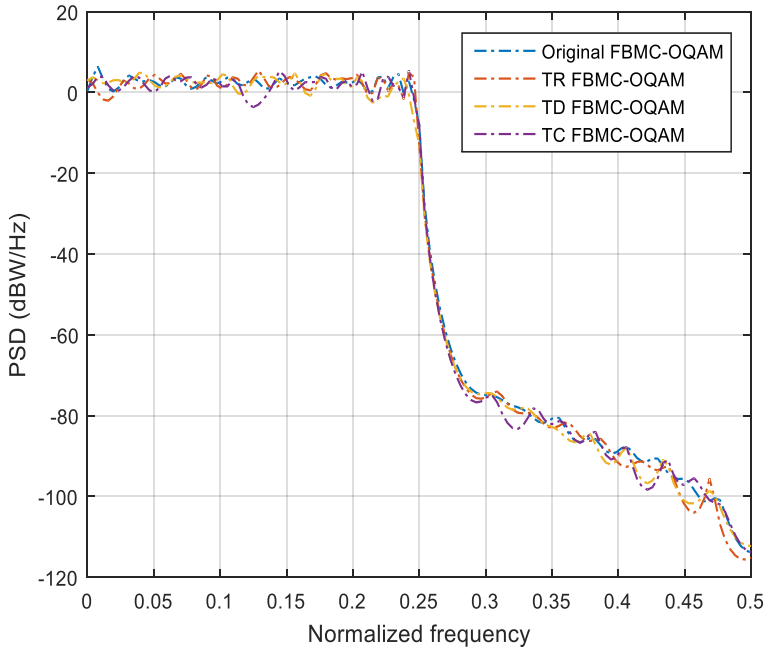

Fig.7. PSD performance of the TD, TC and TR methods.

4.4. Discussion

To complete our investigation, we have introduced a comparative table (see Table 3) of the CCDF, BER performances, and complexity of TD and TC and three cited methods, Hybrid PTS/TR [11], M-Hybrid [11] and Sparse PTS/TR [14]. From the table, we can say that in the case of an FBMC system with 4-OQAM modulation, 64 subcarriers, 16 data blocks and a prototype filter of size $4T$, the Hybrid PTS/TR, M-Hybrid, and Sparse PTS/TR can achieve a significant reduction of PAPR. Also, the proposed TD and TC methods can reduce PAPR considerably. It is clear that TC outperforms Sparse PTS/TR by $0.01dB$, Hybrid PTS/TR by $0.15dB$ and M-Hybrid by $0.05dB$. According to references [11] and [14] and Table 3, we recall that the proposed and cited algorithms do not cause any BER distortions. We have already demonstrated that the complexity of our algorithms TD and TC is always equal to the complexity of TR (see Table 1). According to reference [14] and Table 4, both PTS techniques have high complexities, and in the hybrid case, the complexity will increase. Therefore, we can say that the cited algorithms have very high complexity. The results of this study demonstrate that the proposed TD and TC algorithms are effective techniques for PAPR reduction in FBMC systems. Our finding proved that these algorithms outperform the existing methods in terms of complexity and PAPR reduction while not introducing any BER distortions or requiring additional information 'SI' transmission.

Table 3. Comparative PAPR values, BER loss at 10^{-3} and complexity of proposed and cited methods.

Algorithms	**Parameters**	**Performances PAPR [dB] (CCDF=10^{-3})**		**BER loss [dB]**	**Complexity**
TR	Z=8, γ=2.2	**I=8**	**I=4**	**0**	C_{TR}
		7.77	8.75		
TD	Z=8, γ=2.2, D=3, μ =0.6	**I=8**	**I=4**	**0**	C_{TR}
		7.00	/		
TC	Z=8, γ=2.2, ∂=1	**I=8**	**I=4**	**0**	C_{TR}
		6.36	7.15		
Sparse PTS/TR [14]	Z=8, γ=2.2, K=8, S=4	**I=8**	**I=4**	**0**	$C_{SPTS}+C_{TR}$
		6.46	/		
Hybrid PTS/TR [11]	Z=8, γ=2.2, S=4	**I=8**	**I=4**	**0**	$C_{PTS}+C_{TR}$
		/	7.30		
M-Hybrid [11]	Z=8, γ=2.2, S=4	**I=8**	**I=4**	**0**	$C_{PTS}+C_{TR}$
		/	7.20		

Table 4. Complexity of sparse PTS and segmental PTS.

Methods	**Real-Multiplications**	**Real-Additions**
Sparse PTS	$KS(2^S+1)$	$2KS(S-1)(2^S+1)$
Segmental PTS	$MNS(2^S+1)$	$2NM(S-1)(2^S+1)$

Where *S* is the number of sub-blocks, M is the number of data blocks, *N* is the number of subcarriers, and *K* is the number of iterations of Sparse PTS.

In the end, to recap our investigation, we propose a comparative table. Table 5 compares the performance of various PAPR mitigation algorithms in the FBMC structure. The algorithms are compared on five criteria: SI, BER, PAPR, complexity, and debit loss. From Table 5, we note that our suggested TD and TC algorithms are less complex, and do not require supplementary information (SI) compared to the cited techniques. They are very competitive with hybrid algorithms in the literature in terms of PAPR reduction and do not degrade the BER. However, they introduce bit rate loss like all probabilistic techniques (PTS and SLM).

Table 5. Comparative study of proposed and cited algorithms.

Algorithms	SI	BER Destruction	PAPR Reduction	Complexity	Debit loss
TR	No	No	Moderate	Moderate	Yes
TD	No	No	High	Moderate	Yes
TC	No	No	Very high	Moderate	Yes
Hybrid PTS/TR [11]	Yes	No	High	Very high	Yes
Sparse PTS/TR [14]	Yes	No	Very high	Very high	Yes
M-Hybrid [11]	Yes	No	High	Very high	Yes

5. CONCLUSION

In this paper, two alternative algorithms TD and TC, for PAPR mitigation in FBMC-OQAM systems were suggested. Simulation results demonstrated that the proposed algorithms present a good compromise between the capacity of PAPR reduction, complexity, BER performance and other metric criteria. In addition, for both methods, we can adjust the simulation paramters to get the optimal performance. Moreover, the numerical results are very competitive in terms of PAPR reduction with the cited algorithms in the literature and without additional complexity. The proposed algorithms are expected to be suitable for various communication systems, including 5G and beyond, where high-speed data rate and low latency are required. As a future work, we will involve testing TD and TC algorithms in practical scenarios and exploring their potential for integration with other methods for improved performance.

REFERENCES

[1] G. Monsalve, J. L. Ros, L. Brossier and J. M. Mestdagh, *An improved green OFDM scheme for PAPR reduction*, Telecom, vol.1, pp.196-210, 2020.

[2] P. Xiao, C. Toal, D. Burns, V. Fusco and C. Cown, *Transmit and receiver filter design for OFDM based WLAN systems*, International conference on wireless communication and signal processing (WCSP), 2010.

[3] F. Schaich and T. Wild, *Waveform con-tenders for 5g - OFDM vs. FBMC*. UFMC, International symposium on communications control and signal processing (ISCCSP), pp. 457-460, 2014.

[4] M. Bellanger, D. L. Ruyet, D. Roviras, M. Terre, J. Nossek, L. Baltar, Q. Bai, D. Waldhauser, M. Renfors, T. Ihalainen, et al, *FBMC physical layer : A primer*, Phydyas, pp.7-10, 2010.

[5] N. Michailow, M. Matthe, I. S. Gaspar, A.N.Caldevilla, L.L. Mendes, A. Festag and G. Fettweis, *Generalized frequency division multiplexing for 5th generation cellular networks*, IEEE transactions on communications, vol.62, no.9, pp.3045-3061, 2014.

[6] V. Vikilian, T. Wild, F. Schaich, S. Brink and J. F. Frigon, *Universal filtered multi-carrier technique for wireless systems beyond LTE*, IEEE globecom workshops (GC Wkshps), pp.223-228, 2013.

[7] S. Thota, Y. Kamatham and C. S. Paidimarry, *Analysis of hybrid PAPR reduction methods of OFDM signal for HPA models in wireless communications*, IEEE Access, vol.8, pp.22780-22791, 2020.

[8] R. Gopal and S. K. Patra, *Combining tone injection and companding techniques for PAPR reduction of FBMC-OQAM system*, Global conference on communication technologies (GCCT), pp.709-713, 2015.

[9] M. Laabidi, R.Zayani and R. Bouallegue, *A new tone reservation scheme for PAPR redction in FBMC/OQAM systems*,International wireless communications and mobile computing conference (IWCMC), IEEE, pp.862-867, 2015.

[10] M. Laabidi, R. Zayani, D. Roviras and al., *PAPR reduction in FBMC/OQAM systems using active constellation extension and tone reservation approaches*, IEEE sympsosium on computers and communication (ISCC), pp.657-662, 2015.

[11] H. Wang, X. Wang, L.Xu, and al., *Hybrid PAPR reduction scheme for FABMC/OQAM systems based on multi data block PTS and TR methods*, IEEE access, vol.4, pp.4761-4768, 2016.

[12] H. Wang, *A hybrid reduction method based on SLM and multi-data block PTS for FBMC/OQAM systems*, Information, vol.9, no.10, pp.246.

[13] Z. He, L. Zhou, Y. Chen and al., *Low complexity pts scheme for PAPR reduction in FBMC-OQAM systems*, IEEE communication letters, vol.22, no.11, pp.2322-2325, 2018.

[14] S. Ren, H. Deng, X. Qian, and al., *Sparse PTS scheme based on TR for PAPR reduction in FBMC-OQAM systems*, IET communications, vol.12, no.14, pp.1722-1727, 2018.

[15] D.Kong, X. Zheng, Y. Yang and al., *A novel DFT-based scheme for PAPR reduction in FBMC/OQAM systems*, IEEE wireless communications letters, vol.10, no.1, pp.161-165, 2020.

[16] S. Senhadji, Y. M, Bendimerad, and F. T. Bendimerad, *New scheme for PAPR reduction in FBMC-OQAM systems based on combining TR and deep clipping techniques*, International journal of electrical & computer engineering, vol.11, no.3, pp. 2088-8708, 2021.

[17] S. Senhadji, Y. M, Bendimerad, and F. T. Bendimerad, *Enhancing PAPR reduction for FBMC-OQAM systems by joint both tone reservation and companding methods*, Indonesian journal of electrical & computer engineering, vol.21, no.2, pp.919-926, 2021.

[18] L. Li, L. Xue, X. Chen and al., *Partial transmit sequence based on discrete swarm optimization with threshold about PAPR reduction in FBMC/OQAM system*, IET communications, vol.16, no.2, pp.142-150, 2022.

[19] M. Ango, N. I, Mwangi, and al., *Minimizing the PAPR for FBMC/OQAM Signals using enhanced-PTS with low complexity search*, Journal of communications, vol.17, no.6, 2022.

[20] K. K. Vaigandla, J. Benita., *Selective mapping scheme based on modified forest optimization algorithm for PAPR reduction in FBMC/OQAM System*, Journal of intelligent & fuzzy systems, no preprint, pp.1-15, 2023.

[21] M. Hussien, and al., *Improved harmony search optimization for hybrid clipping-PTS PAPR reduction in FBMC systems*, RS Open journal on innovative communication technologies, vol.3, no.8, 2023.

[22] S. Ramavath and al., *A hybrid approach based on companding and PTS methods for PAPR reduction of 5G waveforms*, International journal of electronics letters, pp.1-13, 2024.

[23] A. Bedoui and M. Et-Tolba, *A deep neural network-based interference mitigation for MIMO-FBMC/OQAM systems*, Frontiers in communications and networks, vol.2, pp.728982, 2021.

[24] F. Hamdar and al, *FBMC-OQAM transceiver for future wireless communication systems*, IEEE open journal of vehicular technology, 2023.

[25] H. Hesham and T. Ismail, *Hybrid NOMA-based ACO-FBMC/OQAM for next-generation indoor optical wireless communications using LiFi technology, optical and quantum electronics*, vol.54, no.3, pp.201, 2022.

[26] P. Siohan, C. Siclet, and N. Lacaille, *Analysis and design of OFDM/OQAM systems based on filter bank theory*, IEEE transactions on signal processing, vol.50, no.5, pp.1170-1183, 2002.

[27] J. Tellado, *Peak to average power reduction for multicarrier modulation*, Stanford University, PHD dissertation, 2000.

[28] S. Kimura and al., *PAR reduction for OFDM signals based on deep clipping*, 3rd international symposium on communications control and signal processing ISCCSP 2008, pp.911-916, 2008.

[29] M. Mounir and M.B. El_Mashade., *On the selection of the best companding technique for PAPR reduction in OFDM systems*, Journal of information and telecommunications, vol.3, no.3, pp.400-411, 2019.

DECENTRALIZED ARCHITECTURES IN IOT DATA SHARING USING BLOCKCHAIN TECHNOLOGY

Cristinel **COSTEA**
Technical University of Cluj-Napoca, North University Centre of Baia Mare
cristinel.costea@ieec.utcluj.ro

Keywords: Content addressable storage, Blockchains, Distributed systems

Abstract*: The development of IoT applications generally relies on centralized architectures, whether they use solutions based on cloud or on premises environments, usually operated by a single entity. However, recent technologies and the increasing number of interconnected intelligent devices are driving new approaches, the essential requirements being scalability and fault-tolerance. This work studies an alternative concept based on a decentralised architecture useful in several scenarios and focuses on available technologies for potential practical implementations.*

1. INTRODUCTION

If IoT devices record data locally for later access by other processes, scalability and access time problems arise due to the volume and rate of data generation. A particular solution is provided by time-series databases, but cloud storage is the most common storage for IoT data [1]. This offers the advantage of easy access to data from anywhere and anytime, as well as the possibility of mass storage. By example, Hadoop is an open-source framework for storing and processing data in large sets, distributed on several servers. It can manage large volumes of structured and unstructured data, being a suitable solution for data generated by IoT equipment.

For latency-sensitive and real-time applications, new paradigms have been developed. In Edge computing the data is stored and processed at the "edge" of the network, close to where it is generated. This reduces latency and allows for a faster response to data. Fog computing storage is a mix between edge computing and cloud storage. In a fog computing

model, data is primarily processed at the "edge" of the network but can also be sent to the cloud for storage and further processing [2]. Storage on gateways: gateways are devices that connect individual IoT devices to the Internet. They can store data from multiple devices, allowing pre-processing and data management. Decentralized storage: approach where data generated by IoT devices is stored in a distributed network of nodes, rather than concentrated in one centralized location. This model provides scalability, resilience and fault tolerance, and with the help of advanced blockchain technology, users can improve data privacy and maintain sovereignty over their data.

2. BACKGROUND

In modern distributed systems the concepts of consistency, availability and partition tolerance play a crucial role in the design and implementation of scalable and fault-tolerant systems. These concepts are essential to understanding and managing decentralized storage, where data is distributed over a global network of nodes.

Consistency is ensured by implementing protocols and algorithms that coordinate and synchronize actions between network nodes. Among the most important consensus protocols studied are Paxos, Raft, Byzantine Fault Tolerance (BFT), Practical Byzantine Fault Tolerance (PBFT), Zab [3]. With the development of blockchain systems, each system perfected a specific protocol, the most famous being Proof of Work (PoW) for Bitcoin or Proof of Stake (PoS) for Ethereum (and not only).

But each distributed system can provide just two of three fundamental properties, not all three at the same time. Specifically, the CAP theorem [4], formulated by Eric Brewer in 2000, states that in a distributed system, consistency (C), availability (A), and partition tolerance (P) cannot be achieved simultaneously. Another theorem developed by Michael J. Fischer, Nancy A. Lynch, and Michael S. Paterson in 1985(FLP theorem) [5], states that in an asynchronous distributed system, where nodes can fail by stopping processing, there is no a deterministic distributed algorithm to make a safe decision when a decision node may fail.

2.1. Distributed ledgers

Distributed Ledgers are a form of data recording that does not require a central authority but uses a distributed network of nodes to validate and store information. There are various types of distributed ledgers, but most approaches refer to blockchains. Two other important approaches are DAG (Directed Acyclic Graph) and Hashgraph [6], each with distinct features and applications. Blockchain is basically a kind of linked list where transaction information is stored in sequential blocks. In blockchain, data is immutable,

meaning that once a transaction is recorded in a block and added to the blockchain, it cannot be changed or deleted.

Some outstanding features of these technologies relate to digital signatures, distributed consensus and smart contracts. Distributed ledgers are implemented on the Internet, so participants are assumed not to trust each other by default, and this is where hashing technologies and public key cryptography come into play.

2.2 Smart contracts

A smart contract is a piece of code that runs on the blockchain and is recorded in a block of the chain. The largest number of smart contracts are registered in the Ethereum network (in 2022 there were about 44 million[1], although only 15 million were original and functional); many other networks have developed similar technologies in various programming languages such as Solana, Cardano, Polkadot, Algorand, Hyperledger, Stellar, Arbitrum, Optimism, Cosmos.

In Ethereum a smart contract has its own persistent data storage that can be modified by specific transactions (calling methods from the smart contract). Anyone with an Ethereum account can initiate a transaction that calls a method on the contract and can change its state. In fact, when a user changes the value of a (state) variable, that transaction returns a new state of the contract, which will be recorded with the transaction that called the contract.

Information about contract states is stored in a trie data structure: Merkle Patricia Tree (MPT) [7]. Like in a radix tree in MPT the key is split into sequential characters; in the lookup procedure each character of the encoded key is used to match the encoded path. Updating a value only involves recalculating the affected paths in the tree, not the entire tree. A new transaction that will modify the same variable will not require a node to go through the entire transaction history in the blockchain.

2.3 Decentralized storage

In the decentralized storage method, the data is distributed over several nodes, often in a peer-to-peer (P2P) network, avoiding concentration in a single location (single point of failure) and avoiding the control of a single centralized entity.

The outstanding example is the Inter-Planetary File System (IPFS) which defines both a protocol and a P2P file system to store and share content on the Internet. IPFS use content addressing: each piece of content is addressed by a unique cryptographic hash named Content Identifiers (CIDs) and generated based on the content.

A distinctive attribute of P2P (Peer to Peer) systems, which include both blockchain and IPFS, is the use of the Distributed Hash Table (DHT) [8] protocol. It offers a scalable way of organizing without the need for a centralized server. The nodes are arranged in a ring

configuration, they can enter and exit the system without significantly disrupting the operation.

When a node joins the IPFS network, it generates a pair of public and private keys, and the public key is used to identify the node in the network. The node must connect to another node in the DHT, usually a bootstrap node that provides information about other nodes in the network. It is an entry point to the network for new nodes or those that want to reconnect. The address of a bootstrap node is often recorded in the source code because these nodes are constantly available and accessible to ensure network stability. Following the connection request the new node will be able to build a routing table and which nodes it should connect to directly. Based on a finger table neighboring nodes will update a replica of records to ensure the appropriate level of redundancy.

2.4 Decentralized applications

A web application can interact directly with Ethereum via a local Ethereum node (with JSON-RPC) or via a Web3 service provider (such as Infura, Alchemy, Chainstack, QuickNode or BlockDaemon). The most popular JavaScript library used in these operations is Web3.js. The web application creates a Web3.js instance and connects to Metamask to communicate with the Ethereum network. Metamask is a browser extension that allows users to interact with decentralized applications (DApps), being a digital wallet required to access the Ethereum network. Under these conditions, a web application can read and write data to Ethereum smart contracts, send transactions and receive events from the blockchain.

3. EXPERIMENT AND RESULTS

The system architecture considered for the simulation includes the following possible components: IoT smart sensors provide messages in JSON format to devices with raw data pre-processing capability, for example gateway devices. They were simulated through a web application that logs the data to a decentralized storage system based on the IPFS protocol. A unique hash is generated for each file stored. This obtained CID is sent to a smart contract to be registered in the Ethereum blockchain. Later, for testing the data retrieval mechanism, a similar contract is used to obtain the CID based on data retrieved from IPFS.

To implement the contract, the Solidity language was used (the latest version being 0.8.24) with online IDE Remix. Each Ethereum user has a wallet that is identified by a specific cryptographically generated address. In this case Metamask (Chrome plug-in) was used to interact with the Web3 application. For the Ethereum Sepolia testnet network there are several online services (faucets) that offer free fractions of ETH coins for the purpose of testing applications. The user can send and receive cryptocurrencies (ETH or other tokens) and

interact with smart contracts to register, update or run.

A smart contract is uploaded to the Ethereum network through a special transaction - contract creation transaction. Such a transaction will include the bytecode of the contract, the address of the sender - the user sending the transaction to the network. The recipient of the transaction is in this case the address 0x0, and the specified value is usually zero. The nonce is a number that increments with each sender transaction and is used to prevent duplicate transactions or to determine the order of transactions. Like any other transaction, it will contain the gas, which is the units of calculation needed to process the transaction, and the gas price, which is the rate paid for each unit of *gas*.

After the contract becomes active, users can interact with it by sending transactions to the smart contract address and calling the functions and methods defined in the contract. The contract registration can be verified (like any other transaction) with Etherscan Explorer. It gives users access to detailed information about blocks, transactions, wallet addresses, smart contracts and more, which are stored on the Ethereum network.

Essentially, once a transaction interacting with a smart contract is confirmed and included in a block, the contract state is updated to reflect the changes made by the transaction. Thus, when a user accesses a variable or calls a read function, the value is returned from the contract state, which is updated and maintained by each node in the network.

```
// SPDX-License-Identifier: MIT
pragma solidity ^0.8.0;

contract SaveMetadataString {
    mapping(address => string) public savedData;

    event IoTDataSaved(address indexed user, string newMetadataString);

    function saveMetadata(string memory _string) public {
        savedData[msg.sender] = _string;
        emit IoTDataSaved(msg.sender, _string);
    }

    function getData() public view returns (string memory) {
        return savedData[msg.sender];
    }
}
```

Fig. 1. Smart contract fragment in Solidity

A fragment of the smart contract is shown in *fig.1* to allow a brief discussion on the working mechanism. This simple example smart contract written in Solidity allows users to save a string associated with their Ethereum address and retrieve it later.

The *mapping* statement associates an Ethereum address (in this case of the user accessing the contract) with a string. The public variable will be accessible directly from

outside the contract. The *IoTDataSaved event* is emitted whenever a user saves a string, thus allowing applications to react to on-chain events. *function getData* returns the string associated with the address of the user who called the function. The function is declared view, which means it will not change the state of the contract and only returns a value.

In this example, there is no restriction limiting access to the contract's *saveMetadata* function. Thus, any user who owns an Ethereum address and has access to the Ethereum network can send a transaction to the smart contract address and record a string using the *saveMetadata* function. Each user who submits a string registration transaction will have their string saved within the contract associated with their Ethereum address. This means that each user can register and retrieve their own string using their Ethereum address. Multiple strings can be stored for each address: for example, a mapping of mappings, where the outer key is the user's address, and the inner key can be a unique identifier associated with each string.

Data immutability on the blockchain does not mean that data cannot be updated, but rather that changes are made by adding new values or updating the state of the contract, and existing data remains intact and available for consultation transparently. There are three types of variables in the Solidity coding language: local variables, global variables and state variables (*World State*). Global variables hold transaction information and blockchain properties like sender or origin, but the state variables are permanently stored in the chain (*smart contract storage*).

Table 1. Time and cost evaluation

1	Time to write in IPFS (JSON 592 bytes)	1570 - 1748 msec
2	Time to read from IPFS	695 - 1020 msec
3	Cost of smart contract deployment (gas) Sepolia Ethereum Testnet	0.00108179 eth 0.00398563 eth
4	Time to write in blockchain	5234 - 9263 msec
5	Cost to write CID (IPFS hash) in blockchain	0.00023343 eth 0.00025173 eth
6	Gas price	2.507532742 Gwei 2.704124527 Gwei
7	Time to read (46b) from blockchain	191 - 197 msec

Updating a variable in a smart contract in Ethereum involves using a transaction recorded on the chain that will update the state of the contract. Thus, reading a variable does not require traversing the entire transaction history.

Table 1 show the times for write and read and the gas used in this experiment; there are one billion gwei (Giga wei) to one ether and one quintillion wei (18 zeros) to one ether.

Ethereum solves the problem of updating state variables through the concept of "world state". At a given moment, world state represents the current state of the smart contract. World

state is a mapping between the Ethereum addresses of accounts and the states of these accounts. When a smart contract is called and changes a state variable, the blockchain history is not changed, but the world state is updated to reflect the new values of the state variables. To implement these functionalities in an Ethereum node there is a database (usually LevelDB or RocksDB) that stores the world state. Regarding the large number of smart contracts (over 45 million), Ethereum manages this by using *gas*. Each instruction executed in Ethereum requires a certain amount of gas, which is paid by the one who initiated the contract call.

4. RELATED WORK

In recent years, more studies are oriented on introducing blockchain technology into the IoT applications – smart grids, smart cities, healthcare [9], supply chain and logistics, autonomous vehicles [10], decentralized identity [11].

In power systems blockchain can be used to build decentralized and secure P2P energy trading platform. An example of existing commercial implementations is PowerLedger. Relevant apps in smart grids are also secure metering and grid monitoring. The paper [12] presented two methods for voltage monitoring and storage. The authors considered that the centralised method is more vulnerable to attacks but the second decentralised solution using Ethereum IPFS and Python enhances security and relatively slow.

As decentralized storage solutions expand and improve, the prices of these services also become more affordable than cloud storage [13]. One of the most well-known storage providers using IPFS is Filecoin which operates a blockchain based on the FIL coin to provide incentives to participants. Thus, this mechanism does not require trust between the contractual parties.

Although the automatic monetization of IoT [14] data appears to be an attractive aspect for data owners, there are still serious regulations issues related to the recognition of cryptocurrencies. However, one promising aspect could be the introduction of Central Bank Digital Currencies (CBDC) [15].

5. CONCLUSIONS

In this paper we have reviewed some aspects related to decentralised data storage and the applications of these techniques for IoT systems. Most solutions use blockchain for access control and data recording in IPFS. We carried out a simple experiment by implementing a web solution with current technologies to analyze the flow of this technique. The level of complexity is higher than in the case of classical solutions, and the access time can be

restrictive for some applications. At the same time, offers benefits: transparency, enhanced data security, autonomy or monetization potential of IoT data.

REFERENCES

[1] T. Samizadeh Nikoui, A. Masoud Rahmani, and A. Balador, H. H. Seyyed Javadi, *Internet of Things architecture challenges: A systematic review*, International Journal of Communication Systems, 2020, 34.

[2] M. Laroui, B. Nour, H. Moungla, M. Ali Cherif, H. Afifi, et al. *Edge and fog computing for IoT: a survey on current research activities & future directions*. Computer Communications, 2021, 180, pp.210-231. 10.1016/j.comcom.2021.09.003.

[3] L. Tseng, *Recent Results on Fault-Tolerant Consensus in Message-Passing Networks*,

[4] Brewer, E. (2000). *Towards robust distributed systems* (PODC keynote). Proceedings of the Nineteenth Annual ACM SIGACT-SIGOPS Symposium on Principles of Distributed Computing, Portland, Oregon, USA, pp. 1.

[5] Fischer, M. J., Lynch, N. A., & Paterson, M. S. (1985). *Impossibility of distributed consensus with one faulty processor*. Journal of the ACM (JACM), 32(2), pp. 374-382.

[6] K. Dinesh Kumar, N. Duraimutharasan, HJ. Shanthi, G. Vennila, B. Prabu Shankar, P. Senthil, *Comparative Analysis of Transaction Speed and Throughput in Blockchain and Hashgraph: A Performance Study for Distributed Ledger Technologies*, Journal of Machine and Computing 3(4), 2023.

[7] K. Jezek, *Ethereum Data Structures*, University of Sydney, [available online] https://arxiv.org/pdf/2108.05513.pdf , 2021.

[8] B. Confais, B. Parrein, J. Lacan, F. Marques. *Characterization of the IPFS Public Network from DHT Request*s. Transactions on Large-Scale Data and Knowledge-Centered Systems, 2023, Lecture Notes in Computer Science, 14280, pp.87-108. 10.1007/978-3-662-68100-8_4.

[9] S. Alam, S. Bhatia, M. Shuaib, MM. Khubrani, F. Alfayez, AA. Malibari, S. Ahmad, *An Overview of Blockchain and IoT Integration for Secure and Reliable Health Records Monitoring*, Sustainability. 2023; 15(7):5660. https://doi.org/10.3390/su15075660

[10] S. Mathur, A. Kalla, G. Gür, M. Kumar Bohra, M. Liyanage, *A Survey on Role of Blockchain for IoT: Applications and Technical Aspects*, Computer Networks, Vol. 227, 2023.

[11] C.D. Nassar Kyriakidou1, A.M. Papathanasiou, G.C. Polyzos, *Decentralized Identity With Applications to Security and Privacy for the Internet of Things*, Computer Networks and Communications, 2023, vol.1(2), 244-271. DOI 10.37256/cnc.1220233048.

[12] S. Mishra, S. Kumar, *Smart Voltage Monitoring: Centralised and Blockchain-based Decentralised Approach*, 2020 IEEE International Conference on Internet of Things and Intelligence System (IoTaIS), BALI, Indonesia, 2021, pp. 49-55.

[13] RW6, M. Irfan Khalid, I. Ehsan, A. Khallel Al-Ani, J. Iqbal, S. Hussain, S. Sajid Ullah, Nayab, *A Comprehensive Survey on Blockchain-Based Decentralized Storage Networks*, IEEE Access, 11:10995-11015, 2023.

[14] RW4, M. Abbasi, J. Prieto, A. Shahraki, J.M. Corchado, *Industrial data monetization: A*

blockchain-based industrial IoT data trading system, Internet of Things, vol.24, 2023.

[15] RW5, N. Pocher; M. Zichichi, *Towards CBDC-based Machine-to-Machine Payments in Consumer IoT*, Conference Proceedings: The 37th ACM/SIGAPP Symposium on Applied Computing (SAC '22), Brno, 2022.

OPTIMIZING DUTY RATIOS IN A GRID-INTERACTIVE INVERTER: A FIVE-LEVEL, THREE-LEG, THREE-PHASE CASCADED H-BRIDGE APPROACH EMPLOYING MPCC WITH AN EXPLICIT INTEGRATION ALGORITHM

Edmund Kwafo **ADJEI-SAFORO**[1,2], Francis Boafo **EFFAH**[1], Misbawu **ADAM**[2], Ebrahimpanah **SHAHROUZ**[3], Emmanuel Asuming **FRIMPONG**[1]

[1]*Kwame Nkrumah Unversity of Science and Technology,* [2]*Kumasi Technical University,* [3]*Wuhan University of Technology*

ekadjeisaforo@st.knust.edu.gh, kingacid17@gmail.com, adam.misbawu@kstu.edu.gh

Keywords: Total harmonic distortion, three level three-leg, model predictive current control

Abstract*: The model predictive current control stands out as a robust control strategy extensively applied in the enhancement of various industrial applications. Renowned for its capacity to handle multiple inputs and generate multiple outputs (MIMO), it is recognized for its consistently excellent performance and unique stable control techniques. However, the computational intensity required to remedy an optimization task at each time step poses a potential drawback, impacting its suitability for real-time control applications and potentially affecting system performance. This study introduces the concept of duty cycle optimization, leveraging the explicit integration approximation. This involves the application of rectangular voltage for both non-zero as well as zero within one control period to minimize current ripples in the grid-interactive system. Additionally, error minimization is achieved through the selection of the duration for the two-rectangular voltage. Experimental and simulation results validate the substantial reductions in ripple current as well as total harmonic distortion achieved through this approach.*

1. INTRODUCTION

To meet the growing electricity demands of end-users and enhance the current power generation capacity, an increasing amount of renewable energy, notably solar and wind power to a greater extent, is being integrated into the grids [1, 2].

Recently, the integration of renewable energy systems into the grid has been achieved by employing multilevel inverters. This choice is attributed to their benefits, including low electromagnetic compatibility and switching losses, as well as high voltage handling capabilities and waveform quality [3, 4, 24]. Multilevel inverters fall into three main categories: flying capacitor, diode-clamped, and cascaded H-bridge (CHB) [5-7]. Model Predictive Control (MPC) comes in two variations: Finite Control Set and Continuous Control Set. The former, recognized as a modern control technique, stands out for its capability to address variable constraints and nonlinearities within a system. Notably, it demonstrates swift control responses to dynamic systems and predicts the future characteristics of a system by minimizing a cost function [9, 10, 18]. Model Predictive Current Control (MPCC), falling under the umbrella of MPC, holds a distinguished status as one of the leading control methods for power converters [22, 23].

This paper focuses on designing Model Predictive Current Control (MPCC) with duty cycle optimization using the Explicit Integration Algorithm for a five-level three-leg three-phase (FTT) cascaded H-Bridge (CHB) interactive inverter with LCL smoother output. To achieve a rapid dynamic response and enhanced steady-state performance, the utilization of both zero and non-zero rectangular voltages within a single control period is recommended. The duration of the non-zero rectangular voltage is determined based on the reduction of current error at the end of the subsequent control duration [14, 17, 18, 20]. The subsequent chapters of the paper are organized as follows: Chapter 2 delves into the five-level three-leg three-phase cascaded H-Bridge inverter with LCL smoother output. Chapter 3 introduces MPCC with duty cycle optimization based on explicit integration approximation. Simulation and experimental results are presented in Chapters 4 and 5 respectively. Finally, Chapter 6 concludes the paper.

2. FIVE-LEVEL THREE-LEG THREE-PHASE (FTT) CHB INVERTER FEATURING LCL SMOOTHER OUTPUT

Figure 1 illustrates a schematic diagram of a FTTCHB grid-interactive inverter with an LCL smoother output. Within the five-level cascaded inverter, each cell is distinct, having its own dedicated DC source and H-bridge inverter [7]. Each cell contributes $V_{dc}/_2$ to the total input DC voltage, denoted as V_{dc}. Then each full-bridge inverter can switch between $V_{dc}/_2$, 0, $-V_{dc}/_2$.

The formula for voltage levels in relation to the number of output phases is provided as follows:

$$m = (2n + 1) \tag{1}$$

where DC source is characterised by n numbers of secluded DC sources. In a FTTCHB inverter, for one cell, the four switches S_1, S_2, S_1' and S_2' are controlled to generate three discreet outputs V_{out} with levels $V_{dc}/_2$, 0, $-V_{dc}/_2$. When When $S_1$and $\boldsymbol{S_2'}$are on, the output is $V_{dc}/_2$; when S_2 and $\boldsymbol{S_1'}$are on, the output is $-V_{dc}/_2$; when either pair S_1 and S_2 or $\boldsymbol{S_1'}$and $\boldsymbol{S_2'}$ are on, the output is 0 [8]. Therefore for having 2 separated DC sources, five possible voltage levels, V_{dc}, $V_{dc}/_2$, 0, $-V_{dc}/_2$, $-V_{dc}$ are created.

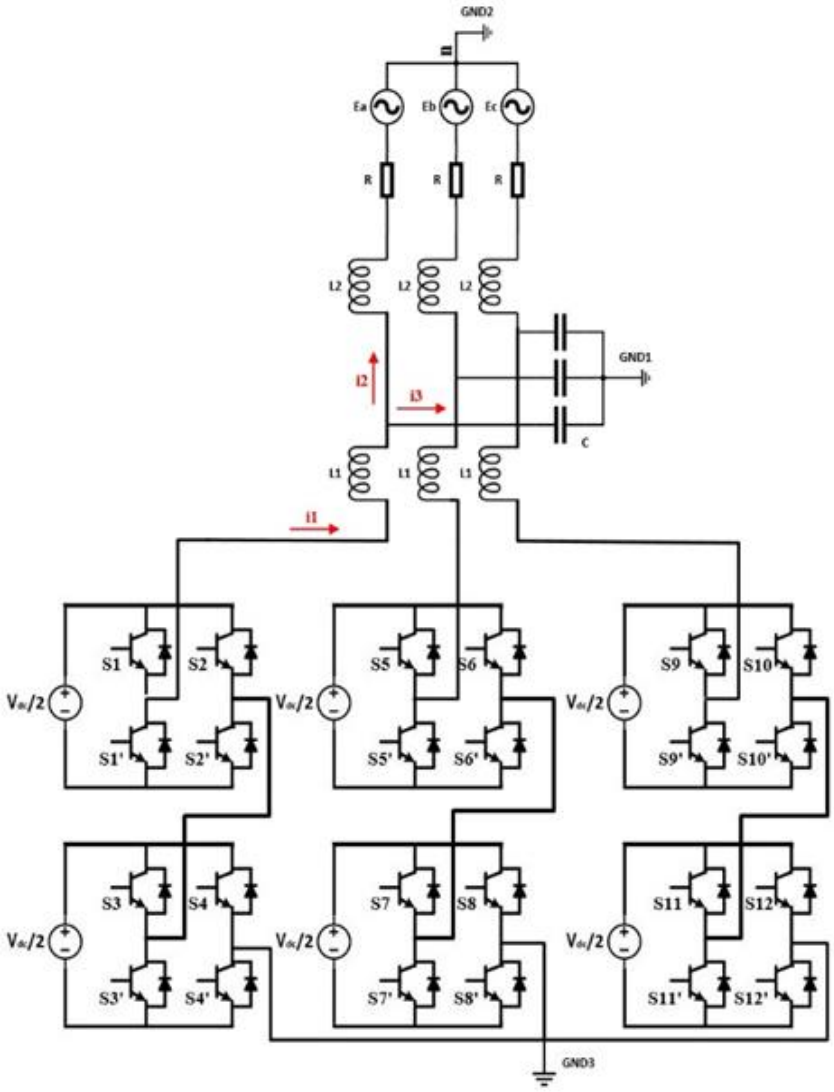

Figure 1. FTT CHB inverter

The output rectangular voltage can be written as:

$$V = \frac{2}{3}(V_{aN} + \alpha V_{bN} + \alpha^2 V_{cN}) \tag{2}$$

where $= e^{j\frac{2\pi}{3}}, \alpha = -\frac{1}{2} + j\frac{\sqrt{3}}{2}$, which represent 120° phase displacement between the phases: V_{aN}, V_{bN} and V_{cN}. The subscripts used denote the phase quantities of the inverter, and the

negative terminal of the DC link is represented by N [9], [24]. By replacing a in equation (2) output voltage vector is calculated as follow:

$$V = \frac{2}{3}V_{aN} - \frac{1}{3}V_{bN} + \mathrm{j}\frac{\sqrt{3}}{3}V_{bN} - \frac{1}{3}V_{cN} - \mathrm{j}\frac{\sqrt{3}}{3}V_{cN} \tag{3}$$

The calculation of the number of voltage level combinations k_m is based on $k_m = 3^m$. Therefore, considering all potential combinations of gating signals for two cells in the three-phase CHB inverter, 125 switching states and corresponding 125 rectangular voltages are obtained (refer to Table 1). However, 64 of these rectangular voltages are redundant, leaving only 61 non-redundant rectangular voltages, as calculated below.

$$k_V = 12C^2 + 6C + 1 \tag{4}$$

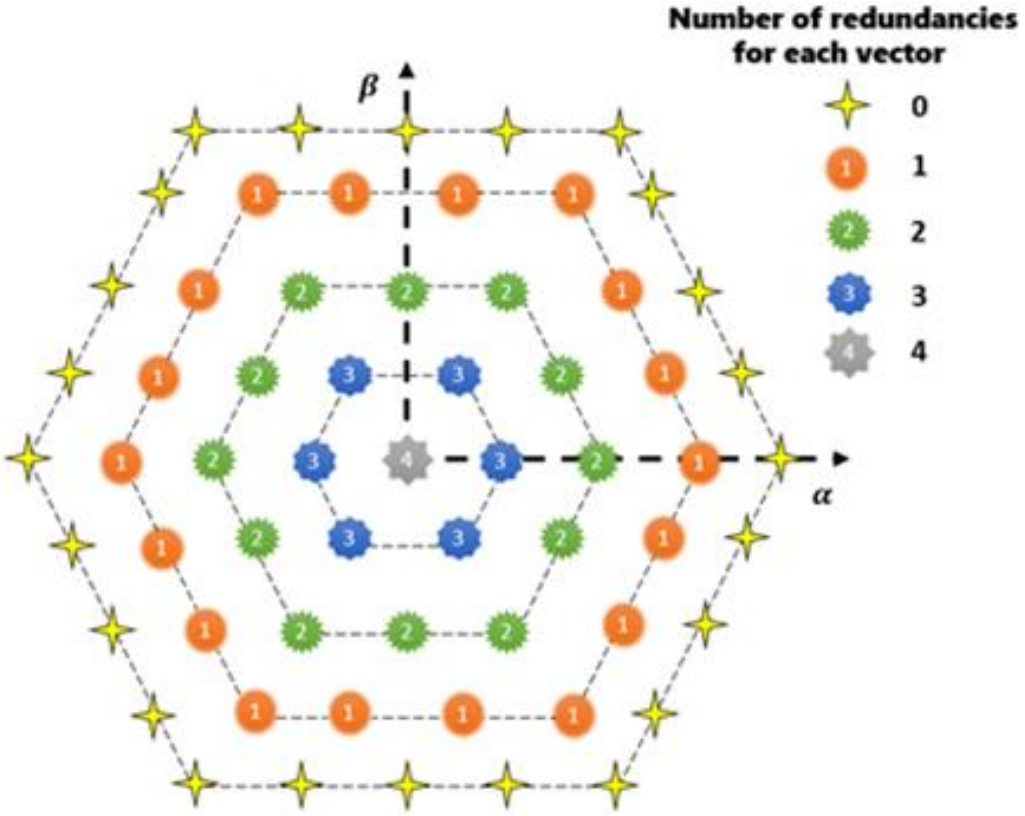

Figure 2. Rectangular voltages for FTT CHB inverter

C represents the number of cells in each leg of the CHB inverter, and k_V denotes the quantity of non-redundant voltage vectors (refer to *figure 2*).

As the impedance of C is considerably larger than the impedance of L_1 and L_2, the current flowing through C can be neglected. Thus, it can be expressed as [11]:

$$i_3 = 0, i_1 = i_2 = i \tag{5}$$

The dynamics of the grid-side current for each phase can be expressed as follows:

$$\begin{cases} V_{an} = L\frac{di_a}{dt} + Ri_a + e_a \\ V_{bn} = L\frac{di_b}{dt} + Ri_b + e_b \\ V_{cn} = L\frac{di_c}{dt} + Ri_c + e_c \end{cases} \quad (6)$$

where R represents the filter resistance and $L = L_1 + L_2$. By substituting (6) into (2), a vector equation expressing the relationship between various parameters for the grid side can be formulated:

$$V = L\frac{d(^2/_3(i_a+ai_b+a^2i_c))}{dt} + R(^2/_3(i_a + ai_b + a^2i_c)) + {}^2/_3(e_a + ae_b + a^2e_c) \quad (7)$$

where: $a = e^{j\frac{2\pi}{3}}$, $a = -\frac{1}{2} + j\frac{\sqrt{3}}{2}$, $i = {}^2/_3(i_a + ai_b + a^2i_c)$ and $e = {}^2/_3(e_a + ae_b + a^2e_c$. Therefore, the system depicted in *figure 1* can be represented by the differential rectangular equation:

$$V = L\frac{di}{dt} + Ri + e \quad (8)$$

In this context, V denotes the rectangular voltage produced by the inverter, i represents rectangular current on the grid-side, and e denotes the rectangular voltage on the grid-side [10].

Table 1. Rectangular voltages and their switching states

V_{aN}	V_{bN}	V_{cN}	Voltage vector	V_{aN}	V_{bN}	V_{cN}	Voltage vector	V_{aN}	V_{bN}	V_{cN}	Voltage vector
0	0	0	0	V_{dc}	$-V_{dc}$	0	$V_{dc} - j\frac{\sqrt{3}}{3}V_{dc}$	$-V_{dc}$	V_{dc}	0	$-V_{dc} + j\frac{\sqrt{3}}{3}V_{dc}$
0	0	V_{dc}	$-\frac{1}{3}V_{dc} - j\frac{\sqrt{3}}{3}V_{dc}$	V_{dc}	$-V_{dc}$	V_{dc}	$\frac{2}{3}V_{dc} - j\frac{2\sqrt{3}}{3}V_{dc}$	$-V_{dc}$	V_{dc}	V_{dc}	$-\frac{4}{3}V_{dc}$
0	0	$\frac{V_{dc}}{2}$	$-\frac{1}{6}V_{dc} - j\frac{\sqrt{3}}{6}V_{dc}$	V_{dc}	$-V_{dc}$	$\frac{V_{dc}}{2}$	$\frac{5}{6}V_{dc} - j\frac{\sqrt{3}}{2}V_{dc}$	$-V_{dc}$	V_{dc}	$\frac{V_{dc}}{2}$	$-\frac{7}{6}V_{dc} + j\frac{\sqrt{3}}{6}V_{dc}$
0	0	$-V_{dc}$	$\frac{1}{3}V_{dc} + j\frac{\sqrt{3}}{3}V_{dc}$	V_{dc}	$-V_{dc}$	$-V_{dc}$	$\frac{4}{3}V_{dc}$	$-V_{dc}$	V_{dc}	$-V_{dc}$	$-\frac{2}{3}V_{dc} + j\frac{2\sqrt{3}}{3}V_{dc}$
0	0	$-\frac{V_{dc}}{2}$	$\frac{1}{6}V_{dc} + j\frac{\sqrt{3}}{6}V_{dc}$	V_{dc}	$-V_{dc}$	$-\frac{V_{dc}}{2}$	$\frac{7}{6}V_{dc} - j\frac{\sqrt{3}}{6}V_{dc}$	$-V_{dc}$	V_{dc}	$-\frac{V_{dc}}{2}$	$-\frac{5}{6}V_{dc} + j\frac{\sqrt{3}}{2}V_{dc}$
0	V_{dc}	0	$-\frac{1}{3}V_{dc} + j\frac{\sqrt{3}}{3}V_{dc}$	V_{dc}	$-\frac{V_{dc}}{2}$	0	$\frac{5}{6}V_{dc} - j\frac{\sqrt{3}}{6}V_{dc}$	$-V_{dc}$	$\frac{V_{dc}}{2}$	0	$-\frac{5}{6}V_{dc} + j\frac{\sqrt{3}}{6}V_{dc}$
0	V_{dc}	V_{dc}	$-\frac{2}{3}V_{dc}$	V_{dc}	$-\frac{V_{dc}}{2}$	V_{dc}	$\frac{1}{2}V_{dc} - j\frac{\sqrt{3}}{2}V_{dc}$	$-V_{dc}$	$\frac{V_{dc}}{2}$	V_{dc}	$-\frac{7}{6}V_{dc} - j\frac{\sqrt{3}}{6}V_{dc}$
0	V_{dc}	$\frac{V_{dc}}{2}$	$-\frac{1}{2}V_{dc} + j\frac{\sqrt{3}}{6}V_{dc}$	V_{dc}	$-\frac{V_{dc}}{2}$	$\frac{V_{dc}}{2}$	$\frac{2}{3}V_{dc} - j\frac{\sqrt{3}}{3}V_{dc}$	$-V_{dc}$	$\frac{V_{dc}}{2}$	$\frac{V_{dc}}{2}$	$-V_{dc}$
0	V_{dc}	$-V_{dc}$	$j\frac{2\sqrt{3}}{3}V_{dc}$	V_{dc}	$-\frac{V_{dc}}{2}$	$-V_{dc}$	$\frac{7}{6}V_{dc} + j\frac{\sqrt{3}}{6}V_{dc}$	$-V_{dc}$	$\frac{V_{dc}}{2}$	$-V_{dc}$	$-\frac{1}{2}V_{dc} + j\frac{\sqrt{3}}{2}V_{dc}$
0	V_{dc}	$-\frac{V_{dc}}{2}$	$-\frac{1}{6}V_{dc} + j\frac{\sqrt{3}}{2}V_{dc}$	V_{dc}	$-\frac{V_{dc}}{2}$	$-\frac{V_{dc}}{2}$	V_{dc}	$-V_{dc}$	$\frac{V_{dc}}{2}$	$-\frac{V_{dc}}{2}$	$-\frac{2}{3}V_{dc} + j\frac{\sqrt{3}}{3}V_{dc}$
0	$\frac{V_{dc}}{2}$	0	$-\frac{1}{6}V_{dc} + j\frac{\sqrt{3}}{6}V_{dc}$	$\frac{V_{dc}}{2}$	0	0	$\frac{1}{3}V_{dc}$	$-V_{dc}$	$-V_{dc}$	0	$-\frac{1}{3}V_{dc} - j\frac{\sqrt{3}}{3}V_{dc}$
0	$\frac{V_{dc}}{2}$	V_{dc}	$-\frac{1}{2}V_{dc} - j\frac{\sqrt{3}}{6}V_{dc}$	$\frac{V_{dc}}{2}$	0	V_{dc}	$-j\frac{\sqrt{3}}{3}V_{dc}$	$-V_{dc}$	$-V_{dc}$	V_{dc}	$-\frac{2}{3}V_{dc} - j\frac{2\sqrt{3}}{3}V_{dc}$
0	$\frac{V_{dc}}{2}$	$\frac{V_{dc}}{2}$	$-\frac{1}{3}V_{dc}$	$\frac{V_{dc}}{2}$	0	$\frac{V_{dc}}{2}$	$\frac{1}{6}V_{dc} - j\frac{\sqrt{3}}{6}V_{dc}$	$-V_{dc}$	$-V_{dc}$	$\frac{V_{dc}}{2}$	$-\frac{1}{2}V_{dc} - j\frac{\sqrt{3}}{2}V_{dc}$

V_{aN}	V_{bN}	V_{cN}	Voltage vector	V_{aN}	V_{bN}	V_{cN}	Voltage vector	V_{aN}	V_{bN}	V_{cN}	Voltage vector
0	$\frac{V_{dc}}{2}$	$-V_{dc}$	$\frac{1}{6}V_{dc}+j\frac{\sqrt{3}}{2}V_{dc}$	$\frac{V_{dc}}{2}$	0	$-V_{dc}$	$\frac{2}{3}V_{dc}+j\frac{\sqrt{3}}{3}V_{dc}$	$-V_{dc}$	$-V_{dc}$	$-V_{dc}$	0
0	$\frac{V_{dc}}{2}$	$-\frac{V_{dc}}{2}$	$j\frac{\sqrt{3}}{3}V_{dc}$	$\frac{V_{dc}}{2}$	0	$-\frac{V_{dc}}{2}$	$\frac{1}{2}V_{dc}+j\frac{\sqrt{3}}{6}V_{dc}$	$-V_{dc}$	$-V_{dc}$	$-\frac{V_{dc}}{2}$	$-\frac{1}{6}V_{dc}-j\frac{\sqrt{3}}{6}V_{dc}$
0	$-V_{dc}$	0	$\frac{1}{3}V_{dc}-j\frac{\sqrt{3}}{3}V_{dc}$	$\frac{V_{dc}}{2}$	V_{dc}	0	$j\frac{\sqrt{3}}{3}V_{dc}$	$-V_{dc}$	$-\frac{V_{dc}}{2}$	0	$-\frac{1}{2}V_{dc}-j\frac{\sqrt{3}}{6}V_{dc}$
0	$-V_{dc}$	V_{dc}	$-j\frac{2\sqrt{3}}{3}V_{dc}$	$\frac{V_{dc}}{2}$	V_{dc}	V_{dc}	$-\frac{1}{3}V_{dc}$	$-V_{dc}$	$-\frac{V_{dc}}{2}$	V_{dc}	$-\frac{5}{6}V_{dc}-j\frac{\sqrt{3}}{2}V_{dc}$
0	$-V_{dc}$	$\frac{V_{dc}}{2}$	$\frac{1}{6}V_{dc}-j\frac{\sqrt{3}}{2}V_{dc}$	$\frac{V_{dc}}{2}$	V_{dc}	$\frac{V_{dc}}{2}$	$-\frac{1}{6}V_{dc}+j\frac{\sqrt{3}}{6}V_{dc}$	$-V_{dc}$	$-\frac{V_{dc}}{2}$	$\frac{V_{dc}}{2}$	$-\frac{2}{3}V_{dc}-j\frac{\sqrt{3}}{3}V_{dc}$
0	$-V_{dc}$	$-V_{dc}$	$\frac{2}{3}V_{dc}$	$\frac{V_{dc}}{2}$	V_{dc}	$-V_{dc}$	$\frac{1}{3}V_{dc}+j\frac{2\sqrt{3}}{3}V_{dc}$	$-V_{dc}$	$-\frac{V_{dc}}{2}$	$-V_{dc}$	$-\frac{1}{6}V_{dc}+j\frac{\sqrt{3}}{6}V_{dc}$
0	$-V_{dc}$	$-\frac{V_{dc}}{2}$	$\frac{1}{2}V_{dc}-j\frac{\sqrt{3}}{6}V_{dc}$	$\frac{V_{dc}}{2}$	V_{dc}	$-\frac{V_{dc}}{2}$	$\frac{1}{6}V_{dc}+j\frac{\sqrt{3}}{2}V_{dc}$	$-V_{dc}$	$-\frac{V_{dc}}{2}$	$-\frac{V_{dc}}{2}$	$-\frac{1}{3}V_{dc}$
0	$-\frac{V_{dc}}{2}$	0	$\frac{1}{6}V_{dc}-j\frac{\sqrt{3}}{6}V_{dc}$	$\frac{V_{dc}}{2}$	$\frac{V_{dc}}{2}$	0	$\frac{1}{6}V_{dc}+j\frac{\sqrt{3}}{6}V_{dc}$	$-\frac{V_{dc}}{2}$	0	0	$-\frac{1}{3}V_{dc}$
0	$-\frac{V_{dc}}{2}$	V_{dc}	$-\frac{1}{6}V_{dc}-j\frac{\sqrt{3}}{2}V_{dc}$	$\frac{V_{dc}}{2}$	$\frac{V_{dc}}{2}$	V_{dc}	$-\frac{1}{6}V_{dc}-j\frac{\sqrt{3}}{6}V_{dc}$	$-\frac{V_{dc}}{2}$	0	V_{dc}	$-\frac{2}{3}V_{dc}-j\frac{\sqrt{3}}{3}V_{dc}$
0	$-\frac{V_{dc}}{2}$	$\frac{V_{dc}}{2}$	$-j\frac{\sqrt{3}}{3}V_{dc}$	$\frac{V_{dc}}{2}$	$\frac{V_{dc}}{2}$	$\frac{V_{dc}}{2}$	0	$-\frac{V_{dc}}{2}$	0	$\frac{V_{dc}}{2}$	$-\frac{1}{2}V_{dc}-j\frac{\sqrt{3}}{6}V_{dc}$
0	$-\frac{V_{dc}}{2}$	$-V_{dc}$	$\frac{1}{2}V_{dc}+j\frac{\sqrt{3}}{6}V_{dc}$	$\frac{V_{dc}}{2}$	$\frac{V_{dc}}{2}$	$-V_{dc}$	$\frac{1}{2}V_{dc}+j\frac{\sqrt{3}}{2}V_{dc}$	$-\frac{V_{dc}}{2}$	0	$-V_{dc}$	$j\frac{\sqrt{3}}{3}V_{dc}$
0	$-\frac{V_{dc}}{2}$	$-\frac{V_{dc}}{2}$	$\frac{1}{3}V_{dc}$	$\frac{V_{dc}}{2}$	$\frac{V_{dc}}{2}$	$-\frac{V_{dc}}{2}$	$\frac{1}{3}V_{dc}+j\frac{\sqrt{3}}{3}V_{dc}$	$-\frac{V_{dc}}{2}$	0	$-\frac{V_{dc}}{2}$	$-\frac{1}{6}V_{dc}+j\frac{\sqrt{3}}{6}V_{dc}$
V_{dc}	0	0	$\frac{2}{3}V_{dc}$	$\frac{V_{dc}}{2}$	$-V_{dc}$	0	$\frac{2}{3}V_{dc}-j\frac{\sqrt{3}}{3}V_{dc}$	$-\frac{V_{dc}}{2}$	V_{dc}	0	$-\frac{2}{3}V_{dc}+j\frac{\sqrt{3}}{3}V_{dc}$
V_{dc}	0	V_{dc}	$\frac{1}{3}V_{dc}-j\frac{\sqrt{3}}{3}V_{dc}$	$\frac{V_{dc}}{2}$	$-V_{dc}$	V_{dc}	$\frac{1}{3}V_{dc}-j\frac{2\sqrt{3}}{3}V_{dc}$	$-\frac{V_{dc}}{2}$	V_{dc}	V_{dc}	$-V_{dc}$
V_{dc}	0	$\frac{V_{dc}}{2}$	$\frac{1}{2}V_{dc}-j\frac{\sqrt{3}}{6}V_{dc}$	$\frac{V_{dc}}{2}$	$-V_{dc}$	$\frac{V_{dc}}{2}$	$\frac{1}{2}V_{dc}-j\frac{\sqrt{3}}{2}V_{dc}$	$-\frac{V_{dc}}{2}$	V_{dc}	$\frac{V_{dc}}{2}$	$-\frac{5}{6}V_{dc}+j\frac{\sqrt{3}}{6}V_{dc}$
V_{dc}	0	$-V_{dc}$	$V_{dc}+j\frac{\sqrt{3}}{3}V_{dc}$	$\frac{V_{dc}}{2}$	$-V_{dc}$	$-V_{dc}$	V_{dc}	$-\frac{V_{dc}}{2}$	V_{dc}	$-V_{dc}$	$-\frac{1}{3}V_{dc}+j\frac{2\sqrt{3}}{3}V_{dc}$
V_{dc}	0	$-\frac{V_{dc}}{2}$	$\frac{5}{6}V_{dc}+j\frac{\sqrt{3}}{6}V_{dc}$	$\frac{V_{dc}}{2}$	$-V_{dc}$	$-\frac{V_{dc}}{2}$	$\frac{5}{6}V_{dc}-j\frac{\sqrt{3}}{6}V_{dc}$	$-\frac{V_{dc}}{2}$	V_{dc}	$-\frac{V_{dc}}{2}$	$-\frac{1}{2}V_{dc}+j\frac{\sqrt{3}}{2}V_{dc}$
V_{dc}	V_{dc}	0	$\frac{1}{3}V_{dc}+j\frac{\sqrt{3}}{3}V_{dc}$	$\frac{V_{dc}}{2}$	$-\frac{V_{dc}}{2}$	0	$\frac{1}{2}V_{dc}-j\frac{\sqrt{3}}{6}V_{dc}$	$-\frac{V_{dc}}{2}$	$\frac{V_{dc}}{2}$	0	$-\frac{1}{2}V_{dc}+j\frac{\sqrt{3}}{6}V_{dc}$
V_{dc}	V_{dc}	V_{dc}	0	$\frac{V_{dc}}{2}$	$-\frac{V_{dc}}{2}$	V_{dc}	$\frac{1}{6}V_{dc}-j\frac{\sqrt{3}}{2}V_{dc}$	$-\frac{V_{dc}}{2}$	$\frac{V_{dc}}{2}$	V_{dc}	$-\frac{5}{6}V_{dc}-j\frac{\sqrt{3}}{6}V_{dc}$
V_{dc}	V_{dc}	$\frac{V_{dc}}{2}$	$\frac{1}{6}V_{dc}+j\frac{\sqrt{3}}{6}V_{dc}$	$\frac{V_{dc}}{2}$	$-\frac{V_{dc}}{2}$	$\frac{V_{dc}}{2}$	$\frac{1}{3}V_{dc}-j\frac{\sqrt{3}}{3}V_{dc}$	$-\frac{V_{dc}}{2}$	$\frac{V_{dc}}{2}$	$\frac{V_{dc}}{2}$	$-\frac{2}{3}V_{dc}$
V_{dc}	V_{dc}	$-V_{dc}$	$\frac{2}{3}V_{dc}+j\frac{2\sqrt{3}}{3}V_{dc}$	$\frac{V_{dc}}{2}$	$-\frac{V_{dc}}{2}$	$-V_{dc}$	$\frac{5}{6}V_{dc}+j\frac{\sqrt{3}}{6}V_{dc}$	$-\frac{V_{dc}}{2}$	$\frac{V_{dc}}{2}$	$-V_{dc}$	$-\frac{1}{6}V_{dc}+j\frac{\sqrt{3}}{2}V_{dc}$
V_{dc}	V_{dc}	$-\frac{V_{dc}}{2}$	$\frac{1}{2}V_{dc}+j\frac{\sqrt{3}}{2}V_{dc}$	$\frac{V_{dc}}{2}$	$-\frac{V_{dc}}{2}$	$-\frac{V_{dc}}{2}$	$\frac{2}{3}V_{dc}$	$-\frac{V_{dc}}{2}$	$\frac{V_{dc}}{2}$	$-\frac{V_{dc}}{2}$	$-\frac{1}{3}V_{dc}+j\frac{\sqrt{3}}{3}V_{dc}$
V_{dc}	$\frac{V_{dc}}{2}$	0	$\frac{1}{2}V_{dc}+j\frac{\sqrt{3}}{6}V_{dc}$	$-V_{dc}$	0	0	$-\frac{2}{3}V_{dc}$	$-\frac{V_{dc}}{2}$	$-V_{dc}$	0	$-j\frac{\sqrt{3}}{3}V_{dc}$
V_{dc}	$\frac{V_{dc}}{2}$	V_{dc}	$\frac{1}{6}V_{dc}-j\frac{\sqrt{3}}{6}V_{dc}$	$-V_{dc}$	0	V_{dc}	$-V_{dc}-j\frac{\sqrt{3}}{3}V_{dc}$	$-\frac{V_{dc}}{2}$	$-V_{dc}$	V_{dc}	$-\frac{1}{3}V_{dc}-j\frac{2\sqrt{3}}{3}V_{dc}$
V_{dc}	$\frac{V_{dc}}{2}$	$\frac{V_{dc}}{2}$	$\frac{1}{3}V_{dc}$	$-V_{dc}$	0	$\frac{V_{dc}}{2}$	$-\frac{5}{6}V_{dc}-j\frac{\sqrt{3}}{6}V_{dc}$	$-\frac{V_{dc}}{2}$	$-V_{dc}$	$\frac{V_{dc}}{2}$	$-\frac{1}{6}V_{dc}-j\frac{\sqrt{3}}{2}V_{dc}$
V_{dc}	$\frac{V_{dc}}{2}$	$-V_{dc}$	$\frac{5}{6}V_{dc}+j\frac{\sqrt{3}}{2}V_{dc}$	$-V_{dc}$	0	$-V_{dc}$	$-\frac{1}{3}V_{dc}+j\frac{\sqrt{3}}{3}V_{dc}$	$-\frac{V_{dc}}{2}$	$-V_{dc}$	$-V_{dc}$	$\frac{1}{3}V_{dc}$
V_{dc}	$\frac{V_{dc}}{2}$	$-\frac{V_{dc}}{2}$	$\frac{2}{3}V_{dc}+j\frac{\sqrt{3}}{3}V_{dc}$	$-V_{dc}$	0	$-\frac{V_{dc}}{2}$	$-\frac{1}{2}V_{dc}+j\frac{\sqrt{3}}{6}V_{dc}$	$-\frac{V_{dc}}{2}$	$-V_{dc}$	$-\frac{V_{dc}}{2}$	$\frac{1}{6}V_{dc}-j\frac{\sqrt{3}}{6}V_{dc}$
$-\frac{V_{dc}}{2}$	$-\frac{V_{dc}}{2}$	0	$-\frac{1}{6}V_{dc}-j\frac{\sqrt{3}}{6}V_{dc}$	$-\frac{V_{dc}}{2}$	$-\frac{V_{dc}}{2}$	$\frac{V_{dc}}{2}$	$-\frac{1}{3}V_{dc}-j\frac{\sqrt{3}}{3}V_{dc}$	$-\frac{V_{dc}}{2}$	$-\frac{V_{dc}}{2}$	$-\frac{V_{dc}}{2}$	0
$-\frac{V_{dc}}{2}$	$-\frac{V_{dc}}{2}$	V_{dc}	$\frac{1}{6}V_{dc}+j\frac{\sqrt{3}}{6}V_{dc}$	$-\frac{V_{dc}}{2}$	$-\frac{V_{dc}}{2}$	$-V_{dc}$	$-\frac{1}{2}V_{dc}-j\frac{\sqrt{3}}{2}V_{dc}$				

3. OPTIMIZING DUTY RATIO FOR MPCC USING EXPLICIT INTEGRATION APPROXIMATIONS

In a conceptual sense, Model Predictive Current Control represents a novel approach to nonlinear current control in three-phase inverters. This predictive control method effectively manages the output current and voltage of the inverter with high dynamics, circumventing the challenges associated with the nonlinear nature of semiconductor power

converters. The underlying principle of this technique lies in generating a limited number of voltage levels at the output of the cascaded H-bridge inverter [12].

By employing an explicit integration approximation, the forthcoming of the load current prediction is represented in terms of the discrete-time equation, offering a simplified derivative approximation to establish the discrete-time model. The derived approximation is expressed as follows [14]:

$$\dot{x} = \frac{x(k+1)-x(k)}{T_{sp}} \tag{9}$$

Here, T_{sp} denotes the sampling time, k represents the sampling of the present time, and the state variable is x. By substituting current derivative on the grid-side $^{di}/_{dt}$ with explicit integration approximation, the derivative can be approximated as follows:

$$\frac{di}{dt} \approx \frac{i(k+1)-i(k)}{T_{sp}} \tag{10}$$

Now, by substituting (10) into (8), the discrete model of the system is derived as follows:

$$V(k) = L\frac{i(k+1)-i(k)}{T_s} + Ri(k) + e(k) \tag{11}$$

Furthermore, based on (11), the future value of the output current can be obtained by:

$$i(k+1) = \frac{T_s}{L}\big(v(k) - e(k)\big) + i(k)(1 - \frac{RT_s}{L}) \tag{12}$$

3.1. Cost Function

As depicted in *figure 3* and *figure 4*, the controller relies on the cost function requiring predicted output currents $i(k+1)$. This function utilizes any permissible output to bring the controlled currents into closer alignment with their reference values. The future value of the grid side current, $i(k+1)$, is forecasted for all 61 potential switching states generated by the inverter. To achieve this, the prevailing grid side current must be measured. After acquiring the predictions, a cost function (g), as expressed in Equation (13), is evaluated for each switching state. The primary objective of the current control scheme is to minimize the discrepancies between the reference currents and the measured values. This necessity is formulated in the shape of a cost function. Consequently, in the subsequent sampling period, the switching state (and thus the rectangular voltage generated by the FTTCHB inverter) that

minimizes g is chosen and applied. If $g = 0$, the reference current equals its output current. Therefore, the Optimization Cost Function aims to attain a g value as close as possible to zero. Subsequently, the rectangular voltage minimizing the cost function is selected and implemented in the next sampling instance [13], [15].

$$g = f(i_{ref}(k+1), i(k+1)) \tag{13}$$

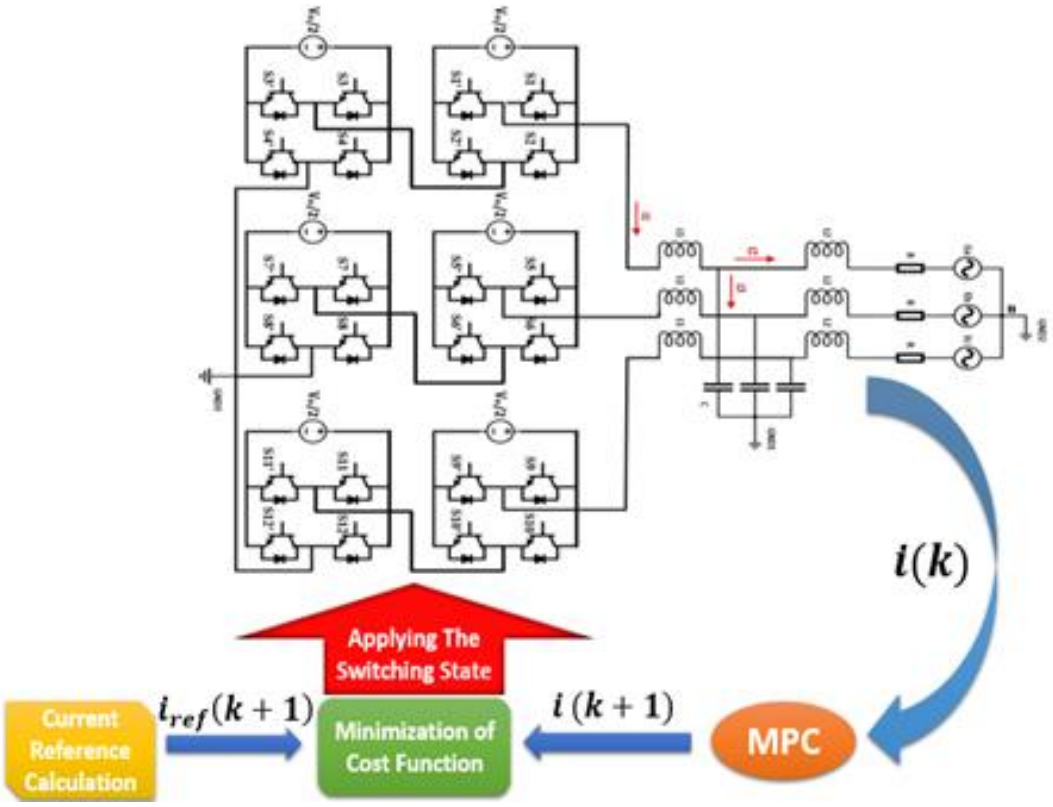

Figure 3. Control strategy of FTT CHB inverter interfaced with an LCL filter and connected to the grid

In the depicted controller shown in *figures 3 and 4*, the cost function (g) necessitates minimizing the predicted currents $i(k+1)$ of the output to minimize errors between measured values and reference currents. The objective of optimizing this cost function is to bring the value of g as close to zero as possible. Consequently, the rectangular voltage is selected and substituted at the instant of the next sampling to reduce the cost function [11], [13]. The subsequent current value is determined by employing Lagrange quadratic extrapolation [16].

$$i_{ref}(k+1) = \Sigma_{l=0}^{n}(-1)^{n-1}\binom{n+1}{l} i_{ref}(k+1-n) \tag{14}$$

For $n \geq 2$ is recommended as sinusoidal reference [10]. Hence, the prediction value with $n = 2$ can be obtained from:

$$i_{ref}(k+1) = 3i_{ref}(k) - 3i_{ref}(k-1) + i_{ref}(k-2) \tag{15}$$

The cost function can be formulated in absolute terms by assessing the error between the reference currents and the predicted currents:

$$g = \left|Re[i_{ref}(k+1) - i(k+1)]\right| + \left|Im[i_{ref}(k+1) - i(k+1)]\right| \tag{16}$$

The cost function, given by equation (16), aims to minimize the error in the output current by utilizing the predicted value $i(k+1)$ from equation (12) and the reference current Iref derived from (15). Consequently, the optimal rectangular voltage can be identified through this process:

$$V_{opt} = V(\min\{g_n\})(n = 0,1,2,\dots,124) \tag{17}$$

where g_n is varietal switching states for the cost function and $V(\min\{g_n\})$ is the optimal cost function of rectangular voltage.

3.2. Optimal Duty Cycle

Within the framework of MPCC, out of 125 rectangular voltages, only 120 non-zero rectangular voltages are required for analysis in equation (16). This is because zero and non-zero rectangular voltages are simultaneously chosen during a single time period. Therefore, accurately calculating the duration of the non-zero rectangular voltage is crucial for system control. The gradients of the grid-side current corresponding to the non-zero voltage vector S_1 and the zero voltage vector S_1 can be readily computed using equation (17) [17], [18].

$$s_1 = \frac{V_{n-z} - e - Ri}{L} \tag{18}$$

$$s_0 = \frac{-e - Ri}{L} \tag{19}$$

The optimal voltage vector, denoted as V_{n-z}, minimizing the cost function, is utilized in the calculation of the output current at the end of the subsequent control cycle.

$$i_{ref}(k+1) = i(k) + \frac{T_{opt}[V_{n-z} - e(k) - Ri(k)] + T_z[V_z - e(k) - Ri(k)]}{L} \tag{20}$$

$$T_{opt} + T_z = T_{sp} \tag{21}$$

$$V_{n-z} + V_z = V(k) \tag{22}$$

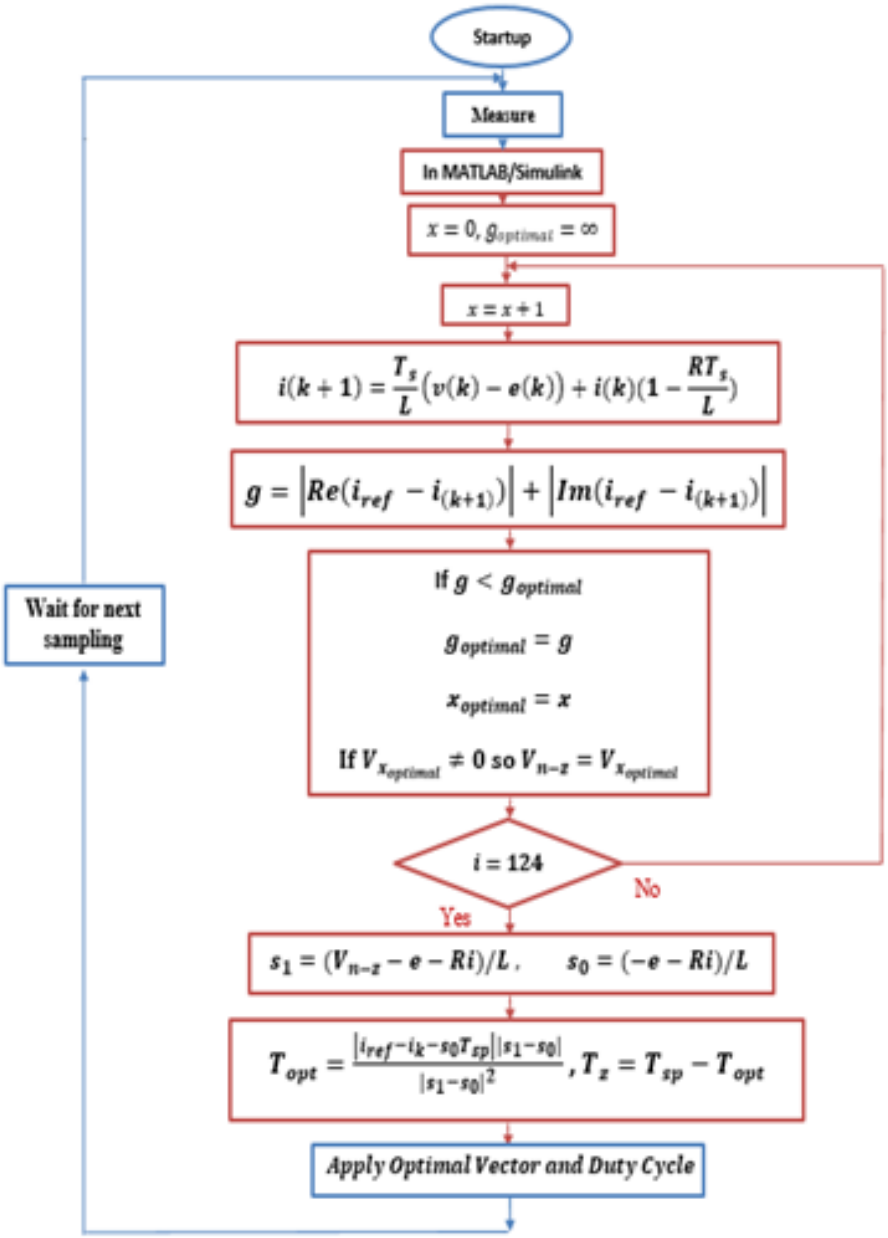

Figure 4. A flow chart illustrating the proposed optimal duty cycle of MPCC

By substituting equations (18) and (19) into equation (20), the output current at the conclusion of the subsequent control cycle can be obtained.

$$(k+1) = i(k) + s_1 \times T_{opt} + s_0 \times (T_{sp} - T_{opt}) \tag{23}$$

The optimal duration, T_{opt}, which minimizes the cost function over a control period, adheres to the following condition.

$$\frac{\partial g}{\partial T_{opt}} = 0 \tag{24}$$

By substituting (23) into (16) and resolving (24), the length of the non-zero rectangular duration can be expressed [19].

$$T_{opt} = \frac{|i_{ref} - i(k) - s_0 \times T_{sp}|}{|s_1 - s_0|} \tag{25}$$

$T_{opt} = 0$, only if $T_{opt} < 0$, and $T_{opt} > T_{sp}$; then, it will be equaled to T_{sp} [20] [21].

3.2. LCL Resonance Damping

The primary circuit of a phase LCL output filter for an inverter is illustrated in *figure 5 (a)*, and its simplified version is presented in *figure 5(b)*, featuring the inductor L_1 on the inverter side, the smoothing capacitor C, and the inductor L_2 on the grid side. In *figure 6 (a)*, a Bode diagram (BD) of the LCL filter without damping is displayed.

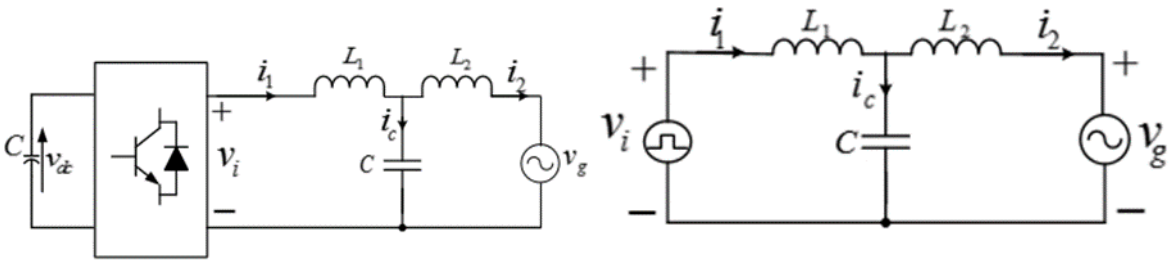

(a) Main circuit *(b) Generic circuit*

Figure 5. A grid-connected system featuring a phase LCL smoother

Considering the transfer function denoted as $H_S = i_2/v_i$, assuming the voltage across the grid system at the point of common coupling (PCC) is an ideal source voltage capable of attenuating all integral multiples of frequencies. When focusing on the inverter-controlled current and assuming V_g is zero, the transfer function can be expressed as follows:

$$i_2 = i_1(s^2 L_2 C + 1)^{-1} \tag{26}$$

$$i_1 = i_2(s^2 L_2 C + 1) \tag{27}$$

$$v_i = i_1\left(sL_1 + \frac{sL_2}{s^2L_2C+1}\right) \tag{28}$$

Substituting equation (2) into (3), we have;

$$0 = {}^{i_2}/_{v_i}\left[(s^2L_2C + 1)\left(sL_1 + \frac{sL_2}{s^2L_2C+1}\right)\right] \tag{29}$$

Therefore, the transfer function

$$H_{(s)} = i(s)v(s)^{-1} = [s^3L_1L_2C + s(L_1{+}L_2)]^{-1} \tag{30}$$

is obtained from equation (4), otherwise;

$$H_{(s)} = [sL_1L_2C(s^2 + \omega_r^2)]^{-1} \tag{31}$$

where $\omega_r = \left(\sqrt{L_1L_2C}\right)^{-1} \cdot \sqrt{L_1{+}L_2}$ and $f_r = {}^{1}/_{2\pi}\,\omega_r$.

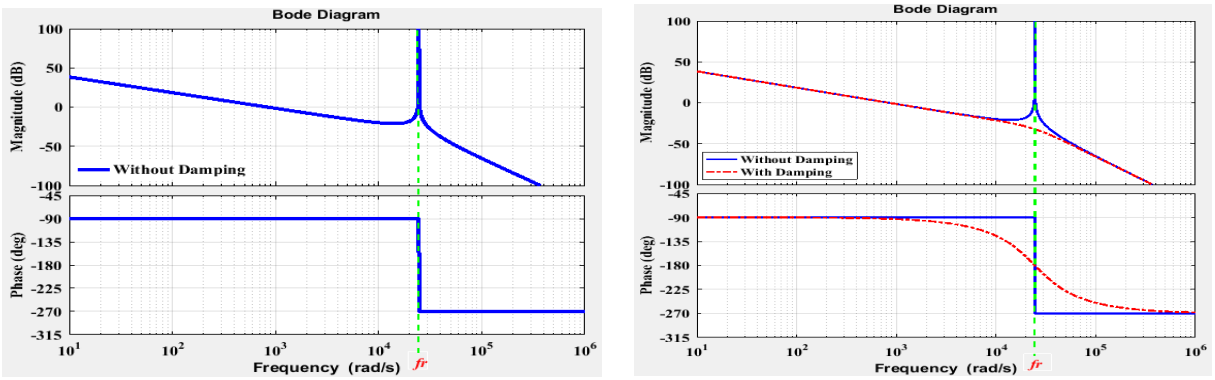

(a) *LCL smoother without damping term* *(b) LCL smoother with damping term*

Figure 6. Bode characteristic representation of LCL smoother

The rapid decrease of -180 at the oscillatory frequency is a result of the LCL smoother oscillation, accompanied by a significant peak magnitude in resonance. This situation poses a potential risk of system instability from a control standpoint [25]. Given that -180 represents a negative crossing, it leads to the formation of complex poles with a pair of closed-loop right-half poles. Introducing damping to subdue the resonance below the $0\,dB$ negative crossing helps avoid these issues. The damping ratio ζ, a first-order term associated with s, is incorporated into the oscillatory term $s^2 + \omega_r^2$ of equation (30) to achieve this.

The dashed lines depicted in *figure 6 (b)* represent the $H_{damp(s)}$ plot. The inclusion of the damping term in the plot demonstrates that while the magnitude and frequency characteristics of the resonance remain unaltered, the oscillatory peak of the smoother is

notably diminished.

3.2.1. LCL Resonance damping: Resistor connected in series with the capacitor

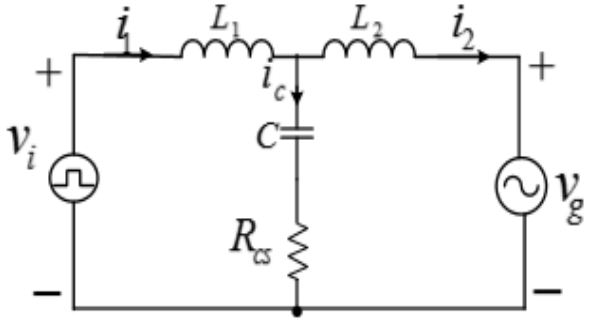

Figure 7. LCL damping technique employing series resistor (R_{cs}) – capacitor (C) connection

The difficulties in controlling the output LCL filter of the Active Power Filter (APF) connected inverter stem from resonance issues. This leads to a sudden -180-degree phase shift with a pronounced resonance peak at the resonance frequency. In [26][27], the paper conduct a thorough examination of various LCL resonance damping methods. Six distinct passive damping strtegies, along with their transfer functions and corresponding Bode diagrams, are scrutinized and contrasted for analysis. The resistor placed in series with capacitor as shown in the figure below is recommended in practice and its corresponding transfer function is given as:

$$H_{R_{cs}(s)} = i(s)v(s)^{-1} = (sR_{cs}C + 1)[s^3(L_1L_2C + s^2R_{cs}(L_1{+}L_2) + s(L_1{+}L_2)^{-1}] \quad (32)$$

4. SIMULATION RESULTS

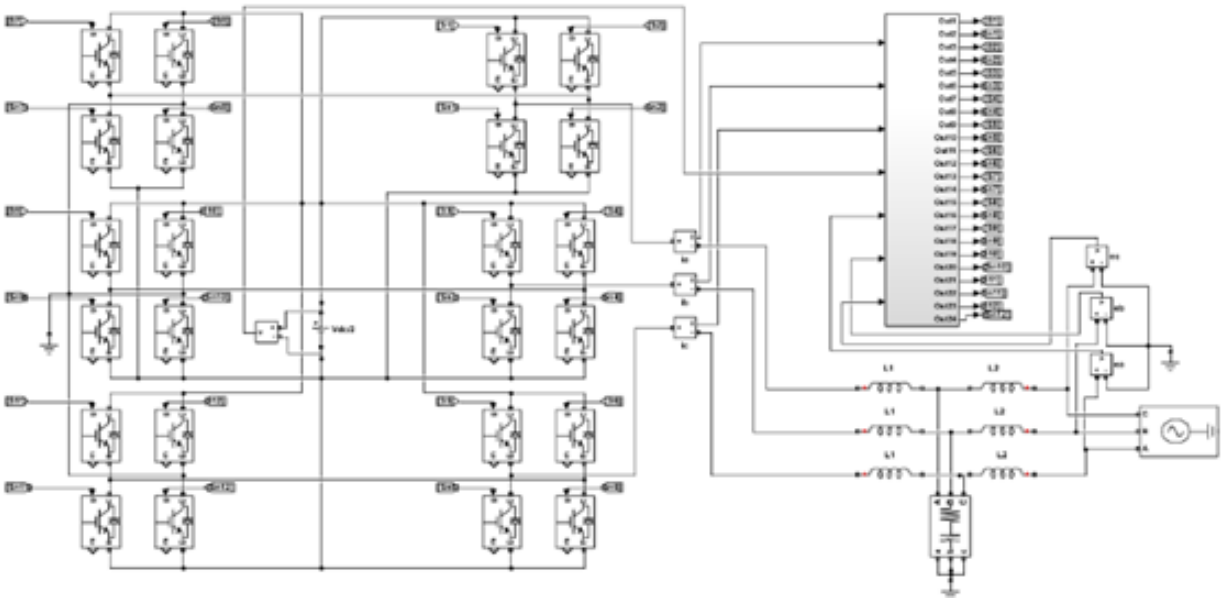

Figure 8. MPCC control strategy for FTT CBH gird-interactive inverter with LCL smoother output

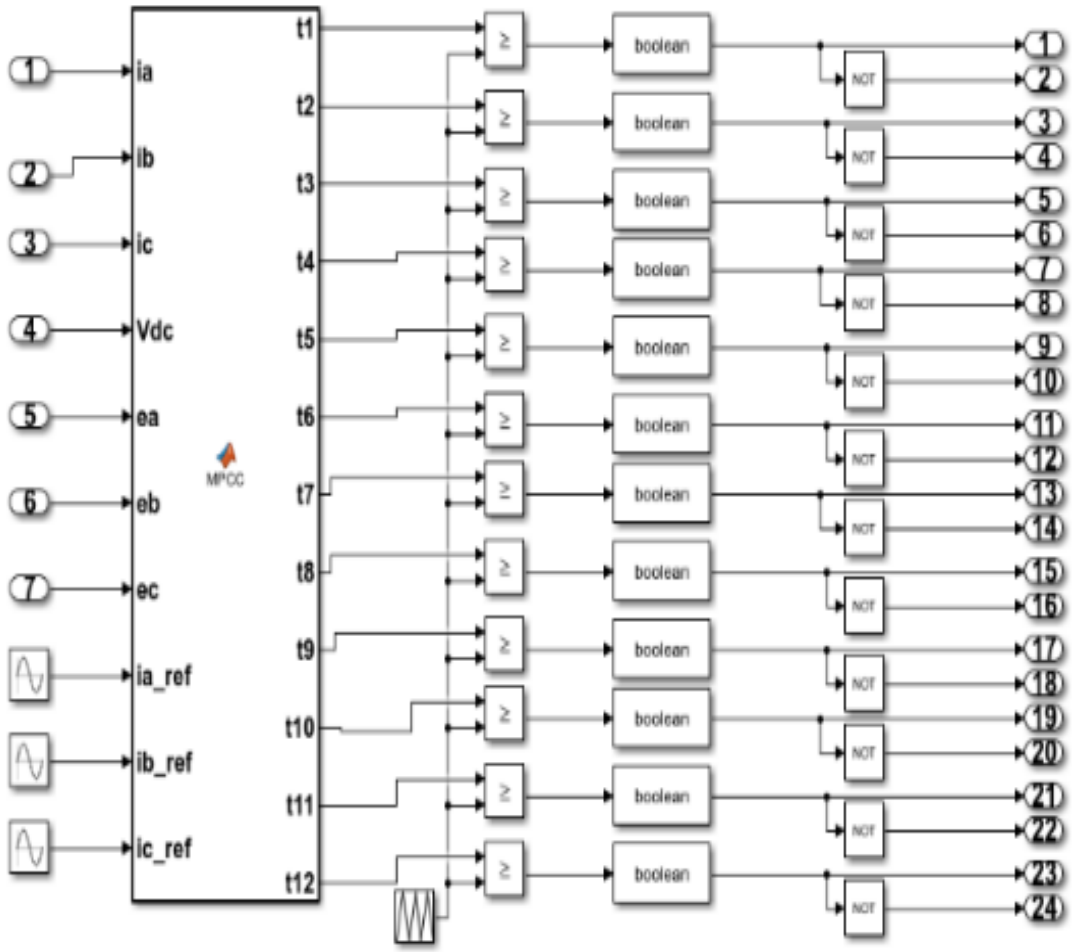

Figure 9. MPCC subsystem with modification

Table 2. Parameters employed for both the simulation and laboratory set-up [21]

Specification for MATLAB Simulation and Laboratory Setup				
Parameters used for the simulation			***Material/specifications for laboratory setup***	
Variable	***Parameters of the system***	***Value***	***Materials***	***Description/Specifications***
V_{dc}	DC-Link voltage	700V	DC Source	Variable 1000 V DC
e	Grid Voltage (RMS)	220V	Gate Drivers	IGBT GD C044BG400 series
f	Line voltage frequency	50Hz	DSP & GUI	32-bit TMS320F28335, 20 kHz
i_{ref}	Reference current peak amplitude	20A	GRID	Variable 700 V AC
L_2	Filter inductance	1mH	LCL filter	400 V AC, 2.5 kHz SF
L_1	Filter Inductance	3mH	Five level three-phase cascaded full bridge inverter	Laboratory built
C_f	Filter Capacitance	15μF	Oscilloscope	Tektonix Mixed Domain
R_f	Filter Resistance	10Ω	Materials	Description/Specifications
T_{sp}	Sampling time	25 to 100 μs		

Simulation models and diverse experiments are employed to validate the performance attributes of the suggested duty ratio optimization for MPCC control techniques applicable to

a five-level three-leg three three-phase (FTT) CHB grid-interactive inverter with LCL smother output, as outlined in Table 2. To facilitate comparison, the outcomes of the conventional MPCC will also be utilized. *Figure 10* illustrates the proposed MPCC with duty cycle optimization.

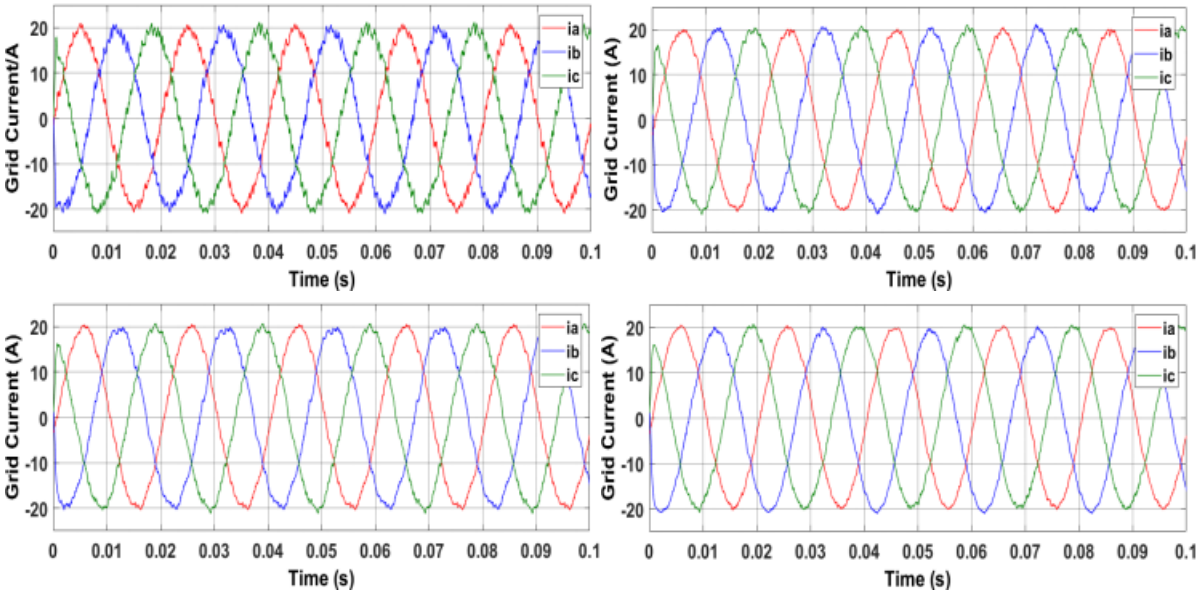

(a) *(b)*

Figure 10. Waveforms from simulation of FTT CHB using explicit integration approximation. (a) The conventional MPCC at the sampling time of 50μs and 25μs, (b) The proposed MPCC with optimal duty cycle at the sampling time of 50μs and 25μs.

Upon comparing the conventional and proposed approaches, as depicted in *figure 10* with regards to grid current waveforms, it is evident that the conventional method exhibits more pronounced distortion in the output current compared to the proposed method. Consequently, the novel method demonstrates reduced current harmonics and lower current ripple.

Another noteworthy observation is apparent in *figure 11*. The Total Harmonic Distortion (THD) for the proposed MPCC is 1.65% and 1.1%, representing a substantial improvement over the 3.11% and 1.42% recorded for conventional MPCC at sampling times of $T_{sp} = 50\mu s$ and $T_{sp} = 25\mu s$, respectively. Once again, the proposed method proves to be effective and efficient, producing output waveforms that closely resemble sinewaves.

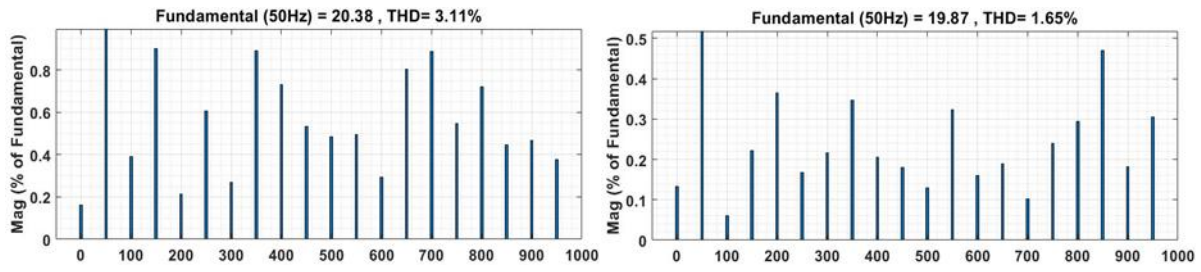

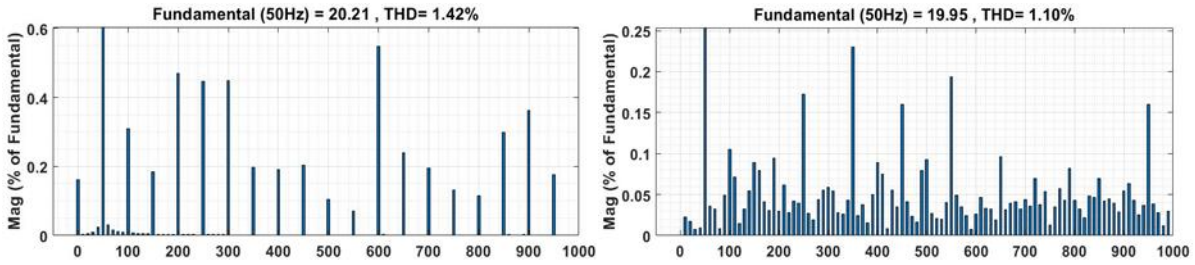

(a) *(b)*

Figure 11. Harmonic spectrum examination of a FTT CHB utilizing explicit integration approximation. (a) MPCC of traditional characteristics at the sampling time of 50µs and 25µs, (b) MPCC with enhanced duty cycle at the sampling time of 50µs and 25µs

Figure 12 illustrates the stability of the proposed method, showcasing a more precise tailing of the output current to its reference. Even in the face of altering the output current, the proposed method exhibits superior accuracy and fewer ripples compared to the traditional method.

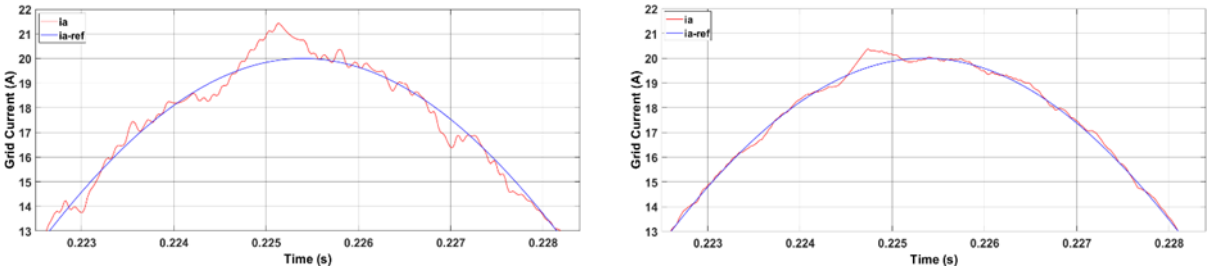

Figure 12. Grid current representation at the 50µs sampling time employing an explicit integration algorithm. (a) The traditional MPCC, (b) Duty cycle control of the modified MPCC

A bar graph depicting the grid current total harmonic distortion (THD) with varying sampling times for both conventional and proposed methods is presented in *figure 13*. It is evident that the proposed method exhibits considerably lower THD values compared to the conventional method, attributed to the duty cycle optimization employed in the proposed Model Predictive Current Control (MPCC). Consequently, the proposed MPCC demonstrates substantial advantages, particularly in applications with increased sampling time.

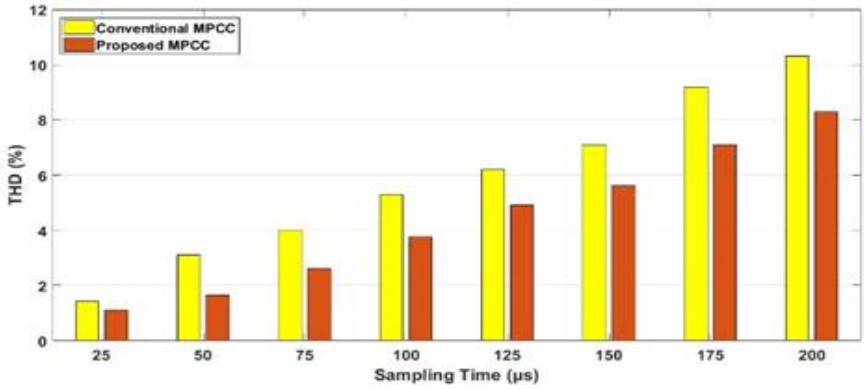

Figure 13. Comparative simulation outcomes of THD in Grid Current for the conventional and proposed MPCC.

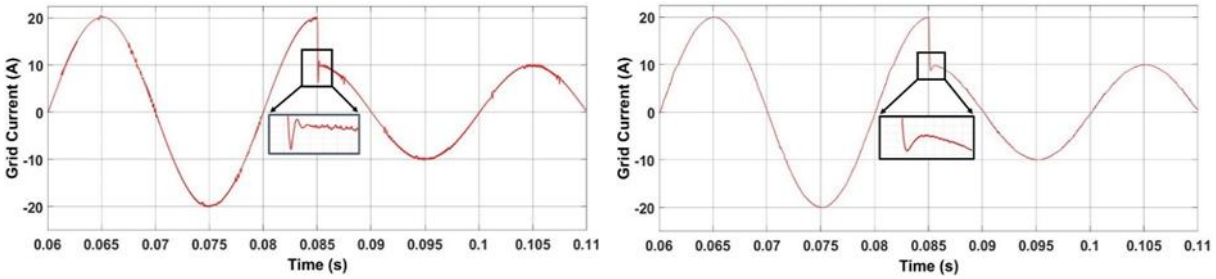

(a) *(b)*

Figure 14. Disruption of the reference current, transition from 20 A to 10 A in phase A of grid current. (a) The traditional MPCC. (b) Modified MPCC with duty cycle control

Results pertaining to reference current step changes indicate that the output current, without a step change, swiftly reaches its reference (see f*igure 14*). In contrast, the conventional method displays a weaker connection with the dynamic response when subjected to step alterations.

The Bode characteristic transfer function is shown *figure 15* where we can observe that the harmonic attenuation ability is better in many frequency ranges as a result of adding a resistor in series with the capacitor of LCL filter.

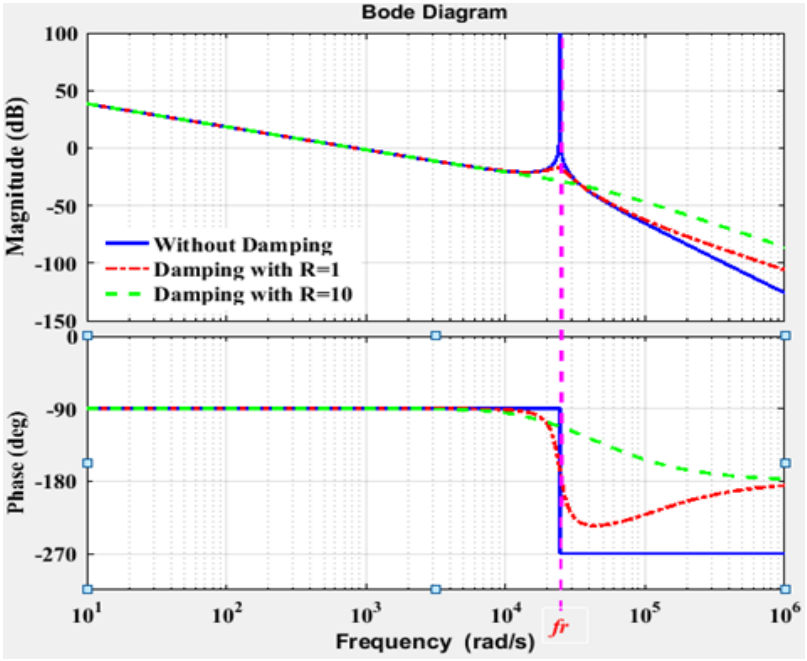

Figure 15. Bode characteristic representation of series resistor-capacitor damping technique

5. EXPERIMENTAL SETUP

To validate the simulation model's realization, an experimental setup featuring a three-level three-leg three-phase CHB grid-interactive inverter with LCL filter output is

implemented in the laboratory, as depicted in *figure 16* and material/specifications captured in Table 2. The experimental prototype system is configured with the algorithm of the proposed MPCC. A 20 kHz TMS320F28335 digital signal processor with 32-bit floating characteristics serves as the platform for the control system, where the coded proposed MPCC algorithm is executed. The parameters, consistent with simulation parameters, are summarized above, and a Tektronix Mixed Domain Oscilloscope (MDO3014) is employed as the measuring equipment.

The experimental and experimental results exhibit some similarities; however, as depicted in *figure 17*, the silhouette of the output current waveforms from the simulation is notably superior and clearer compared to the experimental counterpart. This discrepancy is attributed to the sinusoidal and constant grid voltage employed in the simulation. Nevertheless, it's noteworthy that the output current waveform of the proposed method is smoother than that of the conventional method. *Figure 18* illustrates the Total Harmonic Distortion spectrum for the proposed and convention techniques, indicating values of 4.47% and 2.72%, respectively. Thus, the proposed techniques outperforms the traditional strategy significantly. In summary, the effecacy of the proposed technique has been validated through both simulation as well as experimental results.

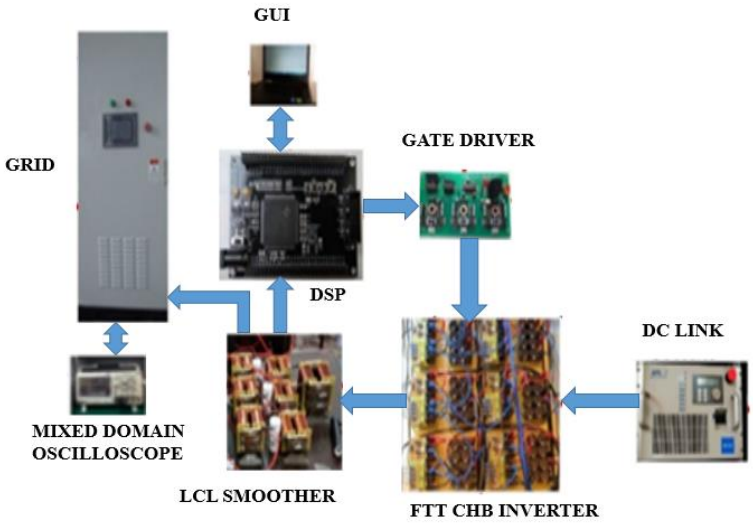

Figure 16. Experimental set-up

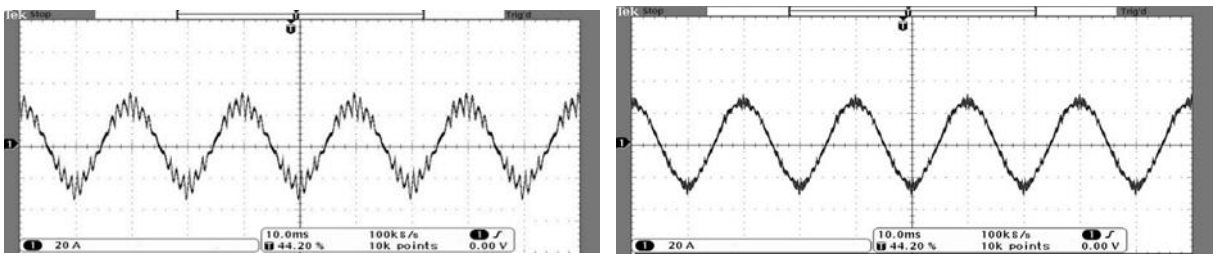

(a) Coventional MPCC *(b) Proposed MPCC*

Figure 17. Waveforms of the three-phase output current

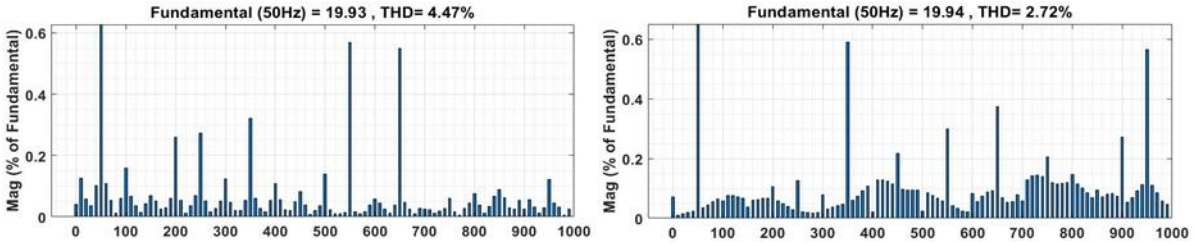

(b) Coventional MPCC *(b) Proposed MPCC*

Figure 18. THD spectrum of the grid current

6. CONCLUSION

In this study, we delved into the intricacies of a five-level three-leg three-phase cascaded H-Bridge (FTTCHB) inverter and devised a Model Predictive Current Control (MPCC) technique tailored for this specific inverter configuration when interfaced with the grid through an output LCL smoother. The evaluation of MPCC for a FTTCHB inverter connected to the grid involved a thorough examination across different sampling times. Our approach systematically scrutinized each of the 61 potential switching states, aiming to identify the state that minimizes the cost function and consequently opting for the one with optimal switching characteristics. To optimize steady-state performance, the proposed MPCC technique necessitates the simultaneous application of both zero and nonzero vectors within a single control period. Ultimately, we conducted simulation and experimental assessments to affirm the efficacy of the proposed MPCC, employing optimal duty cycles and leveraging the explicit integration approximation.

REFERENCES

[1] B. N. L. Ande, N. R. Tummuru, R. T. Pogulaguntla, and B. Ravada, "A Grid-Interactive Power Conversion System for Integrating the PV-Wind Energy Sources," *IEEE Syst. J.*, vol. 16, no. 2, pp. 1851–1860, 2022, doi: 10.1109/JSYST.2021.3071291

[2] A. Raef, A. S. Al-Sumaiti, A. Ibrahim, I. V. Alexandrov, A. G. Garganeev, and A. A. Z. Diab, *Assessment of Model Predictive Voltage Control for Autonomous Four-Leg Inverter*, *IEEE Access*, vol. 8, pp. 101163–101180, 2020, doi: 10.1109/ACCESS.2020.2996753.

[3] A. Goudarzian and A. Khosravi, *Voltage Regulation of a Negative Output Luo Converter Using a PD-PI Type Sliding Mode Current Controller*, International Journal of Engineering, Transaction B: Applications, Vol. 32, No. 2, (2019), 277-285.

[4] X. L. B. Dong, *Improved Variable Switching Frequency Control for Capacitor Voltage Ripple Regulation in Multilevel Flying Capacitor Converter, IEEE Trans. Power Electron*, vol. 38, no. 5, pp. 5700–5705, 2023.

[5] Franquelo, L. G., Rodríguez, Leon, J., Kouro, J. I. S., Portillo, R. & Prats, M. A. M., *The age of multilevel converters arrives*, IEEE Industrial Electronics Magazine, vol. 2 No. 2, (2008) 28–39.

[6] G. Sridhar, P. SatishKumar and M. Sushama, *A Novel Generalized Topology for Multi-level Inverter with Switched Series-parallel DC Sources (RESEARCH NOTE)*, International Journal of Engineering, Transaction C: Aspects, Vol. 30, No. 6, (2017), 851-858.

[7] Alireza Nami and Firuz Zare. *Multilevel Converters in Renewable Energy Systems*, Renewable Energy, T J Hammons (Ed.), (2009).

[8] J. Wen and K. M. Smedley, *Synthesis of Multilevel Converters Based on Single- and/or Three-Phase Converter Building Blocks,* IEEE Trans. Power Electron., vol. 23, no. 3, (2008) 1247–1256.

[9] Patricio Cortés, Gabriel Ortiz, Juan I. Yuz, José Rodríguez, Sergio Vazquez and Leopoldo G. Franquelo, *Model Predictive Control of an Inverter With Output LC Filter for UPS Applications*, IEEE TRANSACTIONS ON INDUSTRIAL ELECTRONICS, vol. 56, (2009), 1875-1883.

[10] Jose Rodriguez, Patricio Cortes, *Predictive control of power converters and electrical drives*, Wiley-IEEE Press (2012).

[11] Sung-Yeul Park, Jih-Sheng Lai, Woo-Cheol Lee, *An Easy, Simple, and Flexible Control Scheme for a Three-Phase Grid-Tie Inverter System*, Energy Conversion Congress and Exposition (ECCE), IEEE Press, (2010), 599-603.

[12] PASTOR Marek, DUDRIK Jaroslav, *Grid-tied Multilevel Inverter With Predictive Current Control*, Journal of Electrical and Electronics Engineering, Volume 5, Number 1, (2012), 173-178.

[13] J. Rodriguez, B. Wu, M. Rivera, C. Rojas, V. Yaramasu , A. Wilson, *Predictive Current Control of Three-Phase Two-Level Four-Leg Inverter*, 14th International Power Electronics and Motion Control Conference (EPE-PEMC), IEEE Press, (2010), 106-110.

[14] Yongchang Zhang, Changqi Qu, Zhengxi Li, Yingchao Zhang, Longhan Cao, *Direct Power Control of PWM Rectifier With Optimal Duty Ratio Under Unbalanced Network*, Power Electronics and ECCE Asia (ICPE-ECCE Asia), IEEE Press, Jun. (2015), 1116 – 1122.

[15] Almaktoof A. M., Raji A. K., & Kahn M. T., *Finite-Set Model Predictive Control and DC-Link Capacitor Voltages Balancing for Three-Level NPC Inverters*, Proceeding of the 16th International Power Electronics and Motion Control Conference and Exposition (PEMC 2014), IEEE Press, (2014), 224 – 229.

[16] Marek Pástor, Jaroslav Dudrik, *Predictive Current Control of Grid-tied Cascade H-bridge Inverter*, ATKAFF, Vol. 54, No. 3, (2013), 308–315.

[17] [Y. Zhang, W. Xie, Z. Li and Y. Zhang, *Model predictive direct power control of a PWM rectifier with duty cycle optimization*, IEEE Trans. Power Electron., vol. 28, no. 11, (2013), 5343-5351.

[18] Yongchang Zhang and Yubin Peng, *Model Predictive Current Control with Optimal Duty Cycle for Three-Phase Grid-Connected AC/DC Converters*, Power Electronics and Application Conference and Exposition (PEAC), IEEE Press, (2014), 837 – 842.

[19] V. Yaramasu, M. Rivera, M. Narimani, B. Wu and J. Rodriguez, *High performance operation for a four-leg NPC inverter with two-sample-ahead predictive control strategy*, Electric Power Systems Research, vol. 123, (2015), pp. 31–39.

[20] Yongchang Zhang, Yubin Peng and Bo Xia, *Efficient model predictive control with optimal duty*

cycle for power converters, Power Electronics and Motion Control Conference (IPEMCECCE Asia), IEEE Press, (2016), 1076 - 1083.

[21] E. K. Adjei-Saforo, E. A. Frimpong, F. B. Effah, M. Adam, E. Shahrous, and S. Hongsheng, *Duty Ratio Optimization for a Multi-Level Poly-phase Cascaded H-Bridge Grid-Interactive Inverter Using Model Predictive Current Control Based on Explicit Integration Algorithm, 2023 IEEE AFRICON Conference*, Nairobi, Kenya, 2023. [CrossRef]

[22] S. Mariethoz and M. Morari, *Explicit model-predictive control of a pwm inverter with an lcl filter*, IEEE Trans. Ind. Electron, vol.56, (2009), 389-399.

[23] O. Rivera, M. Mauledoux, A. Valencia, R. Jimenez and O. Avilés, *Hardware in Loop of a Generalized Predictive Controller for a Micro Grid DC System of Renewable Energy Sources*, International Journal of Engineering, Transaction B: Applications, Vol. 31, No. 8, (2018), 1215-1221.

[24] M. Arehpanahi and D. Paknia, "A New Single-phase Symmetrical Cascade Multilevel Inverter with Low Number of Power Switches", *Hardware in Loop of a Generalized Predictive Controller for a Micro Grid DC System of Renewable Energy Sources*, International Journal of Engineering, Transaction B: Applications, Vol. 31, No. 8, (2018), 1228-1233.

[25] H. A. Salama, S. J. Finney, and B. W. Williams, *Predictive Control of LCL Filters for Grid-Connected Inverters*, IEEE Transactions on Industrial Electronics, Vol. 68, No. 3, pp. 2192-2202, Mar. 2021.

[26] E. K. Adjei-Saforo, M. Adam, S. A. Darko, S. N. Akansake, *Comparative Studies into Resonance Damping of Output LCL Filter For Active Power Filter With Voltage Source Inverter*, International conference on Applied Sciences and Technology (ICAST),pp. 98-109, 2024. [CrossRef]

[27] M. Adam, S. Ebrahimpanah, Y. Chen and Q. Chen, "Performance of CLC Filters with Shunt APF for Harmonic Current Mitigation", DEStech Transaction on Engineering and Technology research, Vol. 2017/15935, pp.32-41, 2017

STUDY ON THE EFFECTS OF MICROWAVES ON WATER HEATING AND THEIR INFLUENCE UPON THE GERMINATION PROCESS

Radu **JOIAN**[1], Dorin **MANCIULA**[2]
Technical University of Cluj-Napoca, Romania, Babes Bolyai University of Cluj-Napoca, Romania
yo5pcw@yahoo.com, iosif.manciula@ubbcluj.ro

Keywords: Microwave, harmful effect, bean germination experiment.

Abstract*: This paper considers an experimental study that considers the effects of heating water in a microwave oven. Thus, we wanted to check how harmful microwave-heated water is, and by extrapolation, how harmful microwave-heated food can be.*

1. INTRODUCTION

In electronics, microwaves work at high frequencies, thus having short wavelengths:

$$\lambda = \frac{c}{f}$$

where:

- *c*, represents the propagation speed specific to electromagnetic waves. When propagating in a free space (vacuum), the speed of electromagnetic waves is $c_0 = 3 \cdot 10^8$ m/s .

As a rule, in the field of microwaves, the wavelengths λ have small values, of the order of millimeters or centimeters, which corresponds to high frequencies, tens of gigahertz. In principle, the microwave field can be defined or has as characteristics the fact that the dimensions of the circuits are almost equal or even greater than the wavelength, the absolute value of the frequency being a secondary characteristic.

With a view to an easier analysis of microwave circuits, specialists in the field have developed certain calculation methods, especially suitable, which allow the determination of the most significant properties of circuits, respectively microwave systems [2].

2. SYSTEMS, CIRCUITS AND ASPECTS OF MICROWAVE PROCESSING TECHNIQUES

They consist of interconnected components/subassemblies. The interconnection element represents the simplest element related to a system. If we talk about low frequencies, the related components of an assembly will be interconnected by metal wires that keep both the voltage and current constant throughout the respective section. In the field of high frequencies, the propagation time relative to the period, which is very short, specific to the signal, cannot be neglected, so the current and voltage are not kept constant along the length of the respective wire. Thus, considering the previously mentioned, these short or long portions of lines are called waveguides. The properties of such a system are dependent on the propagation phenomena along the elements that realize the interconnection and the properties of the component subassemblies.

If we talk about the category of linear circuits, these are all Radio Frequency circuits that work in the range of frequencies corresponding to microwaves and that operate at low signal, such as very low power amplifiers. Electronic circuits are the ones that have brought about the change in the life we live today since the beginning of the 20th century. The digital age was opened, however, with the appearance of the first integrated circuits, followed later by digital computers. But, for electronic circuits that use microwaves, we will talk about a more special category, because high frequencies are circulated here. The specific applications of this field can be found in radio communication equipment, more precisely in satellite communications, television and even the development of the Internet. At high frequencies, more complex microwave circuits in addition to amplification will accurately pick up the signal in noisy conditions. The previously mentioned complex processes will allow the transmission of signals, wirelessly, over very large distances, even if the corresponding stations do not have a fixed point.

In the study presented in this paper, the main element is the microwave oven. From the specialized literature [3] we know that those microwaves are generated by a magnetron, which acts as an emitter for the radiant energy at high frequencies, which will later be transmitted with the help of a tube inside the electronic equipment. The waves are reflected inside with the help of the walls that make up the enclosure, thus a resonance system will be established. The agitator has the role of distributing the microwaves throughout the room. In the case of a 2450 MHz installation (microwaves being the electromagnetic radiation between 300 MHz - 300 GHz) magnetrons are used that have individual powers between 2.5 - 3 kW.

The main elements responsible for the influence of microwave heating are the dielectric properties of food, respectively the thermal and physical properties specific to food. The properties of the microwave source and packaging details should also be mentioned. When food

is placed in a microwave oven, it will absorb the energy of the microwave field. Basically, heating represents an interaction in the created energy that will change the polarity and the elements of which the respective food is made up billions of times per second, thus achieving volume heating. Another property of microwaves is that they can be transmitted, reflected, or absorbed. Food products will be a dielectric material because they are made of carbohydrates, proteins, water, and microwaves will penetrate them without problems, being thus absorbed in a proportion greater than 50% [3].

3. EXPERIMENTAL DETERMINATIONS

The experiment carried out considers the effects of heating water in a microwave oven and the effect upon the germination process of beans.

The experiment wanted to highlight how harmful microwave-heated water is for plants, especially during their germination period and by extrapolation, how harmful microwave-heated food can be for the health of the consumers of food prepared in this way. It is known that this type of heating is based on the "stirring" of the water molecules in the food, by the electromagnetic field of the microwaves. For this reason, materials that do not contain water (or other liquids) are not heated in the microwave oven, they change their temperature only from the transmission of heat from the body to be heated (food, for example) to the vessel in which it is placed.

Description of the experiment. For the experimental part, the following equipment and materials were used: microwave oven (Samsung), two glass containers (370 ml), cotton wool for the germination bed, tap water, beans. Two beans of different varieties were placed in two transparent containers (*figure 1*).

Fig. 1. Experiment preparation

These grains were watered separately, one with tap water (the one labeled "water") and the second with tap water, heated for 2 minutes in the microwave oven, and then cooled (labeled "µwaves").

The same amount of water (10 drops) was put into each vessel at the same time, and the recipients were kept in natural light, in a room with constant temperature of 20 ^{o}C (f*igure 2*).

Fig. 2. Storing pots of beans

The first results of the experiment appeared after five days of watering with the two kinds of water, the grains in the "water" jar sprouted (*figure 3*).

Fig. 3. After 5 days - those watered with tap water sprouted

Those soaked with "microwave" water had no change (*figures 4 - 5*).

Fig. 4. After 5 days - the grains are watered with "microwave" heated water

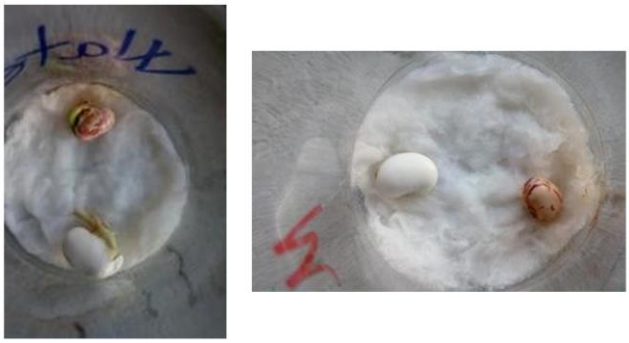

Fig. 5. Day 6 - "µwaves" no change (!)

After seven days, the first green sprout appeared in the vessel in which the plant was watered with "clean" water, while in the other vessel there was no change (*figure 6*). After eight days, the green sprouts continued their growth, but on top of those soaked in microwave water, mold begins to form and, in the end, they rotted (*figures 7 - 8*).

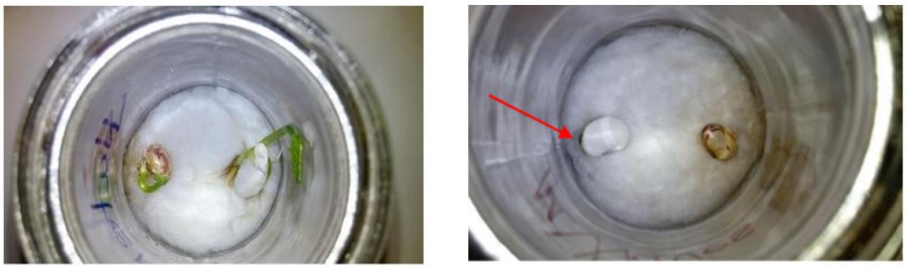

Fig. 6. Day 7. The appearance of mold on the one from the "μwaves"

Fig. 7. Day 8. Plant grows (tap water-left) and mold grows (microwave heated water-right).

Fig. 8. Day 9. The plant watered with "tap water" grows. Mold expands in"μwaves"

On the tenth day, only the "moldy" grain from the "μwaves" jar was watered with 4-5 drops of tap water. The next day it sprouted. Thus, the clean water was beneficial to the vegetal material and the grain recovered (*figures 9 - 10*).

Fig. 9. Day 11. The plant watered with "pure water" grows and the the sprouts with mold recover after they were watered with tap water.

The watering of the grains continued, exactly as at the beginning of the experiment. Those watered with tap water continued to grow, and those that received microwave heated water stopped their evolution (*figure 10*).

Fig. 10. Day 13. The plant watered with tap continues to grow. The grains watered with microwave heated water do not evolve anymore.

4. CONCLUSION

The experiment presented focuses on the effects of heating water in a microwave oven and the germination process of grains. The results indicate that water heated in a microwave oven negatively affects the germination process of grains compared to tap water. This finding raises concerns about the potential harmful effects of microwave-heated water on plants and, by extrapolation, on the health of consumers who use this method of food preparation.

Following the analysis of the results it was found that the grains watered with microwave-heated water had a slower and less efficient germination process compared to those watered with tap water. After five days, the beans watered with regular water began to

germinate, while those watered with microwave-heated water showed no signs of germination. This difference increased over time, and after eight days, the grains soaked in microwaved water developed mold and began to deteriorate, while the others continued to grow healthy. After heating the water in the microwave oven, its properties change and it cannot trigger "life" for some simple plants that, under normal conditions, evolve very quickly. After the tenth day, the water treated with microwaves had no influence on the growth and development of the plants, comparing to the tap water, and in addition it determined the appearance of mold and finally the complete degradation of the plant material. Also, the involvement of mold suggests that this water may create a favorable environment for the growth of harmful microorganisms.

Although the study discusses the process of grain germination and the effects of exposure to microwaves on it, we mention that these results are preliminary and are part of a larger experiment designed to explore the influence of other factors on the experimental results, among which are exposing water samples to electro-magnetic, energetic and radiative fields with varying frequencies, in order to understand the impact of these factors on the process of plant germination, their interaction with the soil, as well as the thermal and chemical effects of different heating methods on the environment, plant health and implicitly human health.

REFERENCES

[1] J.P. Dunsmore, *Handbook of Microwave Component Measurements: with Advanced VNA Techniques*, 2nd Edition, 2020.

[2] G. Lojewski, *Microwave devices and circuits*, Edituta Tehnică, 2005.

[3] N. Crișan, *Microwave antennas and circuits*, Editura Risoprint, 2008.

[4] D. M. Pozar, *Microwave Engineering*, John Willey & Sons, Inc, 1998.

[5] R. E. Collin, *Foundations for Microwave Engineering*, IEEE Press Series on Electromagnetic Wave Theory, John Willey & Sons Inc., 2001

[6] M. Golio, *The RF and Microwave Handbook*, Boca Raton: CRC Prec LLC, Library of Congress Cataloging in Publication Data, 2001.

[7] J. F. White, *High Frequency Techniques – An Introduction to RF and Microwave Engineering*, IEEE Press, John Willey & Sons Inc., 2004

INVESTIGATING MAGNETIC CONTROLLED REACTOR PRINCIPLES AND CHARACTERISTICS UTILIZING ANSYS IN AN IN-DEPTH STUDY

Samuel Addo **DARKO**[1], Edmund Kwafo **ADJEI-SAFORO** [1,2], Misbawu **ADAM**[1], Solomon Nchor **AKANSAKE**[2]

[1] *Kumasi Technical University,* [2]*Kwame Nkrumah University of Science and Technology, kingacid17@gmail.com, adam.misbawu@kstu.edu.gh*

Keywords: Magnetic controlled reactor (MCR), core structure, magnetic field distribution, magnetic saturation

Abstract*: The inherent complexity leads to intricate equations, making it challenging for design engineers and researchers to model and analyze MCRs effectively. Despite the increasing attention given to MCRs in power systems, the need for simplified theoretical foundations and design models persists. This paper addresses the challenges posed by the complex excitation conditions of magnetic controlled reactors (MCRs), which are subject to both alternating current and direct current excitations by presenting the theoretical basis, ontological structure, working principle, and design model of MCRs in a systematic manner for enhanced comprehension. Graphical and equivalent electric circuit approaches are employed to derive mathematical expressions, while ANSYS simulation is utilized to create a 3D structure model of the MCR. The simulation results, compared with theoretical analyses, demonstrate that the MCR exhibits alternate magnetization and demagnetization between its two core limbs in a cycle. This suggests that the magnetic valves on both sides alternate between saturation and unsaturation in each cycle. Furthermore, the research reveals that the MCR's entire capacity can be smoothly adjusted by varying the saturation degree of the magnetic valve core. Overall, this research contributes to a deeper understanding of MCRs under actual operating conditions and serves as a crucial foundation for further investigations into their performance design.*

1. INTRODUCTION

Although transformers are inevitable in power generation, power transmission and power distribution stations, in recent years, however, MCR has also become one of the most

essential equipment used in long distance EHV and UHV transmission lines, as well as substations with high voltage fluctuations, because of its good control flexibility, high reliability and simple maintenance [1] [2] [3] [4]. MCR is a type of reactive power compensation equipment which can reduce grid losses, eliminate generator self-excitation, control power frequency over-voltage, limit short-circuit current and control operations automatically [5] [6] [7]. Currently, more than 8 GVA of total reactor capacity have been successfully installed around the world in various voltage buses, from 10 to 500 kV and still counting [8] [9]. On the basis of that, there are currently considerable worldwide research activities all over the world especially, Russia, America, Germany, United Kingdom, Brazil and China.

From the early 1950s, General Electric Company of England installed more than fifty magnetic controlled reactors with the capacity from few to hundreds MVA in electric grids of different countries [10]. However, due to economic and technical performance limitations, such as high material cost, low speed, limited control range and low power efficiency, manufacturing of these machines were brought to a halt. In 1971, H. Becker studied on the first three-phase three-winding magnetic controlled reactor model which the magnetic iron core legs have cylindrical winding [11]. Many modern designs of MCR can be traced as a prototype of his construction. A suggestion was also made by him that MCR would be useful for compensating reactive power. In the 1980s, Alma-Ata University in USSR investigated and developed more prototypes. In the year 1990 to 1992 at Zaporozhye Transformer Factory (ZTR) in collaboration with V.I.Lenin All-Soviet Electrotechnical Institute built a full-scale 500 kV / 60 MVA single-phase MCR and successfully put into test at a high-voltage test facility near Moscow, Russia. Since then, many different capacities have been designed and produced, including the first commercialized 60 MVA / 500 kV 3-single-phase units in 2005, and the first three-phase 180 MVA unit in 2009 [12]. In September 2007, China Electric Power Research Institute cooperated with Shenyang Transformer Factory also proudly produced the first 120 MVA / 500 kV magnetic controlled reactor in China, which was successfully put into operation at Jiang Ling Converter Substation [13]. In June 2013, the three-phase 110 MVA / 750 kV magnetic controlled reactor developed by TBEA Shen Chang Company was also successfully put into operation at Qinghai Yuka Switch Station.

MCR is mostly designed either a single-phase or three-phase, where its cooling system can be air type or oil-immersed type depending on the application it is subjected to. Its technical core involves ferromagnetic material characteristics, magnetic circuit design, nonlinear theory, AC and DC co-excitations and control system characteristics. Along with its good developmental trend, simplification in modeling and analysis has become more and more difficult, deterring new and young researchers to dive into.

This paper thoroughly analyzes MCR's theory, provides simplified mathematical calculations and establishes a 3D MCR prototype model in ANSYS Maxwell. Hence, providing convenience for design engineers and research works as a whole.

2. THE CORE STRUCTURE AND WORKING PRINCIPLE

2.1. Core structure and winding configurations

The configuration of the Magnetic Controlled Reactor (MCR) resembles that of a transformer but functions on the principle of a magnetic amplifier. Its adaptability has led to various core structures and connections. *Fig. 1* and *2* depict the typical core structure and winding arrangements for a single-phase MCR, featuring an iron core with magnetic valves, working winding, and control winding [14].

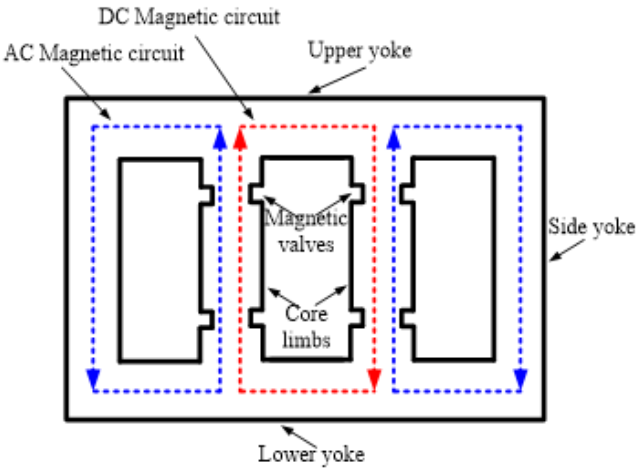

Fig. 1. Core structure of a single phase MCR

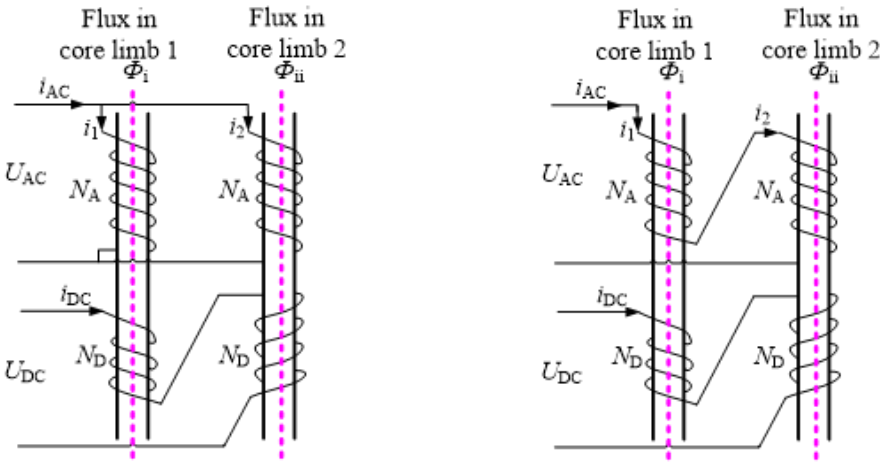

(a) Working winding in parallel *(b) Working winding in series*

Fig. 2. Winding arrangements

The iron core comprises two parallel limbs and two side yokes, offering a closed-loop path for magnetic flux during excitation [15]. Both working and control winding are affixed to the core limbs, with N_A representing the number of working winding turns and N_D representing

the number of control winding turns [16] [17]. U_{DC} represents a DC source of voltage that creates DC current I_{DC} flowing within the control winding which induces DC magnetic flux in the core limb *i* and core limb *ii* with an equal magnitude but opposite direction [18]. The working winding are sometimes referred to as AC winding because their terminals are directly connected in parallel to the power network and control winding are also referred to as DC winding because their terminals are connected to DC source where the MCR is being controlled [19]. The DC winding are wired in reverse-series so that the fundamental component of the voltages is annihilated. This helps to minimize the insulation of the equipment and achieve a better level in control characteristics [20].

To achieve control over the magnetic saturation in Magnetic Controlled Reactors (MCRs), both the winding connection and magnetization characteristics play crucial roles. When the DC control excitation current is nil, the inductance L of the working winding is maximized, and the current in these winding is minimized. This scenario characterizes the MCR as functioning equivalently to the ideal operation of a transformer [21]. However, as the DC bias excitation current starts flowing and gradually intensifies in the control winding, the current in the working winding also proportionally increases. This implies that variations in the control current lead to changes in the magnetic saturation level of the iron core. Consequently, the magnetic permeability of the core fluctuates, allowing precise adjustment of the impedance value of the MCR in accordance with the formula [22]:

$$X = \omega L = \omega \frac{\mu_0 \mu_r N_A^2 A_c}{l_c} \tag{1}$$

where $\omega = 2\pi f$ is the angular frequency, A_c is the cross sectional area of the iron core, l_c is the effective length of the magnetic circuit, μ_0 is the vacuum permeability, μ_r is the relative permeability of the core material and N_A is the winding turns.

2.2. Ferromagnetic materials and magnetizing curve of MCR

Ferromagnetic materials are key elements in all instances of generation, transmission, and conversion of electrical energy. They have great technological and social value, far beyond their mere economic significance [23]. The characteristics of ferromagnetic materials play a very essential role as long as MCR is a concern, because they determine how the saturable core will behave. The magnetic properties of the iron core material determine the performance of the magnetic device and are the basis for the analysis and calculation of magnetic devices. At the same time, the properties of magnetic devices are also largely related to the structure, shape, size and manufacturing process of iron cores. At present, the ferromagnetic materials that are widely used in the area of saturable reactors can be grouped into the following three parts according to their properties and chemical composition [24]:

(1) Silicon steel sheet is mainly used in power frequency high power reactor and power transformers.

(2) High conductivity magnetic nickel alloy is mainly used in magnetic amplifiers, DC current transformers, magnetic modulators, power transformers with special requirements and low power sensitive high frequency pulse saturable reactor.
(3) Ferrite is commonly used for high frequency and pulse excitation components.

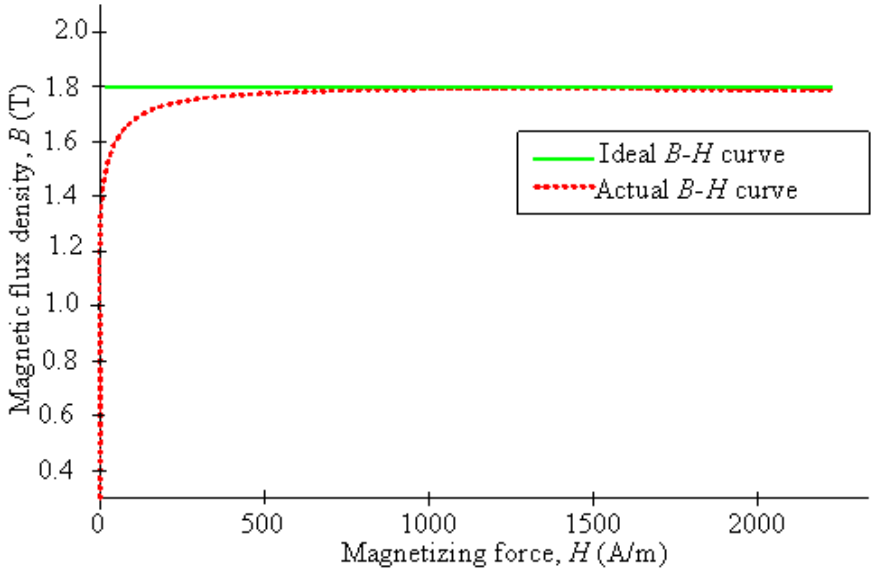

Fig. 3. Magnetization curve of ideal and actual model

The basic magnetizing curve of the silicon steel sheet used for MCR and its ideal magnetizing curve is shown in *fig. 3*. Where the solid green line represents the ideal model and the dot red line represents the actual DC magnetizing curve. However, it should be noted that the core magnetic material used in this paper is the B30G130 grain-oriented magnetic steel sheet type, which its data was published by Wuhan Iron and Steel Mining Company. Moreover, the characteristics and magnetization curves of many different kinds of ferromagnetic materials are presented in detail in literature [23] [25] [26]and [27].

2.3. Magnetic valve of MCR

2.3.1. Characteristics of magnetic valve

Magnetic controlled reactor is said to have a magnetic valve if the core magnetic path is made up of a large area (A_c), (length l_c) and a small area (A_v), (length l_v) in series. Essentially, the magnetic valve can easily be saturated with a small DC bias when has a small area, which of course can greatly save cost. Because the iron core in the large area is always in the unsaturated linear region, the entire capacity of the MCR is determined by changing only the saturation degree of the magnetic path in the magnetic valve [28]. The greater the DC bias, the higher the saturation degree of the valve, and the smaller the equivalent inductance of the MCR. In addition, the magnetic valve can contribute to the mitigation of harmonics when it is carefully designed [29].

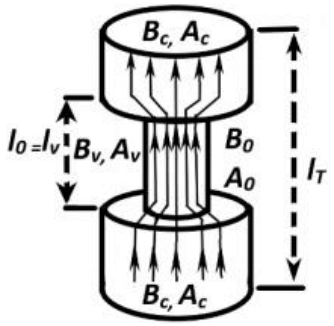

(a) Magnetic valve unsaturated *(b) Magnetic valve fully saturated*

Fig. 4. Characteristics of magnetic valve

Fig. 4 shows unsaturated and saturated characteristics of the magnetic valve. Where l_T is the length of the core limb (m), A_c is the core limb cross-sectional area (m^2), B_c is the core limb flux density (T), l_v is the valve length, A_v is the valve cross-sectional area (m^2), B_v is the valve flux density (T), l_0 is the air-gap length, A_0 is the air-gap cross-sectional area (m^2) and B_0 is the air-gap flux density (T). In *fig. 4(a),* under unsaturated condition, the iron core cross sections, A_v and A_c are in the unsaturated linear zone, and almost all the magnetic lines of force pass through the iron core. The magnetic reluctance is at a minimum and the magnetic valve is said to be fully open. At this point MCR is equivalent to a no-load transformer. In *fig. 4(b)* under saturated condition, only the iron core cross-section, A_v is fully saturated, and its permeability is very small and close to the permeability of the air gap. The reluctance is at a maximum and the magnetic valve is said to be almost close. At this point, the MCR is said to be operating at its maximum design capacity. In other cases where the condition lies in between unsaturated and fully saturated, part of the magnetic lines will pass through the air gap with an area of A_0. The other part of the magnetic line will pass through the magnetic valve, A_v. The magnetic reluctance of A_0 is linear, but that of A_v is non-linear.

2.3.2. Magnetic circuit and equations of magnetic valve

According to Ampere's law relating to current in the coil or turns of wire, the magnetic field created by current following any path is the integral of the fields due to segments along the path. And Faraday's law relating to the voltage applied across the inductor can be expressed in (2):

$$\left.\begin{aligned} F = NI = \oint \vec{H} \cdot d\vec{l} = Hl \\ \vec{B} = \mu\vec{H} = \frac{\mu NI}{l} \\ \emptyset = BA = \frac{\mu NIA}{l} \\ LI = \emptyset N \\ L = \frac{\mu N^2 A}{l} \\ \Re = \frac{l}{\mu A} = \frac{l}{\mu_0 \mu A} \\ L = \frac{N^2}{\Re} \end{aligned}\right\} \quad (2)$$

where H is the magnetic field intensity, $\Re$ is the magnetic reluctance, N is the number of winding, l is the length of the magnetic path (m), A is the magnetic cross-sectional area (m^2), $\mu = \mu_0\mu_r$ is the permeability of the medium (H/m), and μ_0 is the permeability of air, $4\pi \times 10^{-7}$ (H/m), μ_r is the relative permeability and Φ is magnetic flux. The magnetic path of the MCR can be equivalent to the series-parallel circuit shown in f*ig. 5* can be expressed in (3).

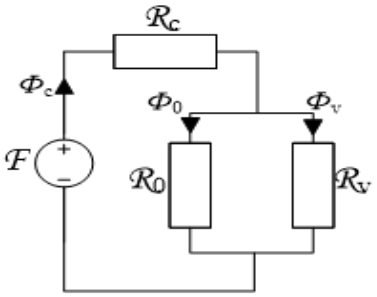

Figure 5. Equivalent circuit (including $\Re_c$)

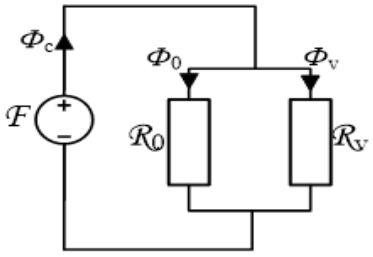

Figure 6. Equivalent circuit (excluding $\Re_c$)

$$\Re_t = \Re_c + \frac{\Re_0 \Re_V}{\Re_0 + \Re_V} \tag{3}$$

where Φ_c is the core limb magnetic flux, Φ_0 is the air gap magnetic flux and Φ_v is the valve magnetic flux, $\Re_c$ is the magnetic reluctance in the core limb, $\Re_0$ is the magnetic reluctance in the air gap, $\Re_V$ is the magnet c reluctance in the valve. From Equation (3), magnetic reluctance $\Re_c$ can be ignored as shown in *fig. 6*, for the reason being that the iron core in the large segment is always in the unsaturated linear region within the entire adjustment range of the MCR, as a result, its magnetic reluctance is much smaller than the magnetic valve segment reluctance [30]

$$\Re_t = \frac{\Re_0 \Re_V}{\Re_0 + \Re_V} \tag{4}$$

It can be seen from (4) that if saturation degree across magnetic-valve can be smoothly changed in the purpose of adjusting the reluctance, then its reactive power can be adjusted accordingly to achieve flexible continuous regulation of output power of the power network.

Now, when the small sectional area of the iron core is in saturation state, and the fringing effect shown in *fig. 4(b)* is neglected, then equations is as below [30]:

$$\emptyset = A_C B = A_0 B_0 + A_V B_V \tag{5}$$

The equation (6) can be obtained through equation (5).

$$B = \frac{A_0}{A_C} B_0 + \frac{A_V}{A_C} B_V \tag{6}$$

Since the small sectional area of iron core and air-gap have the same magnetic field intensity $f(B_v)$, B_0 can be written as:

$$B_0 = \mu f(B_V) \tag{7}$$

Substituting equation (7) into equation (6), B is given by:

$$B = \frac{A_0}{A_C}\mu_0 f(B_V) + \frac{A_V}{A_C}B_V \tag{8}$$

According to the supposition of small slope magnetization curve, when $B_V \leq B_{Vsat}$, the magnetic field intensity of the small sectional area of the iron core $f(B_v) = 0$, then B is expressed as [30]:

$$B = \frac{A_V}{A_C}B_V \tag{9}$$

So, the magnetic field intensity of the equivalent iron core is zero in $0 \leq B \leq (A_V/A_C)B_{Vsat} = B_{sat}$ range. On the other hand, when $B_V \geq B_{Vsat}$, the small sectional area of iron core is then saturated, so magnetic field intensity is expressed as:

$$H = \frac{B_V - B_{Vsat}}{\mu_0} \tag{10}$$

Substituting equation (8) into equation (10), the magnetization curve model of MCR is given in equation (11). And its magnetization curve is presented in *fig. 7.*

$$H = f(B) = \begin{cases} \frac{B+B_{sat}}{\mu_0} & B < -B_{sat} = -\frac{A_V}{A_C}B_{Vsat} \\ 0 & -B_{sat} \leq B \leq B_{sat} = \frac{A_V}{A_C}B_{Vsat} \\ \frac{B-B_{sat}}{\mu_0} & B > B_{sat} = -\frac{A_V}{A_C}B_{Vsat} \end{cases} \tag{11}$$

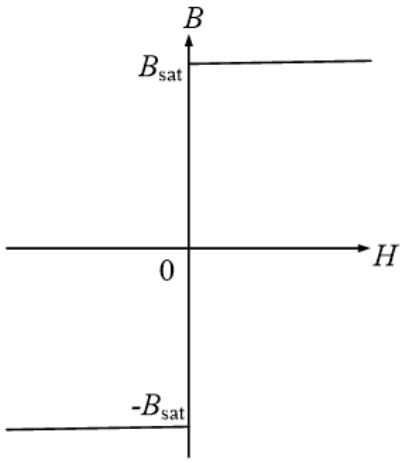

Fig. 7. Ideal core magnetization curve

2.4 Magnetic field analysis of MCR under excitation

To simplify the analysis, the working winding resistance of the magnetically controlled shunt reactor is ignored. Again, it is assumed that the MCR is connected to the power supply with a sinusoidal voltage, $U_{AC} = U_{max} \sin \omega t$. The basic equations of the MCR can be expressed as follows [31]:

$$\begin{cases} \mu_{AC} = E_{max} \sin(\omega t) = A_V N_A \left(\frac{dB_i}{dt} + \frac{dB_{ii}}{dt}\right) \\ U_{DC} = R_D i_{DC} + A_V N_D \left(\frac{dB_i}{dt} - \frac{dB_{ii}}{dt}\right) \\ l_i H_i = i_{AC} N_A + i_{DC} N_D \\ l_{ii} H_{ii} = i_{AC} N_A - i_{DC} N_D \\ H_i = f(B_i) \\ H_{ii} = f(B_{ii}) \end{cases} \tag{12}$$

According to *fig. 2*, the induced EMF in the control winding can be obtained as:

$$U_{DC} = U_{Di} - U_{Dii} = A_V N_D \left(\frac{dB_i}{dt} - \frac{dB_{ii}}{dt}\right) \tag{13}$$

And the induced EMF in the working winding can also be obtained as:

$$U_{AC} = U_{Ai} - U_{Aii} = A_V N_A \left(\frac{dB_i}{dt} + \frac{dB_{ii}}{dt}\right) \tag{14}$$

where U_{Di} and U_{Dii} are the induced EMFs in the control winding while U_{Ai} and U_{Aii} are the induced EMFs in working winding on core I and II, respectively.

Since the working state of the two core structures and winding arrangements are symmetrical, the corresponding magnetic flux density should have the following relationship:

$$\begin{cases} B_i(\omega t) = -B_{ii}(\omega t + \pi) \\ B_{ii}(\omega t) = -B_i(\omega t + \pi) \end{cases} \tag{15}$$

When there is no DC current in the control winding, thus $I_{DC} = 0$, $B_{DC} = 0$, as well, and the AC magnetic flux density B_i, B_{ii} varies only between $-B_{sat}$ and $+B_{sat}$, and the amplitude is$B_{max} = B_{sat}$. Now, increasing the DC bias excitation in the control winding increases the DC component in B_i, B_{ii}, so that their top rises (drops) beyond the $+B_{sat}$ ~ $-B_{sat}$ range as shown in *fig. 8*.

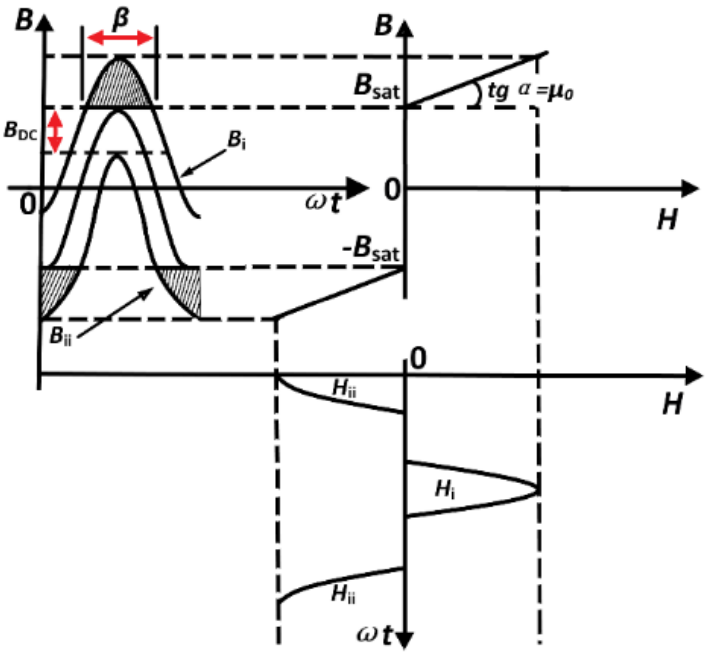

Fig. 8. DC bias core magnetic saturation schematic diagram

The horizontal axis portion corresponding to the shaded portion in the *fig.* (electrical angle is 2β) indicates the core saturation time of the half core limb in the power frequency for one cycle and is expressed by β, which is called magnetic saturation. In the theoretical analysis of MCR, a magnetic saturation β plays a very essential role. When the control current is zero, B_{DC} = 0, the half core limb is not saturated in a complete power frequency cycle, so $\beta = 0$. As the control current increases, the saturation time of the half core limb in one cycle increases. When the half core limb is fully saturated in one complete cycle, the magnetic saturation, $\beta = 2\pi$. At this moment, β reaches the maximum limit. Therefore, the magnetic saturation β reflects the degree of saturation of the core, and its values vary from 0 to 2π. Ignoring the effect of flux density harmonics, magnetic saturation can be obtained from Equation (16).

$$\beta = 2arcos\left(\frac{B_{sat}-B_{DC}}{B_{sat}}\right) \tag{16}$$

And DC flux density is

$$B_{DC} = B_{sat}\left[1-\cos\left(\frac{\beta}{2}\right)\right] \tag{17}$$

Through the corresponding B-H curve, the magnetic field strength of the core limb I and II can be obtained as follows:

When

$$\left(\pi-\frac{\beta}{2}\right) \le \omega t \le \left(\pi+\frac{\beta}{2}\right)$$

$$H_i = \frac{B_{sat}}{\mu_0}\left(-\cos\omega t-\cos\frac{\beta}{2}\right) \tag{18}$$

But when

$$0 \le \omega t < \frac{\beta}{2} \text{ or } \left(\pi + \frac{\beta}{2}\right) < \omega t \le 2\pi$$

$$H_i = 0$$

$$0 \le \omega t < \frac{\beta}{2} \text{ or } \left(2\pi - \frac{\beta}{2}\right) < \omega t \le 2\pi$$

$$H_{ii} = \frac{B_{sat}}{\mu_0}\left(-\cos \omega t - \cos\frac{\beta}{2}\right) \tag{19}$$

But when

$$\frac{\beta}{2} \le \omega t \le \left(2\pi - \frac{\beta}{2}\right)$$

$$H_{ii} = 0$$

If the working current of MCR is given as $i_{AC} = \frac{l}{2N_A}(H_i + H_{ii})$, then the amplitude of current fundamental component is:

$$i_{ACn} = \frac{2}{\pi}\int_0^{\pi} i_{AC} \cos \omega t \, d\omega t = \frac{2}{\pi}\int_0^{\pi} \frac{l}{2N_A}(H_i + H_{ii}) \cos \omega t \, d\omega t$$

$$= \frac{lB_{sat}}{\pi\mu_0 N_A}\int_{\pi-\frac{\beta}{2}}^{\pi}\left(-\cos \omega t - \cos\frac{\beta}{2}\right) \cos \omega t \, d\omega t + \int_0^{\frac{\beta}{2}}\left(-\cos \omega t + \cos\frac{\beta}{2}\right) \cos \omega t \, d\omega t$$

$$i_{ACn} = \frac{lB_{sat}}{2\pi\mu_0 N_A}(\beta - \sin \beta) \tag{20}$$

The working current of MCR reaches maximum at $\beta = 2\pi$ is:

$$i_{AC\,max} = \frac{lB_{sat}}{\mu_0 N_A} \tag{21}$$

It is realized from Equation (21) that the maximum working current of the MCR depends only on the effective length of the magnetic circuit, magnetic flux density, winding turns and vacuum permeability.

On the other hand, if the control current is $i_{DC} = \frac{l}{2N_A}(H_i - H_{ii})$, then the amplitude of control current fundamental component is:

$$i_{DCav} \approx \frac{1}{\pi}\int_0^{\pi} i_{DC}\, d\omega t = \frac{l}{2\pi N_A}\left[\int_0^{\pi}(H_i + H_{ii})\ d\omega t\ \right]$$

$$\frac{lB_{sat}}{2\pi\mu_0 N_A}\int_{\pi-\frac{\beta}{2}}^{\pi}\left(-\cos\omega t - \cos\frac{\beta}{2}\right)\ d\omega t - \int_0^{\frac{\beta}{2}}\left(-\cos\omega t + \cos\frac{\beta}{2}\right)\ d\omega t$$

$$= \frac{lB_{sat}}{\pi\mu_0 N_A}\left(\sin\frac{\beta}{2} - \frac{\beta}{2}\cos\frac{\beta}{2}\right) \tag{22}$$

The control current of MCR reaches maximum at $\beta = 2\pi$ is:

$$i_{DC\,max} = \frac{lB_{sat}}{\mu_0 N_A} \tag{23}$$

2.5 Harmonic characteristics of MCR

The magnetic controlled reactor takes advantage of the saturation of the small cross-sectional area of the core and the nonlinearity of the core magnetization curve. The working region must be in the nonlinear region; therefore, it will inevitably produce harmonics [32]. It should be noted that the core saturation corresponding to the capacity of the MCR is the rated magnetic saturation, which is β_n. The harmonic characteristics of MCR are analyzed by comparing the maximum value of each harmonic current with the rated fundamental current in the range of the reactor capacity. The calculation of the maximum value of each harmonic wave at$0 \le \beta \le 2\pi$ is shown in Equation (16), in which the base value is the maximum value of the rated fundamental current.

$$\begin{cases} I_{1m}^{*} = \frac{1}{2\pi}(\beta - \sin\beta) \\ I_{(2n+1)m}^{*} = \frac{1}{2\pi(2n+1)}\left[\frac{\sin n\beta}{n} - \frac{\sin(n+1)\beta}{n+1}\right] \\ (n = 1,2,3,\dots) \end{cases} \tag{24}$$

The harmonic current distribution of the magnetic controlled reactor is shown in *fig. 9* using Equation (24). The curves of the per-unit value of fundamental wave, 3rd, 5th and 7th harmonic current with saturation β calculated by Equation (24) are also shown in *fig. 9*. It is clear from the *fig.* that the nth harmonic component of the current of the MCR has n zero points and (n-1) extreme points. Each extreme point is symmetrically distributed with $\beta = \pi$

as the center, and the maximum extreme points of each harmonic are all close to $\beta = \pi$. Again, the whole capacity of the MCR, the maximum content of the total harmonic is not more than 8%. It can also be observed that the maximum amplitude of the 3rd harmonic is about 6.89% of the rated fundamental current, the maximum amplitude of the 5th harmonic is about 2.52%, and the maximum amplitude of the 7th harmonic is about 1.29%, respectively. The distortion coefficient of the current waveform will be smaller because the maximum value of each harmonic wave is staggered.

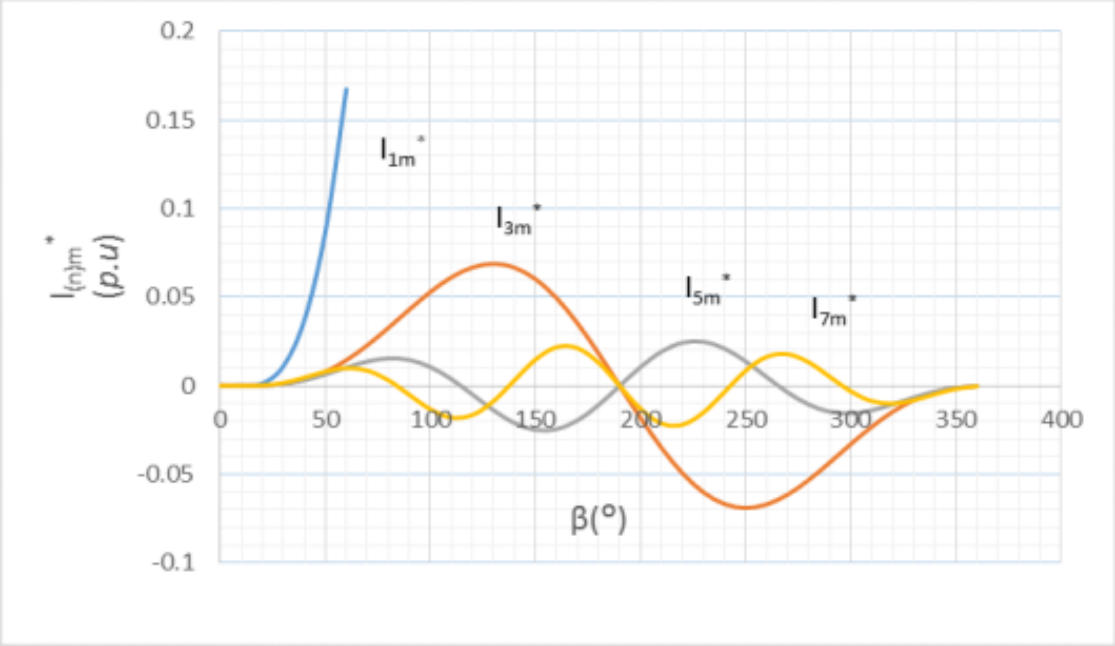

Fig. 9. Harmonic current distribution of MCR

2.6 Equivalent Circuit of MCR

Under rated sinusoidal power supply voltage, the relationship between the amplitude of the fundamental current and the change of the control angle α of MCR is called control characteristics [33]. To control the DC bias excitation current in the control winding, the thyristor control angle needs to be adjusted. So, by adjusting the thyristor angle, however, we can control the added DC bias excitation current to vary the unsaturated regions to change their degree of saturation. Therefore, the magnitude of MCR excitation current depends on the control angle. The smaller the angle, the greater the excitation current, and the magnetization intensity of the unsaturated region and the saturated region is enhanced at the same time. In this way, the reactance value can be continuously and smoothly adjusted. By increasing the DC excitation current, the speed of excitation can be improved, and the dynamic performance of MCR becomes better.

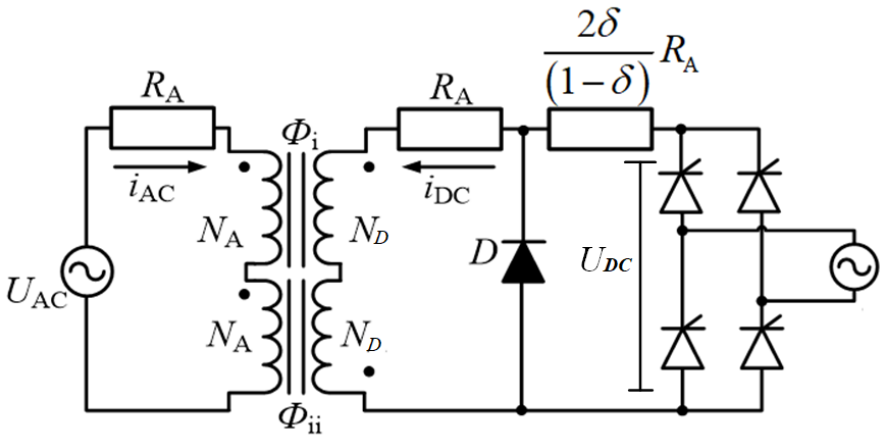

Fig. 10. MCR equivalent circuit

2.6.1 Relationship between control angle and magnetic saturation

The relationship between the control angle α and the saturation β can be obtained from the electromagnetic equation of MCR. From the equivalent circuit in *fig. 10*, if the internal resistance $\frac{2\delta}{1-\delta}R_A$ of the power supply is ignored, and the control angle of MCR is α, then the DC component of control voltage U_{DC} can be derived:

$$U_{DC} \approx \frac{1}{\pi}\int_{\alpha}^{\pi}\frac{\delta E_{max}\sin\omega t}{1-\delta}d\omega t = \frac{\delta E_{max}(1+\cos\alpha)}{\pi(1-\delta)} \tag{25}$$

Where R_A is the winding resistance, E_{max} is the maximum working voltage, α is the control angle of the thyristors and tap ratio $\delta = N_D/N_A$, is the factor which is determined by varying range of reactance in MCR and is usually in between 0.015 to 0.05. A suitable selection of δ can make the wave form better, harmonic components small of the reactor current [33].
By $U_{DC} = i_{DC}R_A$, considering the equations (22) and (25) are:

$$U_{DC} = \frac{\delta E_{max}(1+\cos\alpha)}{\pi(1-\delta)} = \frac{lB_{sat}R_A}{\pi\mu_0 N_A}\left(\sin\frac{\beta}{2} - \frac{\beta}{2}\cos\frac{\beta}{2}\right) \tag{26}$$

When the control angle $\alpha = 0$, the saturation $\beta = 2\pi$, substituting into Equation (26) is:

$$U_{DC\,max} = \frac{2\delta E_{max}}{\pi(1-\delta)} = \frac{lB_{sat}R_A}{\mu_0 N_A} \tag{27}$$

The relationship between the control angle α and the saturation β can be obtained by combining the above two Equations (26) and (27):

$$\cos\alpha = \frac{2}{\pi}\left(\sin\frac{\beta}{2} - \frac{\beta}{2}\cos\frac{\beta}{2}\right) - 1 \tag{28}$$

The relationship between control angle and magnetic saturation using Equation (28) can be obtained graphically as shown in *fig. 11.* The observation result is relatively intuitive. As a matter of engineering practice, the core magnetic saturation β can be obtained according to the fundamental reactive current value I_{1m}, and then the control angle of thyristor α can be calculated.

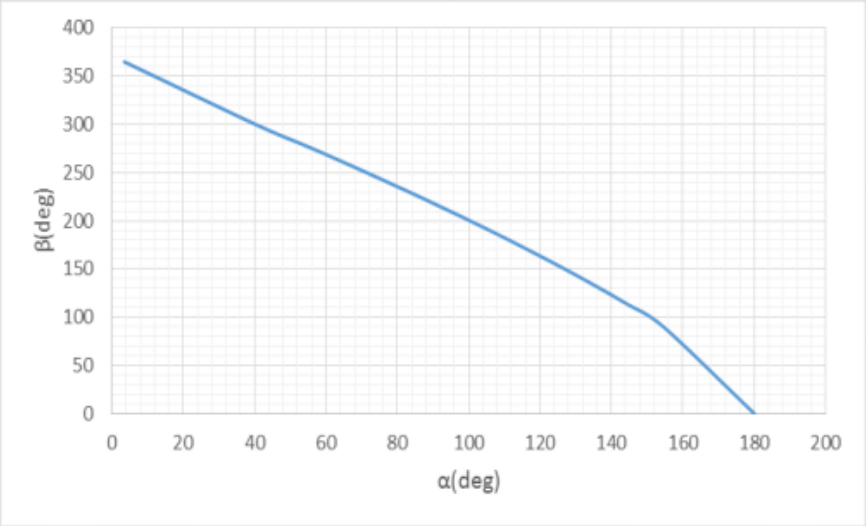

Fig. 11. Relationship between trigger conduction angle and magnetic saturation

2.6.2 Relationship between control angle and working current

When the control angle α of the thyristor changes, the core magnetic saturation degree changes, and then the inductance changes, thereby leading to the adjustment of the working current. The combination of Equations (24) and (28) can be used to obtain the relationship curve of the control angle α and I_{1m}^* of the thyristor in the magnetic controlled reactor, as shown in *fig. 12*. It can be seen that there is an obvious nonlinear between the current value and the control angle of the MCR, and it is an approximate cosine relationship.

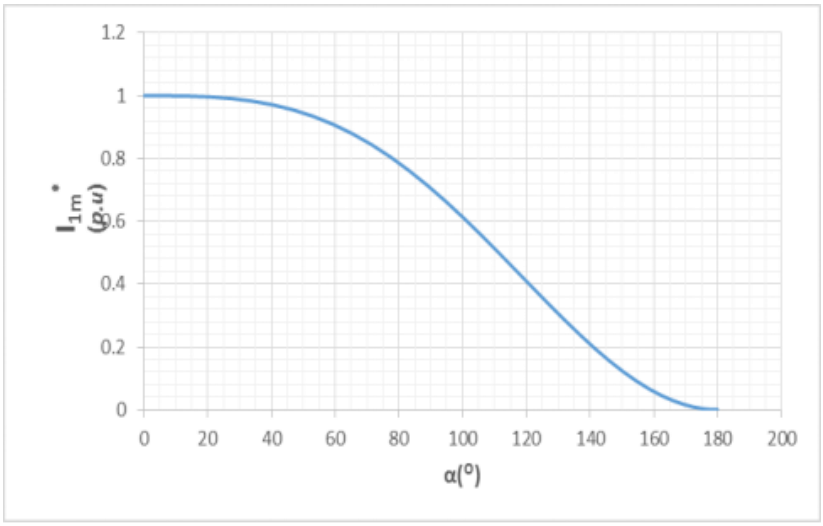

Fig. 12. Control characteristic curve of MCR

The average output voltage of the single-phase controlled rectifier bridge type shown in *fig .10* is:

$$U_{DC} = i_{DC}\left(R_A + \frac{2\delta}{1-\delta}R_A\right) \tag{29}$$

From Equations (27) and (29), at steady state, the average control current i_{DC} can be written as:

$$i_{DC} = \frac{\delta E_{max}(1+\cos\alpha)}{R_A\pi(1-\delta)} \tag{30}$$

Equating Equations (22) and (30) will yield:

$$U_{DC} = \frac{\delta E_{max}(1+\cos\alpha)}{R_A\pi(1-\delta)} = \frac{lB_{sat}R_A}{\pi\mu_0 N_A}\left(\sin\frac{\beta}{2} - \frac{\beta}{2}\cos\frac{\beta}{2}\right) \tag{31}$$

Therefore, control current amplitude of MCR when the control angle $\alpha = 0$, the saturation $\beta = 2\pi$:

$$i_{DC} = \frac{2\delta E_{max}}{R_A\pi(1+\delta)} \tag{32}$$

Combining Equations (23) and (31) is:

$$\frac{2\delta E_{max}}{R_A\pi(1-\delta)} = \frac{\pi lB_{sat}}{\mu_0 N_A} \tag{33}$$

Combining Equations (20) and (31), average working current is:

$$i_{ACn} = \frac{\delta E_{max}}{R_A\pi^2(1-\delta)}(\beta - \sin\beta) \tag{34}$$

Therefore, the working current amplitude of MCR when the control angle = 0 , and the saturation $\beta = 2\pi$:

$$i_{ACm} = \frac{2\delta E_{max}}{R_A\pi(1+\delta)} \tag{35}$$

It is evident from Equation (35) that the working current amplitude of the MCR does not depend only on the applied voltage, but also on the winding resistance and tap ratio. Combining Equations (21) and (35), we obtain:

$$\frac{2\delta E_{max}}{R_A\pi(1+\delta)} = \frac{lB_{sat}}{\mu_0 N_A} \quad (36)$$

Therefore, tap ratio δ can also be written as:

$$\delta = \frac{\pi l B_{sat} R_A}{(2\mu_0 N_A E_{max}) - \pi l B_{sat} R_A} (37) \quad (37)$$

This is to say that, when designing the MCR, the effective length of the magnetic circuit, the flux density of the core material, winding resistance, winding turns and rated voltage should satisfy Equation (37) else, there is a possibility that the magnetic controlled reactor will not function properly.

3. SIMULATION MODEL OF MCR AND RESULTS

3.1. Simulation

The dimensions and specifications of the magnetic controlled reactor used for the simulation are shown in Table 1. A 3D model shown in *fig. 13* is successfully designed using ANSYS. The 3D simulation calculation was adopted in this paper over the 2D because of its high accuracy of simulation results, howbeit it can take an appreciable time. The method of transient solution is also applied because it simultaneously has AC and DC sources. As shown in the simulation circuit (*fig. 14*), the excitation source uses voltage source in place of the current source, because the use of the current source will produce excessive harmonics in the working winding that will seriously affect the current waveform which is not consistent with the actual waveform. The magnetic field distribution, magnetic saturation degree, winding currents and control angle are mainly obtained with a varied control voltage of 0 V to 6.12 V. *fig. 15* to *fig. 24* show the simulation results of the MCR under the same control voltage. Furthermore, the numerical values are presented in Table 2.

Table 1. Dimensions and specifications of the MCR

Parameter		Numerical Value
Total Winding Turns	N_A	194
Control Winding Turns	N_D	6
Winding Resistance (mΩ)	R_A	320
Valve Cross-Section (mm^2)	A	1408
Valve Length (mm)	l	10
Magnetic flux density (T)	B_{sat}	1.8
DC Voltage (V)	U_{DC}	6.12
AC Voltage (V)	U_{AC}	220
Frequency (Hz)	f	50

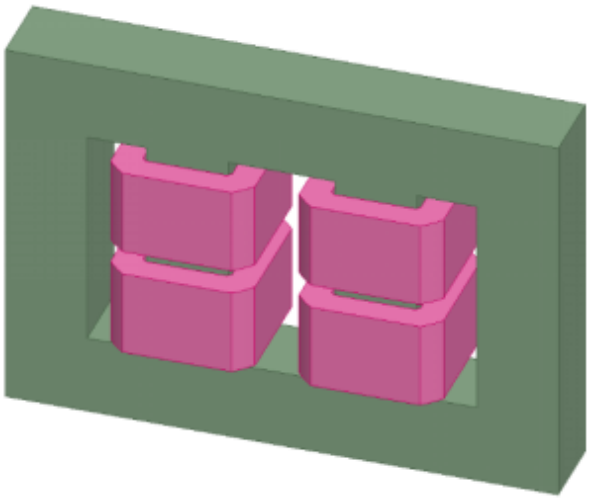

Fig. 13. 3D simulation model of MCR

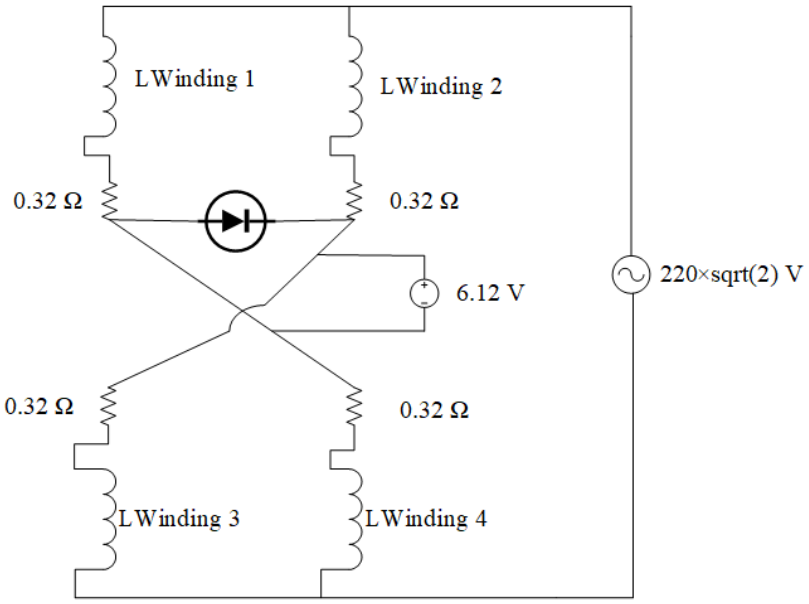

Fig. 14. Simulation circuit of MCR

3.2 Simulation results

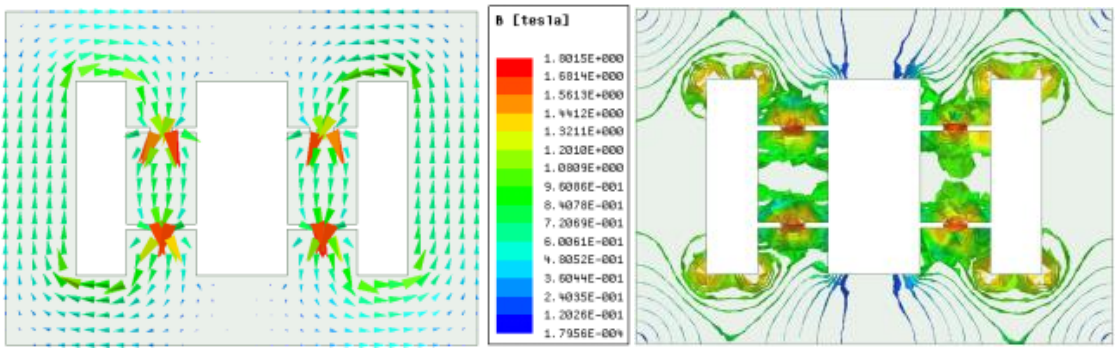

(a) Magnetic flux direction *(b) Magnetic flux density*

Fig. 15. Magnetic flux distribution of MCR in a cycle at t = 9.99s

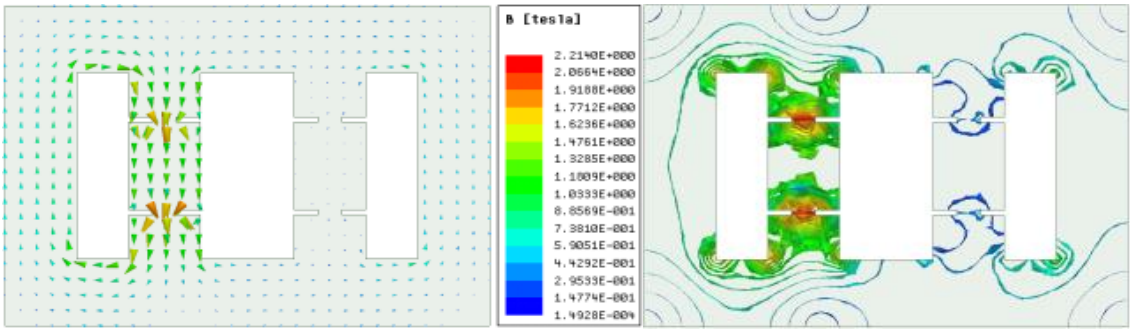

(a) Magnetic flux direction (b) Magnetic flux density

Fig. 16. Magnetic flux distribution of MCR in a cycle at t = 3.389s

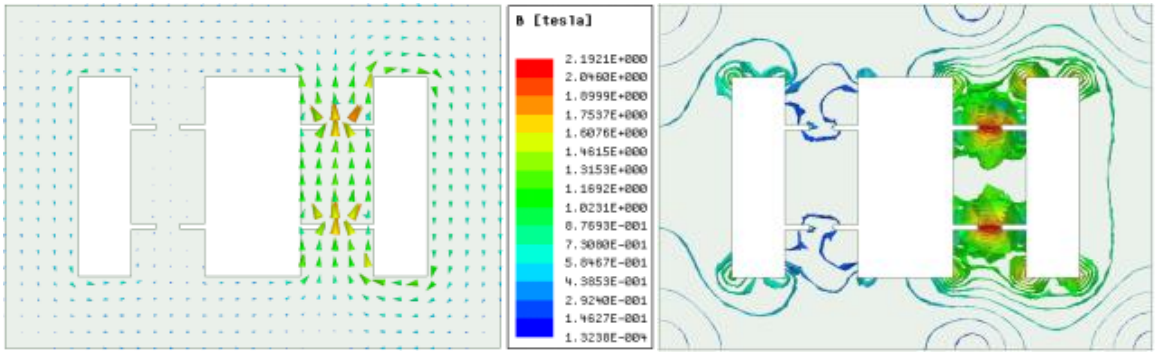

(a) Magnetic flux direction (b) Magnetic flux density

Fig. 17. Magnetic flux distribution of MCR in a cycle at t = 3.399s

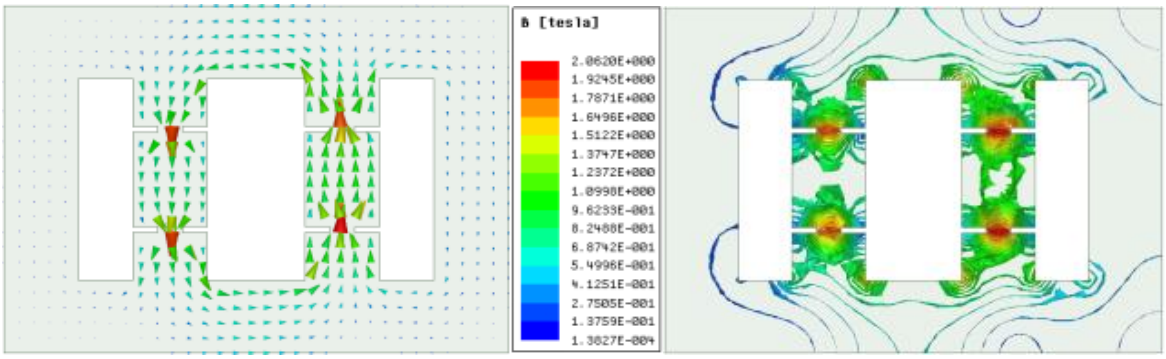

(a) Magnetic flux direction (b) Magnetic flux density

Fig. 18. Magnetic flux distribution of MCR in a cycle at t = 3.355s

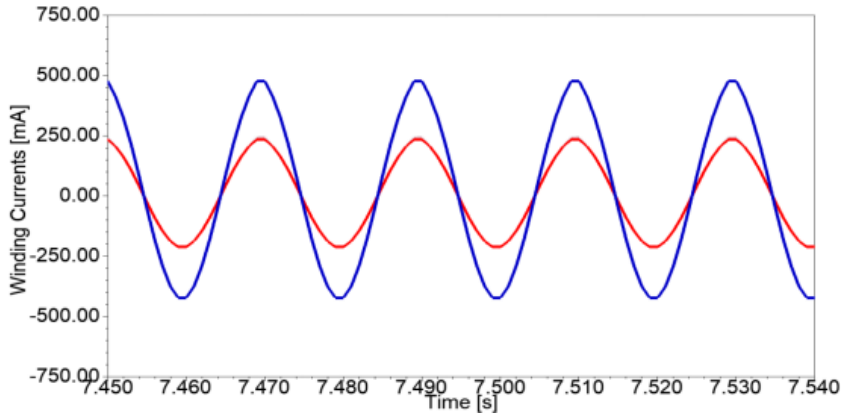

Fig. 19. Simulation results at $U_{DC} = 0\ V$ and Windings current waveform at steady state i_1, i_2 (red line) and i_{AC} (blue line)

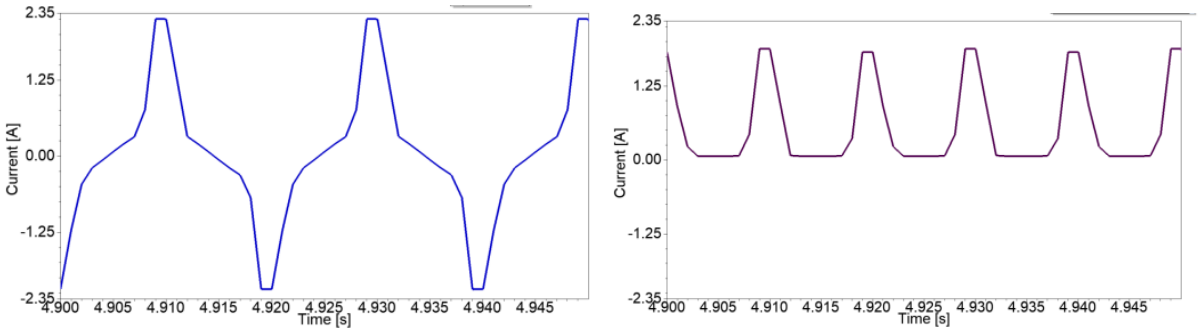

(a) Working current waveform at steady state (i_{AC}) *(b) Control current waveform at steady state (i_{DC})*

Fig. 20. Simulation results at U_{DC}=0.19 V

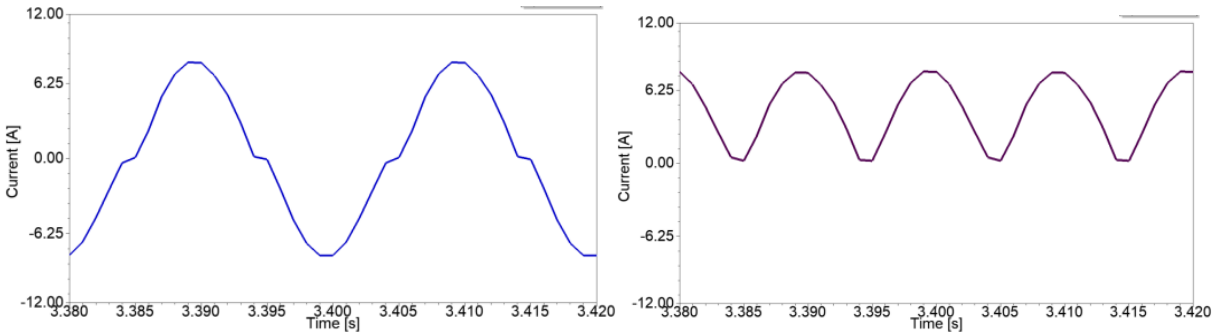

(a) Working current waveform at steady state (i_{AC}) *(b) Control current waveform at steady state (i_{DC})*

Fig. 21. Simulation results at U_{DC}=1.53 V

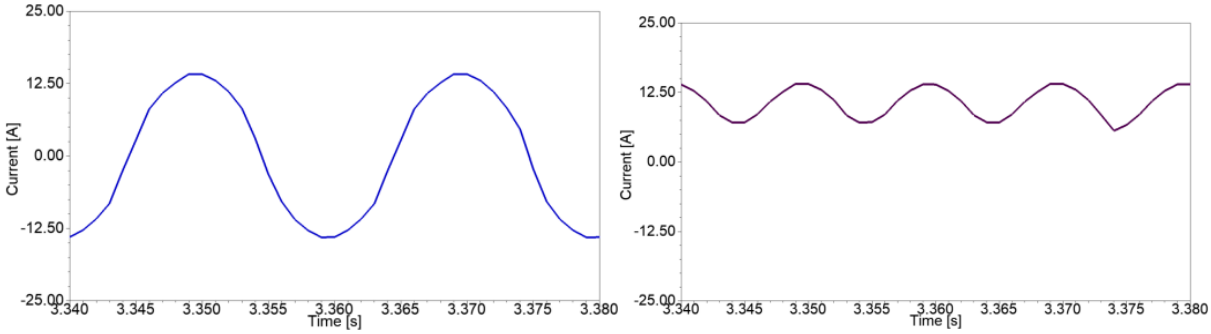

(a) Working current waveform at steady state (i_{AC}) *(b) Control current waveform at steady state (i_{DC})*

Fig. 22. Simulation results at U_{DC}=3.6 V

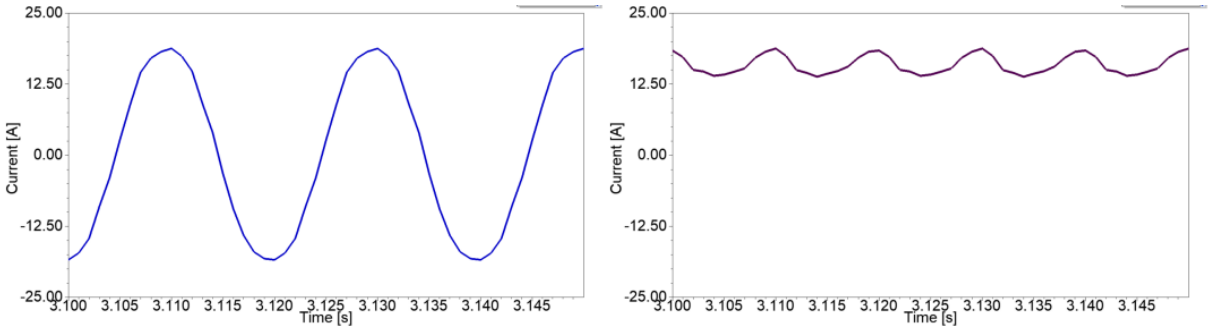

(a) Working current waveform at steady state (i_{AC}) *(b) Control current at steady state (i_{DC})*

Fig. 23. Simulation results at U_{DC}=5.41 V

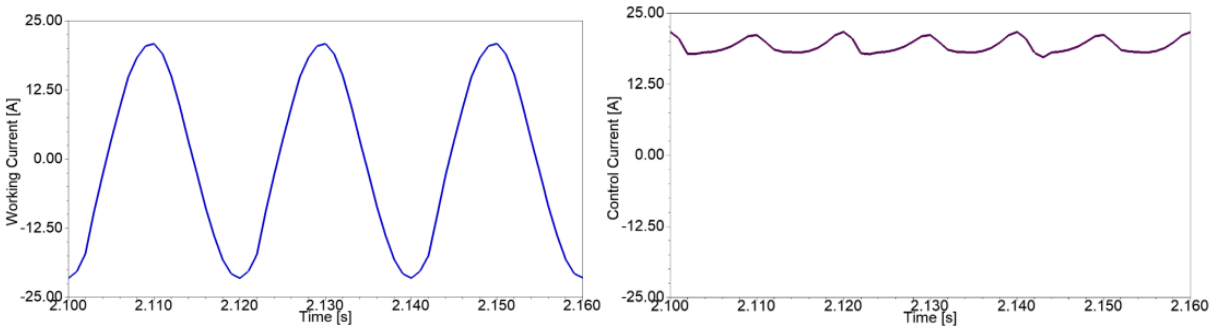

(a) Working current waveform at steady state (i_{AC}) (b) Control current waveform at steady state (i_{DC})

Fig. 24. Simulation results at U_{DC}=6.12 V

Table 2. Calculation results of the MCR model

U_{DC} (V)	i_{DC} (A)	i_{AC} (A)	α (0^O)	β (0^O)	B_{DC} (T)
0.000	0.00	0.00	180.00	0.00	0.00
0.19	0.54	1.04	160.00	76.48	0.09
0.72	2.11	3.76	140.00	123.10	0.23
1.53	4.51	7.38	120.00	163.52	0.38
2.53	7.45	11.06	100.00	200.68	0.52
3.60	10.58	14.17	80.00	235.60	0.65
4.59	13.52	16.33	60.00	269.00	0.75
5.41	15.92	17.52	40.00	300.00	0.82
5.94	17.49	17.97	20.00	331.00	0.87
6.12	18.03	18.03	0.00	360.00	0.88

Table 3. Simulation results of the MCR model

U_{DC} (V)	i_{DC} (A)	i_{AC} (A)	α (0^O)	β (0^O)	B_{DC} (T)
0.00	0.00	0.58	180.00	0.00	0.00
0.19	1.83	2.25	161.70	72.00	0.12
0.72	4.63	5.01	138.64	126.00	0.25
1.53	7.73	7.98	120.80	162.00	0.38
2.53	11.13	11.34	111.31	180.00	0.53
3.60	13.92	14.07	80.94	234.00	0.64
4.59	16.49	16.61	70.25	252.00	0.73
5.41	18.40	18.65	48.04	288.00	0.80
5.94	19.54	19.81	36.51	306.00	0.84
6.12	21.12	21.10	24.68	324.00	0.85

4. RESULTS. DISCUSSION

4.1. Analysis of MCR magnetic field distribution

The ultimate purpose of the magnetic controlled reactor with regards to regulating the grid voltage is achieved by adjusting the control winding current value to change the core magnetic saturation. Therefore, in order to obtain the accurate electromagnetic characteristics of the MCR, it is necessary to analyze the characteristics of each working state, and finally summarize if it is in conformity with electromagnetic characteristics of the MCR. The magnetic field distribution can effectively judge whether the simulation calculation result is accurate or not. In order to comprehensively analyze the magnetic field distribution of magnetic controlled reactor in the whole working interval, this paper mainly analyzes the four most critical stages of the magnetic field distribution of MCR.

Fig. 15 to *18* present magnetic field distribution inside the MCR core in a complete cycle during steady-state under different working conditions. The results of the simulation showed that magnetic flux distribution in the side yokes is uniform but nonuniform in the core limbs because of the magnetic valves in them. However, the introduction of these magnetic valves helps the MCR to function in the saturation region of the *B-H* magnetic characteristic curve.

It can be observed from *fig.15 (a)* and *(b)* that concentration of the magnetic flux is mostly in-between core limbs and side yokes, leaving the middle of the lower and upper yokes with least flux. In this instant, there is no DC excitation current in the control winding, so no DC flux is present and as a result, the core limbs mainly have AC flux produced by the working winding. Moreover, most of the AC flux circulates via the core limbs and side yokes, so the working winding reactive value is very large, allowing a very small amount of current to flow in the winding. In this case, the MCR is equivalent to an unloaded transformer, because both the core and magnetic valves are in an unsaturated state. The magnitude of magnetic flux density is almost 1.8T.

Fig. 16(a) and (b) show the influence of the superimposed magnetic field generated by the AC flux and the DC flux when 1.53 V was applied to the control winding. It can be observed that, in the first half cycle at time t =3.389s, the core limb I has more magnetic flux, followed by the left-side yoke, the right-side yoke and the core limb II respectively. This is because, at this moment, the AC voltage and current of the power supply are in positive and negative directions, and the DC excitation current is in the same direction with the AC on core limb I, which plays a role of enhancing magnetism, while the AC on core limb II is in opposite direction to the DC excitation current, which plays a role of demagnetization. Therefore, the magnetic valves on core limb I are largely in a saturated state, while the

magnetic valves on core limb II are still in an unsaturated state as expected. The magnetic flux density is obviously greater than 1.8T.

Fig. 17(a) and *(b)*, show the behavior of the magnetic flux in the second half cycle when the control voltage is still maintained at 1.53 V. It can be seen that at time t =3.399s, the magnetic flux on the core limb II is denser, followed by the right-side yoke, left-side yoke, and the magnetic flux on the core limb I is the least. This is because, over time, the AC reverses direction and follows the DC excitation current direction on core limb II, thereby, increasing the magnetization. At the same time, the AC on core limb I turns in the opposite direction to the DC excitation current, which leads to demagnetization. The magnitude of magnetic flux density is almost 2.1921T.

Fig.18 (a) and *(b)*, demonstrate the behavior of the magnetic flux when the control voltage is set to the half of the rated value, 3.6 V. It is obvious that at time t=3.355s, most of the magnetic flux is circulating between core limb I and core limb II. In this instant, there is no AC excitation current in the working winding, so no AC flux is present and as a result, most of the DC flux flow through core limb I and core limb II, and a small amount of DC flux flows through the side yokes. Thus, conforming to the principle of MCR.

4.2. Analysis of MCR control characteristics

The control characteristic refers to the correspondence between the working winding current and the control DC bias excitation of the magnetic controlled reactor.

Through the simulation, working winding current values of the MCR under different control DC bias excitations can be obtained.

The comparison between calculation and simulation of the MCR control characteristics is shown in Table 1 and 2 respectively. When the control angles of the calculation and simulation are at 0^0, the working winding current is at a maximum, and when both are at 180^0 the working winding current is at a minimum. This means that, in the range between 0^0 and 180^0, the output capacity of MCR can be smoothly regulated. It can also be seen from the same tables that when the control voltage value is 0 V, corresponding working current value with respect to the calculation is also 0.00 A, but the simulation current value is 0.58 A. This is because the calculation method is modeled based on an ideal situation while the simulation model adopted the actual working situation.

So, the simulation current value represents the magnetization current of the MCR under no-load condition. Again, it can be seen from *fig. 25* that the simulation current curve is slightly larger than that of the calculation curve. This is due to the small difference in the *B-H* curve data. Nevertheless, there is a good correlation among them and in line with the principle of MCR.

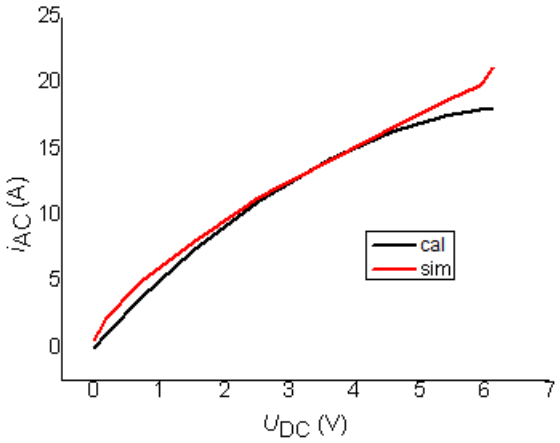

Fig. 25. Control characteristic curve of MCR

4.3. Analysis of MCR harmonics and time difference

It can be seen from *fig. 20* that when control winding current value is relatively small, the working winding current distortion is relatively large and the harmonic content is relatively high. As the control winding current increases, the working winding current waveform tends to be smooth with positive and cosine function waveform as shown in *fig. 21* to *24*. This is caused by the nonlinear magnetic properties of the ferromagnetic material. When the control current is relatively low, the MCR core works at the inflection point of the B-H magnetic characteristic curve, and the working winding current distortion rate is relatively high. It can also be seen that the steady-state period in *fig. 19* is the longest, followed by *fig.20, 21* to *24* respectively. This is possible because when the control excitation is low, the core operates below the inflection point of the B-H magnetic characteristic curve. But when control current starts to increase to a higher value, the time during which the core operates at the inflection point of the magnetic characteristic curve is decreasing continuously. At this juncture, the time for operating in the saturation state is due, and the distortion rate of the winding current waveform is decreased and appeared as a sine wave. This implies that for MCR working current to reach steady-state, harmonics and time vary in proportion to the control DC bias excitation.

4.4. Calculation and simulation of magnetic saturation degree results

The comparison between calculation and simulation of the MCR magnetic saturation degree is shown in *fig. 26*, it can be seen that the magnetic saturation curve measured by simulation is in good agreement with that of the calculation values. With the increase of control voltage from 2 V, the magnetic saturation degree obtained from calculation tends to be a little higher than that measured by the simulation. This is because assumptions were made in the calculation in arriving at idealizing the magnetic characteristic curve, while the simulation results exhibit the real working performance of the magnetic controlled reactor. However, there is a good correlation among them and in line with the principle of MCR.

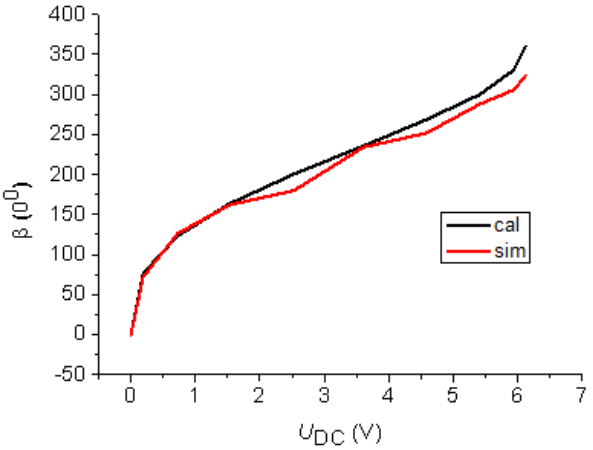

Fig. 26. Magnetic saturation degree of MCR

4.5. Analysis of MCR Inductance

The impedance of the MCR is $= U_{AC}/I_{AC}$. In reference to the data given and results of the simulation, reactance X_{L} is far bigger than winding resistance R_{A}, therefore, Z can be considered as X_{L}. The relationship between X_{L} and L is$X_L = \omega L = 2\pi f L$. The control DC bias excitation is varied in the range 0 V to 6.12 V, in which the change of inductance values is obtained as shown in *fig. 27*. It can be observed from the *fig.* that with the increase of control voltage the saturation degree of the core increases and the reactance value of the winding decreases. This is because the inductance of a coil is directly proportional to the permeability of its core material. When the voltage level of control winding increases to a certain extent, the core is completely saturated and the winding reactance value tends to be constant. It can also be seen from the same *fig.* that the inductance curve of the simulation is steeper than that of the calculation curve which truly reflects the difference in the *B-H* curve data. It is evidentiary from *fig. 27* that the AC inductance value equivalent of the working winding can be smoothly regulated with the change of the control DC bias excitation to achieve the purpose of adjusting the output capacity of the MCR. The simulation results are consistent with the theoretical analysis.

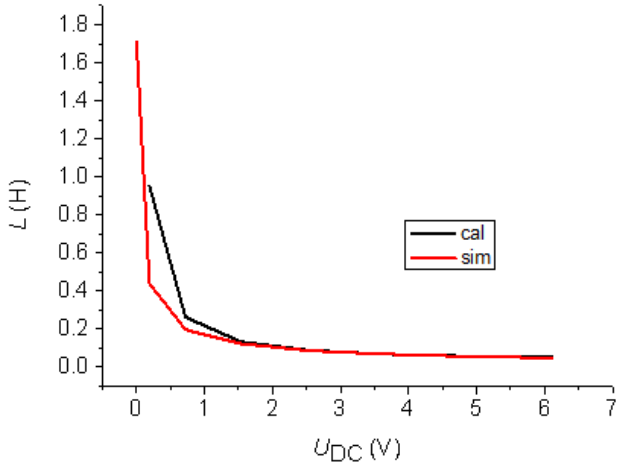

Fig. 27. Inductance curve of MCR

5. CONCLUSIONS

This paper mainly discussed the theoretical basis, structure, working principle and design model of a magnetic controlled reactor. The engineering simulation tool ANSYS Maxwell was used to establish the MCR model and calculate the magnetic field distribution and working characteristics.

Comparison of the calculation and simulation of the MCR model produced encouraging results under no-load to full-load working conditions. The results show that MCR alternately magnetize and demagnetize in between the left and right core limbs in one cycle which means that, the magnetic valves on both sides are alternately saturated and unsaturated in the cycle. At the same time, it has been verified that no matter how deep the magnetic valves saturate, no saturation phenomenon will occur in the core with large cross-section within the entire adjustable range. Therefore, the whole capacity of the MCR is smoothly adjusted by changing only the magnetic saturation degree of the magnetic valve core. The magnetic controlled reactor has approximately linear control characteristic curve, but when the current value of the control winding is increased to the rated value, the slope of the curve increases slowly and finally tends to a stable value. Through simulation and comparison, it is found that a small difference in the magnetic saturation characteristic curve can significantly affect the performance of MCR.

This research has given impetus to the understanding of MCR under actual operating condition. In addition, it has provided a vital basis for further research on the performance design of MCR.

REFERENCES

[1] T. Ben, L. Hou, L. Chen, P. Zhang, Y. Kong, R. Yan, *The Vector Electromagnetic Vibration of Magnetically Controlled Reactor Considering the Vector Hysteretic Magnetostriction Effect,* IEEE Transactions on Magnetics, vol. 58, 2022.

[2] A. V. R. Manuel, M. L. J. Vanessa, D. L. Cesar, *The Magnetically Controlled Reactor Applied to Peruvian Power System,* IEEE Latin America Transactions, vol. 18, pp. 1785 – 1792, 2020.

[3] A. V. Golovina, O. O. Pereslytskikh, A. S. Rodionova and A. N. Belyaev, *Analysis of Operation and Stability of Ultra-long Transmission Lines with Controlled Shunt Compensation,* in IEEE Conference of Russian Young Researchers in Electrical and Electronic Engineering (EIConRus), Russian, 2019.

[4] X. Gu, Y. Wu, T. Qu, W. Xu and D. Liu, *The simulation of the controllable reactor and it's application in Ultra High VoltageTransmission Lines,* in IEEE, Beijing, China, 2011.

[5] Z. Keju, W. Xin, B. He, *Research on Reactive Power Compensation Based on Magnetic*

Saturation Controllable Reactor, IEEE Access, vol 10, pp. 31377 – 31384, 2022.

[6] T. Ben, F. Chen, L. Chen, A. A. Siada, L. B. Jing, R. Yan, *Electromagnetic Vibration Analysis of Magnetically Controlled Reactor Considering DC Magnetic Flux*, IEEE Access, vol 8, pp. 170271 – 170280, 2020.

[7] L. L. S. D. Y. L. Wenye Liu, *Overview of Power Controllable Reactor Technology*, ELSEVIER Energy Procedia, vol. 17, no. Pt. A, pp. 483-491, 2012.

[8] A. Feshin and V. S. Chudny, *Transient stability of oil-field isolated power systems with magnetically controlled shunt reactors*, in 2016 IEEE NW Russia Young Researchers in Electrical and Electronic Engineering Conference (EIConRusNW), St. Petersburg, Russia, 2016.

[9] B. V. Oleksyuk, V. N. Tulsky and S. Palis, *Magnetically Controlled Shunt Reactors as Sources of Current and Voltage Harmonics*, IEEE Transactions on Power Delivery, vol. 33, no. 4, pp. 1818-1824, August 2018.

[10] E. Freedlander, *Static network stabilization—Recent progress in reactive power control*, GEC J, vol. 33, no. 2, pp. 58-65, 1966.

[11] H. Becker, *Die steuerbare Drosselspule. Ein statischer Phasenschieber zur Kompensation von Blindlaststosen*, ETZ-B23, vol. H.12, pp. 293-295, 1971.

[12] A. Bryantsev, *Magnetically Controlled Electrical Reactors*, Collection of Articles, 2012.

[13] Z. Shi-shuo, Y. Zhong-dong and P. Li, *Research of Magnetically Controlled Reactor*, in Proceedings of The 7th International Power Electronics and Motion Control Conference, Harbin, China, 2012.

[14] X. Chen, B. Chen and C. Tian, *A Novel Control Method for Magnetic-Valve Controllable Reactor*, in 2009 First International Workshop on Database Technology and Applications, IEEE, Wuhan, Hubei, China, 2009.

[15] J. Pei, T. Mingxing and Z. Huiying, *Winding Design and Control Method of A Novel Quick Response Magnetic-valve Controllable Reactor*, in 2019 22nd International Conference on Electrical Machines and Systems (ICEMS, Harbin, China, China, 2019.

[16] T. Mingxing, L. Qingfu and W. Shuhong, *An Equivalent Physical Model and a Mathematical Model of the MCR*, Transactions of China Electrotechnical Society, no. TM471, pp. 18-21+35, 08 2002.

[17] H. Zhang, M. Tian and P. Jing, *Effect of Magnetization Curve Model and Winding Connection Mode on Magnetically Saturated Controllable Reactor Based on ANSYS*, in 2019 22nd International Conference on Electrical Machines and Systems (ICEMS), Harbin, China, China, 2019.

[18] M. A. Khan, Z. Tao and L. Xiaoxiao, *Analysis of Faults and Protection Schemes for Magnetically Controlled Shunt Reactor*, in 2018 2nd IEEE Conference on Energy Internet and Energy System Integration (EI2), Beijing, China, 2018.

[19] M. Tümay, T. Demirdelen, S. Bal, R. İ. Kayaalp, B. Doğru and M. Aksoy, *A review of magnetically controlled shunt reactor for power quality improvement with renewable energy applications*, Renewable and Sustainable Energy Reviews, pp. 215-228, 12 04 2017.

[20] J. Dai, W. J, W. L, C. D, H. X and Z. W, *Reactive Power-Voltage Integrated Control Method Based on MCR*, in Proceedings of the 11th International Conference on Control Automation Robotics & Vision (ICARCV), 2010.

[21] Y. Po, Y. Zhongdong, C. Ruochen and K. Ning, *Analysis of Reactor Magnetic Circuit Based on ANSYS Command Flow*, Trans Tech Publications, Switzerland, Vols. 383-390, pp. 2256-2261, 22 11 2011.

[22] X. Cai and Y. Gao, Principle, *design and application of controllable saturable reactor*, Beijing: China Water Conservancy and Hydropower Press, 2008, pp. 3-5.

[23] F. Fiorillo, G. Bertotti, C. Appino and M. Pasquale, *soft magnetic materials*, J.Webster (ed.), Wiley Encyclopedia of Electrical and Electronics Engineering, pp. 1-42, 2016.

[24] Z. Lixia, *Mathematical analysis and Simulation of magnetic valve controllable reactor [Master 's Thesis]*, in Mathematical analysis and Simulation of magnetic valve controllable reactor [Master 's Thesis] , Beijing, North China Electric Power University, 2006, pp. 14-30.

[25] H. K. Chisepo, C. Guant and L. D. Borrill, *Measurements and FEM analysis of GIC/DC effects on transformer*, in IEEE PowerTech Milano, Milano, Italy, 2019.

[26] H. K. Chisepo, L. D. Borrill and C. T. Gaunt, *Measurements show need for transformer core joint details in finite element modelling of GIC and dc effects*, Compel International Journal of Computation and Mathematics in Electrical and Electronic Engineering, vol. 37, no. 3, pp. 1011-1028, 2018.

[27] T. Mingxing, Z. Qianru, Y. Jianning and L. Yibin, *Simulation and Analysis of Electromagnetic Transient Characteristics of Controllable Reactor of Transformer Type*, WSEAS Transactions on Circuits and Systems, vol. 14, 2015.

[28] C. Xuxuan, C. Baichao and T. Cuihua, *Two-stage saturable magnetically controlled reactor harmonic suppression optimization technique*,, Electric power automation equipment, vol. 31, no. 5, pp. 71-74, 2011.

[29] S. A. Darko, M. X. Tian and H. Y. Zhang, *Research on Magnetic-Valve Controllable Reactor Based on ANSYS*, International Journal of Recent Technology and Engineering (IJRTE), vol. 8, no. 3, pp. 671-675, September 2019.

[30] C. Baicao, T*heory and application of new controllable saturable reactor [M]*, Wuhan: Wuhan University of water conservancy and electric power press, 1999, pp. 45-73.

[31] W. Jun, Z. Hao, C. Baichao, L. WenHua, Y. ZhangTing, Z. ShengLong, Y. jiaxin and T. CuiHua, *Winding Loss Mechanism Analysis of Magnetic Valve Controlled Reactor*, International Journal of Control and Automation, vol. 9, no. 3, pp. 51-60, 2016.

[32] L. Yakun, *Research on Optimization of Dynamic Characteristics of Magnetic Control Reactor [D]*, Beijing : Beijing Jiaotong University, 2016, pp. 13-15.

[33] R. N. Jenipher and K. V. Chandrakala, *Magnetically controlled reactor based harmonic and voltage profile improvement in long transmission lines*, in 2017 Innovations in Power and Advanced Computing Technologies (i-PACT), IEEE, Vellore, India, 2017.

INSTRUCTIONS FOR AUTHORS

Name **SURNAME**[1], Name **SURNAME**[2], **...**

[1] *Affiliation of 1st author,* [2] *Affiliation of 2nd author, ...*

Email of 1st author, Email of 2nd author, ...(it is compulsory only for the first author)

Keywords: List 3-4 keywords *(aligned to the left, 10 pt. bold, separated by commas; please choose keywords from IEEE Approved Indexing Keyword List)*

Abstract: *Abstract of max. 200 words, justify, 10 pt. italic.*

1. INTRODUCTION

The paper must be written in English. It shall contain at least the following chapters: introduction, research course (mathematical algorithm); method used; results and conclusions, references.

1.1. Fonts

Use DIN A4 Format (297 x 210 mm) MSWord format. Margins: top, bottom, left and right 2.5 mm each. The text should be written on one side of the page only. Use Times New Roman fonts, line spacing 1.3. The font formats are: paper title: 14 pt, bold, italic, capital letters, author's name(s): 12 pt, regular for name and 12 pt., bold, for surname; Affiliation: 11 pt., italic; key words: 10 pt., bold; Abstract: 10 pt., italic, word Abstract in 10 pt., bold; chapter titles (do not use automatic numbering): 12 pt., bold, capital letters; subtitles: 12 pt., bold, lower case letters; subsubtitles: 12 pt., italic, lower case letters; body text: 12 pt., regular; tables and figures caption: 11 pt.; italic; references: author 11 pt.; regular, title 11 pt. italic, year, pages, ... in regular.

1.1.1. Number of pages

The number of pages is not restricted.

2. FIGURES AND TABLES

Figures have to be made in high quality, which is suitable for reproduction and printing. Don't include photos or color prints if there are not clearly intelligible in gray scale option. Place figures and tables at the top or bottom of a page wherever possible, as close as possible to the first reference to them in the paper. In text, use either *fig. 1* or *figure 1* when necessarily.

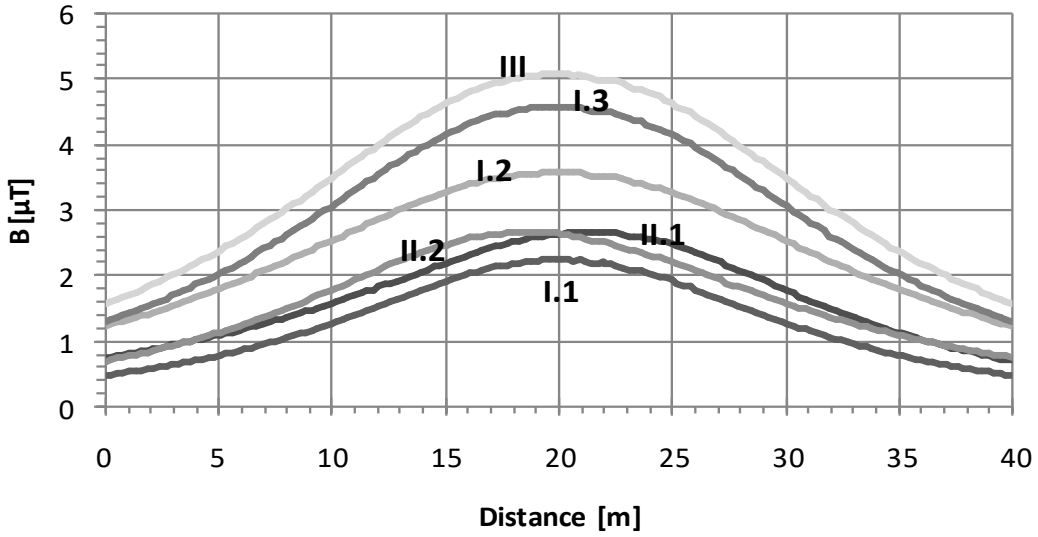

Fig. 1. Magnetic flux density at 1 m above the ground

Table 1. Transposing principle

	Circuit											
	1	*2*	*1*	*2*	*1*	*2*	*1*	*2*	*1*	*2*	***1***	***2***
1/3 line length	*R*	*T*	***R***	***R***	*R*	*S*	*R*	*T*	*R*	*S*	***R***	***R***
	S	***S***	*S*	*T*	*S*	*R*	*S*	*R*	*S*	*T*	***S***	***S***
	T	*R*	*T*	*S*	***T***	***T***	*T*	*S*	*T*	*R*	***T***	***T***
1/3 line length	*T*	*S*	***T***	***T***	*T*	*R*	*T*	*S*	*T*	*R*	***T***	***T***
	R	***R***	*R*	*S*	*R*	*T*	*R*	*T*	*R*	*S*	***R***	***R***
	S	*T*	*S*	*R*	***S***	***S***	*S*	*R*	*S*	*T*	***S***	***S***
1/3 line length	*S*	*R*	***S***	***S***	*S*	*T*	*S*	*R*	*S*	*T*	***S***	***S***
	T	***T***	*T*	*S*	*T*	*S*	*T*	*S*	*T*	*R*	***T***	***T***
	R	*S*	*R*	*T*	***R***	***R***	*R*	*T*	*R*	*S*	***R***	***R***
Name	***I.1***		***I.2***		***I.3***		***II.1***		***II.2***		***III***	

3. EQUATIONS

Equations are centered on page and are numbered in round parentheses, flush to right margin.

$$a = b + c \tag{1}$$

Between equations, not interfered by text, there is only one empty line:

$$a = b + c \tag{2}$$

$$a = b + c \tag{3}$$

In text respect the following rules: all variables are italic, constants are regular; the references are cited in the text between right parentheses [1], the list of references has to be arranged in order of citation.

REFERENCES

[1] International Commission on Non-ionizing Radiation Protection, *Guidelines for limiting exposure to time-varying electric, magnetic and electromagnetic fields (Up to 300 GHz)*, Health Physics, vol. 74, no. 1, pp. 494-522, 1998.

[2] A. Marincu, M. Greconici, *The electromagnetic field around a high voltage 110 KV electrical overhead lines and the influence on the biological systems*, Proceedings of the 5th International Power Systems Conference, pp. 357-362, Timisoara, Romania, 2003.

[3] J. He, R. Zeng, B. Zhang, Methodology and Technology for Power System Grounding, Wiley-IEEE Press, Singapore, 2012.

9th International Conference

INNOVATIVE IDEAS IN SCIENCE 2023

Banja Luka, 21-22th September 2023, Bosnia and Herzegovina

Selected papers by the IIS Scientific Committee

Organizer:

Technical University of Cluj Napoca, Romania
Independent University Banja Luka, Bosnia and Herzegovina
University of Applied Sciences Kempten, Germany

Sponsored by:

Academic Organization for Research, Innovation
and Professional Development

IIS CONFERENCE COORDINATOR

Cristian BARZ, Technical University of Cluj-Napoca, Romania
Vesna RODIC, Independent University Banja Luka, Bosnia and Herzegovina

IIS ORGANIZING COMMITTEE

Zoltan ERDEI, Technical University of Cluj-Napoca, Romania
Claudiu LUNG, Technical University of Cluj-Napoca, Romania
Mircea HORGOȘ, Technical University of Cluj-Napoca, Romania
Mirela ILIA, SC FDEE Electrica Distributie Transilvania Nord SA, Romania
Olivian CHIVER, Technical University of Cluj-Napoca, Romania
Ramona DEMARCSEK, Tehnical University of Cluj Napoca, Romania
Domide GHERASIM, Technical University of Cluj-Napoca, Romania
Patricia TRIF, Technical University of Cluj-Napoca, Romania
Larisa POP, Technical University of Cluj-Napoca, Romania
Goran KALINIĆ, Independent University Banja Luka, Bosnia and Herzegovina
Dragana POPOVIC, Independent University Banja Luka, Bosnia and Herzegovina
Radmila ČOKORILO Independent University Banja Luka, Bosnia and Herzegovina
Kristina KUZMANOVIĆ, Independent University Banja Luka, Bosnia and Herzegovina
Luka SAVIĆ, Independent University Banja Luka, Bosnia and Herzegovina
Mladen BUBONJIĆ, Independent University Banja Luka, Bosnia and Herzegovina
Kristina KAJIŠ, Independent University Banja Luka, Bosnia and Herzegovina
David MILJANOVIČ, Independent University Banja Luka, Bosnia and Herzegovina
Vladimir GAČANOVIČ, Independent University Banja Luka, Bosnia and Herzegovina

IIS SCIENTIFIC COMMITTEE COORDINATOR

Ostoja BARAŠIN, Independent University Banja Luka, Bosnia and Herzegovina
Vasile TOPA, Technical University of Cluj-Napoca, Romania
Ludovic Dan LEMLE, "Politehnica" University of Timisoara, Romania

IIS SCIENTIFIC COMMITTEE

Petrică POP SITAR, Technical University of Cluj-Napoca, Romania
Gabor SZIEBIG, The Arctic University of Norway, Norway
Luigi VLĂDĂREANU, Romanian Academy - Institute of Solid Mechanics, Romania
Doina PISLA, Technical University of Cluj-Napoca, Romania
Branko BLANUSA, University of Banja Luka, Bosnia and Herzegovina
Silviu Dan MANDRU, Technical University of Cluj-Napoca, Romania

Nicolae POP, Romanian Academy - Institute of Solid Mechanics, Romania
Radu Adrian TIRNOVAN, Technical University of Cluj-Napoca, Romania
Parimal ACHARJEE, National Institute of Technology Durgapur, India
Lesya SHKITSA, Ivano-Frankivsk National Technical University of Oil and Gas, Ukraine
Dorin Dumitru LUCACHE, "Gheorghe Asachi" Technical University of Iasi, Romania
Predrag Miodrag ŽIVKOVIĆ, University of Niš, Serbia
Vasile NĂSUI, Technical University of Cluj-Napoca, Romania
Rolf JUNG, University of Applied Sciences Kempten, Germany
Marian POBORONIUC, "Gheorghe Asachi" Technical University of Iasi, Romania
Nicolae UNGUREANU, Technical University of Cluj-Napoca, Romania
Sorin DEACONU, "Politehnica" University of Timisoara, Romania
Mihai BĂNICĂ, Technical University of Cluj-Napoca, Romania
Mihai ALBU, "Gheorghe Asachi" Technical University of Iasi, Romania
Mirjana STOJANOVIC-TRIVANOVIC, Independence University Banja Luka, Bosnia and Herzegovina
Cristiana ISTRATE, "Gheorghe Asachi" Technical University of Iasi, Romania
Marius Calin BENEA, “Politehnica” University of Timişoara, Romania
Marius PISLARU, "Gheorghe Asachi" Technical University of Iasi, Romania
Cristian BARZ, Technical University of Cluj-Napoca, Romania
Tihomir Savo LATINOVIC, University in Banja Luka, Bosnia and Herzegovina
Miorita UNGUREANU, Technical University of Cluj-Napoca, Romania
Nikola VOJVODIĆ, University of Business Engineering and Management, Banja Luka, Bosnia and Herzegovina
Anamaria DĂSCĂLESCU, Technical University of Cluj-Napoca, Romania
Przemysław SYREK, AGH University of Science and Technology, Krakow, Poland
Ružica ĐERVIDA, Independent University Banja Luka, Bosnia and Herzegovina
Branka MARKOVIĆ, Independent University Banja Luka, Bosnia and Herzegovina
Marinko MARKIĆ, Independent University Banja Luka, Bosnia and Herzegovina
Marijian MIJATOVIĆ, Independent University Banja Luka, Bosnia and Herzegovina
Saša ČEKRLIJA, Independent University Banja Luka, Bosnia and Herzegovina
Mirko SAJIĆ, Independent University Banja Luka, Bosnia and Herzegovina
Srđan LJUBOJEVIĆ, Independent University Banja Luka, Bosnia and Herzegovina
Borka VUKAJLOVIĆ, Independent University Banja Luka, Bosnia and Herzegovina
Mladen BUBONJIĆ, Independent University Banja Luka, Bosnia and Herzegovina
Dragana PRERADOVIĆ, University of Banja Luka, Bosnia and Herzegovina
Dragana DIMITRIJEVIĆ, University of Niš, Serbia
Vesna RODIC, Independent University Banja Luka, Bosnia and Herzegovina
Mihaela POPA, "Politehnica" University of Timisoara, Romania

SIMULATION-BASED APPLICATION OF SAFETY OF THE INTENDED FUNCTIONALITY TO MITIGATE FORESEEABLE MISUSE IN AUTOMATED DRIVING SYSTEMS

Milin **PATEL**[1], Rolf **JUNG**[2]

[1] *Institute for Advanced Driver Assistance Systems and Connected Mobility, Germany,* [2]*Kempten University of Applied Sciences, Germany*

milin.patel@hs-kempten.de , rolf.jung@hs-kempten.de

Keywords: ADS, FM, Simulation-based testing, SOTIF

Abstract*: The development of Automated Driving Systems (ADS) has the potential to revolutionize the transportation industry, but it also presents significant safety challenges. One of the key challenges is ensuring that the ADS is safe in the event of Foreseeable Misuse (FM) by the human driver. To address this challenge, a case study on simulation-based testing to mitigate FM by the driver using the driving simulator is presented. FM by the human driver refers to potential driving scenarios where the driver misinterprets the intended functionality of ADS, leading to hazardous behavior. Safety of the Intended Functionality (SOTIF) focuses on ensuring the absence of unreasonable risk resulting from hazardous behaviors related to functional insufficiencies caused by FM and performance limitations of sensors and machine learning-based algorithms for ADS. The simulation-based application of SOTIF to mitigate FM in ADS entails determining potential misuse scenarios, conducting simulation-based testing, and evaluating the effectiveness of measures dedicated to preventing or mitigating FM. The major contribution includes defining (i) test requirements for performing simulation-based testing of a potential misuse scenario, (ii) evaluation criteria in accordance with SOTIF requirements for implementing measures dedicated to preventing or mitigating FM, and (iii) approach to evaluate the effectiveness of the measures dedicated to preventing or mitigating FM. In conclusion, an exemplary case study incorporating driver-vehicle interface and driver interactions with ADS forming the basis for understanding the factors and causes contributing to FM is investigated. Furthermore, the test procedure for evaluating the effectiveness of the measures dedicated to preventing or mitigating FM by the driver is developed in this work.*

1. INTRODUCTION

Automated Driving System (ADS) is a complex system that is designed to perform some or all of the driving tasks that are traditionally performed by a human driver [1]. This includes acceleration, braking, steering, and navigation with the goal of improving road safety and reducing driver workload. Safety is crucial in ADS due to its reliance on perception sensors and complex algorithms for situational awareness. Malfunctions or failures in these systems can have hazardous consequences for vehicle occupants and other road users.

Foreseeable Misuse (FM) refers to the potential for human drivers to intentionally or unintentionally misuse ADS, leading to unsafe situations. This can occur when drivers do not fully understand the capabilities and limitations of the ADS, or when they engage in behaviors that are not consistent with the intended use of the system. FM can also occur when drivers fail to take over control of the vehicle when required, such as in situations where the system is unable to operate safely, or when the driver is required to take over control due to a system malfunction [2].

The safety challenges associated with FM are significant because they can lead to serious accidents and injuries. To address these challenges, it is important to develop and implement effective mitigation measures that can prevent or reduce the risk of FM. This requires a comprehensive evaluation of the ADS that considers a wide range of driving scenarios and human factors, including the driver's understanding of the system's capabilities and limitations, their responsibilities, and their ability to comprehend and respond to warnings and alerts.

To illustrate the significance of addressing FM, consider the fatal accident involving a Tesla Model S in 2016. The driver was using the Autopilot system, which is intended to assist with steering, braking, and acceleration. However, the driver was not paying attention to the road and did not take over control of the vehicle when required. As a result, the autopilot system failed to detect a truck that was crossing the road, and the vehicle collided with the truck, resulting in the driver's death [3].

ISO 21448[2] is the standard for Safety of the Intended Functionality (SOTIF) that provides guidance to identify and analyze potential hazards and risks associated with the intended functionality of an ADS that may arise due to foreseeable misuse by human drivers. In the following, the term ‘system’ is used in place of ADS.

Testing for FM is a challenging task due to the system's complexity and the vast range of potential misuse scenarios. Anticipating all potential misuse scenarios poses challenges in designing and testing the system to effectively prevent or mitigate such occurrences. Additionally, testing for FM can be time-consuming and expensive, requiring extensive testing and evaluation to ensure that the system meets intended safety requirements.

Simulation-based testing overcomes the above-mentioned challenges by creating a controlled environment to systematically evaluate potential misuse scenarios, replicating challenging or hazardous real-world scenarios. Simulation-based testing offers a safer and more efficient means of comprehensively evaluating a system's responses, robustness, and ability to effectively prevent or mitigate misuse effects.

Patel et al.[4] proposed a simulation-based approach for testing FM by the driver in highly automated driving systems and discussed the importance of managing driver-system interactions and the implications of driver-vehicle-interface design on these interactions. However, the proposed approach in the paper[4] does not focus on the mitigation of FM.

Mitigation of FM refers to the process of identifying potential misuse of the intended functionality of the system and taking measures to reduce the associated risks to an acceptable level.

The major contribution of the presented work lies in defining the simulation-based test procedure for evaluating the effectiveness of the measures dedicated to preventing or mitigating FM by the driver. In this context, the main contributions of this work are to:

- Define the test requirements: The test requirements must specify the simulation environment, including the vehicle model, the sensor models, and the simulation software. The test requirements must be designed to ensure that the simulation accurately represents the real-world scenario and that the system's response to the scenario can be evaluated.
- Formulate evaluation criteria: The evaluation criteria must be designed to ensure that the measures are effective in preventing or mitigating FM and that they do not introduce new hazards or adversely affect the vehicle's intended functionality.
- Propose an approach to evaluate the effectiveness of measures dedicated to preventing or mitigating FM: The approach must include testing the system's response to potential misuse scenarios, to ensure that the system can detect and respond appropriately to these scenarios.

A. Structure of the paper

The subsequent chapters of this paper are organized as follows: Chapter 2 presents an extensive background, briefly explaining misuse types in ADS, factors and causes of misuse, accompanied by a case study on simulation-based testing of foreseeable misuse. In Chapter 3, the concept for simulation-based application is proposed, detailing the workstation setup and defining essential test requirements. Chapter 4 delves into approach to evaluate the effectiveness of measures dedicated to prevent or mitigate FM, emphasizing conditional probability analysis and the assessment of simulation results. Finally, Chapter 5 concludes by summarizing key findings and implications, and suggesting future research directions.

2. BACKGROUND

A. Types of Misuse

ISO 21448[2] defines two types of misuse in the ADS: direct misuse and indirect misuse. Direct misuse involves conditions that can trigger hazardous behavior in the system, while indirect misuse refers to driver behavior that reduces controllability or increases the severity of an accident without directly causing hazardous behavior in the system.

Instances of direct misuse in ADSs include overconfidence in system performance, misunderstanding of the system's capabilities, lack of understanding regarding system functions, incorrect assumptions about driver interaction based on design specifications, and driver expectations that do not align with the system's capabilities [2].

Indirect misuse instances involve driver fatigue leading to decreased ability to interact with or monitor automation features, distractions stemming from mobile devices or other passengers, reduced attentiveness due to prolonged use or monotonous driving conditions, and over-reliance on automated driving functions without maintaining situational awareness [2].

B. Factors and causes of misuse

Driver Recognition (DR), and Driver Judgment (DJ) are factors and causes of misuse that can contribute to direct or indirect misuse scenarios.

Driver Recognition (DR): Driver recognition refers to the process of perceiving and interpreting the driving environment, including the road, traffic, and surrounding objects. Failures in driver recognition may manifest when drivers overlook the limitations of ADS or misinterpret the driving environment.

For example, a driver may fail to recognize that the ADS is not capable of detecting certain objects like pedestrians or bicycles, and may rely on the system to avoid collisions. This can lead to unsafe situations if the ADS fails to detect these objects, and the driver does not take appropriate action.[5]

Driver Judgment (DJ): Driver judgment refers to the process of making decisions based on the driving environment and the capabilities of the ADS. FM related to driver judgment can occur when drivers make erroneous decisions based on incorrect assumptions about the ADS or the driving environment.

For example, a driver assuming that the ADS is capable of navigating through heavy rain or fog, even though the system is not designed for this purpose. The ADS may not be

able to detect the road markings or other objects in such conditions, and the driver may not take appropriate action, leading to a collision. [5]

C. Case Study on Simulation-based testing for Foreseeable Misuse by the driver

Patel et al.[4] proposed a strategy for implementing simulation-based testing of FM resulting from the system-initiated transition between the human driver and the ADS. The system-initiated transition is the process and period for transferring responsibility and driving control over some or all aspects of the driving tasks between the human driver and the system.

Simulation-based testing involves using a driving simulator to simulate a modeled misuse scenario in the virtual test environment and analyzing the results to determine whether the system meets the intended safety requirements. However, simulation can be limited by the underlying assumptions about environmental conditions, sensors, and the vehicle model.

Patel et al. [4] acknowledged that the strategy presented is to demonstrate an approach for simulation-based testing of FM and is not intended to be a distinctive or optimal measure dedicated to mitigating FM. Also, the implementation of the strategy has not been evaluated in practice, and therefore, the effectiveness of the measures dedicated to preventing or mitigating FM has not been evaluated.

3. PROPOSED CONCEPT FOR SIMULATION-BASED APPLICATION

A. Determining SOTIF-related Misuse Scenario

To derive a misuse scenario, various sources, including lessons learned, expert knowledge, and brainstorming, can be utilized. ISO 21448 (Annex B1) provides a systematic approach for deriving an SOTIF-related misuse scenario. [2]

The process for identifying a misuse scenario begins with understanding the intended functionality of the system. This entails comprehending the system's purpose, its designated user base, and the environment in which it will operate. Once the intended functionality is understood, the next step is to identify potential misuses of the system. This includes understanding how the system could be used in unintended ways and how these misuses could lead to hazards. [6]

The potential misuses can be categorized based on their severity and likelihood. This helps prioritize the misuses that pose the greatest risk to safety. Based on the potential misuses identified, a misuse scenario should be developed. The misuse scenario should describe how the system could be misused, the potential consequences of the misuse, and the likelihood of the misuse occurring. [6]

Lastly, the evaluation of the misuse scenario is crucial to determine its impact on the

safety of the ADS. This includes assessing the likelihood of the misuse occurring, the severity of the consequences, and the effectiveness of any mitigation measures that could be implemented. It is important to note that misuse scenarios should not only consider deliberate violations but also human driver errors that could lead to the unintended use of the system.

The Table 1 depicts a description of a misuse scenario derived from [4], in accordance with an example methodology outlined in ISO 21448 (Annex B1).

Table 1: Description of SOTIF-related misuse scenario, adapted from [2]

<table>
<tr><td rowspan="2">Potential SOTIF-related misuse scenario</td><td rowspan="2">Stake-holder</td><td colspan="2">Foreseeable Misuse</td><td rowspan="2">Driver-System Interac-tions</td><td rowspan="2">Environ-mental Condi-tions</td><td rowspan="2">Derived Haz-ardous Scenario</td></tr>
<tr><td>Factors</td><td>Causes</td></tr>
<tr><td rowspan="2">Described below [1]</td><td rowspan="2">Driver</td><td>Recogni tion</td><td>False recogni-tion</td><td rowspan="2">Described below [2]</td><td rowspan="2">Described below [3]</td><td rowspan="2">Described below [4]</td></tr>
<tr><td>Judgeme nt</td><td>Misjugm ent</td></tr>
</table>

[1] The Ego-Vehicle encounters a road with missing lane markings during automated driving on a two lane one-way highway and executing lane change maneuver from right to left lane. The camera sensor cannot estimate the location of the lane boundary due to a performance limitation of the camera sensor. Ego-Vehicle starts to leave the lane and driver is notified to take control of the driving tasks by means of Take-Over-Request (TOR).

[2] “Delayed Take-over” and/or “Take-Over and perform Over/Understeer”

Weather: clear

Light Condition: daylight

Traffic Condition: light traffic

Roadway Surface and Features: missing lane markings

[4] Driver fails to take-over the control of the driving tasks, resulting in lane departure of Ego-Vehicle.

B. Workstation setup for Simulation-based Testing

The workstation has been developed with an integrated driving simulator equipped with hardware tools, including the Logitech G29 steering wheel, pedals, and gearbox, integrated with a simulation tool, IPG CarMaker, to perform simulation-based testing of foreseeable misuse. The driving simulator is static simulator that allows a human driver to engage in the simulation-based application.

The block diagram in *figure 1* represents a workstation setup consisting of several components that collaborate to execute driving tasks.

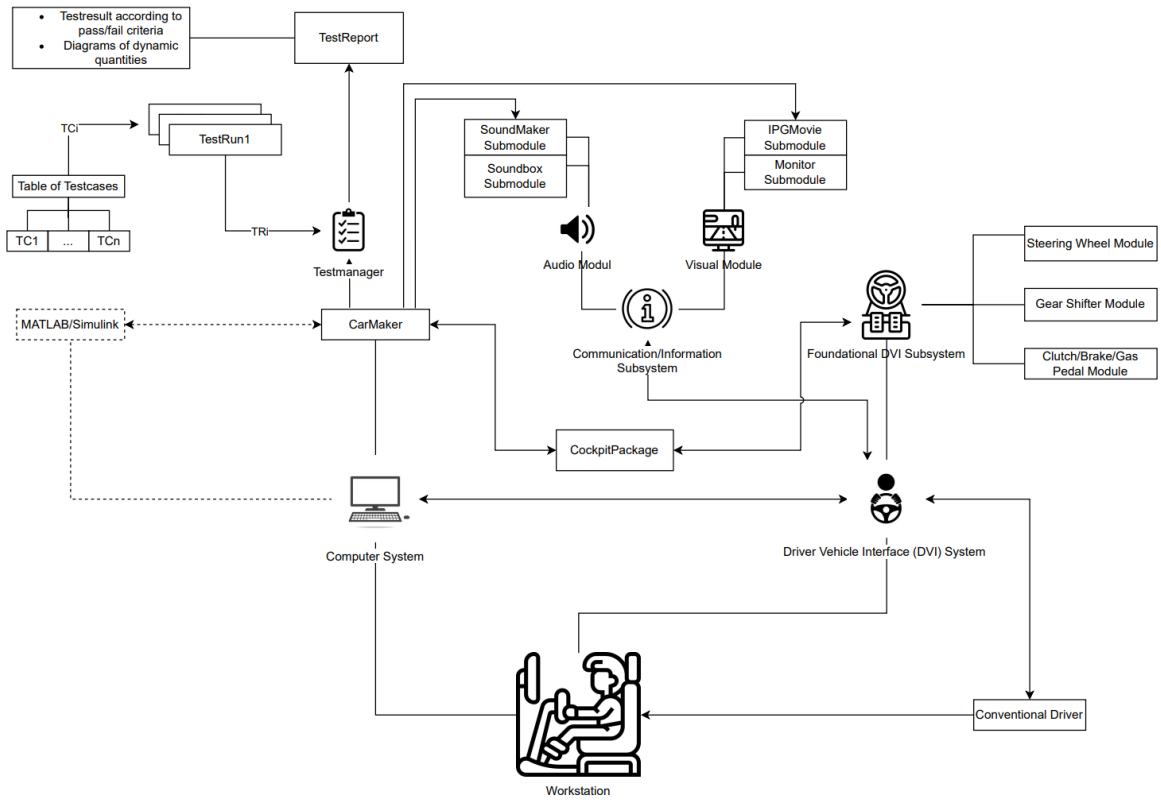

Fig. 1: Representation of a workstation setup to perform simulation-based testing of foreseeable misuse by the driver

The “Foundational DVI subsystem” is responsible for man- ual driving and allows the driver to interact with sensor module, controller module, environment module, and other ehicle modules.

“CarMaker” is a software tool for developing and testing virtual vehicle models, while “CockpitPackage” is an exten- sion in CarMaker that facilitates the integration of hardware components including steering wheels, clutch/brake/gas ped- als, and gear shifters into the simulation environment.

The “Communication/Information” subsystem provides vi- sualization of the simulation and includes modules like IPG- Movie for real-time 3D animation of the virtual driving simulation and Sound-Maker software for 3D audio. It also en- compasses the Visual Module, which contains the Instruments Panel sub-module for providing information to the driver about the current status of the driving mode and warnings in case of upcoming events.

TestManager is a software tool employed in CarMaker for simulating Test Cases (TC). It permits the creation, execution, and management of TC. The test cases are a set of predefined procedures that are used to verify the functionality of the system under test. The TestManager sequentially invokes the TestRuns to execute a Test-case Series (TCS). After each TCS, a TestReport is generated, displaying all executed TC and their outcomes. The TestManager also allows the addition of pass/fail criteria to determine TCS success.

C. Defining test requirements for performing simulation-based testing

The simulation requirements become relevant at different phases of simulation-based testing. Therefore, test requirements are formulated in form of a checklist, encompassing a series of questions. The checklist is presented in form of question cards.

Table II illustrates the template of the presented question cards. In the top-right corner of the question card, the question number is denoted by [1, 2, ..., n], followed by the primary question. On the bottom-left, possible responses to the ques- tion are provided. An explanation for the respective question is provided in the bottom-right corner of the table.

Table 2: Template of the checklist

Question Number	**[1,2,. . . ,n]**
Main Question	
Possible Response	Explanation

In the following, a set of questions (No.1 – No.10) representing the requirements for the simulation-based testing are provided in Table 3 below.

Table 3: Question Cards

Question Number	**1**
Does the system performs automated driving of the ego-vehicle by providing longitudinal and lateral control in the modeled scenario?	
Yes / No	The simulation starts initially in automated driv-ing mode. It is intended to provide longitudinal control of the Ego-Vehicle on a right lane in a one way two-lane highway environment. All automated driving function should be active and work.
Question Number	**2**
Does the Ego-Vehicle encounters a road with unclear lane markings during the initialization of the lane change from right lane to left lane?	
Yes / No	The Ego-Vehicle encounters a part of the road with unclear lane markings while executing lane change maneuver from right to left lane.
Question Number	**3**
Does the ADS send a warning to the driver when the Ego-Vehicle encounters the specified road conditions in Question 3?	
Yes / No	Visually and auditory warning is sent out at 6.04 seconds of the simulation time and the lane departure warning is activated because unclear lane markings are detected.
Question Number	**4**
If the driver not respond to the warnings, does the system notify the driver by issuing imminent Take-Over-Request (TOR)?	

Yes / No	If the driver not response to the warning then the ADS will request the driver to Take-Over (TO). The TOR is sent at 7.96 seconds of the simulation time.
Question Number	**5**
Does the driver response to the TOR?	
Yes / No	The driver can respond to the TOR and does the TO of driving task by means of driver- vehicle-interface (Logitech G29 Steering Wheel buttons). The system is expected to remain op- erational in automated driving mode until the driver is able to regain control of the driving task.
Question Number	**6**
Does the system transition into automated driving with reduced function-ality mode and performs minimal risk maneuver?	
Yes / No	If the driver does not TO the driving tasks in the event of TOR, the system will transition to the automated driving with reduced functionality. Subsequently, a minimal risk maneuver is per- formed by the system to keep the Ego-Vehicle in its lane and to automatically stop the Ego- Vehicle on the side of the road in a safe manner [7].
Question Number	7
Does the driver TO of the driving task in the specified time?	
Yes / No	The driver does take-over in time, if the TO time is less than 1.77 seconds [8]. The TO-time is the difference between TOR and TO. Take-over after 1.77 seconds are considered as delayed TO (i.e., considered as FM).
Question Number	**8**
Does the adjusted Steering wheel Angle (SWA) by the driver after TO lead to Oversteer or Understeer (i.e, considered as FM) ?	
Yes / No	Ideal SWA could be defined as the SWA that will centre the Ego-Vehicle in the middle of the current lane (left lane). • Over-steer if the adjusted SWA is greater than ideal SWA. • Understeer if the adjusted SWA is smaller than ideal SWA.
Question Number	**9**
Does the FM by the driver lead to Hazard?	
Yes / No	Hazard if the Ego-Vehicle departs lane. a. Lane departure towards the east from left lane or b. Lane departure towards the west from left lane
Question Number	**10**
Does the driver able to handle the driving situation (after TO by driver), measured as controllability?	
Yes / No	Likelihood that the driver can cope with driving situations including the system limits and system failures is defined as “controllability” [9]. • Controllability is provided if driver does TO successfully without leading to hazard. • Controllability is not provided if driver TO unsuccessfully leading to hazard.

4. APPROACH TO EVALUATE THE EFFECTIVENESS OF MEASURES DEDICATED TO PREVENTING OR MITIGATING FORESEEABLE MISUSE

A. Conditional Probability Analysis

Conditional probability analysis is chosen as the primary approach to establish a systematic and quantifiable approach to understanding relationships between factors and causes of FM within the ADS. In particular, the focus is on two key elements: False Recognition (FR) and Misjudgment (MJ).

The choice of employing the conditional probability anal- ysis approach is informed by the methodology outlined by Mkrtchyan et al. [10], which demonstrates the applicability of this approach in evaluating safety-critical systems.

The below provided analysis is based on considering the SOTIF-related misuse scenario described in *Table 1*, and in accordance with defined requirements in *Table 3*.

Misjudgment (MJ): It relates to situations where the driver makes an erroneous decision during the Take-Over (TO) pro- cess, potentially resulting in under-steering or over-steering, and potential for a lane departure (i.e., hazard).

The probability of Misjudgment is assessed under two conditions:

1) when there is no delayed take-over (TO ≤ 1.77 seconds) and a Hazard (H) is present, mathematically expressed as:

$$P(MJ|TO \leqslant 1.77\,s, H) = \frac{P(TO \leqslant 1.77\,s \cap H)}{P(MJ \cap TO \leqslant 1.77\,s \cap H)} \quad (1)$$

2) when there is a delayed take-over (TO > 1.77 seconds) in the presence of a Hazard (H), mathematically expressed as:

$$P(MJ|TO > 1.77\,s, H) = \frac{P(TO > 1.77\,s \cap H)}{P(MJ \cap TO > 1.77\,s \cap H)} \quad (2)$$

False Recognition (FR): It occurs when the driver fails to promptly recognize the necessity of take-over control. This can result in delayed takeover, leading to a delayed take-over and the potential for a lane departure (i.e., hazard).

The probability of False Recognition is evaluated under the condition of a delayed take-over (TO > 1.77$ seconds) when a hazard (H) is present, mathematically expressed as:

$$P(FR|TO > 1.77\,s, H) = \frac{P(TO > 1.77\,s \cap H)}{P(FR \cap TO > 1.77\,s \cap H)} \quad (3)$$

As a visual aid, *figure 2* illustrates a probability tree dia- gram depicting the relationships between Misjudgment (MJ) and False Recognition (FR). This diagram provides a struc- tured representation of conditional probabilities, enhancing the understanding of the interactions among various factors and causes of FM.

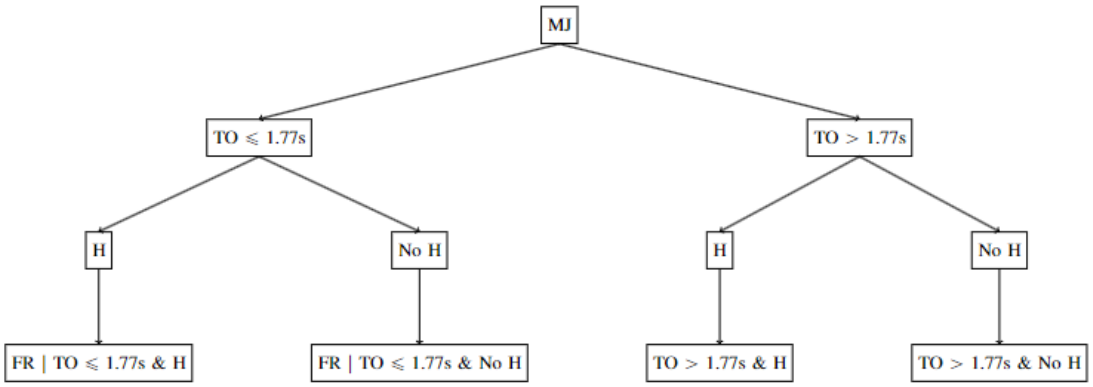

Fig. 2: Probability Tree Diagram for Misjudgment (MJ) and False Recognition (FR)

- The top level represents the conditional probability of Misjudgment (MJ).
- The second level represents the two scenarios based on Takeover (TO) time being less than or greater than 1.77 seconds.
- The third level represents the presence or absence of Hazard (H) in each scenario.
- The last level represents the conditional probability of False Recognition (FR) based on the Takeover (TO) time and Hazard (H) conditions.

B. Evaluation of simulation-based application

An exemplary Table 4 of Test Case Series (TCS) is presented based on results of simulation-based application of FM. Because of the high amount of TC, all simulation results of TC are not entailed. Only a exemplary Table 4 is provided to demonstrate the results.

TestManager is a tool employed in software CarMaker for simulating Test Cases (TC). TestManager allows the creation, execution, and management of TC. The TestManager sequen- tially invokes the TC to execute a Test-case Series (TCS).

Table 4: Exemplary Test Case Series (TCS)

TC	TO	TO t2 [s]	delta T2 [s]	DelTO	SWA [deg]	H	H t3 [s]	delta T3 [s]
1	1	10.2300	2.2700	1	12.5144	0	0.0000	0.0000
2	1	10.7300	2.7700	1	3.2086	0	0.0000	0.0000
3	1	11.0800	3.1200	1	15.2058	1	11.1000	0.0200
4	1	9.1200	1.1600	0	32.1657	1	10.4000	1.2800
5	1	11.3500	3.3900	1	10.5064	1	11.1000	0.4600
...	...	...	...	...	...	...	...	...
TC*n*	...	...	...	...	...	...	...	...

The Test Cases (TC) encompass various parameters, includ- ing Takeover (TO), Delayed TO (DelTO), and Hazard (H), which are logic values, either 0 or 1. The explanations for each parameter are presented below.

1) *Takeover (TO):* The parameter "TO" signifies whether the driver take-over control of the driving task in a given TC. A value of 1 indicates a take-over of the driving task by the driver.
2) *Delayed Takeover (DelTO):* The parameter "DelTO" is set to 1 when the driver take-over control after or/ more than 1.77 seconds. To calculate DelTO, "delta_T2" is used, representing the time difference between the Takeover Re- quest (TOR) time (fix value=7.96 seconds [4]) and the actual Takeover time (TO_t2). For instance, in TC 1, "DelTO" is 1 because the driver does take-over after 2.27 seconds.
3) *Hazard (H):* The parameter "H" indicates the lane departure of the vehicle (i.e., hazard) during a TC. It equals 1 if a hazard occurs. For instance, In TC 3, TC4 and TC5, "H" is 1 that indicates a lane departure.
4) *Hazard Time (H_t3)* and *Delta_T3*: The parameter "H_t3" represents the time of a hazard in a TC, and "Delta T3" is the time difference between "H_t3" and "TO_t2". In TC_3, "H_t3" is 11.1 seconds, and "Delta_T3" is 0.02 seconds.
5) *Steering Wheel Angle (SWA):* The parameter "SWA" reflects the driver's steering input at take-over. It is calculated as the difference between SWA at "TO_t2" and the maximum steering input immediately after take-over.

C. Assessment of Simulation Results

As mentioned in requirement Table 3, question 10, likeli- hood that the driver can cope with driving situations including the system limits and system failures is defined as "controlla- bility".

Within the simulation-based application, a total of 50 Test Cases (TC) were conducted. Among these, 22 TC (44%) exhibit controllability, signifying that the driver could regain control of the vehicle after a take-over. Conversely, 28 TC (56%) revealed a lack of controllability, resulting in hazard.

Table 5 presents probability analysis results based on simulation results. It outlines the likelihood of different events related to driver controllability. The outcomes reflect the chances of a specific scenario, including Misjudgment (MJ) and False Recognition (FR) under different driving conditions:

Table 5: Probability Analysis Results Based on Simulation Data

Probability Condition	Number of Test Cases	Percentage
P(TO 1.77s X H)	10	20%
P(MJ X TO 1.77 s X H)	6	12%

Probability Condition	Number of Test Cases	Percentage
P(TO 1.77 s X H)	2	4%
P(MJ X TO 1.77 s X H)	8	16%
P(FR X TO 1.77 s X H)	2	4%

The conditional probabilities, as outlined in Table 5, can be calculated from Chapter 4.A

Misjudgment (MJ) Probability:

1) When there is no delayed take-over (TO ≤ 1.77 seconds) and a Hazard (H) is present

$$P(MJ|TO \leqslant 1.77\,s, H) = \frac{10}{6} = 1.67 \tag{4}$$

This signifies that a driver is 1.67 times more likely to misjudge a situation when there is no delayed take-over (TO ≤ 1.77 seconds) and a Hazard (H) is present.

2) When there is a delayed take-over (TO > 1.77 seconds) in the presence of a Hazard (H):

$$P(MJ|TO > 1.77\,s, H) = \frac{2}{8} = 0.25 \tag{5}$$

In this case, the likelihood of misjudgment is significantly reduced when there is a delayed take-over (T O > 1.77 seconds) in the presence of a Hazard (H).

False Recognition (FR) Probability: The probability ofFalse Recognition is evaluated under the condition of a delayed take-over (T O > 1.77 seconds) when a hazard (H) is present:

$$P(FR|TO > 1.77\,s, H) = \frac{2}{2} = 1 \tag{6}$$

This implies that the probability of false recognition remains at 100% when there is a delayed take-over (TO > 1.77 seconds) and a Hazard (H) is present, indicating a high likelihood of recognizing a false situation.

It is important to note that these calculated probabilities are specific to particular conditions and a scenario with a limited number of test cases used in the simulation. These values are derived based on a specific threshold of 1.77 seconds for take-over time, and results may vary with different thresholds. Additionally, these results do not account for other potential factors that could influence driver behavior.

5. CONCLUSION AND FUTURE WORK

The paper introduces a comprehensive strategy for eval- uating the effectiveness of measures designed to prevent or mitigate Foreseeable Misuse (FM) within Automated Driving Systems (ADS). The primary approach employed for the assessment is Conditional

Probability Analysis (CPA), with a specific focus on key factors and causes for FM, including False Recognition (FR) and Misjudgment (MJ). The applica- tion of CPA is directed applied to a Safety of the Intended Functionality (SOTIF)-related misuse scenario.

The analysis provides valuable insights into the conditional probabilities associated with the occurrence of Misjudgment and False Recognition under various driving conditions. It is notably observed that the likelihood of Misjudgment diminishes significantly when a delayed Take-Over (TO) takes place, especially in the presence of a hazard (H). In contrast, the probability of False Recognition remains considerably high when TO is delayed and leads to a Hazard (H).

While these findings offer valuable insights into the evalu- ation of FM within ADS, it is essential to acknowledge that the calculated probabilities are specific to a specific misuse scenario and limited number of Test-cases utilized in the simulation. These values provide a foundational starting point for further refinement and adaptation to real-world scenarios, accounting for variations in threshold values for TO and other potentially influential factors affecting driver behavior.

There are several promising directions for future research. To begin, future investigations should prioritize the collection and analysis of real-world data to authenticate the outcomes from the simulation-based approach. Validating these findings in actual driving scenarios is pivotal for a more precise understanding of Foreseeable Misuse (FM).

Additionally, conducting sensitivity analyses on the thresh- old value of Take-Over (TO) time is crucial. This exploration will provide more insights into how alterations in the TO threshold value affect conditional probabilities. Moreover, an extensive examination of driver behavior and cognitive pro- cesses during take-over scenarios is necessary. This research should explore elements like driver fatigue, distractions, and driver experience and their conspicuous influence on FM likelihood.

REFERENCES

[1] SAE J3016, *Taxonomy and definitions for terms related to driving automation systems for on-road motor vehicles - ground vehicle stan- dard: On-road automated driving (orad) committee*, United States, April.2021.

[2] ISO 21448:2022, *Road vehicles – safety of the intended functionality*, Switzerland, 2022-06. [Online]. Available: https://www.iso.org/standard/ 77490.html.

[3] National Transportation Safety Board, *Collision between a car oper- ating with automated vehicle control systems and a tractor-semitrailer truck near Williston*, Florida, May 7, 2016. Available: https://www.ntsb.gov/investigations/AccidentReports/Reports/HAR1702.pdf.

[4] M. Patel, R. Jung, and Y. Cakir, *Simulation-based testing of foresee- able misuse by the driver applicable for highly automated driving*, in Proceedings of Eighth International Congress on

Information and Communication Technology, X.-S. Yang, R. S. Sherratt, N. Dey, and A. Joshi, Eds. Singapore: Springer Nature Singapore, 2024, pp. 183– 191.

[5] C. Becker, J. C. Brewer, and L. Yount, *Safety of the Intended Functionality of Lane-Centering and Lane-Changing Maneuvers of a Generic Level 3 Highway Chauffeur System*, 2020. [Online]. Available: https://rosap.ntl.bts.gov/view/dot/53628.

[6] F. Warg, S. Ursing, M. Kaalhus, and R. Wiik, *Towards safety analysis of interactions between human users and automated driving system*, 2020.

[7] M. Wood et all., *Safety First For Automated Driving*, 2019. [Online]. Available: https://www.aptiv.com/docs/default-source/white-papers/safety-first-for-automated-driving-aptiv-white-paper.pdf

[8] A. Eriksson and N. A. Stanton, *Takeover time in highly automated vehicles: Noncritical transitions to and from manual control*, Human Factors, vol. 59, no. 4, pp. 689–705, 2017.

[9] A. Knapp, M. Neumann, M. Brockmann, R. Walz, and T. Winkle, *ADAS Code of Practice (Code of Practice for the Design and Evaluation of ADAS)*, 2009.

[10] L. Mkrtchyan, L. Podofillini, and V.N. Dang, *Methods for building conditional probability tables of bayesian belief networks from limited judgment: An evaluation for human reliability application*, Reliability Engineering & System Safety, vol. 151, pp. 93–112, 2016. [Online]. Available: https://www.sciencedirect.com/science/article/pii/S0951832016000132.

COMPUTER NETWORK SECURITY

Marijan **MIJATOVIĆ** [1], Marko **MIJATOVIĆ**[2]
[1] *Nezavisni Univerzitet Banja Luka,* [2]*Sveučilište Hercegovina*
photo.by.mile@gmail.com, marko.mijatovic@hercegovina.edu.ba

Keywords: networks, protocols, packets, LAN, cryptography.

Abstract*: Computers that we connect to a network serve to exchange data, which is located in the computer's working memory. Data transmission can also be done through electronic signals, and these connections can be wireless networks or wired networks. The bits that are sent one after another simultaneously correspond at an appropriate speed, converting digital signals into analog signals and vice versa, which is a modern process. Computers can also be connected to a local network and a branched network. Each computer connected to the network has its own unique number (address) from which it can be recognized on which continent it is, in which country, and to which server address it is connected. Data is sent according to a pre-agreed protocol, in the form of packets. Security measures for protecting sensitive data and documents have existed for a long time in the world. Throughout history, many methods have been developed regarding data protection and internet security. Methods of providing protection on the internet were sometimes not effective and did not provide the necessary level of protection. With the development of cryptography and technology, very good methods of encryption and document protection have been discovered. Information systems are the foundation of basic and modern business operations. Their fundamental task is to be based on network systems, as well as their operation and security. That's why it's extremely important to familiarize ourselves with the security issues of computer networks and the ways in which these problems are resolved.*

1. INTRODUCTION

Computer networks were initially designed to connect computers situated in locations enabling them to exchange and share data simultaneously essentially allowing communication. In the past the majority of data transmitted through these networks was, in

form. However with the advancements in multimedia and network technologies today multimedia content has become a part of the internets evolution.

Various products like internet telephony, internet television, video conferences and others have emerged on the market as a result. In scenarios people will increasingly rely on services such as distance learning and distributed simulations that won't necessitate team members being physically present within the building or even country. The economic advantages of arrangements are quite evident.

To facilitate better quality communication for business purposes network services need to develop hardware and software infrastructure along with tools that support the transmission of multimedia services within computer networks.

The utilization of computers as communication tools will contribute significantly to enhancing network services. There is a belief that in course multimedia networks will replace phones, televisions and other inventions that have played pivotal roles in reshaping our lives in the past.

Fast forward sixty years later; information systems have permeated every aspect of activity. In todays world existence, without computer networks and their associated security measures is simply unimaginable.

2. HISTORY OF COMPUTER NETWORKS

Computer networks emerged as a result of applications developed for large corporate companies. Companies recognized the efficiency problem of their employees who had to transfer the written material to disk units in order to print it. They had to copy certain types of data to a computer with a connected printer before being able to print a specific document.

To simplify and, above all, reduce costs in business operations, companies began to invest in network technology and their security for better and more secure business practices. In the early 1980s, computer networks experienced tremendous growth, although the early networks were quite insecure.

Due to the rapid expansion of computer networks and their security, there was a period of incompatibility among network systems funded by different companies. The solution to this problem was the LAN (Local Area Network). Perhaps the most important moment was in 1983 when the network, using NCP-A (Network Control Protocol), transitioned to TCP/IP (Transmission Control Protocol / Internet Protocol), a newer technology that is widely used in the world today.

Packet-Switched technology describes the sending of specific data in small packaged units called packets. They are routed through the network using the targeted IP address contained in the packet. The packet traveling this way will reach its destination, and it is crucial that all other packets also reach their destinations.

Sharing data for packet transmission allows the same communication network to be shared among a larger number of users in the network. Each computer connected to the network also has its own unique number (address) from which it can be identified in which part of the world, in which country, and through which server it is connected. Data in the network is sent according to agreed-upon protocols and in the form of packets.

3. NETWORKS AND THEIR DIVISION

The division and types of services that an information network should provide are as follows:

- In speech and communication, in digital form, through channel or packet procedures, text communication, data communication through real-time or delayed procedures, access to banking and computer data services, and their processing.
- Image communication, videophone, telefax, multimedia communication, and remote control.

In addition to the physical format for network connections, computer networks can also be distinguished by size:

- Local Area Network (LAN): Simple networks where two computers are connected via cable.
- Home Area Network (HAN): These are computers within a single household that connect personal electronic devices such as mobile phones, laptops, and HDTVs.
- Wide Area Network (WAN): These are computers spread worldwide and connected through telephone lines, satellite links, and radio links.
- Metropolitan Area Network (MAN): Data network in larger cities that connects large companies.

4. TYPES OF NETWORK MEDIA

Media used for transmission, also known as physical media, are used to connect computer devices in a network and consist of:

- Electrical cables (ETHERNET, Home PNA, network communication).
- Optical cables (fiber-optic communication).
- Radio waves (wireless communication).

In the OSI model, they are defined in layers 1 and 2, the physical layer and the data link layer.

The widely adopted family of transmission media used in LAN technology is known as the ETHERNET cable. Data transmission is carried out over copper and optical cables.

Standard wireless LAN networks also use radio waves and other frequencies as means of transmission. Communication through electrical lines utilizes a network cable for data transmission.

5. DEVICES AND NETWORK NODES

In addition to any physical media transmission that exists, networks comprise additional and fundamental system blocks, such as Network Interface Controller (NIC), repeaters, HUBs, bridges, switches, routers, modems, and other protective barriers (FIREWALL)."

5.1. Network User Interface

Network Interface Control is a computer hardware component that enables a computer to access and transmit data, and has the capability to process network information at a lower level. NIC can have a connector for accepting a cable or an antenna for wireless data transmission. NIC responds to traffic directed to either the NIC itself or to the computer alone.

In Internet networks, each controller has its unique MAC (Media Access Control) address, which is 6 octets long (e.g., 00-0a-83-B1-c0-b8) and is typically stored in the controller's permanent memory. To avoid address conflicts between network devices, the Institute of Electrical and Electronics Engineers (IEEE) maintains and administers the uniqueness of MAC addresses.

5.2. Repeaters and Hubs

A repeater is a network device that receives a network signal, cleans it from unnecessary noise, and regenerates (amplifies) it. The signal is then retransmitted at a higher power level or on the other side of an obstacle, allowing it to cover greater distances without degradation.

In Internet configurations, repeaters are necessary for cables longer than 100 meters, while with optical fibers, they can be located tens, or even hundreds of kilometers apart. Repeaters with multiple ports are more commonly known as hubs, and they operate at the physical layer of the OSI model.

5.3. Bridge

A network bridge connects and filters traffic between two network segments at the data link layer of the OSI model to form a single network. This breaks up the network domain

while maintaining the broadcast domain. Network segmentation divides a large congested network into smaller, more efficient networks, and there are three basic types:

• Local bridges: connect LANs.

• Remote bridges: can be used to create a WAN between LANs. Remote bridges, where the connection is slower than the end networks, have mostly been replaced by routers.

• Wireless bridges: can be used to connect LANs or link remote devices to LANs.

5.4. Switch

A network switch is a device that manages the flow of data between parts of a local area network (LAN). Unlike a hub, a switch divides network traffic and sends it to specific locations, while a hub sends data to all devices on the network. They are used for medium-sized networks because they are more efficient and effective than hubs. A switch provides a computer with the full network speed, while other computers connected to a hub only receive a portion of the connection.

5.5. Routers

A router, or network router, is a device used to interconnect computer networks. It has the function of determining the exact path each data packet should take and forwarding that same packet to the next device in the sequence. In local networks, a router is usually set up as the link between the network and the internet, i.e., it is assumed to be the network exit point (GATEWAY).

5.6. Wireless Access Point (WAP)

A WAP is a network hardware device that allows a device compatible with a WiFi network to connect to a wired network. A WAP is usually connected to a router (via a wired network) as a standalone device, but it can also be an integral part of the router itself. A WAP differs from a hotspot, which is a physical location where WiFi access to a wide area network (WAN) is available.

5.7. Modem

Modems (modulators-demodulators) are used to connect network nodes using wires originally not designed for digital network traffic or for wireless connections. Modems are commonly used for telephone lines, utilizing digital subscriber line technology. They modulate the digital signal into a form suitable for transmission over communication channels, and subsequently demodulate it back to its original form after transmission.

5.8. Firewall

A firewall is a network device used for security control and access rules in a network. They are typically configured to reject access from unknown sources while allowing actions from known ones. They play a vital role in network security with the constant rise of cyber attacks.

6. PROTECTION AND SECURITY OF COMPUTER NETWORKS

There has always been a need to protect sensitive data, and consequently, documents containing such information. Throughout history, many methods have been developed in attempts to preserve the confidentiality of important data. Many of these methods were simple and did not provide sufficient protection, often resulting in breaches of confidentiality. With the development of cryptography and technology, very effective encryption methods and document protection techniques have been discovered.

Encryption is a good way to prevent unauthorized individuals from accessing the content of a sensitive document. However, once a document is decrypted with a secret key, a malicious authorized person can save, copy, print, or forward the document. Restricting access to a document to a select few individuals is one approach to document protection, but there is always a possibility that one of the trusted individuals may disclose the information.

In such a case, it is necessary to identify the person who leaked the information, which is not always a straightforward task. A solution that ensures the protection of sensitive information cannot rely on a single technology.

6.1. Antivirus Protection

Antivirus programs constitute a specific category of software designed primarily for the identification, neutralization, and elimination of viruses, worms, trojans, and other malicious programs. The fundamental task of an antivirus program is to recognize a virus and protect the system from its effects. If a computer is infected with a virus, the antivirus program must isolate and remove it. Antivirus definitions are used to identify viruses. Each virus is characterized by a specific sequence of octets (character codes), as it is fundamentally a computer program. After detecting a viral sequence in a file, the antivirus program will:

- Attempt to repair the file by removing the virus itself,
- Place the file in quarantine so that no program can access it, preventing the virus from spreading further,
- Delete the infected file.

Since viruses are constantly evolving, the database of virus definitions and their codes needs to be constantly updated, often multiple times a day. This is typically done by the antivirus programs themselves. If the definitions were not updated, the antivirus program would not be able to recognize new viruses.

The failure to update virus definitions is the main reason for the continued spread of some long-known viruses. To outsmart virus detection mechanisms, virus developers often create so-called oligomorphic, polymorphic, or metamorphic viruses. These viruses change their form and source code, aiming to go unnoticed in each subsequent "incarnation."

Another way antivirus programs operate is by monitoring the behavior of all programs. If a program attempts to write data into the executable code of another program, access the network, or try to send data to a specific port, the antivirus program will signal and notify the user.

6.2. Encryption

An important part of protecting documents stored on computer hard drives, especially laptops, is encryption. Through this relatively simple process, it is possible to prevent the exposure of confidential information in the event of a lost laptop, as well as attacks by malicious users who gain physical access to the computer. Most modern operating systems have built-in mechanisms that allow for the encryption of stored data.

The encryption process involves transforming open or clear text into text that is unintelligible to unauthorized individuals. The individuals for whom the document is intended and who are allowed to read it must possess a special key to convert the document back into clear text, or decrypt it. There are symmetric and asymmetric cryptographic systems.

In a symmetric cryptographic system, the key for encrypting or transforming the document into unintelligible text is the same as the key for decrypting it, while in an asymmetric cryptographic system, this is not the case. In communication through messages, there is usually a sender and a recipient of the message.

Asymmetric cryptographic systems are based on certain properties of numbers explored in number theory. The idea is explained by the following example. Ana creates her own pair of keys: one for encryption and one for decryption. Assuming that asymmetric encryption is a form of computer encryption, Ana's encryption key is one number, and the decryption key is another number. Ana keeps her decryption key secret, which is why it is usually referred to as the private key. However, she publicly publishes her encryption key, making it available to everyone.

An example of the most commonly used asymmetric cryptographic system is RSA, authored by Ron Rivest, Adi Shamir, and Len Adleman. Other examples of such algorithms include ElGamal, NTRUEncrypt, LUC, and others. The security of encrypted documents

depends on which algorithm is used for encryption and the length of cryptographic keys. Attackers may conduct cryptanalysis on the text they want to decrypt.

6.3. The IPSec protocol

(IP Security) is a set of extensions to the IPv4 protocol that ensures basic security aspects of network communication, including confidentiality, integrity, authentication, and non-repudiation. It's worth noting that IPSec, in addition to extending the currently used IPv4, also comes as an integral part of the IPv6 protocol. As it integrates with the IP protocol, IPSec implements secure network communication at the third, or network layer, of the ISO OSI model of this protocol, i.e., the internet layer when considering the TCP/IP stack. Of course, security can also be implemented in other layers, from the physical to the application layer (such as SSH, SSL/TLS). Each implementation has its own advantages and disadvantages.

REFERENCES

[1] B. Djordjevic, D. Pleskonjic, N. Macek, *Operating Systems: UNIX and Linux, Higher*.

[2] M. Cagalj, *Security in Wireless Computer Networks*, Faculty of Electrical Engineering, Mechanical Engineering and Naval Architecture, Split, 2006.

[3] A. Darko; *Basic Network Terminology*, Electrical Engineering School, Belgrade, 2004.

[4] B. Eugene; *Introduction to Data Communications*, 1999.

[5] S. Ilisevic, *Quick Guide to Home Networks*, BUG & SysPrint, Zagreb, 2003.

[6] S. Jusic, *Security of Web Applications*. Communication Technologies and Standards in Computer Science, 2003.

[7] M. Bojovic, *Squid Proxy Server*, diploma thesis, Higher Electrical Engineering School, Belgrade, 2005.

[8] M. Zivkovic, *Algorithms*, Faculty of Mathematics, Belgrade, 2000.

[9] K. Milan and C. Dario, *Introduction to Computer Networks*, Zagreb, 2014.

[10] V. Muzic, *Methodology of Pedagogical Research*, Svjetlost, Sarajevo, 1982.

[11] B. Olivier *Computer Networking: Principles, Protocols, and Practice*, 2011.

[12] T. Pralas, *Computer Networks - Passive and Active Equipment*, Sys portal, Zagreb, 2004.

[13] M. Randic, *Network and Service Management*, Faculty of Electrical Engineering and Computing, Zagreb, 2004.

[14] V. Sinkovic, *Information Networks*, School Book, Zagreb, 1994.

[15] Srdic, Ida, Hrpka, Branko, K; Goran, *Textbook of Computer Science*, ALFA d.d., Zagreb, 2007.

[16] S. Skundric, A. Sok, *Analysis of Computer Network* at the Technical Faculty in Rijeka, Technical Faculty, Rijeka, 2007.

[17] P. Toni; *Computer Networks* - OSI Reference Model, 2008.

[18] V. Vasiljevic, P. Gavrilovic, B. Krneta, M. Krstanovic, N. Macek, B. Bogojevic, *Manual for Computer Network Administration*, Higher Electrical Engineering School, Belgrade, 2004.

WATERFALL OR SCRUM METHODOLOGY - HOW TO CHOOSE ACCORDING TO THE SPECIFIC PROJECT?

Mirko **SAJIĆ**[1], Saša **ČEKRLIJA**[1], Mladen **BUBONJIĆ**[1], Goran **KALINIĆ**[1], Radmila **BOJANIĆ**[1], Slađana **BABIĆ**[2]

[1]*Independent University of Banja Luka,* [2]*Blicnet*

Keywords: Waterfall, Agile, Scrum, CBS, Product Owner, Gantt chart, Project Chart

Abstract*: This paper aims to perform a comparison of two methodologies used in project management and project work. It first describes the basic characteristics, strengths, and weaknesses of both methodologies to facilitate reaching certain conclusions. Then, it derives specific conclusions through a cross-comparison.*

1. INTRODUCTION

As an introduction, we will first briefly explain the concept of "project management." Project management is the process of planning, executing, and controlling activities with the aim of achieving specific goals within a defined timeframe, budget, and resources. Key elements of project management include: (R. Mulcahy, 2013)

1. Goal Definition: Setting clear and measurable project objectives to understand what needs to be accomplished.
2. Planning: Developing a detailed plan that includes tasks, resources, timelines, and budgets.
3. Execution: Carrying out activities according to the plan, monitoring progress, and addressing emerging issues.
4. Risk Management: Identifying and managing potential risks that may impact project success.
5. Monitoring and Controling: Regularly tracking project progress compared to the plan and properly managing changes.

6. Communication: Effective communication with team members, stakeholders, and decision-makers.

7. Project Closure: Assessing achieved results and closing the project once objectives are met.

Project management requires a balance between precision in planning and the ability to adapt to changes. Learning from experiences and continuous improvement are also critical aspects of project management. In this regard, it's essential not to limit oneself to a single project management methodology, but to explore various methodologies, as each has its strengths and weaknesses that come to the fore depending on the project type and its planning and execution circumstances.

In the following text, we will compare the previously dominant Waterfall (Natural, Traditional) methodology with one of the most well-known agile methodologies, the Scrum methodology. However, to do this, we will first introduce both methodologies, discuss their fundamental characteristics, strengths and weaknesses, mention the "Agile Manifesto," and then, through analysis based on a hypothetical scenario, arrive at a conclusion regarding when and how to use these project management methodologies.

2. BASIC CHARACTERISTICS OF THE WATERFALL METHODOLOGY

Project management in the Waterfall methodology is a traditional approach to project management that consists of sequential phases executed in order, with minimal backtracking to previous phases. The fundamental characteristics of this methodology are: (Project Management Institute, Inc., 2013)

- The project is divided into clearly defined phases, such as initiation, planning, execution, control, and closure.
- Each phase is executed sequentially, then proceeds to the next phase. Before moving to the next phase, each phase must have clearly defined objectives and specifications. This means that all project requirements and goals are identified and documented in advance.
- The Waterfall approach is carried out linearly, meaning there is no going back to previous phases. Each phase must be fully completed before moving on to the next.
- Quality control activities are conducted in each phase to ensure that objectives are met, and results are satisfactory.
- Projects managed with the Waterfall methodology often require detailed documentation in each phase, including plans, specifications, analyses, and reports.
- The Waterfall methodology is most suitable for projects that can be fully planned in advance and where significant changes are not expected during execution.
- The Waterfall approach can be rigid and less flexible for projects that require significant number of changes or adaptations during execution.

The advantages of the Waterfall methodology can be summarized as follows:

- The Waterfall approach provides a clear structure and precisely defined phases, making it easier to understand and manage the project. Each phase has its specific objectives and tasks, ensuring precision in planning and execution.

- Phases in a Waterfall project often include quality control and verification activities. This allows problems to be identified and addressed in the early stages of the project, reducing the risk of unexpected issues later on.

- The Waterfall methodology requires detailed documentation, including plans, specifications, and reports. This documentation facilitates project progress tracking, communication with stakeholders, and a better understanding of project requirements.

- The Waterfall methodology works best for projects whose requirements and goals can be fully planned in advance and are not expected to change significantly during execution. This is particularly useful for projects with strict regulations, such as healthcare, aviation, and military projects.

- The Waterfall methodology simplifies project planning, monitoring, and management because everything is predefined. This is valuable for organizations that prefer structured processes and precisely controlled end results.

While the Waterfall methodology has its advantages, such as a clear structure and documentation, it may be less suitable for projects that change rapidly or require flexibility. In practice, this means that, for example, if you have a project that demands a highly developed user interface, the delivery of that interface, along with other parts of the software, will only occur during the execution phase. However, during the planning phase, the client did not have a clear plan for this interface, and ideas for improvements only emerged after receiving the finished product. This becomes problematic because there is no going back to previous project phases. The only solution is to open a new project, which introduces new problems, a new budget, additional time spent, and so on. This example is not exotic but something that occurs more frequently, especially with projects heavily involving information technology. Hence, other methodologies, such as agile approaches, have been developed to provide greater adaptability during project execution.

3. AGILE MANIFEST

Agile methodologies have been developed to enable rapid, flexible, and collaborative delivery of software projects and products. The core principles of agile methodologies are outlined in the "Agile Manifesto," which comprises 12 principles: (https://agilemanifesto.org/principles.html)

1. Customer Satisfaction: The primary purpose of software development is customer satisfaction. The agile approach focuses on delivering value to users.

2. Change Is Welcome: Agile teams welcome changes in requirements, even late in development. Agility means being able to adapt to changes to deliver greater value.
3. Frequent Deliveries: Software deliveries should be regular and frequent, with an emphasis on quickly delivering value. This allows users to see and use new features sooner.
4. Collaboration with Customers: Teams and customers should work together throughout the entire project. Open communication and collaboration are crucial.
5. Build Around Motivated Individuals: Provide individuals with the tools and support they need to get the job done. Motivated individuals make a difference.
6. Working Solutions Over Documentation: Agile teams focus on delivering software, i.e., work that brings value. This means less documentation and more action.
7. Maintain a Sustainable Pace: Establishing a stable work rhythm helps maintain productivity and quality. Work should be sustainable in the long run.
8. Technical Excellence: Technical excellence is essential. Teams should aim for high-quality standards and technological solutions.
9. Simplicity: The best way to convey information and solve problems is through simplicity. Avoid unnecessary complexity.
10. Self-Organization: Teams are responsible for planning and decision-making. Self-organized teams better understand and accept responsibilities.
11. Reflection and Adaptation: Regularly monitor team work and continuously adapt to achieve better results. This includes retrospectives and continuous improvement.
12. Team Spirit: Teams should collaborate, communicate, and act as a whole. Team spirit and unity are key to success.

These principles collectively shape the agile approach to software development and projects, enabling teams to be efficient, adaptable, and value-oriented. Reading these principles, it's clear that the aim is to have smaller, more flexible teams that are highly team-oriented and, as such, are flexible enough to deliver product increments during development, which can now be tested and adjusted in the early stages. It's evident that agile methodologies are highly adaptable for managing software projects.

4. BASIC CHARACTERISTICS OF SCRUM PROJECT MANAGEMENT METHODOLOGY

The Scrum methodology relies on incremental and iterative development, where functionalities are developed in small cycles known as sprints. Each sprint brings additional functionalities and enables the team to rapidly deliver new, incremental value. The key characteristics of this project management methodology are: (K. Schwaber, J. Sutherland,

2017)

- Scrum methodology relies on self-organizing teams responsible for developing, testing, and delivering software products. Teams are typically small, self-organizing, and aim to be sufficiently trained to independently perform assigned tasks.

- In Scrum methodology, there is a role called the Product Owner who is responsible for defining priorities and product requirements. The Product Owner communicates with the team and makes decisions about what will be developed. From other side he communicates with stakeholders and he is some kind of interfaces between team and stakeholders.

- The team plans and conducts sprints, typically lasting 2 to 4 weeks. Each sprint begins with planning, where goals and tasks to be completed during that sprint are defined.

- Teams hold daily Scrum meetings to synchronize, share progress information, and identify obstacles. These meetings are short and direct.

- At the end of each sprint, teams hold retrospectives to identify what can be improved in the upcoming sprints.

- Teams use visual control boards (Scrum boards) to track progress and see what is currently in progress, what is completed, and what is remaining.

- The Scrum methodology places a strong emphasis on delivering value to customers after each sprint. The goal is to provide functionality that is usable and can be immediately utilized. Incremental value means that, with each sprint, all the functionalities that were delivered before are in working condition, plus new functionalities resulting from the observed sprint.

- The Scrum methodology allows changes in requirements and priorities during development, facilitating adaptation to changes in the environment.

- The Scrum methodology promotes a culture of continuous improvement and learning from experience to enhance processes and outcomes.

Scrum methodology offers several advantages over the waterfall methodology, especially for projects facing changes and dynamic requirements: (F. Heath, 2021)

- Scrum is highly flexible, enabling teams to adapt to changes in requirements during development. In a waterfall approach, changes are harder to accommodate and often require significantly more effort and resources.

- Scrum allows for early collection of user feedback because functionalities are delivered in short iterations. This helps in identifying and addressing issues and changes before they become significant.

- Scrum focuses on delivering value to customers after each sprint, whereas the waterfall approach typically requires the entire project to be completed before users receive any value.

- Scrum promotes transparency in the project. All team members have insight into progress, priorities, and obstacles, making project management more efficient.

- Scrum encourages teamwork and shared responsibility. Each team member is

accountable for delivering value, which fosters better collaboration and engagement.

- Risks are identified and managed early in Scrum. Teams work on risks in real-time, reducing the likelihood of serious issues in later project stages.

- Scrum enables faster delivery of functionality, which is particularly important in dynamic markets where rapid responses to changes are highly valued.

- Scrum strongly focuses on customer satisfaction. Teams regularly communicate with users and adjust products to meet their needs.

- Scrum fosters continuous process improvement and better results through retrospectives and iterations.

- Scrum allows for better cost and resource control as teams regularly estimate and adjust the scope of work.

Scrum is an agile methodology used for developing software products, but it can be applied to other domains as well. The primary goal of the Scrum methodology is to enable efficient project management and deliver value to customers in iterative cycles. While Scrum methodology has many advantages, it's important to note that it is not a one-size-fits-all solution and may not be suitable for all projects. Some projects, such as those with strict and well-defined requirements, may work better with a waterfall approach. The choice between Scrum and the waterfall methodology depends on the specific project requirements and circumstances.

5. COMPARISON OF SCRUM AND WATERFALL METHODOLOGIES

It is clear from the above that for smaller software-oriented projects, agile methodologies, especially the Scrum methodology, have prevailing advantages over the Waterfall methodology. However, what happens when managing large projects with well-defined requirements and a heterogeneous composition of participants (meaning that project members are not only IT professionals)? In these situations, project management can be complex, and the choice between Scrum and the Waterfall project management methodology will depend on the specific needs and characteristics of the project. Accordingly, the following key factors should be considered:

- If the project requirements are tightly defined, and changes are not expected or are minimal, the Waterfall methodology may be appropriate. In the Waterfall methodology, all phases are meticulously planned in advance, which can be useful for projects with clear requirements.

- If there is a need for greater flexibility in the project, Scrum can be beneficial. Scrum allows for quick adaptation to changes and adjustments during development, which is particularly useful if the project faces uncertainty or changing requirements.

- In some cases, projects may use "hybrid approaches" that combine elements of both Scrum and Waterfall methodologies. For example, a project may use the Waterfall methodology for the planning and design phase and then switch to Scrum for the execution and testing phase.

- Projects with a heterogeneous composition and a large scope often carry higher risks. Scrum can enable better risk management because risks are identified and managed in real-time during iterations.

- It's important to consider the level of experience and training of project participants. Scrum requires a certain understanding of agile principles and practices, while the Waterfall methodology may be more familiar and easier to apply, especially for project members who are not from an IT background.

- Projects with a diverse composition often require good communication and collaboration. Scrum promotes this type of interaction, while the Waterfall methodology may require a stricter communication structure.

- Large projects require efficient monitoring and management. The Waterfall methodology can provide a clear structure for monitoring, while Scrum requires continuous tracking of progress during iterations.

In essence, the choice between Scrum and Waterfall for larger projects depends on the specific characteristics of the project, as well as the needs and preferences of the team and organization. It is possible to combine elements of both approaches to achieve the best balance between control and flexibility. It's important to thoroughly consider all factors and make a decision that best suits the project.

To delve deeper into this comparison, consider a situation where we want to convince the bank's management to support the replacement of the Core Banking System (CBS) with a newer one from another vendor, using the Scrum methodology, for example. Scrum methodology can be beneficial, although it requires a different approach compared to traditional Waterfall methodologies. One possible scenario could be:

1. Create a sprint campaign plan: Begin by defining sprint campaigns, i.e., sets of goals that will be achieved during each sprint. The goals should be focused on preparing for the replacement of the CBS and achieving concrete steps in the process.
2. Identify key functionalities and requirements: Think about the key functionalities and requirements of the new CBS and identify them in advance. This will help prioritize the development and implementation of these features.
3. Create a backlog: Create a backlog, a list of requirements and functionalities that will be implemented during the sprint campaign. This list will serve as the basis for planning and tracking work during sprints.
4. Assemble a Scrum team: Put together a Scrum team to work on the project. This team should be multifunctional and include members with different skills required for the implementation of the new system.

5. Sprint planning: Plan sprints with the aim of achieving concrete value and progress towards replacing the CBS. Decide how long each sprint will last and what the priorities will be for each sprint.
6. Regularly communicate with the bank's management: In Scrum methodology, transparency and regular communication are key. Therefore, regularly update the management on the project's progress and the achievement of goals defined in the sprint campaigns. Organize Sprint Review meetings to present the progress made and engage in open discussions with significant stakeholders.
7. Adapt to changes: Scrum allows for quick adaptation to changes. If new information or changes in priorities arise during the project, the Scrum team can easily adjust the plan and priorities.
8. Continuous improvement: After each sprint, organize retrospectives to identify what worked well and what can be improved. These retrospectives enable the team to continuously enhance their work.
9. Documentation and risk monitoring: While Scrum promotes "less documentation and more action" it's still important to document key aspects of the project and monitor risks. This will help stay within the boundaries and be prepared to respond to possible challenges.

At first glance, it might be said that using Scrum can achieve better transparency, a faster response to changes, and a focus on delivering value during the CBS replacement process. It's essential to highlight the advantages of the agile approach, such as quicker adaptation to changes and continuous improvement, to convince the management of the benefits of this approach in such a project. However, in practice, management may demand precise indicators, particularly costs, employee engagement, duration estimates. Additionally, considering that more banking professionals are involved in the project than programmers, it raises the logical question of what to expect in such a case.

In such cases, the traditional Project Chart (Gantt chart) can provide more clarity and precision in project management compared to agile methodologies like Scrum. Taking this into consideration, we arrive at the following comparison:

1. Developing a Project Chart involves:
   - Precision in planning: The Project Chart enables detailed planning and provides accurate estimates for each project phase. This is useful for budgeting and cost management.
   - Defined deadlines: The Gantt chart allows for clearly defined deadlines for each project phase, aiding in time tracking and management.
   - Easier communication with management: The Project Chart offers a visually clear representation of the project, simplifying communication with management and conveying critical information.

- Compatibility with the Waterfall method: The Project Chart aligns better with this approach as it provides a stricter plan and control.

2. Scrum methodology implies:
   - Flexibility: As mentioned before, Scrum is flexible and allows for adaptation to changes. This is useful when it's challenging to predict all project elements accurately in advance. It's worth noting that for a project that is mostly well-planned but has some less certain parts, Scrum can be beneficial in such cases.
   - Focus on value: Scrum concentrates on delivering value throughout the project's development. This can help in demonstrating progress during the early project phases.
   - Improved interaction with end-users: Scrum enables regular interaction with users, which can enhance understanding of their needs and promote their involvement in the development process.
   - Continuous improvement: Scrum encourages continuous process and results improvement, valuable for optimizing the team's performance over time.

The choice between a Project Chart (Gantt chart) and Scrum methodology depends on the specific needs and requirements of the project, as well as the preferences and expectations of management. In situations where precise costs, accurate deadlines, and a firm plan are of utmost importance, the Project Chart may be the better choice. However, Scrum can be useful in projects where there is a need for greater flexibility, faster adaptation to changes, and improved interaction with end-users.

Here, some of the characteristics of the Scrum methodology, which were not critical in the previous example, have been intentionally reiterated. We will attempt to further elaborate on the fact that the success of the Scrum methodology primarily depends on the ability of Scrum teams to independently perform their assigned tasks, be self-organizing, and act as a homogeneous team. Additionally, one of the tenets of the Scrum methodology is that the Developer team is structured in a way that eliminates titles and rankings within the team (to facilitate homogeneity) and that there is only collective responsibility for the work done. On the other hand, banks are traditionally organized hierarchically, which can pose a challenge when forming Scrum teams.

But first, let's consider the challenge of building a good Scrum team and what it takes to achieve that. Creating a highly-profiled, homogeneous team can be challenging, especially in situations where teams are new and have limited experience with Scrum. In such cases, it would be useful to do the following:

1. The first step is to provide team members with education on Scrum methodology and agile principles. Understanding the basics of Scrum is crucial for successful implementation.
2. Engaging mentors or Scrum experts can be helpful, especially in the early stages of team work. Mentors can share their experience and provide guidance.
3. It's important for team members to build trust among themselves. Encourage open communication and collaboration to create a positive work atmosphere.

4. Define clear goals and expectations for the team. Each member should understand what is expected of them.
5. Encourage team members to take responsibility for their work and contribute to the team's goals.
6. Teams without experience should receive ongoing support and learning opportunities. This may include regularly conducting retrospectives and identifying areas for improvement.
7. Help the team understand the focus on delivering value. Encourage them to concentrate on customer satisfaction and achieving project goals.
8. Scrum promotes continuous improvement. Encourage the team to identify and resolve issues to improve their work over time.
9. Developing a high-performing Scrum team takes time. Expect challenges at the beginning and be prepared to address them together with the team.
10. Creating a positive team environment is essential. Encourage the team to innovate, collaborate, and engage in continuous learning.

Developing such a team requires patience and dedication, but it can result in a highly efficient and productive team capable of self-organizing, self-managing, and successfully completing projects. It's important to support the team and work together to develop skills and capabilities.

Let's now consider the conclusion regarding the development of a Scrum team, which is patience and dedication. Does this mean that a bank looking to transition to a new program should first form Scrum teams, train them, and patiently wait for them to mature? How long would this maturation process take, and on the other hand, the bank is naturally impatient as it wants to renew its program to remain competitive in the market?

In such situations, there are several strategies that an organization can employ to expedite the maturation process of Scrum teams:

- As mentioned earlier, engaging experienced agile coaches can accelerate the learning and implementation of Scrum. They can work directly with the teams to provide guidance and support.

- An organization can consider a hybrid approach, combining elements of Scrum with some traditional methods to meet the need for quick responsiveness. For example, teams can use Scrum for software development aspects of the project while employing a traditional approach for other project aspects.

- Intensive training programs and mentorship can help teams quickly grasp Scrum and apply it. This involves working with experts who collaborate with the teams until self-organization, self-management, and high efficiency are achieved.

- The bank can hire experts in the banking industry who understand the specific needs and regulations of the sector. This can help teams develop solutions that align with banking requirements more rapidly.

- Defining clear and measurable project goals can help teams focus on delivering value as quickly as possible.

- Regular monitoring and evaluation of team progress are essential. This will allow the identification of project areas that need improvement and the opportunity for quicker adaptation.

It's important to note that there's no universal timeframe for the maturation of Scrum teams, and the speed of maturation will depend on various factors, including the current knowledge and skills of the teams, the resources available for training and support, and the complexity of the projects on which the teams work. Organizations aspiring to adopt an agile way of working should be aware that it takes time to achieve a high level of self-organization, self-management, and efficiency. In the meantime, organizations can use hybrid approaches to balance the need for rapid responsiveness with the development of agile teams.

Among the aforementioned tips, the one mentioning the adoption of a hybrid method is particularly interesting, especially in situations where there are many non-IT professionals involved in the project, as they are more challenging to train within Scrum teams. A hybrid approach can be an effective way to strike a balance between the need for agility and flexibility and the requirements for clear planning and control, especially in situations such as the replacement of the CBS in a bank.

A hybrid approach can be considered beneficial for several reasons:

- Flexibility in Implementation: A hybrid approach allows for selecting the best elements from different methodologies to meet the specific needs of a project. For example, it can involve using agile methodologies for software development while simultaneously applying the traditional Gantt chart for planning and tracking activities.

- Managing Complexity: Large projects, especially in the banking sector, are often extremely complex and require detailed planning and management. A hybrid approach can provide better management of this complexity.

- Incorporating Non-IT Team Members: Team members who are not from an IT background may feel unprepared to work in a fully agile environment. A hybrid approach can accommodate their needs and comfort.

- Regulatory Compliance: Banking is often subject to strict regulations. A hybrid approach can facilitate reporting processes and compliance with regulatory requirements.

- Balancing Speed and Control: A hybrid approach allows an organization to maintain a balance between the speed of delivery and project control.

It's essential for the organization to carefully consider the specific requirements of each project and adapt the methodology accordingly. A hybrid approach can be especially useful in situations where different team members have varied skills and constraints.

Given all these analyses, one proposed approach for the described case of replacing the CBS in a bank is as follows:

- Organize Scrum teams with IT professionals and banking technologists who have expertise in specific areas.

- Use the Waterfall methodology for other aspects of the project.

- Generally proceed with the Waterfall method, while handling critical tasks such as GAP analysis (which identifies differences between the existing and new CBS to support already sold products not covered by the new software solution) and the user interface development iteratively through small groups organized into Scrum teams.

This approach offers several key advantages:

- Rapid Value Delivery: By using Scrum teams for critical IT project components, software and technology aspects that are of paramount importance can be developed and delivered more swiftly. The mentioned GAP analysis can be carried out through Scrum teams, while parallel work is done on iterative user interface development, training, and more.

- Greater Adaptability: Scrum allows for quick adaptation to changes, which is valuable in the IT field where requirements often change, especially for user interface development, for instance.

- Precision in Traditional Aspects: The Waterfall methodology enables precise planning and control of other project segments, making it easier to organize team members who are not in Scrum teams.

- Clear Deadlines and Budget: Using the Waterfall approach allows for precisely defined deadlines and budgets, which are crucial for projects in the banking industry.

- Resource Optimization: Teams specialized in specific areas can efficiently leverage their skills and resources.

- Risk Mitigation: Combining agile and Waterfall methodologies can help reduce risks and facilitate project management.

The key is to carefully assess where Scrum and agile approaches best meet the project's needs and where precision and clearly defined control are necessary. A hybrid methodology can be a highly effective way to strike a balance between these requirements. It's crucial to involve relevant experts and adapt the approach to the specific characteristics of the project.

6. CONCLUSION

Based on everything discussed, the conclusion would be as follows. For purely IT software projects, Scrum is the best solution. For well-defined large projects that require "military" precision, the Waterfall methodology emerges as the best solution. In other variations, especially when it's a mixture of IT and business, as in the case of replacing a CBS in a bank, it's best to go with a hybrid method.

For - Scrum (Agile Approach for IT Projects):

- Scrum enables rapid value delivery through iterations, which is useful for IT software projects where requirements often change.
- The agile approach allows better adaptation to changes in requirements.
- Regular interaction with users improves understanding of their needs and enhances user satisfaction.

Against - Scrum:

- Implementing Scrum may require changes in an organization's culture and practices, which can be challenging to carry out. For example, reconciling an extremely hierarchical approach in an organization (such as a bank or the military) with Scrum's logic of self-organizing teams where self-management and equality prevail.
- Scrum is less precise in terms of long-term planning and budgeting.

For - Waterfall Methodology (for well-defined projects):

- The Waterfall methodology allows detailed and precise project planning, which is useful for projects where requirements are well-defined in advance.
- The Waterfall methodology provides clearly defined deadlines and budgets, which are important in situations where precision is critical.

Against - Waterfall Methodology:

- The Waterfall methodology can be inflexible when changes in requirements are needed during the project.
- Long-term projects are susceptible to unforeseen issues, which can increase risk.

For - Hybrid Methodology (for projects that require a balance between precision and agility):

- A hybrid methodology allows balancing between agility (through Scrum) and precision (through Waterfall) according to project needs.
- Projects can be effectively managed by following agile principles for rapid delivery and precise methodologies for control and planning.

Against - Hybrid Methodologies:

- Requires effective management by experienced managers to ensure that both components (agile and Waterfall) work together and achieve the project's goals.

In the end, it's important for each organization to carefully consider the specific needs of its project and environment and choose the methodology that best suits those needs. Each of the mentioned methodologies has its advantages and disadvantages, and the right adapted methodology can help in the successful completion of the project. It's also important for the organization to be ready to adapt its approach to deal with changes during the project.

REFERENCES

[1] R. Mulcahy, *PMP Exam Prep*, Eighth Edition, RMC Publications, Inc., 2013.

[2] *A Guide to the Project Management Body of Knowledge (PMBOK® Guide)* – Fifth Edition, Project Management Institute, Inc., 2013.

[3] *Principles behind the Agile Manifesto*, https://agilemanifesto.org/principles.html, visited 15.10.2023.

[4] K. Schwaber, J. Sutherland, *The Scrum Guide. The Definitive Guide to Scrum_ The Rules of the Game-Scrum*, 2017.

[5] F. Heath, *The Professional Scrum Master* (PSM I) Guide Copyright ©, Packt Publishing, 2021.